Winter 2017

The Proton Spin Structure Function G2P at Low Momentum Transfer

Tobias Badman
University of New Hampshire, Durham

THE PROTON SPIN STRUCTURE FUNCTION G_2^P AT LOW MOMENTUM TRANSFER

BY

TOBY BADMAN

B.S. in Physics, Florida Institute of Technology, 2009

DISSERTATION

Submitted to the University of New Hampshire
in partial fulfillment of
the requirements for the degree of

Doctor of Philosophy

in

Physics

December, 2017

This dissertation has been examined and approved in partial fulfillment of the requirements for the degree of Doctor of Philosophy in Physics by:

Dissertation Director, Karl Slifer
Associate Professor, Physics

John Dawson, Emeritus Professor, Physics

Nadia Fomin, Assistant Professor, Physics

Maurik Holtrop, Professor, Physics

Mark McConnell, Professor, Physics

On September 14, 2017

Original approval signatures are on file with the University of New Hampshire Graduate School.

For my parents, Dennis and Brenda. I stand on the shoulder of giants.

Acknowledgments

I find it difficult to summarize in a few paragraphs the gratitude that is owed to those who helped to see this work come to fruition. So many of my family, friends and colleagues have helped, both in knowledge and patience, in this endeavour and I thank you all for your unwavering support.

Above all I want to thank my advisor, Karl Slifer. Even in the most difficult of times your perseverance and positivity was an inspiration. I have found throughout my graduate career that an advisor with such investment and care in the success of his students is a rarity. I can say with certainty that I could not have asked for a better mentor.

I would not have survived the graduate coursework at UNH without the help of my fellow classmates. Thank you to Ian and Alex, the long days spent in the TA lounge were made bearable by your lighthearted conversation and antics. Thanks to Narges for your endless positivity, even after hours of questions and studying. And, of course, thank you to Dan and Max and the true friendship that formed over pints at Caras. I never would have achieved this without your help.

The g_2^p experiment was no easy feat by any means. The duration was long and the problems were plentiful. The success of the experiment is owed entirely to its collaboration members. Thank you to the spokespeople Jian-Ping Chen, Alexandre Camsonne, Don Crabb and again my advisor, Karl Slifer, for seeing to it that we made the best of what we were given. Your experience and dedication is what saw this monumental effort through to its end. Coming into this extraordinarily complex work as a naïve graduate student was made easier by the help of the post-docs Kalyan Allada, Ellie Long, James Maxwell, Vincent Sulkosky and Jixie Zhang. Thank you for your patience in answering my every mundane question and guiding me on the right track. Thank you to my fellow graduate students, Melissa Cummings, Chao Gu, Min Huang, Jie Liu, Pengjia Zhu and Ryan Zielinski. I am truly honored to have worked with such an intelligent group of students. Not to

mention the endless midnight-to-8am ‘owl shifts’ that were made bearable as a team.

Finally, I want to thank my family. Thank you to my sisters Margie and Millie for always believing in me, even when you weren’t quite sure exactly what I was doing. And thank you to my parents, Brenda and Dennis. Through all of the science kits and camps, your support is what brought me to where I am today.

Table of Contents

List of Tables

List of Figures

ABSTRACT

THE PROTON SPIN STRUCTURE FUNCTION G_2^P AT LOW MOMENTUM TRANSFER

by

Toby Badman

University of New Hampshire, December, 2017

Over the past several decades Jefferson Lab National Accelerator Facility has proven to be extremely successful in its endeavor to study the polarized structure of nucleons. Measurements of these nucleon structure functions have proven to be powerful tools in testing and understanding a number of effective theories of QCD. The neutron spin structure functions, $g_{1,2}^n$, and the proton spin structure function, g_1^p, have been measured to very high precision over a wide kinematic range. However, the second proton structure function, g_2^p, remained largely unmeasured. The primary goal of Jefferson Lab Hall A experiment E08-027 was to perform an inclusive measurement of the proton g_2 structure function for the first time in the low momentum transfer range of $0.01 < Q^2 < 0.13$ GeV^2. The experiment acquired data at Jefferson Lab in Hall A during February - May of 2012. Experiment E08-027 utilized a polarized frozen NH_3 target and a polarized electron beam to examine inclusive eP scattering in the resonance region. Dynamic Nuclear Polarization was used to drive proton target polarizations to upwards of 70% at 5T and 15% at 2.5T for high statistics measurements of the double spin asymmetry. Using a convolution of the Bosted/Christy model and data for the unpolarized cross section contribution, the spin structure function g_2^p was extracted for two low Q^2 bins. Results for the moments of these structure functions find reasonable agreement with χ_{PT} predictions.

Chapter 1

Introduction

The nature of physics is to understand and categorize the observable Universe. In a completely literal sense observations are done when light scatters off of an object and into the eye. The brain interprets the scattered light and an image is formed. This is a kind of 'scattering experiment' in the most basic of forms and creates the foundation on which significantly more complicated systems are built. The necessity for complexity arises when we ask the question: What happens when the object we want to observe is too small for the human eye to resolve? Lenses can be used to increase magnification and focus scattered light as it enters the eye, but these tools can only bring us so far. It wasn't until 1911 that a physicist by the name of Ernest Rutherford thought to scatter positively charged alpha particles off of a gold foil material and detect the scattered particle in a scintillating material instead [13]. With this method the structure of an individual atomic nucleus, with a massive positively charged center, could be resolved. Thus the modern era of scattering experiments was born.

Soon after, a complete picture of the atomic structure was formed. At it's core, the atom contains a cluster of positive and neutral charged nucleons called Protons and Neutrons, with an orbital cloud of electrons around it. Fundamental observables like 'mass' and 'charge' for each of these particles allowed for a better understanding of how they interact with the known forces. In 1922, two german physicists by the names of Otto Stern and Walther Gerlach attempted a new kind of experiment where they passed a beam of silver atoms through an inhomogeneous magnetic field [14]. To their

surprise, the emerging particles were detected at two highly localized points. This could not be explained with the understanding of electron properties at the time. The concept of 'spin', a new fundamental observable, was introduced shortly after to attempt to account for this result.

Spin is an interesting phenomena. In theory a particle behaves like a tiny globe rotating on its

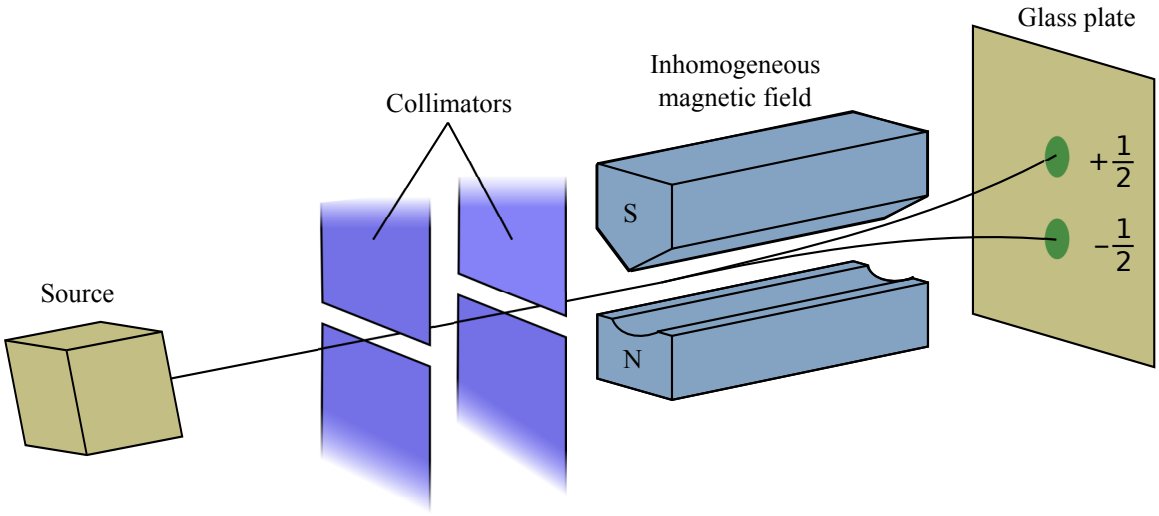

Figure 1-1: An overview of the Stern-Gerlach experiment. Vertical deflection of a beam of silver atoms was observed as it passed through a magnetic field.

axis. The direction of the particles spin is along it's axis of rotation, pointing 'up' when looking at the particle rotating 'counter-clockwise'. When a charged particle rotates on its axis, it creates a dipole magnetic field, defined as it's 'magnetic moment', and so naturally aligns itself with any external magnetic field. The problem with this approach comes from the fact that the electron appears to be a point-like particle. All evidence to date indicates that the electron is without any dimensionality whatsoever. So how can an object without size rotate on it's axis? We are simply forced to abandon the classical notion of spin and assign it as a fundamental property of the particle.

The theorist Paul Dirac formulated the magnetic moment of a point-like spin-1/2 particle to be

$$\mu = \frac{e}{2M} \tag{1.1}$$

where e represents the particles charge, and M it's mass. This agreed very well with the experimental evidence for the electrons magnetic moment. In 1933 Stern and Gerlach attempted their experiment again, but this time measuring the protons magnetic moment [15]. The result was yet another surprise. It was found that the proton had a magnetic moment that disagreed with Dirac's prediction by 150%. This discrepancy was the first clear indication that the proton was not a point-like particle.

The ability to peer inside of the proton to see what this internal structure looked like required a huge leap in technological advancement. Decades after the discovery of the proton's 'anomolous magnetic moment', linear accelerators were used to verify that the Proton did, indeed, have a substructure, and an entire field of Physics emerged that began mapping out the nature and behavior of these constituents.

1.1 Scattering Experiments

Modern linear accelerators utilize the exact same method of scattering that Rutherford developed in 1911. A beam of particles is incident on the target material of interest. The particles in the beam are deflected by the target by some angle where a detector is set up to record each event. This is exactly the Rutherford scattering experiment, the only difference being the scale. Rutherford used a relatively low energy alpha beam to resolve the nucleus, so the entire experiment was able to be set up on a table in a laboratory room. Modern accelerators seek to peer much deeper into the atom, this requires significantly higher energy and more statistics. The Jefferson Laboratory accelerator, where the work of this thesis was done, is a quarter of a mile long with a detector stack three stories tall.

Despite the difference in scale, the fundamental quantity that is measured in any scattering experiment is the same. This quantity is known as the particle 'cross section'. The cross section defines the solid angle in which a particle is deflected into in terms of its closest distance of approach to the

scattering center and its energy, as shown in Figure 1-2. With this basic setup, inferences about

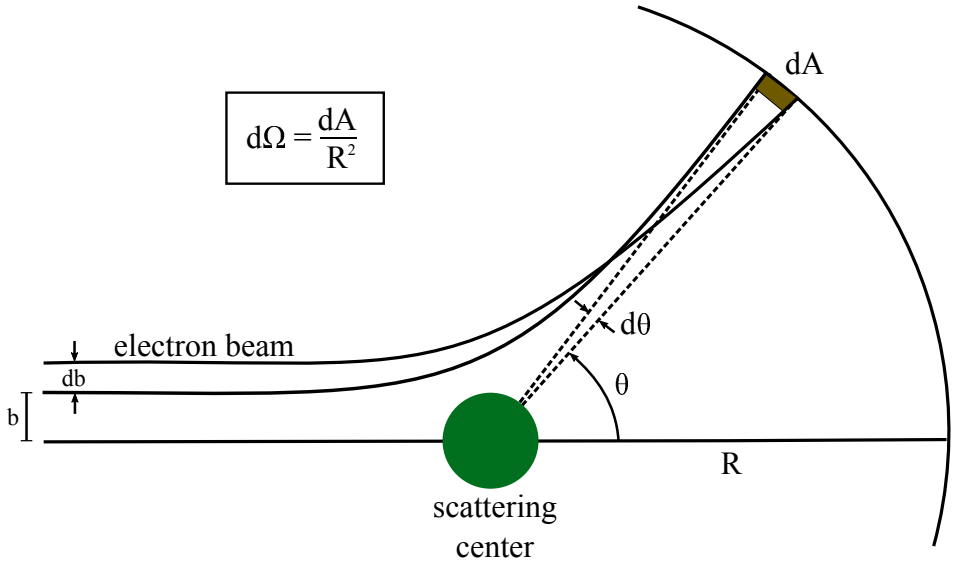

Figure 1-2: The basic machinery behind a scattering interaction. An incoming particle with impact parameter 'b' is deflected by a fixed scattering center into some solid angle, dΩ.

the structure and behavior of the scattering center can be made from the cross section as detected by the scattered particle. The details of this process are discussed in the following sections.

Chapter 2

Inclusive Electron Scattering

The fundamental observable in any scattering interaction is the cross section. Using the knowledge of lepton scattering from the well understood framework of Quantum Electrodynamics, the measured cross section can be a powerful tool in studying the internal structure of the nucleon. This is done by relating the cross section to kinematically defined 'structure functions' which describe the nucleons internal structure. This chapter will focus on the derivation of the structure functions and the different kinematic regions of interest.

2.1 Kinematic Variables

Before deriving the details of the inclusive scattering cross section a number of commonly used variables must be defined. The purpose of these variables is to represent the scattering interaction in terms of its kinematic quantities. The first order Born approximation for such an interaction is shown in Figure 2-1. In this interaction an incoming lepton (in the form of an electron) with four momentum $k^\mu = \left(E, \vec{k}\right)$ exchanges a single 'virtual photon' with a fixed hadron target (in the form of a proton) with initial four momentum $P^\mu = \left(\epsilon, \vec{P}\right)$ which scatters the electron by an angle θ with final state four momentum $k'^\mu = \left(E', \vec{k'}\right)$ giving the proton a final four momentum state of $P'^\mu = \left(\epsilon', \vec{P'}\right)$. For an inclusive scattering experiment the final proton state goes unobserved, but its kinematics can be reconstructed from its initial state together with the initial and final states of the electron. The virtual photon exchanged in the interaction carries four momentum $q^\mu = (\nu, \vec{q})$.

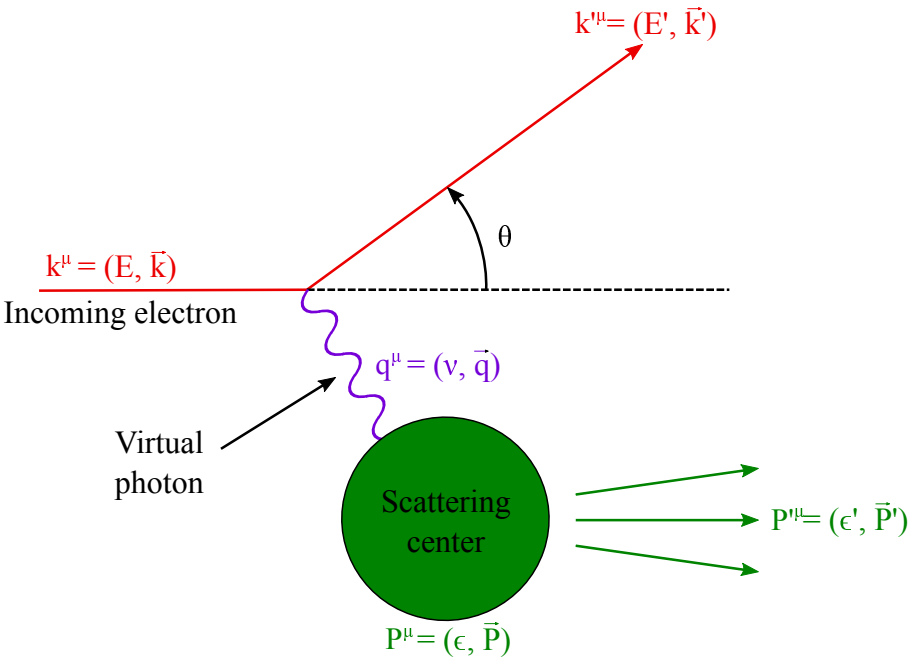

Figure 2-1: First order Born approximation for the lepton-hadron scattering interaction.

Using conservation of energy and momentum we see that ν is just the energy carried away by the electron, while q is the exchanged momentum and has the property $q^2 < 0$ due to being a space-like virtual photon. Since q^2 is less than zero it is convenient to introduce a new variable $Q^2 = -q^2$, the four momentum transfer squared of the process. Since only the electron final state is observed, an additional quantity, called the invariant mass, is defined to represent the proton final state, $W = \sqrt{(p+q)^2}$. If we consider the laboratory reference frame, where $P^\mu = (M, 0)$, the following kinematic relations are defined:

$$\nu = E - E' = \epsilon - \epsilon', \tag{2.1}$$

$$Q^2 = -q^2 = 4EE' \sin^2 \frac{\theta}{2}, \tag{2.2}$$

$$W = \sqrt{M^2 + 2M\nu - Q^2}. \tag{2.3}$$

2.2 Scattering Cross Sections

The formal definition of the scattering cross section as measured in the laboratory is given by

$$\sigma \equiv \frac{P/\delta x}{N} \tag{2.4}$$

where P gives the probability of an event at a specific kinematic 'unit' δx, and N is the number of scattering centers in the target. In reality the cross section must be defined in a way that it can be compared to models created over a wide kinematic range. To achieve this, the cross section is measured in bins that cover small kinematic regions over the area of interest, and this specific 'differential cross section', $d^2\sigma/d\Omega dE$, is integrated to find the total cross section as defined in Equation 2.4.

Rutherford showed that the differential cross section for a positively charged nucleus can be expressed in terms of measurable quantities as

$$\left(\frac{d\sigma}{d\Omega}\right)_{Rutherford} = \frac{Z^2e^4}{16E^2}\frac{1}{\sin^4(\theta/2)} \tag{2.5}$$

where Ze is the nuclear charge, E is the energy of the scattered particle, and θ is the scattered angle [16]. The above equation for the cross section makes a number of assumptions, namely that the target nucleus has no recoil effects, and is spin independent. If we include a nuclear recoil factor of the form E/E' and spin dependance of the interaction to conserve helicity, we arrive at the familiar Mott cross section for a point particle,

$$\left(\frac{d\sigma}{d\Omega}\right)_{Mott} = \frac{\alpha^2}{4E^2}\left(\frac{\cos^2(\theta/2)}{\sin^4(\theta/2)}\right)\frac{E'}{E} \tag{2.6}$$

where $\alpha \simeq 1/137$ is the fine structure constant. The Mott cross section represents helicity dependent scattering of two particles with no internal structure. A measurement of this quantity

experimentally for the proton would find some deviation due to internal contributions. The real experimental proton cross section is then given by

$$\left(\frac{d\sigma}{d\Omega}\right)_{exp} = \left(\frac{d\sigma}{d\Omega}\right)_{Mott} \times |F(\vec{q^2})|^2 \tag{2.7}$$

where any internal structure of the proton is lumped together in the structure function $|F(\vec{q^2})|^2$. To determine information about the form and kinematic behavior of the structure function a more rigorous approach to the cross section derivation is required.

2.2.1 Tensor Formulation

According to Fermi's Golden Rule the differential cross section can be written as

$$\frac{d\sigma}{d\Omega} = \frac{1}{j}\frac{2\pi}{\hbar}|\mathfrak{M}|^2 \tag{2.8}$$

where j is the electron current density and $\mathfrak{M} = \langle\psi_f|\mathscr{H}_{int}|\psi_i\rangle$ is the transition amplitude for the specific hamiltonian of the interaction of interest which contains all of the physical dynamics of the electron-nucleon interaction. The transition amplitude for an interaction can be derived using the covariant Feynman Rules for quantum electrodynamics [17]. If we consider the Feynman diagram for the scattering interaction of two point-like particles, as shown in Figure 2-2, a transition amplitude can be constructed by assigning factors based on the features of the diagram itself. For the specific case of electron-muon scattering this results in a transition amplitude of

$$\langle|\mathfrak{M}|^2\rangle = \frac{(4\pi\alpha)^2}{q^4}L_e^{\mu\nu}L_{\mu\nu}^m \tag{2.9}$$

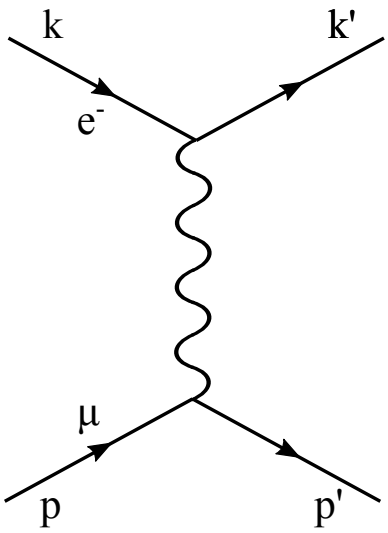

Figure 2-2: First order Feynman diagram interaction approximation for two particles with no substructure.

where we have deconstructed the amplitude into electron and muon 'tensors' which contain all of the relevant information for each particle,

$$L_e^{\mu\nu} = 2\left(k^\mu k'^\nu + k^\nu k'^\mu + g^{\mu\nu}(M^2 - k\cdot k')\right), \tag{2.10}$$

$$L_{\mu\nu}^m = 2\left(p_\mu p'_\nu + p^\nu p'^\mu + g^{\mu\nu}(m^2 - p\cdot p')\right) \tag{2.11}$$

where k and p are momentum vectors as defined in Section 2.1 and $g^{\mu\nu}$ is the coupling strength of each interaction vertex. Using the kinematic relations discussed earlier, and by substituting Equations 2.9, 2.10 and 2.11 into 2.8 we arrive at a formal definition of the differential cross section in terms of experimental quantities for electron-muon scattering

$$\frac{d\sigma}{d\Omega} = \frac{\alpha^2}{4E^2\sin^4(\theta/2)}\frac{E'}{E}\left(\cos^2\frac{\theta}{2} - \frac{q^2}{2M^2}\sin^2\frac{\theta}{2}\right). \tag{2.12}$$

If we consider the limiting case where the mass of the scattering center is much larger than the scattering energy ($M \gg q$) we return to the Mott cross section result (Equation 2.6) as derived in Section 2.2.

To extend this formalism to the hadronic case, such as electron-proton scattering, the muon tensor in Equation 2.9 must be replaced by a more complex hadron tensor

$$\langle|\mathfrak{M}|^2\rangle = \frac{(4\pi\alpha)^2}{q^4} L_e^{\mu\nu} W_{\mu\nu}^{proton} \tag{2.13}$$

where $W_{\mu\nu}^{proton}$ is the new proton tensor function to be constructed. By considering all possible covariant four-vector terms in the lepton-hadron scattering interaction, and demanding conservation of current, we arrive at the following definition for the hadron tensor [18]

$$W_{\mu\nu} = W_1\left(\nu, Q^2\right)\left(-g_{\mu\nu} + \frac{q_\mu q_\nu}{q^2}\right) + \frac{W_2\left(\nu, Q^2\right)}{M^2}\left(p_\mu + \left(\frac{q\cdot p}{q^2}\right)q_\mu\right)\left(p_\nu + \left(\frac{q\cdot p}{q^2}\right)q_\nu\right) \tag{2.14}$$

where W_1 and W_2 are kinematic form factors which parameterize all of the physical information at the interaction vertex between the lepton and the hadron. Substituting Equation 2.14 into the definition of the cross section and using known kinematic relations, in similar fashion to the electron-muon derivation, we arrive at a formal cross section definition for electron-proton scattering,

$$\frac{d\sigma}{d\Omega} = \frac{\alpha^2}{4E^2\sin^4(\theta/2)}\frac{E'}{E}\left(W_2\cos^2\frac{\theta}{2} + 2W_1\sin^2\frac{\theta}{2}\right). \tag{2.15}$$

The kinematic form factors W_1 and W_2 encompass all of the unknown behavior of the interaction vertex between the proton and electron. To further understand these form factors and interpret their physical meanings we must break down the kinematic regions based on the Q^2 of the interaction. The reasoning behind this is that changing the Q^2 of the scattering interaction acts to change the resolving power of the protons structure. At low Q^2 the proton begins to approach the behavior of a point-like particles where the scattering occurs only at the surface, as Q^2 is increased internal structure is revealed. It is clear from this behavior that the form factors are highly Q^2 dependent and different approaches to their physical meaning must be utilized depending on the resolving

power being used.

Elastic Scattering

When electrons are scattered elastically the proton appears to be a point-like particle with mass M. In this kinematic region the energy and scattering angle are fixed by conservation laws. Here it is convenient to define two new quantities, G_E and G_M such that

$$G_E^2 \equiv (1+\tau)W_2 - W_1 \tag{2.16}$$

$$G_M^2 \equiv \frac{W_1}{\tau} \tag{2.17}$$

where $\tau \equiv \nu^2/Q^2$. Substituting G_E and G_M into Equation 2.15 gives the well-known Rosenbluth cross section formula

$$\frac{d\sigma}{d\Omega} = \frac{\alpha^2}{4E^2\sin^4(\theta/2)}\frac{E'}{E}\left(2\tau G_M^2\sin^2\frac{\theta}{2} + \frac{G_E^2+\tau G_M^2}{1+\tau}\cos^2\frac{\theta}{2}\right). \tag{2.18}$$

G_E and G_M are known as the Sachs magnetic and electric form factors. The fourier transform of these form factors gives the magnetic density and charge distributions of the proton, respectively.

Deep Inelastic Scattering

As Q^2 and the invariant mass of the proton final state continues to increase, i.e. the proton is hit harder, individual structure within the hadron becomes distinguishable. In this limit the form factors reduce to functions only of the kinematic quantities Q^2 and the energy transferred in the interaction [19]. We define a new dimensionless constant, Bjorken x, in this region that parameterizes the form factors

$$x_b = \frac{Q^2}{2M\nu}. \tag{2.19}$$

In this 'Bjorken limit' it is convenient to express the form factors as dimensionless functions of x, which become independent of Q^2,

$$F_1(x) \equiv MW_1(\nu, Q^2), \tag{2.20}$$

$$F_2(x) \equiv \nu W_2(\nu, Q^2). \tag{2.21}$$

Where $F_{1,2}$ are the unpolarized parton 'structure functions' which describe the momentum distribution of partons within the proton. The fact that the structure functions are independent of Q^2 indicates that the partons are point-like particles with no internal structure.

The experimentally measured structure functions have been shown to share the following relationship:

$$2xF_1(x) = F_2(x) \tag{2.22}$$

which is known as the Callan-Gross relation and is predicted to hold for all spin-1/2 particles. The structure functions F_1 and F_2 continue to be measurements of interest in accelerator experiments. Experimental results for the proton showing Q^2 independence is seen in Figure 2-3.

2.2.2 Polarized Structure Functions

To extend the formulation of Section 2.2.1 to the case of polarized lepton-hadron scattering the lepton and hadron tensors must be broken down into symmetric and antisymmetric components,

$$L^{\mu\nu} = L_S^{\mu\nu} + L_A^{\mu\nu}, \tag{2.23}$$

$$W_{\mu\nu} = W_{\mu\nu}^S + W_{\mu\nu}^A. \tag{2.24}$$

The symmetric components of the tensor functions are, by definition, invariant under the exchange of the indeces μ and ν because the scattering is identical in all reference frames. This is the case

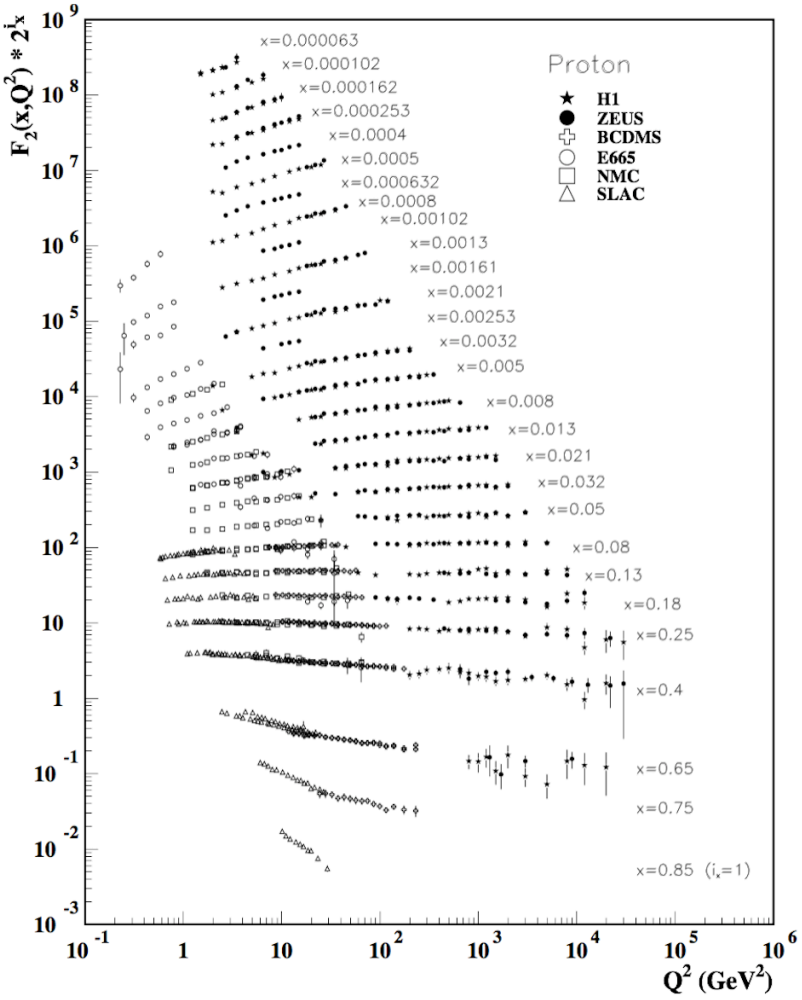

Figure 2-3: Scaling in the structure function F_2 for several values of x.

for unpolarized electron-proton scattering, so the full tensor formulation of Section 2.2.1 can be lumped into the symmetric component. The antisymmetric component of the tensor function arises from introducing spin to the scattering interaction. Following reference [20], for a spin-$\frac{1}{2}$ lepton the antisymmetric tensor is calculated as

$$L^{\mu\nu}_{A\pm} = \mp 2i\epsilon_{\mu\nu\alpha\beta}k^{\alpha}k'^{\beta} \tag{2.25}$$

while the most general antisymmetric hadron tensor is given by

$$W^A_{\mu\nu} = i\epsilon_{\mu\nu\alpha\beta}q^\alpha \left(G_1 S^\beta + \frac{G_2}{M^2}(S^\beta p\cdot q - p^\beta S\cdot q)\right) \tag{2.26}$$

where $\epsilon_{\mu\nu\alpha\beta}$ is the anitsymmetric Levi-Civita tensor and S is the proton spin vector as defined in nonrelativistic quantum angular momentum theory. Just as the symmetric component of the tensor gave rise to two unpolarized form factors W_1 and W_2, the antisymmetric component gives rise to two polarized form factors G_1 and G_2. Analogous to the unpolarized case, we define two new structure functions, g_1 and g_2, such that

$$g_1 \equiv M\nu G_1 \tag{2.27}$$

$$g_2 \equiv \nu^2 G_2 \tag{2.28}$$

then, by substituting Equations 2.27 and 2.28 into 2.26, we obtain the antisymmetric hadron tensor in terms of the polarized structure functions,

$$W^A_{\mu\nu} = iM\frac{\epsilon_{\mu\nu\alpha\beta}q^\alpha}{\nu}\left(g_1 S^\beta + g_2\left(S^\beta - M\frac{S\cdot q}{\nu}p^\beta\right)\right) \tag{2.29}$$

Experimentally, access to the spin dependent structure functions is done by flipping the lepton spin while keeping the hadron spin locked. An asymmetry measurement between the two lepton spin directions allows for the symmetric tensor component of the cross section to drop out, leaving only the antisymmetric component. Then by using the kinematic relations in conjunction with Equation 2.4 the cross section differences can be written as

$$\Delta\sigma_\parallel = \frac{d\sigma}{d\Omega}(\downarrow\Uparrow - \uparrow\Uparrow) = \frac{4\alpha^2}{MQ^2\nu}\frac{E'}{E}\left((E + E'\cos\theta)g_1 - \frac{Q^2}{\nu}g_2\right) \tag{2.30}$$

$$\Delta\sigma_{\perp} = \frac{d\sigma}{d\Omega}(\downarrow\Leftarrow - \uparrow\Leftarrow) = \frac{4E\alpha^2 \sin\theta\cos\phi}{MQ^2\nu^2}\frac{E'}{E}\left(\nu g_1 + 2E g_2\right) \tag{2.31}$$

where the electron polarization direction is either parallel ($\uparrow$) or antiparallel ($\downarrow$) and the proton polarization direction is either longitudinal ($\Uparrow$) or transverse ($\Leftarrow$) to the electron polarization. The addition of the $\cos\phi$ term in the perpendicular case accounts for the fact that the proton spin polarization vector is not aligned with the momentum vector, where ϕ is the angle between the two. We finally arrive at a formal definition for the spin structure functions in terms of the measured cross section differences.

2.3 The Parton Model

We now have a description of the proton made up of semi-free partons described by four structure functions but the question remains, what exactly are these partons? In 1969 Feynman and Bjorken introduced the parton model which describes the structure of the nucleon in terms of charged 'quarks' and neutral 'gluons' [21]. Quarks comprise two different roles in the hadron: bound valence quarks which carry all of the information about the nucleon, and sea-quarks, which are quark-antiquark pairs constantly being created and annihilated in the vacuum. Gluons are the mediator of the strong force. Much like the photon being categorized as either a positively or negatively charged boson in QED, the gluon is categorized as a boson of one of six 'color charges' in QCD.

In this new parton model we can consider each quark to carry some fraction of the total nucleon momentum. If we neglect parton mass and consider the nucleon mass M^2 to be small compared to the momentum transfer Q^2, this momentum fraction is just equal to the scaling factor Bjorken x, discussed in the previous section. We may also define the structure functions in terms of the probability distributions of quarks. By defining $q_f(x)$ and $\overline{q}_f(x)$ as the probability distribution of

quarks and antiquarks in some region dx, the structure functions can be expressed as

$$F_1(x) = \frac{1}{2}\sum_f z_f^2 \left[q_f(x) + \overline{q}_f(x)\right] \tag{2.32}$$

$$g_1(x) = \frac{1}{2}\sum_f z_f^2 \left[q_f(x) - \overline{q}_f(x)\right] \tag{2.33}$$

and, using the Callan-Gross relation discussed in the previous section, $F_2(x) = 2xF_1(x)$. In the parton model the g_2 structure function has no physical meaning. Here is where the simple quark parton model begins to break down. The problem arises from a fundamental assumption of the parton model: In a fast moving reference frame, the transverse momentum and nucleon rest mass can be neglected. In this scenario the entire nucleon structure can be described by the longitudinal momentum of the constituent quarks. To determine g_2 we must begin to consider this previously neglected transverse momentum distribution.

2.4 Virtual Photoabsorption Cross Sections

Before diving into a detailed study of the g_2 structure function it is useful to look at an alternate approach to the cross section. Equivalent to using the structure functions g_1, g_2, F_1 and F_2, the differential cross section can be described in terms of four virtual photoabsorption cross sections as [22]

$$\frac{d\sigma}{d\Omega} = \Gamma\left(\sigma_T + \epsilon\sigma_L - hP_x\sqrt{2\epsilon(1-\epsilon)}\sigma_{LT} + hP_z\sqrt{1-\epsilon^2}\sigma_{TT}\right) \tag{2.34}$$

where $h = \pm 1$ is the polarization of the incoming electron, $P_{z(x)}$ is the polarization of the proton with respect to the virtual photon momentum and ϵ is the ratio of the longitudinal to transverse virtual photon polarization, given by

$$\epsilon = \left(1 + 2\left(1 + \frac{\nu^2}{Q^2}\right)\tan^2\frac{\theta}{2}\right)^{-1} \tag{2.35}$$

where ν, Q^2 and θ are kinematic variables, defined in Section 2.1, and the virtual photon flux factor Γ, given by

$$\Gamma = \frac{\alpha}{2\pi^2 Q^2} \frac{E'}{E} \frac{K}{1-\epsilon}. \tag{2.36}$$

The photon flux factor is a function of the convention dependent photon flux K. Three common conventions for the flux factor are [23–25]

$$K_A = \nu \tag{2.37}$$

which relates the flux to the energy ν carried by the virtual photon,

$$K_G = \sqrt{\nu^2 + Q^2} \tag{2.38}$$

called Gilman's convention, which relates the flux to the four momentum of the virtual photon, and

$$K_H = \frac{W^2 - M^2}{2M} = \nu(1-x) \tag{2.39}$$

called Hand's convention, which relates the flux to an equivalent photon energy in terms of the interactions missing mass, and the mass of the proton. The last convention can be thought of as the energy required in an equivalent interaction with a real photon. At $Q^2 = 0$, that is, no four momentum carried by the virtual photon, all three conventions reduce to ν, the photon energy. The cross section also gives similar results for any chosen convention in the deep inelastic region, but between these two regions the cross section is very sensitive to the photon flux K, so care is required when choosing a convention.

The four virtual photon cross sections in Equation 2.34 ($\sigma_T, \sigma_L, \sigma_{TT}, \sigma_{LT}$) are functions of the photon energy and four momentum ν and Q^2. $\sigma_T(\sigma_L)$ represents the transverse (longitudinal) photoabsorption cross section in the interaction, while $\sigma_{LL}(\sigma_{LT})$ represent the longitudinal-longitudinal

(longitudinal-transverse) interference terms. For the unpolarized case with $Q^2 = 0$ the longitudinal term vanishes and the virtual photon cross section is given in terms of only σ_T. σ_{LT} and σ_{TT} can only be measured with a polarized electron and target, where the cross section is expressed relative to the two polarization directions.

The virtual photon cross sections can be related back to the structure functions, defined in the previous section, as

$$\sigma_L = \frac{4\pi^2\alpha}{K}\left(\frac{F_2}{\nu}\left(1+\frac{Q^2}{\nu^2}\right) - \frac{F_1}{M}\right), \tag{2.40}$$

$$\sigma_T = \frac{4\pi^2\alpha}{K}F_1, \tag{2.41}$$

$$\sigma_{LT} = \frac{4\pi^2\alpha}{K}\frac{Q^2}{\nu^2}(g_1+g_2), \tag{2.42}$$

$$\sigma_{TT} = \frac{4\pi^2\alpha}{MK}\left(g_1 - \frac{Q^2}{\nu^2}g_2\right). \tag{2.43}$$

Chapter 3

The g_2 Structure Function

In the previous chapter we related the measured differential cross section to four 'structure functions' that parameterize the internal behavior of the proton. It was shown in Section 2.3 that these structure functions can be interpreted as quark momentum and spin distributions but it was found that the second spin structure function, g_2, has no physical meaning in this context. In this chapter we will take a closer look at the characteristics of g_2 and the predictions about the behavior of its moments through the framework of QCD.

3.1 Chiral Perturbation Theory

A key concept in the discussion of QCD is the idea of 'asymptotic freedom', which refers to the fact that the coupling strength between quarks increases as Q^2 decreases. Asymptotic freedom allows for a perturbative approach to QCD at high energies by expanding in powers of the coupling constant in a method that is aptly named perturbative QCD (pQCD). For low energy interactions $\left(Q^2 < 1 \text{ GeV}^2\right)$, the coupling constant is of order one which makes the perturbative method no longer useful and other approaches must be considered.

The complete QCD Lagrangian is [26]

$$\mathcal{L}_{\text{QCD}} = \sum_f \bar{q}_f (i \not{D} - m_f) q_f - \frac{1}{4} \mathcal{G}^{\alpha}_{\mu\nu} \mathcal{G}^{\mu\nu}_{\alpha} \tag{3.1}$$

where $\mathcal{G}$ is the field strength tensor, q is the quark spinor, m is the quark mass, the summation is over all six quark flavors and $\not{D}$ is the covariant derivative defined as

$$\not{D}_{\alpha\beta} q_\beta \equiv \left(\delta_{\alpha\beta} \partial_\mu - \frac{i}{2} g \lambda_{\alpha\beta} \right) \gamma^\mu q_\beta. \tag{3.2}$$

The up and down quark masses at the low energy scale of ≈ 1 GeV are [18]

$$m_u = (4 \pm 2)\text{MeV}, \tag{3.3}$$

$$m_d = (8 \pm 4)\text{MeV}. \tag{3.4}$$

These masses are small compared to the composite hadron ($m_P = 938$ MeV) so we consider the quark masses to be zero and treat any deviation from this assumption as a perturbation.

In the zero quark mass picture the helicity of the particle, which is defined as the spin vector projected onto the momentum axis ($h = \vec{S} \cdot \vec{p}$) is indentical to its chirality, or 'handedness'. We introduce a 'left' and 'right' handed quark field as

$$q_{L,R} = \frac{1}{2}(1 \mp \gamma_5) q \tag{3.5}$$

which are decoupled from each other. The consequence of this is an additional symmetry in the QCD Lagrangian, called chiral symmetry. The Lagrangian can now be rewritten as [27]

$$\mathcal{L}^0_{\text{QCD}} = \sum_f \left(\bar{q}_{R,f} i \not{D} q_{R,f} - \bar{q}_{L,f} i \not{D} q_{L,f} \right) - \frac{1}{4} \mathcal{G}^\alpha_{\mu\nu} \mathcal{G}^{\mu\nu}_\alpha \tag{3.6}$$

where the summation is now over the massless quarks. This form of the QCD Lagrangian exhibits a $\text{SU}(3)_L \times \text{SU}(3)_R$ symmetry. The existence of a small quark mass breaks this symmetry and can

be treated as a perturbation in the Lagrangian

$$\mathcal{L}_{\text{QCD}} = \mathcal{L}_0 + \mathcal{L}' \tag{3.7}$$

where $\mathcal{L}'$ is the symmetry breaking part due to the quark mass

$$\mathcal{L}' = -\sum_f \bar{q}_f m_f q_f. \tag{3.8}$$

A low energy expansion in momenta is used in the result of any scattering amplitude calculation using this perturbed Lagrangian. The result is a power series in terms of the energy or momenta of the interacting particles. The framework for this power series expansion is called chiral perturbation theory (χPT) and is a very accurate extension of QCD in the low energy scattering region.

3.2 Operator Product Expansion

The Operator Product Expansion (OPE) is a method developed by K. Wilson in 1968 as an attempt to provide direct QCD predictions for moments of the structure functions [28]. The underlying idea behind the OPE is to evaluate the product of operators by separating the product into two parts, a perturbative part and a non-perturbative part. As an example, the product of two operators can be expressed as the sum over local operators as

$$\lim_{x\to 0} \mathcal{O}_a(x)\mathcal{O}_b(0) = \sum_k C_{abk}(x)\mathcal{O}_k(0) \tag{3.9}$$

in the limit of the spatial four-vector $x \to 0$, where C_{ab} are known as the 'Wilson coefficients' which contain all of the spatial dependence of the sum. Because of the nature of asymptotic freedom in QCD, the coupling constant is small at short distances. This allows the Wilson coefficients to be calculated perturbatively in the spatial four-vector limit.

To interpret the spin structure functions in terms of the OPE, the hadron tensor is first written in terms of the commutator of electromagnetic currents J_μ and J_ν:

$$W_{\mu\nu} = \frac{1}{2\pi} \int d^4x e^{iq\cdot x} \langle P,S| \left[J_\mu(x), J_\nu(0)\right] |P,S\rangle. \tag{3.10}$$

where x is the virtual photon four-momentum and P and S are the target four-momentum and spin, respectively. By taking the Fourier transform of Equation 3.9 we get the momentum space version of the OPE

$$\lim_{q\to\infty} \int d^4x e^{iq\cdot x} \mathcal{O}_a(x)\mathcal{O}_b(0) = \sum_k C_{abk}(q)\mathcal{O}_k(0). \tag{3.11}$$

In the limit that $q \to \infty$, the Fourier transform in Equation 3.10 forces $x \to 0$ so the OPE can be used. The result is an expansion of the electromagnetic currents in terms of local operators multiplied by coefficients which are functions of q. The local operators in the expansion are quark and gluon operators with arbitrary dimension d and spin n. The contributions of any of these operators to the tensor product is of the order [29]

$$x^{-n} \left(\frac{M}{Q}\right)^{\tau-2} \tag{3.12}$$

where $\tau \equiv d-n$ is defined as the 'twist'. As higher twist terms are suppressed by increasing powers of $\frac{M}{Q}$ the leading twist terms dominate in the Bjorken limit. For small values of Q^2 higher twist becomes more important. Using dispersion relations the OPE can be applied to the hadron tensor to find expressions for the moments of the structure functions [30]

$$\int_0^1 x^{n-1} g_1(x,Q^2)dx = \frac{1}{2}a_{n-1}; \quad \text{for } n = 1,3,5... \tag{3.13}$$

$$\int_0^1 x^{n-1} g_2(x,Q^2)dx = \frac{n-1}{2n}(d_{n-1} - a_{n-1}); \quad \text{for } n = 3,5... \tag{3.14}$$

where a_{n-1} and d_{n-1} are matrix elements of the twist-2 and twist-3 quark and gluon operators, respectively.

3.2.1 Wandzura-Wilczek Relation

Equation 3.13 relates the g_1 structure function to the twist-2 matrix element a_n. If we replace a_n with the corresponding moments of g_2 we get

$$\int_0^1 x^{n-1}\left(g_1\left(x,Q^2\right)+\frac{n}{n+1}g_2\left(x,Q^2\right)\right)dx=\frac{1}{2}d_n;\quad \text{for } n=3,5... \tag{3.15}$$

where the leading twist terms have cancelled. Using the convolution property of Mellin transforms we are able to invert Equation 3.15 as:

$$g_1(x,Q^2)+g_2(x,Q^2)=\int_0^1\frac{dy}{y}g_1(y,Q^2) \tag{3.16}$$

where we have set the twist-3 d_n term equal to zero. This is known as the Wandzura-Wilczek relation [31]

$$g_2^{WW}(x,Q^2)=-g_1(x,Q^2)+\int_0^1\frac{dy}{y}g_1(y,Q^2). \tag{3.17}$$

This relation shows that the leading twist term in g_2 is determined entirely by g_1. As a direct consequence of this, the leading twist part of g_2 is interpretable in the naive parton model.

We can now express g_2 in terms of the leading twist contribution and higher order terms

$$g_2(x,Q^2)=g_2^{WW}(x,Q^2)+\bar{g}_2(x,Q^2). \tag{3.18}$$

In the Bjorken limit it is a reasonable approximation to define g_2 entirely in terms of g_1 through the Wandzura-Wilczek relation. As Q^2 decreases higher twist terms can no longer be ignored and $\bar{g_2}$ becomes increasingly important.

The higher twist component of g_2 can be further broken down into a transversity twist-2 term and a twist-3 term as [32]

$$\bar{g}_2(x,Q^2) = -\int_x^1 \frac{\partial}{\partial y}\left[\frac{m_q}{M}h_T(y,Q^2) + \xi(y,Q^2)\right]. \tag{3.19}$$

The transversity term, h_T, is due to transverse quark polarization distributions, and is suppressed by the quark mass ($m_q \ll M$). The second term, $\xi(x,Q^2)$, is a twist-3 term that comes from quark-gluon interactions. At g_2^p kinematics the structure function deviates strongly from leading twist behavior which allows for the unique measurement of higher twist effects.

3.2.2 Burkhardt-Cottingham Sum Rule

It is important to note that the OPE for the g_2 structure function, Equation 3.14, does not say anything about the $n = 1$ term of the expansion. In 1970, H. Burkhardt and W. Cottingham proposed a sum rule to describe the first moment of g_2 [33]:

$$\Gamma_2\left(Q^2\right) = \int_0^1 g_2\left(x,Q^2\right)dx = 0, \tag{3.20}$$

which is expected to hold at all values of Q^2. The result of this moment, called the 'BC Sum Rule', is derived from the relation of the g_2 structure function to the virtual Compton scattering amplitude. If this sum rule is violated it could imply one of the following circumstances,

1. g_2 is so singular that the integral $\int_0^1 g_2(x,Q^2)dx$ does not exist.

2. g_2 has a delta function singularity at $x = 0$.

3.2.3 Higher Twists

The Wandzura Wilczek relation splits the g_2 structure function into a leading twist term plus higher orders. As discussed in Section 3.2.1, the leading order term can be expressed entirely in terms of

g_1 and is thus representable in the classical parton model. The interesting part of g_2 resides in the higher order term, $\bar{g}_2$, which can be expressed in terms of it's moments using Equation 3.14 as

$$\int_0^1 x^n \bar{g}_2(x, Q^2) dx = \frac{n}{4(n+1)} d_n(Q^2). \tag{3.21}$$

These moments are of twist-3, which can be thought of as interactions involving more than one parton in the hadron scattering process [34]. Parton-parton interactions are manifested as helicity exchanges in the scattering interaction which arise from either transversely oriented angular momentum in the parton, or interaction of the parton with a transversely polarized gluon. In other words, where leading order twist describes individual quark behavior in the nucleon, the twist-3 interaction is beginning to probe the interaction of quarks through gluon exchange. These higher twist interactions allow us to paint a more complete picture of the hadron as a network of interacting particles, instead of single, non-interacting, parton distributions.

3.3 Spin Polarizabilities

The spin polarizabilities, γ_0 and δ_{LT}, describe the relation between the structure functions and the virtual Compton scattering amplitudes [35]. They can be thought of as a nucleon's helicity response to a polarized virtual photon. Since the Compton scattering amplitudes can be calculated theoretically, the polarizabilities allow for a unique benchmark test in the framework of QCD.

To derive the polarizabilities we consider the forward doubly-virtual Compton scattering of a virtual photon with space-like four-momentum $q^2 = -Q^2 < 0$. The absorption of a virtual photon is related to the inclusive cross sections σ_T, σ_L, σ_{TT} and σ_{LT}, as discussed in Section 2.4. For this discussion we will concentrate on the spin-dependent partial cross sections, σ_{TT} and σ_{LT}. By considering a

scattering amplitude, g_{TT}, an unsubtracted dispersion relation leads to [36]

$$\Re\left[g_{TT}(\nu,Q^2)-g_{TT}^{pole}(\nu,Q^2)\right]=\frac{\nu}{2\pi^2}\mathcal{P}\int_{\nu_0}^{\infty}\frac{K(\nu',Q^2)\sigma_{TT}(\nu',Q^2)}{\nu'^2-\nu^2}d\nu' \tag{3.22}$$

where g_{TT}^{pole} is the elastic contribution to the scattering amplitude, K is the virtual photon flux, σ_{TT} is the Compton scattering cross section (both discussed in Section 2.4), and the integral over ν begins at the pion threshold, ν_0. A low energy expansion gives:

$$\Re\left[g_{TT}(\nu,Q^2)-g_{TT}^{pole}(\nu,Q^2)\right]=\frac{2\alpha}{M^2}I_{TT}(Q^2)\nu+\gamma_0(Q^2)\nu^3+O(\nu^5)., \tag{3.23}$$

where $I_{TT}(Q^2)$ is the coefficient of the $O(\nu)$ term which leads to a sum rule for the generalized Gerasimov-Drell-Hearn integral [22] and γ_0 is the coefficient to the $O(\nu^2)$ term which leads to the generalized forward spin polarizability. Using Equations 2.40-2.43 the polarizability can be related back to the spin dependant structure functions g_1 and g_2:

$$\begin{aligned}\gamma_0(Q^2)&=\frac{1}{2\pi^2}\int_{\nu_0}^{\infty}\frac{K(\nu,Q^2)}{\nu}\frac{\sigma_{TT}(\nu,Q^2)}{\nu^3}d\nu\\&=\frac{16\alpha M^2}{Q^6}\int_0^{x_0}x^2\left[g_1(x,Q^2)+\frac{4M^2}{Q^2}x^2g_2(x,Q^2)\right]dx.\end{aligned}$$

If we look instead at the Compton scattering amplitude for the longitudinal-transverse cross section, g_{LT}, and use the same method as discussed above, we arrive at an expression for the longitudinal-transverse polarizability in terms of the spin structure functions,

$$\begin{aligned}\delta_{LT}(Q^2)&=\frac{1}{2\pi^2}\int_{\nu_0}^{\infty}\frac{K(\nu,Q^2)}{\nu}\frac{\sigma_{LT}(\nu,Q^2)}{Q\nu^2}d\nu\\&=\frac{16\alpha M^2}{Q^6}\int_0^{x_0}x^2\left[g_1(x,Q^2)+g_2(x,Q^2)\right]dx,\end{aligned}$$

where δ_{LT} represents the coefficient to the second order term in the expansion of g_{LT}.

3.4 Model Predictions

Several models exist which fit existing structure function world data in order to make predictions in currently unmeasured kinematic regions. Before moving on to discuss the g_2^p experiment and analysis we will take a brief aside to discuss some of these models and their contributions to the analysis of E08-027.

3.4.1 Polarized MAID Model

The Unitary Isobar Model (MAID) [37] contains phenomenological fits to world pion photo- and electroproduction data. The major resonances are modeled using Breit-Wigner functions:

$$\sigma_{\frac{1}{2}(\frac{3}{2})} = \frac{4M}{W_0\Gamma_0} A^2_{\frac{1}{2}(\frac{3}{2})} B(\nu, Q^2) \tag{3.24}$$

where $B(\nu, Q^2)$ is the generalization of the Breit-Wigner form to electroproduction, $A^2_{\frac{1}{2}(\frac{3}{2})}$ are the photoproduction helicity amplitudes, W_0 is the relevant resonance mass, and Γ_0 is the resonance width. The fit covers a region from the single-pion production threshold to the resonance region limit of 2 GeV.

3.4.2 Polarized CLAS EG1b

The CLAS EG1b model [38] will be referred to in this work as the polarized 'Hall B' model. The model is comprised of a fit to the virtual photon asymmetries A_1 and A_2 which can then be related back to the spin structure functions g_1 and g_2. The Hall B model becomes increasingly useful as the low Q^2 region is constrained by existing photo-production data and parameterizations exist in both the resonance and DIS regions. At DIS the g_2 contribution is given by the Wandzura-Wilczek relation (Section 3.2.1) which assumes only leading twist behavior.

3.4.3 Unpolarized Bosted-Christy Model

The Bosted-Christy model was developed by P. Bosted and M.-E. Christy to represent an empirical fit to inclusive measurements of inelastic electron-deuteron scattering [39]. The fit covers the resonance region for $Q^2 < 10$ GeV^2.

The Bosted model can be described as a convolution of two fits, one parameterizing the 'dip' region between the quasi-elastic peak and the $\Delta(1232)$ resonance, and the other parameterizing the average nucleon cross section integrated over the nucleon Fermi momentum, $\vec{k}$,

$$\sigma(W, Q^2) = \sigma_{dip}(W, Q^2) + \int \sigma(W', Q'^2)\Phi^2(\vec{k})d^3\vec{k}. \tag{3.25}$$

The agreement between the fit and data in the g_2^p kinematic region is on the order of 5%.

Chapter 4

The Experiment

Experiment E08-027 (g_2^p) ran in February - May of 2012 in Hall A of Thomas Jefferson National Accelerator Facility (JLab) in Newport News, Virginia. The experiment measured inclusive polarized electron cross sections in the low momentum transfer region of $0.01 < Q^2 < 0.13$ GeV^2. Full

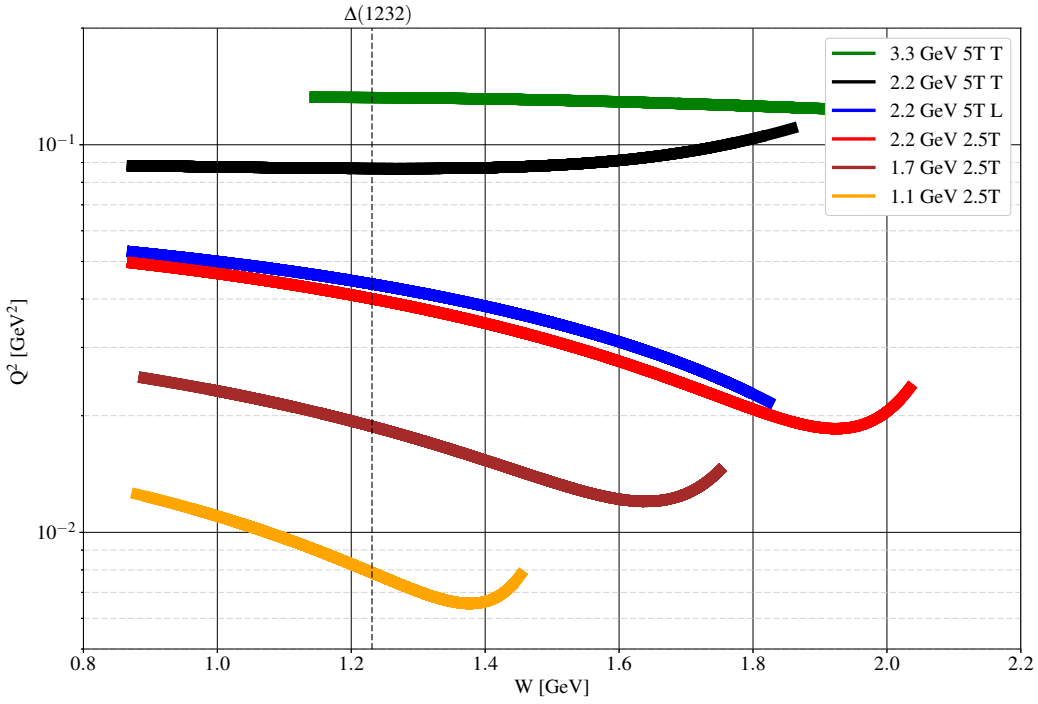

Figure 4-1: Kinematic coverage for the six settings of E08-027. An exponential fit to the central scattering angle was used to find the Q^2 of each momentum setting. Also shown is the $\Delta(1232)$ resonance, which is used as the extrapolation point of each setting to a constant Q^2 (Section 7.5.1).

kinematic coverage for the experiment is shown in Figure 4-1. To calculate the spin dependent

structure functions, $g_1\left(x, Q^2\right)$ and $g_2\left(x, Q^2\right)$, both a total electron cross section and a scattering asymmetry are needed. For this purpose a longitudinally polarized electron beam with incident energy between 1.1 GeV and 3.3 GeV was scattered off of a stationary proton target with polarization direction either transverse or longitudinal to the electron beam polarization. E08-027 ran at a total of five beam-energy/target polarization 'configurations'. The details of each configuration are shown in Table 4.1. The hall A beamline was outfitted with new beam diagnostic hardware

Table 4.1: E08-027 Experimental Configurations.

Beam Energy	Target Field	Target Orientation	Approximate Q^2
3.350 GeV	5T	90°	0.12 GeV^2
2.254 GeV	5T	90°	0.086 GeV^2
2.254 GeV	5T	0°	0.043 GeV^2
2.254 GeV	2.5T	90°	0.048 GeV^2
1.710 GeV	2.5T	90°	0.025 GeV^2
1.157 GeV	2.5T	90°	0.010 GeV^2

and raster tools to account for the low current running required to maintain target polarization, the details of which will be discussed in Section 4.2. A beam current of <100nA was used to allow for slower target depolarization.

The experiment utilized two indentical High Resolution Spectrometers positioned at $\pm 12.5^\circ$ relative to the beamline. This represents the smallest possible angle that the High Resolution Spectrometer arms are capable of closing to. The kinematic range of the experiment required detection of electrons at an angle of roughly $\pm 6^\circ$ so a septum magnet was added to allow for the selection of scattered electrons at previously inaccessible angles.

The High Resolution Spectrometers contained 3 quadrupole focusing magnets and 1 dipole magnet to bend scattered electrons into the detector housing. A sieve slit was placed before the septum magnet to be used in conjuction with the Vertical Drift Chambers in the detector housing for the reconstruction of detected electron positions at the target. Gas Čerenkov and lead glass scintillators were used for particle ID and energy measurements in the detector housing.

In this chapter, the Electron Beam Injector and Linear Accelerator at JLab will be discussed in

detail, along with the various components of experimental Hall A that were directly utilized in the running of E08-027.

4.1 The Accelerator

The JLab Continuous Electron Beam Accelerator Facility (CEBAF) can be broken down into four major components. The *Injector* is where the polarized electron beam is produced and accelerated by 45 MeV onto the main ring. The north and south *Linacs*, or Linear Accelerators, are a series of RF cavities capable of accelerating the beam by approximately 400 MeV per pass. The *recirculation arcs* connect the two linacs to allow for up to 5 passes and a maximum beam energy of 12 GeV [3]. It is important to note that at the running of the experiment the accelerator had a maximum beam energy of 6 GeV, it has since been upgraded with an additional experimental hall and improved beamline tools. Since these upgrades occured after the running of E08-027 they will not be discussed in this work. Finally, after reaching the required beam energy, the beam is delivered to the three *experimental halls* for data taking. A detailed overview of the accelerator and its various components is shown in Figure 4-2.

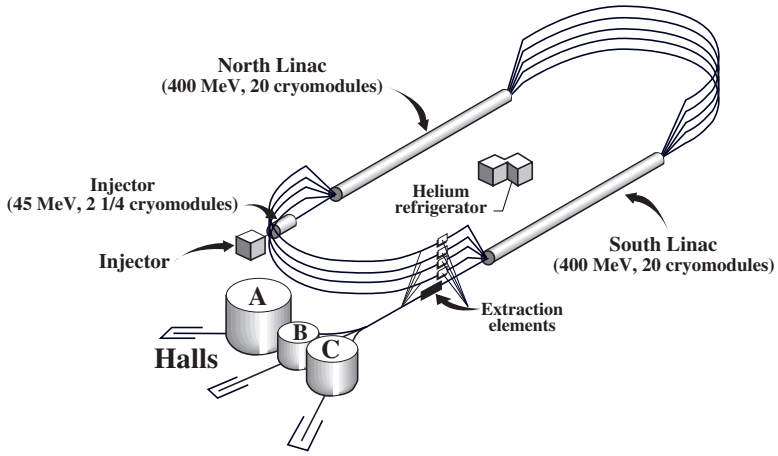

Figure 4-2: Jefferson Lab Linear Accelerator. See text for details. Reproduced from [3].

4.1.1 Injector

There are three main components required to generate a polarized electron beam. The first is a light sensitive material called a photocathode from which electrons will be ejected when excited with an energy source. The second is a laser light source which provides the energy required to excite the electrons into the conduction band. Finally an electric field is used to accelerate electrons in the conduction band. At the CEBAF accelerator a Gallium Arsenide (GaAs) photocathode is used as an electron source. A circularly polarized 1.497 GHz diode laser is incident on the GaAs crystal with a wavelength of 780 nm which matches the bandgap energy of the material. Unfortunately, the valence band of GaAs is degenerate. This means there are four possible valence states at the same energy level, so when polarized laser light of the correct frequency is incident on the crystal it will excite 3 electrons to one spin state for every 1 electron excited to the opposite spin state, as per the Clebsch Gordan coefficients for such a transition. This is shown in more detail in Figure 4-3.

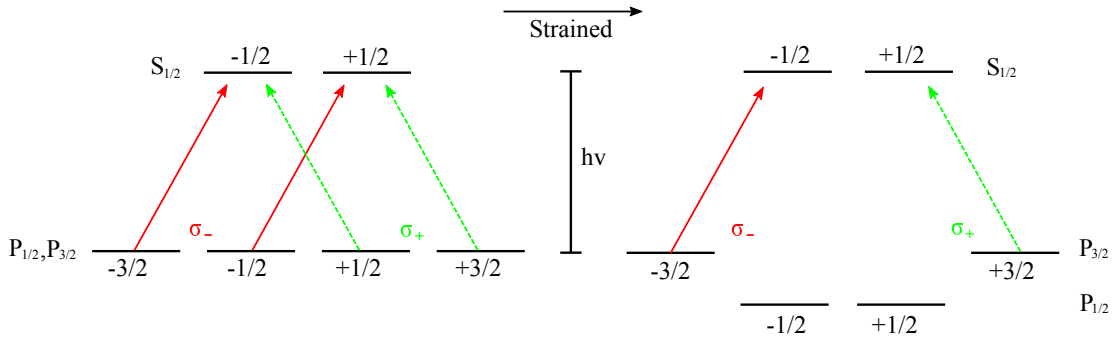

Figure 4-3: Possible transition states for GaAs before (left) and after (right) mechanically strained with phosphorus.

This will result in a theoretical maximum electron polarization of 50%. To increase the maximum polarization the GaAs crystal is mechanically strained with phosphorus which separates the $P_{3/2}$ and $P_{1/2}$ states. Then incident laser light with only enough energy to excite electrons from the $P_{3/2}$ states is applied, giving a theoretical maximum polarization of 100% [40].

In order to measure asymmetries and cross section differences, and to minimize time dependent polarization effects in the experimental hall equipment, a pseudo-random bitwise algorithm is used

to flip the polarization direction of the laser light at a 30Hz frequency. The polarization of the laser is flipped using a quarter-wave retardation plate called a Pockels Cell. When a high voltage is applied to the Pockels Cell it will act to flip the state of the circularly polarized laser, thus flipping the helicity, or direction of polarization, of the electron beam. The high voltage sent to the Pockels Cell is regulated by a logic generator called the Helicity Control Board which is running a 30-bit pseudo-random algorithm that generates a 0 or 1, corresponding to + or − laser polarization, at 30Hz [41]. The algorithm is shown in Figure 4-4. The signal from the Helicity Control Board is

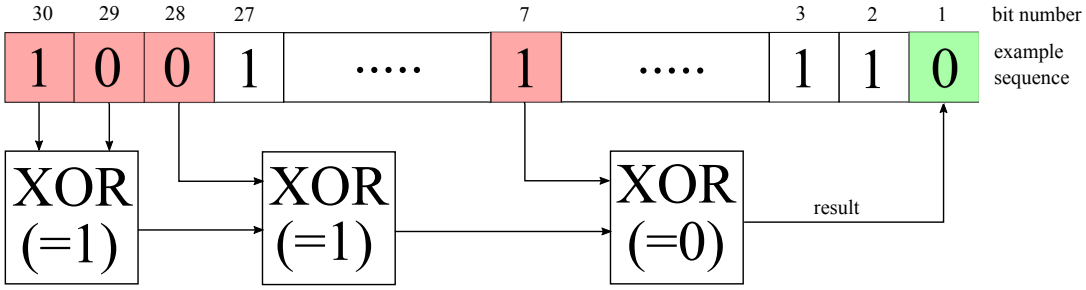

Figure 4-4: The 30-bit shift register in the Helicity Control Board. The new pattern is determined using an XOR (exclusive 'or' logic statment) on bit 30, 29, 28 and 7 of the register. The resulting bit value (green box) determines the beam polarity, then the entire register is shifted left by one bit and the calculation is repeated. Reproduced from [4].

also sent directly to the experimental hall where it can be decoded so the real helicity state of the detected electron can be known. This process is known as helicity reconstruction, and is discussed in more detail in Ref [4]. The polarized electrons are then accelerated up to 67 MeV before being injected into the accelerator.

4.1.2 Accelerator

The main facility consists of 2 antiparallel linear accelerators (north and south linacs) and 2 recirculation arcs. Each linac consists of 20 cryomodules each containing 8 superconducting niobium RF cavities cooled to 2 Kelvin [3]. Electrons passing through the cavities are accelerated by the 1.497 MHz RF wave in each cavity. At the end of the linac the beam enters a chicane system, called a CEBAF spreader, which sorts the beam according to its energy. From here the beam

enters the recirculation arc which bends the beam 180° into the south linac. After undergoing a second acceleration stage the beam hits the extraction elements where an RF separator magnet can direct the beam into the experimental halls for data taking, or send it into another separator and into the second recirculation arc to make another full pass. One electron bunch can make up to 5 passes, reaching a maximum beam energy of just under 6 GeV.

4.2 The Hall A Beamline

The electron beam enters the Hall A beamline from the RF separator and travels approximately 20 meters through several beam diagnostic sensors before reaching the stationary target at the center of the hall. The beamline itself consists of several isolated sections separated by vacuum ports. The pressure is maintained at $\leqslant 10^{-6}$ Torr by an ion pump system. Due to the unique conditions required for the running of E08-027, a large portion of the beamline equipment was newly introduced for the experiment. Each component of the beamline will be carefully addressed in the following sections.

4.2.1 Beam Current Monitors

The first component that the beam sees as it enters the hall is the Beam Current Monitor (BCM). The monitor consists of two resonant cavities, an Unser monitor and associated electronics. The entire system is enclosed in a temperature stabilized box around the beamline. The two RF cavities are stainless steel cylindrical waveguides tuned to the beam frequency of 1.497 GHz [42]. This results in an output voltage from the cavity that is proportional to the beam current.

Between the two cavities is a Parametric Current Transformer, called an Unser monitor, which is normally used as a calibration tool for the RF cavities. This is done by passing a known current through a wire inside the beam pipe. The current is ramped between zero and a maximum current several times to improve the accuracy of the voltage output on the cavity. Using the known current

and the output voltage, a constant of proportionality can be determined and used for the duration of the experiment with a stability of ±0.5%. Unfortunately, this method is only accurate down to roughly 1μA, below this current the absolute uncertainty in the Unser monitor, 250 nA, becomes a problem. The low current running of E08-027 required an alternate method for beam current measurements.

In lieu of an Unser monitor, an invasive tungsten calorimeter was used to calibrate the RF cavities. The calorimeter consisted of a vacuum chamber containing a block of tungsten with a known heat capacity of 8.55 kJ/K [43]. During calibration the tungsten was invasively moved into the beamline where it heated as charge was deposited onto the block. After a set amount of time the beam was shut off and the block was given time to thermalize before a temperature measurement was taken. The relationship between temperature and charge is given by

$$Q_{beam} = K \times T \tag{4.1}$$

where K is the heat capacity of the tungsten and T is the measured temperature. The calculated charge was then compared to the voltage read out by the RF cavities during the same period of time, and a constant of proportionality was found. The BCM monitors could then be used, non-invasively, for an extended period of time to determine the beam charge.

4.2.2 Rasters

When the electron beam enters the hall it has an approximate diameter of 100 μm. To prevent rapid depolarization, uneven heating and uneven densities in the target material, a method is required to spread the beam heat load out to a larger, uniform diameter. The standard method for doing this is a dual horizontal and vertical air core magnet coil called the fast raster. Each coil accepts a 20 kHz oscillating triangular wave pattern with a 90° phase separation [44] which result in a 2mm diameter square beam pattern on the target as shown in Figure 4-5a.

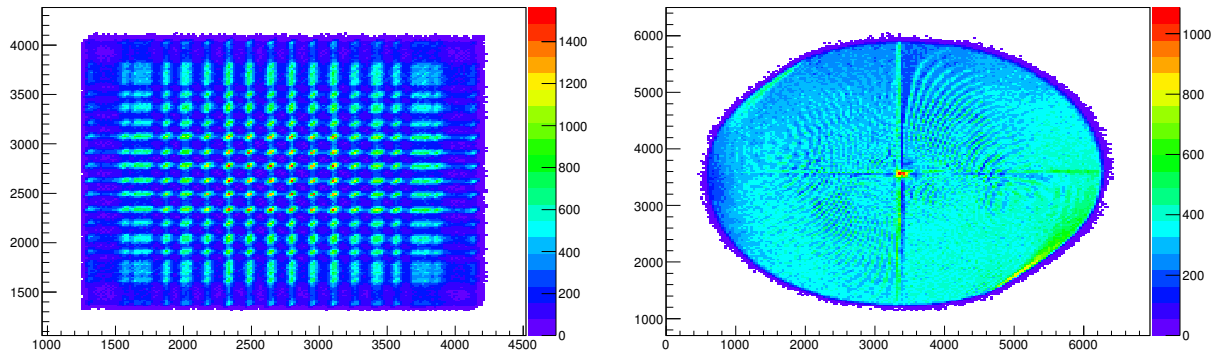

(a) Fast raster

(b) Slow raster

Figure 4-5: Raster patterns at the target, units are arbitrary. Fast raster(a) is roughly 2mm in diameter, slow raster(b) is roughly 2cm in diameter.

E08-027 used a target with a circular cross-sectional diameter of 2cm. To reduce rapid depolarization of the target material due to concentrated radiation dose, a second raster was introduced. This second raster, called the slow raster, was powered by three waveform generators. Two waveforms generated 100Hz sine waves with a 90° phase separation, while the third waveform performed a 30Hz amplitude modulation of the function $r(t) \sim \sqrt{t}$. These waveform generators drive the x and y directional slow raster deflection magnets [45]. The resulting raster is a 2cm circular raster pattern at the target, shown in Figure 4-5b.

4.2.3 Møller Polarimeter

A high precision measurement of the beam polarization in the hall was required to calculate the electron scattering asymmetry. The standard Hall A beamline is equipped with a Møller polarimeter which exploits the well understood cross section of Møller scattering to determine the beam polarization. The polarimeter uses a ferromagnetic foil, magnetized in a 24 mT field for scattering. The Møller scattering interaction, $\vec{e}^{\,-} + \vec{e}^{\,-} \rightarrow e^- + e^-$, will occur between the polarized beam and foil and the resulting scattered asymmetry is measured in a pair of lead-glass calorimeter modules. The reaction cross section of Møller scattering is a function of both the beam and target foil

polarization as

$$\frac{d\sigma}{d\Omega} = \left(\frac{d\sigma}{d\Omega}\right)_0 \left[1 + \sum_{i=X,Y,Z} \left(A_{i,i} \cdot P_i^{\text{target}} \cdot P_i^{\text{beam}}\right)\right] \tag{4.2}$$

where $i = X, Y, Z$ defines the projections of the polarizations on each axis and $A_{i,i}$ is defined as the *analyzing power* and is a function of only the center of mass scattering angle, θ_{CM} [5]. Here $\left(\frac{d\sigma}{d\Omega}\right)_0$ is the unpolarized cross section:

$$\left(\frac{d\sigma}{d\Omega}\right)_0 = \left[\frac{\alpha(1+\cos\theta_{CM})(3+\cos^2\theta_{CM})}{2m_e \sin^2\theta_{CM}}\right]^2 \tag{4.3}$$

where α is the fine structure constant and m_e is the electron mass. So the beam polarization is directly calculable with a well understood target polarization and cross section. Experimentally, the asymmetry is measured instead of the cross section. This allows many cross section systematic uncertainties to cancel in the ratio.

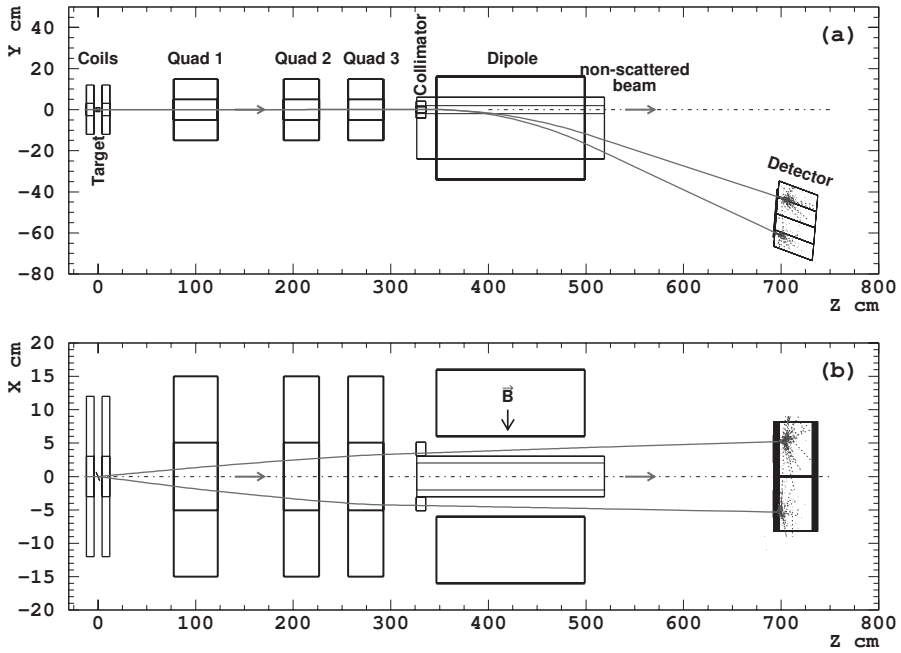

Figure 4-6: Side view (a) and top down view (b) of the Møller polarimeter. Beam enters from the left and scatters off the target. Scattered events are bent out of plane in the dipole and detected below the beam line. Reproduced from [5].

A diagram of the Møller polarimeter is shown in Figure 4-6. The target material is a Cobalt-

Iron alloy cooled to 115K in a 28 mT target field. Polarizations on the order of 7.95±0.24% were obtained. The error includes uncertainty in the foil size, as well as uncertainty in the stability of the target field. The polarimeter measurements are invasive and take approximately one hour of beam time. Because of the invasive nature of the measurement and the stability of the beam polarization, only 9 beam polarization measurements were taken during the experiment. The results are shown in Table 4.2. Measurements are considered constant to within statistical uncertainty for the duration between measurements. Flips in sign correspond to the beam line insertion of a polarity flipping half-wave plate.

Table 4.2: Møller Polarimeter results [1].

Measurement	Date (2012)	Result
1	March 3	-79.91 ± 0.20 (stat.) ± 1.7% (sys.)
2	March 30	-80.43 ± 0.46 (stat.) ± 1.7% (sys.)
3	March 30	+79.89 ± 0.58 (stat.) ± 1.7% (sys.)
4	April 10	-88.52 ± 0.30 (stat.) ± 1.7% (sys.)
5	April 23	+89.72 ± 0.29 (stat.) ± 1.7% (sys.)
6	May 4	-83.47 ± 0.57 (stat.) ± 1.7% (sys.)
7	May 4	-81.82 ± 0.59 (stat.) ± 1.7% (sys.)
8	May 4	+80.40 ± 0.45 (stat.) ± 1.7% (sys.)
9	May 15	+83.59 ± 0.31 (stat.) ± 1.7% (sys.)

4.2.4 Beam Position Monitors

Two Beam Position Monitors (BPMs) were located directly upstream of the target for high precision measurements of the beams x and y coordinates within the beamline. The BPM monitors are resonant cavities with resonant frequency tuned to match the beam frequency. Four antenna are located inside each cavity, 2 'x-directional' antenna and 2 'y-directional' antenna [5]. An asymmetry measurement of the voltages in antenna opposite each other gives the central beam position in that corresponding direction.

To get the absolute beam position, the BPM's were calibrated using an intrusive mechanism called the Harp. The Harp consists of three wires stretched across a metal tong. One wire is vertical

with respect to the beam direction, while the other two are at 45° to the beam direction. During calibration the Harp is stepped across the beamline using a high precision stepper motor. A spike is seen in the signal from the wire when it crosses the beam location. Using the step motor location and signal from the three wires the exact beam position can be calculated and used to calibrate the beam position monitors for non-intrusive measurements.

4.2.5 Chicane

Experiment E08-027 ran in a total of six different beam energy and target field configurations. Of the six configurations, five of them called for a target field perpendicular to the beam direction. For these settings the beam would experience out-of-plane bending while it travels through the target field so two additional dipole magnets had to be installed upstream of the target field to ensure the beam hit the target center [46]. The beam trajectory through the chicane and target field is shown

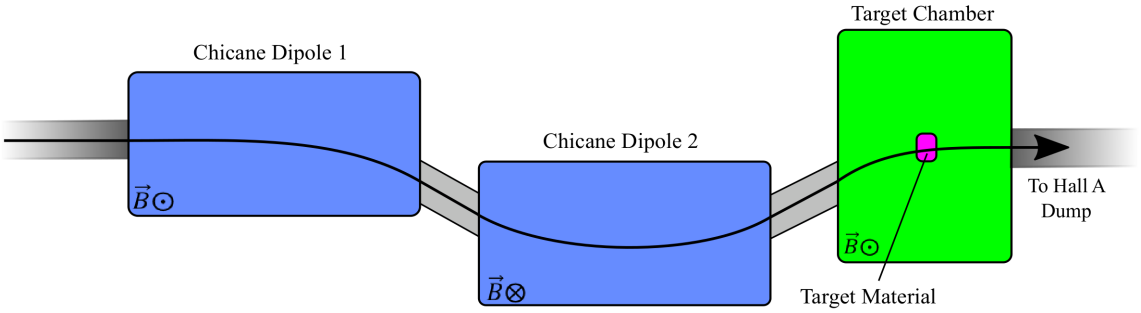

Figure 4-7: Side view of the chicane setup for E08-027. Beam enters from the left.

in Figure 4-7.

The chicane consisted of two dipole magnets, the first to kick the beam out of plane, and the second to bring the beam back into the target chamber. The vertical positioning of the magnets was unique to each beam energy setting such that it would hit at exactly the target center. The angular deflection of the upstream chicane for each energy setting is shown in Table 4.3. After hitting the target cup the beam will continue to experience downward bending by the target field. In two specific beam energy settings, 3.350 GeV and 2.254 GeV at 5T, the bending downstream

Table 4.3: Vertical deflection of incident electron beam in the chicane

Energy (GeV)	Deflection Angle
1.157	11.7^o
1.710	7.6^o
2.254	5.9^o
3.350	3.9^o

of the target cup was such that the beam would be unable to reach the Hall A beam dump, for these situations a local beam dump was installed immediately downstream of the target. The beam dump system is discussed in more detail in Section 4.2.7.

4.2.6 Septum

Several experiments in Hall A called for forward angle scattering measurements less than 12.5°. However, the High Resolution Spectrometer arms are only capable of closing to 12.5°. The reason for this is that the HRS dipole magnets, which act to bend scattered electrons up into the detector stack, cannot move to smaller angles without physically overlapping the beam pipe. To overcome this issue a superconducting dipole magnet, called the septum, was placed in front of the acceptance for each spectrometer arm. The septum allowed for 6° central angle scattered electrons to be bent into the HRS acceptance window.

During the running of E08-027 the septum encountered several issues. About 8 weeks into the experiment one of the coils on the right dipole shorted. The standard coil configuration was three groups of coils, one with 48 turns and two with 12 turns each (the 48-12-12 configuration). After one of the coils shorted, one of the groups was bypassed entirely. This resulted in a second coil configuration, aptly named the 48-0-12 configuration for the number of coils used. Several weeks later a second coil group shorted and had to be bypassed. We introduced a third coil configuration, called 48-0-0, for the last few weeks of experiment running. The current in each configuration was adjusted so that the effect on the acceptance was minimal. But, due to the septum field changing because of the different geometric orientation of the coils, different optics matrices had

to be found for each configuration. This quickly became one of the most prominent complications for the analysis of experiment E08-027. At the time of this writing an acceptance study is still underway which is discussed in more detail in Section 6.5.

4.2.7 Local and Hall Dump

After traveling through the target field the beam continues along the beamline to the far end of Hall A and into the beam dump. The dump consists of two 6.3 mm thick beryllium foils with water flowing between them that act to diffuse the beam before being deposited on the surface of the dump itself, 23 m inside the dump tunnel. The dump is designed to operate at a maximum current of 190 μA [5].

For those settings where the beam was unable to reach the hall beam dump due to downward bending of the target field, a localized beam dump was installed immediately downstream of the target chamber. The local beam dump consisted of a single tungsten block which the beam was deposited on to. Due to the increased irradiation, the use of the local beam dump was kept to a minimum, and used only during the last two configurations of the experiment.

4.3 High Resolution Spectrometers

Hall A contains two spectrometer arms able to pivot around the target chamber so as to detect scattering from various angles. The two spectrometers are nearly identical and contain three quadrupole focusing magnets, labeled Q_1, Q_2 and Q_3 and one dipole bending magnet, labeled D_1. The spectrometer arms are arranged in a QQDQ configuration as shown in Figure 4-8 with D_1 capable of a 45° vertical bending of scattered particles and a momentum resolution on the 10^{-4} level over a 0.8 to 4.0 GeV/c momentum range. The quadrupoles are arranged such that Q_1 provides focusing in the vertical plane while Q_2 and Q_3 provide focusing in the transverse plane. This provides an angular resolution of <1 mrad in both the horizontal and vertical direction.

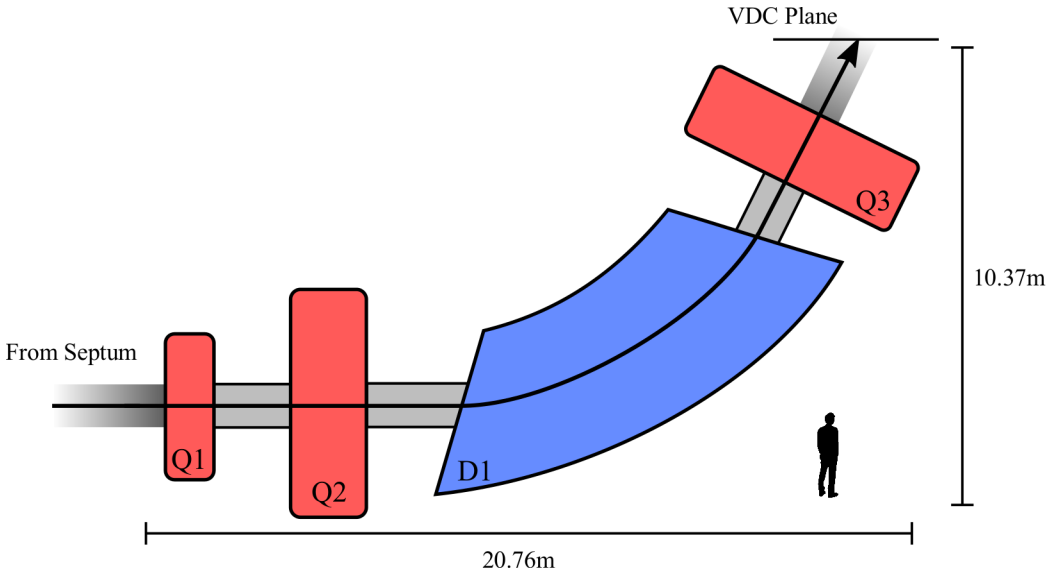

Figure 4-8: Side view of one High Resolution Spectrometer in Hall A. Beam enters from the left.

The magnetic field of each dipole is measured using an array of three NMR field probes which provide a measurement range from 0.17 to 2.10 T with an accuracy at the 10^{-5} level. The spectrometer central momentum is then selected by setting the dipole field under the relation:

$$P_0 = \Gamma \cdot B_0 \tag{4.4}$$

where Γ is a calibrated spectrometer constant and B_0 is the dipole field.

4.4 Detector Package

Experiment E08-027 used the standard Hall A detector package for each spectrometer arm. A general overview of each component of the detector housing can be found in the Hall A *Nuclear Instruments and Methods* (NIM) paper [5]. This includes a vertical drift chamber in each arm to be used in conjunction with a sieve plate for position tracking, lead-glass shower counters and a gas Čerenkov for particle ID, and a pair of plastic scintillator planes for triggering. The two detector housings were virtually identical for E08-027 so only the left spectrometer arm will be discussed

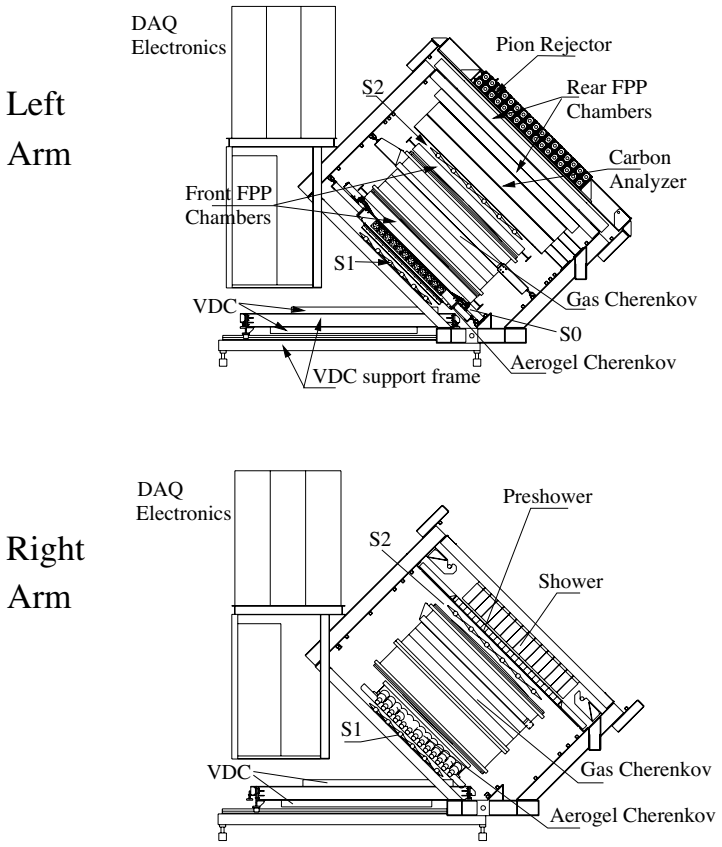

Figure 4-9: Diagram of the detector housing for both the left and right spectrometers. It is important to note that for the running of g_2^p the FPP chambers and the Carbon Analyzer were not used.

in the following sections. It can be assumed that the right spectrometer mirrors this discussion exactly, unless otherwise stated.

4.4.1 Detector Hut Shielding

All of the detector panels discussed in this section are housed inside of a concrete shielding hut located 10 meters above the Hall floor. There are two main components to the detector shielding: a block meant to protect the detectors from direct line of site to the scattering chamber, and the

shielding hut itself, meant to protect the detectors from radiation sources in any direction. The Line-of-Sight block is a 2 meter thick concrete block position above quadrupoles Q_1 and Q_2 which serve to limit the muon rate seen at the detectors. The shielding hut is a square enclosure around the detectors. It consists of a 5 cm lead layer sandwiched between a 10 cm steel frame, surrounded by up to 100 cm of concrete. The radiation level inside the shielding hut is below 1 mrem per hour with a beam luminosity on the order of 10^{38} $cm^{-2}s^{-1}$.

4.4.2 Vertical Drift Chambers

The vertical drift chambers (VDC) provide position and angle tracking of scattered particles in the detector housing. Each VDC detector consists of two wire planes separated by about 335 mm. The wires in each plane are oriented 90° to each other, and lie flat as seen in Figure 4-9. Each plane consists of 368 'sensing' wires spaced 4.24 mm apart [47]. The entire wire chamber volume is sealed and filled with a gaseous mixture composed of 62% argon and 38% ethane. An electric field is applied to each wire plane using gold-plated Mylar and kept at a voltage differential of -4.0 kV. The argon in the gas mixture acts as an ionizing medium for electrons traveling through the detector. The ionized electrons will accelerate along the electric field lines in the detector which in turn ionize more argon, the resulting avalanche of electrons travel down to the closest wire and produce a detectable signal on the wire itself. The signal is read out by a LeCroy amplifier card positioned 30 cm away from the chamber.

The VDC plane is positioned parallel to the hall floor. Electrons passing through the wire chamber in this configuration will enter at an angle, causing them to nominally cross four to six wires per plane. By using time-to-digital converters (TDCs) the drift distance of each electron avalanche is determined and a cross-over point of the electron track can be determined. This is shown more clearly in Figure 4-10. Using the cross-over point on each VDC plane the particle trajectory can be calculated with an angular resolution on the order of 0.5 mrad.

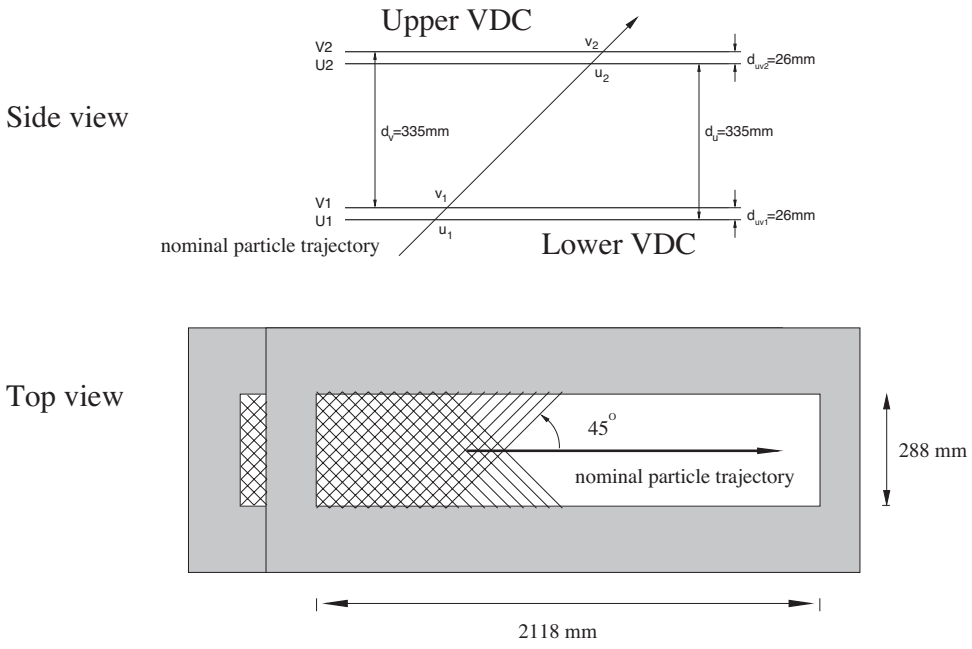

Figure 4-10: Vertical Drift Chambers (VDCs). Reproduced from [5].

4.4.3 Scintillators and Triggers

Two plastic scintillator planes are used to form the triggers for E08-027. Triggers are a set of logical statements, using signals from these detectors, that must be satisfied in order for the data acquisition system (DAQ) to record the signal as an 'event' to be stored and analyzed. The detectors used in forming the triggers are two sets of plastic scintillator planes, called s1 and s2m. The s1 scintillator plane consists of six 5 mm thick pieces of scintillating material in a 1 x 6 arrangement, while the s2m consists of sixteen 5 cm thick paddles in a 1 x 16 arrangement. The two scintillator planes are separated by about two meters in the detector hut.

The main trigger for E08-027, called T_1 on the right spectrometer and T_3 on the left spectrometer, was defined by a signal in both scintillator planes. It was formed using the following logic statement:

- The left and right PMTs on a paddle of s1 both fire.

- The left and right PMTs on a paddle of s2m both fire.
- The event causes both s1 and s2m to fire.

This trigger is formed after introducing a signal delay to s1 to account for the travel time of particles between the two scintillator planes, on the order of several nanoseconds. A second trigger, called the efficiency trigger, was created to persistently check the efficiency of the scintillator planes. This trigger, T_2 on the right spectrometer and T_4 on the left spectrometer was formed using the following logic statement:

- The left and right PMTs on a paddle of either s1 OR s2m fire, but not on both.
- The signal is seen in the gas Čerenkov.

If an event is seen in the gas Čerenkov (Section 4.4.4) it is potentially a good event that one of the scintillator planes failed to detect. The efficiency of the scintillator planes is then defined as

$$\epsilon_{trigger} = \frac{T_{1(3)}}{T_{1(3)} + T_{2(4)}} \tag{4.5}$$

where $T_{1(3)}$ and $T_{2(4)}$ are the total right(left) spectrometer main and efficiency triggers, respectively. After the triggers are formed, they are sent to the trigger supervisor module which determines if the event should be recorded. After an event is recorded there is a set recovery time before the data acquisition system can accept another event. If an event is accepted by the trigger supervisor during this window it is unable to be recorded, contributing to the data acquisition *deadtime*, or DT. To minimize the DT during periods of high event rates, a prescale factor was introduced that limits the number of recorded events by a set amount. For example, by setting a prescale value to 3, only every third event from the trigger supervisor was recorded. This fixed limiter made it possible to keep the DT to a minimum during high event rate situations.

4.4.4 Gas Čerenkov Detector

A gas Čerenkov detector was used as a pion rejector. The Čerenkov detector exploits the fact that the velocity of light is fractionally reduced by $1/n$ when traveling through a gas with index of refraction 'n'. If a particle traveling through the same medium exceeds the speed of light (in the medium) a conical wave of light, called Čerenkov radiation, will be emitted along the particles trajectory. The threshold for the production of Čerenkov radiation is

$$\beta c \geq \frac{c}{n} \tag{4.6}$$

where β is the particles velocity in the medium. This allows for a very effective method of particle discrimination based on its velocity (or, as a direct consequence, its momentum) simply by picking a medium with the appropriate index of refraction.

For the E08-027 experiment, a gas Čerenkov detector in each spectrometer arm was filled with atmospheric CO_2 with an index of refraction of 1.00041 [48]. Plugging this into Equation 4.6 and using the relation

$$P_{th} = \frac{mc}{\sqrt{1-\beta^2}} \tag{4.7}$$

results in an electron threshold momentum of 18 MeV/c and a pion threshold of 4.87 GeV/c. The momentum range for E08-027 was 0.52 GeV/c to 3.0 GeV/c which is well below the pion threshold. So all incident electrons will emit Čerenkov radiation, while pions will not. This provides a very effective method for pion rejection.

Each detector houses 10 spherical mirrors, in a 2 x 5 configuration, positioned at the correct conical half angle to reflect Čerenkov radiation into the corresponding photomultiplier tubes. The half angle position is a function of the index of refraction of the medium.

4.4.5 Lead Glass Detectors

When a high energy particle travels through a very dense material it produces a cascade of secondary particles and photons. As this secondary 'shower' of particles continues through the dense material eventually all of its energy is converted into light. The light can then be detected using photomultiplier tubes. Two such detectors were used for E08-027, named the 'pre-shower' and 'shower' detectors. The pre-shower detector consisted of 48 lead glass blocks, with each block measuring 10 cm x 10 cm x 35 cm in a 24 x 2 block configuration. The second shower detector consisted of 80 lead glass blocks, with each block measuring 15 cm x 15 cm x 35 cm in a 16 x 5 block configuration. The shower detector is the final detector that the traveling particle sees in the detector hut, and it is sufficiently thick to be considered a 'total absorption' calorimeter. This means that all of the particle's energy is converted to light while traveling through the lead glass blocks. A measure of the emitted light in the photomultiplier tubes is directly proportional to the total energy of the particle.

4.4.6 Data Acquisition System

The g_2^p experiment used the standard HRS data acquisition (DAQ) system to record event information. The DAQ system consisted of three fastbus modules, the trigger supervisor and one HAPPEX crate in each HRS detector stack. The trigger signals (Section 4.4.3) were fed into the trigger supervisor. When a trigger was satisfied by an event, all detector information about the event was fed into a data file in the Hall A DAQ (ADAQ) machines in the counting house. The data files contained timestamp information for the events, along with beam and electron helicity information, electron position and momentum information from the detectors, and EPICS information from the accelerator such as beam energy, polarization and current. Data was organized into segmented, user controlled, lengths of time called 'runs'. A dedicated run operator chose when to start and end a run using the CEBAF Online Data Acquisition system (CODA). During a run all

event information was appended to a single data file to simplify the analysis process. Run lengths were chosen to be roughly one hour long, or seven million detected events, whichever came first. All run files were copied to the JLab tape library daily for long term storage and offline analysis.

Chapter 5

Polarized Target

Calculation of the proton spin structure function requires two main components, an unpolarized proton cross-section and a proton double spin asymmetry. In order to measure the spin asymmetry it is necessary to have a highly polarized proton target. For this purpose the g_2^p experiment used an irradiated solid NH_3 target submersed in a LHe bath cooled to approximately 1K. High proton polarizations are necessary to reduce the final uncertainties in the double spin asymmetry measurement. The NH_3 material was polarized in a high magnetic field using the well understood process of Dynamic Nuclear Polarization (DNP). An accurate method for continuously measuring the polarization was also needed as material depolarization happened rapidly while the target material was exposed to beam. Polarization was measured every few seconds by Nuclear Magnetic Resonance (NMR) using a small coil embedded in the target material.

The original target system intended to be used for g_2^p was previously designed for the JLab Hall C SANE experiment [49]. Due to issues during target setup the SANE target system had to be scrapped and replaced by a modified version of the JLab Hall B target. The final magnet setup consisted of a superconducting Helmholtz coil capable of being rotated so that both the longitudinal and transverse double spin asymmetries could be measured. The performance of the target system and polarization results are published in *Nuclear Instruments and Methods* [50]. A detailed description of the magnet systems, DNP and NMR processes, and polarization analysis are discussed in the following sections.

5.1 Target Setup

The target system consisted of three components. First, the magnet system, which contained the superconducting Helmholtz coils submersed in a 4K liquid Helium (LHe) bath capable of on axis rotations for polarization measurements in various directions. Second, the evaporation refrigerator, located at the center of the magnet, was used to cool LHe from 4K down to the necessary 1K for high material polarization. Finally, the target insert, located inside the refrigerator, was used to hold several material samples at the center of the target field in the 1K fridge bath and contained NMR components for polarization measurements along with microwave components for DNP. A diagram of where these systems were in relation to each other is shown in Figure 5-1.

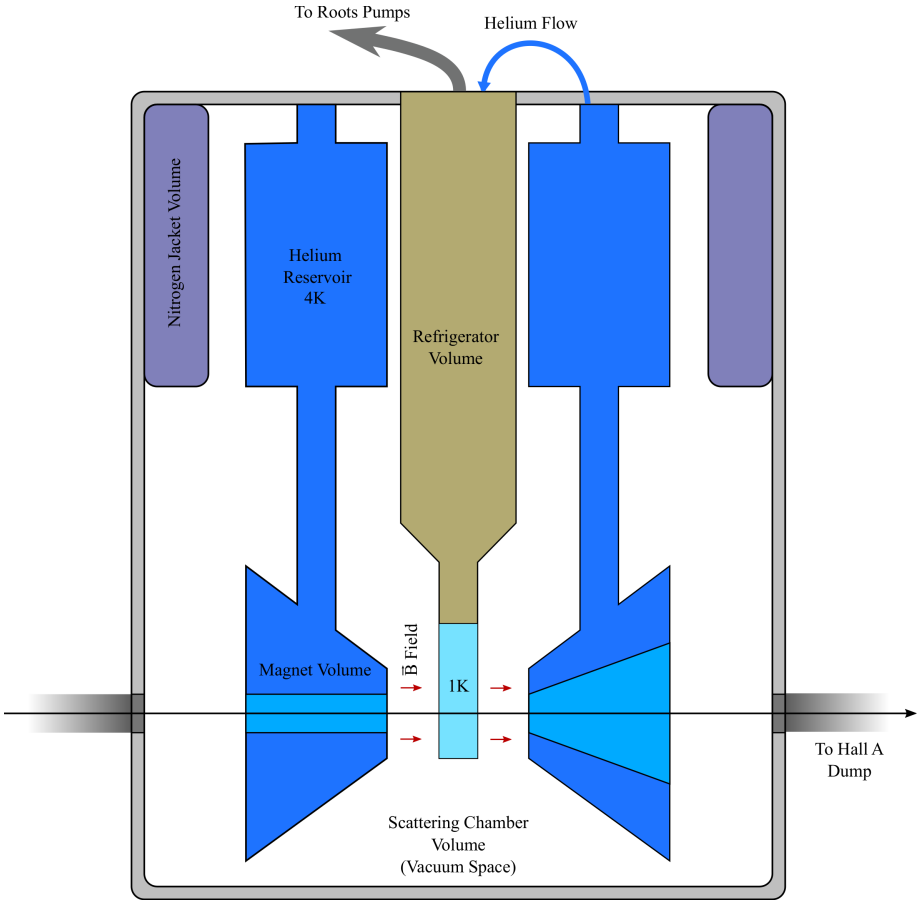

Figure 5-1: The various components of the g_2^p target system.

5.1.1 Magnet System

A 5 Tesla superconducting Helmholtz coil was used for the g_2^p experiment. The coils were obtained from the JLab Hall B polarized target and suspended in the Hall C helium dewar. The magnet system contained four openings, two longitudinal to the magnetic field and two perpendicular. Figure 5-2 shows a photograph of the magnet system wrapped in super insulation. The entire

Figure 5-2: The g_2^p polarized target magnet covered in insulation suspended from the LHe cryostat. The magnet is in the longitudinal field configuration from the perspective of the camera.

cryostat system was rotatable from the top plate so both field configurations could be used during the experiment. The coils produced a relative field uniformity at the center of $< 10^{-4}$ over a cylindrical volume 20mm in diameter and 20mm long [50]. Unfortunately the size of the target material was larger than the field uniformity at 25mm in diameter and 30mm long, but no adverse

affects on the polarization were observed.

The magnet coils were required to be submersed in 4K LHe for the duration of the experiment to maintain superconductivity. To achieve this the magnet volume was connected to a large Helium buffer reservoir capable of storing up to 80 liters of LHe. A helium level probe in the cryostat monitored the liquid level while LHe was continuously supplied to the reservoir from the JLab liquefier. The reservoir in the cryostat was connected to the magnet volume by a small stainless steel hose. The entire magnet volume was suspended inside of a vacuum sealed shell, called the scattering chamber, to insulate the LHe reservoir and refrigerator from the room temperature air around it. The scattering chamber was evacuated to 10^{-7} Torr using a diffusion pump.

5.1.2 Evaporation Refrigerator

The 4K LHe supplied by the JLab liquefier is too warm to achieve the polarization levels required by g_2^p. To further cool the LHe, an evaporation refrigerator was installed in the center of the magnet coil volume. The refrigerator worked by siphoning LHe from the 4K LHe reservoir into a 1 liter stainless steel cylindrical volume called the 'separator'. The separator was bisected by a 1mm thick perforated plate that allowed liquid to pass though while vapor was pumped away through a series of copper heat exchangers by a continuously running diaphragm pump. The vapor flow was monitored and kept at around 5 liters per minute to ensure the heat exchangers were brought down to around 70K. The liquid in the separator was drained through another series of heat exchangers before being deposited into a small bath at the bottom of the fridge called the 'nose'. Helium vapor produced in the bath was quickly pulled away by a large, 12,000 m^3hr^{-1} Roots pump set which further cooled the heat exchangers [50]. A needle valve on the LHe fill line was connected to a computer-controlled feedback loop to maintain a constant LHe level in the nose. With this setup a base temperature of about 0.9K at the nose could be achieved.

At the center of the fridge, traversing its entire length, was a 2 in. stainless steel tube for easy

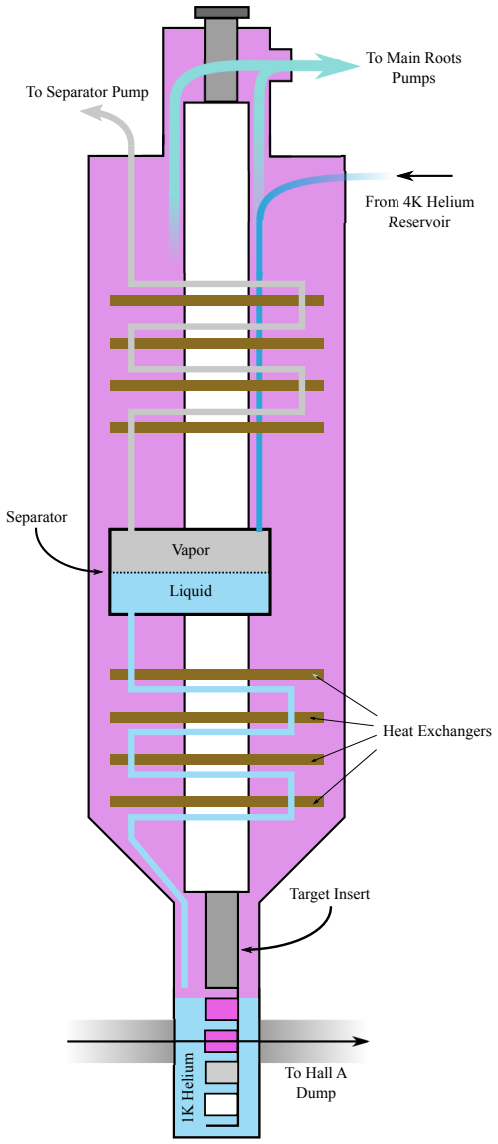

Figure 5-3: Diagram of the g_2^p evaporation refrigerator and its various components.

access to the nose volume. Various temperature and pressure sensors were attached to the insert tube for monitoring LHe levels and temperatures at the nose. Finally, a small wire heating element was attached to the bottom of the tube for annealing (Section 5.4.4).

5.1.3 Target Insert

The next piece of the target system was the removable target stick which contained the various g_2^p target materials. The target stick was a long carbon fiber tube with an aluminum ladder attached

to one end. The ladder had four cups attached to it as seen in Figure 5-4. One of the cups contained

Figure 5-4: Side view of the ladder attached to the end of the target stick resting in a liquid nitrogen bath. From left to right the cups are: Empty cup (contains only LHe), dummy cup (contains a wire coil and foil endcaps), bottom NH_3 target material, a hole (for optics and alignment), top NH_3 target material. The bottom of the microwave horn can be seen on the far right.

only foil windows and an NMR coil for background subtraction studies, the second had a carbon disk in it for optics and dilution studies, while the remaining two contained NH_3 target material. The entire stick was placed vertically in the center of the fridge volume and could be raised or lowered to place any of the four cups in the beam line, depending on what the experiment called for. The top of the target stick was attached to a stepper motor and the physical position of each cup position was calibrated to the center of the target field, making it trivial to switch between target cups when necessary.

An extended interaction oscillator (EIO) tube at the top of the magnet system generated 70GHz (140GHz) microwaves necessary for the DNP process in a 2.5T (5.0T) magnetic field. The tube was connected to a waveguide that transmitted the microwaves down the target stick and into the target material via a microwave horn. The microwave system was capable of transmitting about 1W of power at 140GHz and more than 2W of power at 70GHz.

Small CuNi induction pickup coils were embedded in each of the NH_3 material cups on the target stick. The coils were connected to copper wire that travelled up the length of the target stick and into the NMR system for measuring the NH_3 polarization.

5.2 Dynamic Nuclear Polarization

The method used during the g_2^p experiment to polarize the proton target material is called dynamic nuclear polarization (DNP). This process involves exploiting electron-proton (eP) spin coupling interactions by injecting microwaves into the target material at the correct frequency to drive eP pair spin flips. This, combined with low temperatures and high magnetic fields, allowed for proton polarizations sufficient enough for g_2^p asymmetry measurements. In this section the details of DNP and why it was necessary will be discussed.

5.2.1 Thermal Equilibrium Polarization

Polarization can be achieved simply by placing a nucleon with an intrinsic spin in a magnetic field. Due to the nucleon's nonzero magnetic moment, it will tend to align its spin with the magnetic field. Zeeman splitting dictates that for a spin $\frac{1}{2}$ particle in a magnetic field two energy sublevels are created whose population ratio is defined by Boltzmann statistics as

$$\frac{N_\uparrow}{N_\downarrow} = e^{\frac{2\mu B}{kT}} \tag{5.1}$$

where $\pm\vec{\mu}\cdot\vec{B}$ is the energy of each state due to Zeeman splitting, k is the Boltzmann constant, T is the temperature and $\frac{N_\uparrow}{N_\downarrow}$ is the ratio of spin $+\frac{1}{2}$ to spin $-\frac{1}{2}$ particles. From here it is useful to look at the degree of polarization (or vector polarization[1]), representing the net polarization of all particles in the target field.

$$P_{TE} = \frac{e^{\frac{\mu B}{kT}} - e^{\frac{-\mu B}{kT}}}{e^{\frac{\mu B}{kT}} + e^{\frac{-\mu B}{kT}}} = \tanh\left(\frac{\mu B}{kT}\right) \tag{5.2}$$

Assigning some known quantities to Equation 5.2 the problem with this simplistic approach to polarization becomes apparent. For a 5T magnetic field at 1K the electron polarization is approx-

[1]For a spin $\frac{1}{2}$ particle the tensor polarization component is always zero.

imately 92%, but the proton polarization, with a substantially smaller magnetic moment, is only about 0.3% [51]. This is insufficient for an effective proton asymmetry measurement so the method of dynamic nuclear polarization has to be used in order to drive proton polarizations higher.

5.2.2 Zeeman Interactions and the Solid-State Effect

The process of dynamic nuclear polarization (DNP) involves doping a material of polarizable nucleons with paramagnetic radicals, or free electrons. As seen in the previous section the electron polarization is much higher than that of the nucleon. By introducing free electron radicals into the material the dipole-dipole interaction between the electron and nucleon can be exploited, effectively having the electron 'pull' the nucleon into a polarized state [52]. This dipole-dipole interaction in a magnetic field leads to four possible energy levels, as shown in Figure 5-5. The energy difference between levels is well known so, by introducing microwaves at the correct frequency, a spin flip to the desired state can be induced in the dipole-dipole system. For example, by introducing microwaves at the frequency $\nu_\mu = \nu_{EPR} - \nu_{NMR}$, the spin flip $e_\downarrow p_\downarrow \rightarrow e_\uparrow p_\uparrow$ is induced. The electron

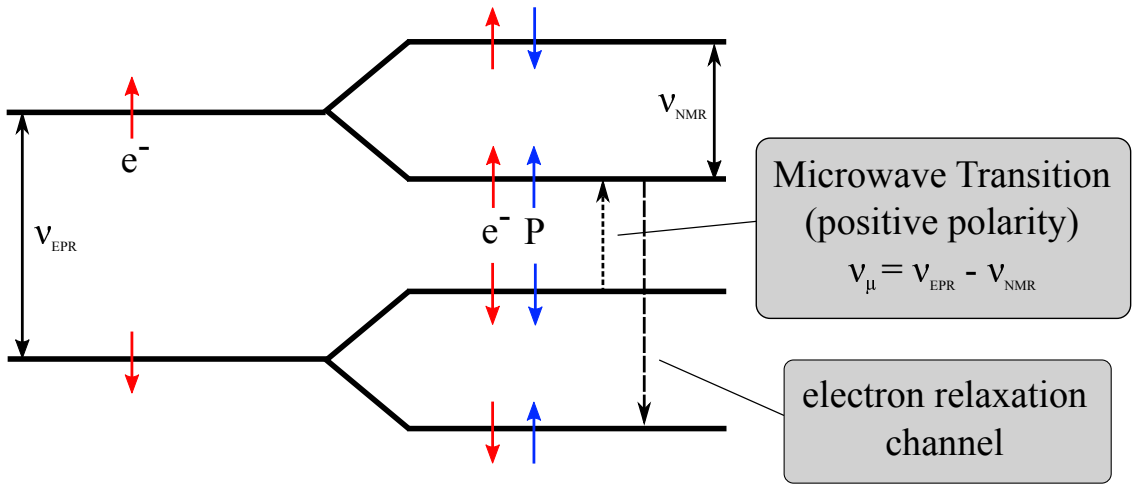

Figure 5-5: Hyperfine splitting due to the dipole-dipole interaction of the electron-proton pair in a magnetic field.

spin relaxation time is on the order of milliseconds, while the proton spin relaxation time is tens of minutes. This difference in relaxation time allows the electron to relax to the lowest energy

state and polarize another proton, continuously driving proton polarization. Positive and negative proton polarization can both be achieved using this method simply by altering the microwave frequency to match the desired final spin state. Where the transition to the spin-up state is driven by $\nu_\mu = \nu_{EPR} - \nu_{NMR}$, the proton spin-down state can be driven by $\nu_\mu = \nu_{EPR} + \nu_{NMR}$. This conveniently allows for polarization flipping during experimental running to remove any systematic effects from polarization in a single direction.

The above process is known as the solid-state effect, an idealized method developed in 1958. Unfortunately this method makes several assumptions that cannot be neglected in practice. The first is the electron doping concentration. Typically the electron concentration in the lattice crystal is on the order of $10^{-4} - 10^{-3}$ electrons per nucleus. This means that one electron is required to polarize several protons an a large area. A 'leakage' term has to be introduced to account for proton relaxation via other means in the imperfect lattice when free neighboring electrons are not available. This term acts to reduce the maximum achievable proton polarization.

In present day polarizable target materials, such as the frozen NH_3 used in g_2^p, the abundance of free radicals introduces another complication to the process of DNP. Spin-spin interactions between electron pairs in the material can't be ignored. These interactions are weak compared to the Zeeman interaction from the electron-proton pairs, so what is effectively created is a quasi-continuous energy state at each Zeeman level that represents the various electron energy states from electron spin-spin interactions. Instead of requiring a single microwave frequency, ν_μ, to induce an electron-proton spin flip, a range of frequencies is acceptable, defined by $\nu_\mu - \Delta$. Here Δ represents the energy absorbed by the electron-electron pair. The acceptable range for energy absorption at each Zeeman level is defined by a Boltzmann distribution with temperature given by the electron spin-spin interaction reservoir. This is a simplified description of what is called the 'Equal Spin Temperature Theory' [53] which further modifies the solid-state effect.

5.3 Nuclear Magnetic Resonance

A high precision measurement of the polarization provided by the DNP method is essential to the analysis of a double spin asymmetry experiment. The method for measuring target polarization during g_2^p is known as nuclear magnetic resonance (NMR). This well established method exploits the same energy level splitting of a dipole in a magnetic field that DNP uses, but on a much smaller scale. By embedding a small inductance coil in the material and varying the current a small, time varying, magnetic field is generated which induces spin flips in the nuclei. The total energy absorbed or emitted by these spin flips is proportional to the number of polarized particles. This gives a convenient, non-intrusive, way to continuously measure the material polarization.

5.3.1 NMR Theory

In the g_2^p experiment the target material was placed in an induction pickup coil connected to a series tuned LCR circuit. An RF generator was connected to the circuit and used to sweep a frequency around the proton Larmour frequency. Similar to using microwaves to induce electron spin flips in DNP, when the RF generator matches the Larmour frequency of the proton it caused a spin flip in the small secondary field generated by the pickup coil. The act of spin flipping the polarized nucleons alters the inductance of the LCR circuit due to the magnetic susceptibility of the material [52].

$$L(\omega) = L_0 (1 + 4\pi\eta\chi(\omega)), \tag{5.3}$$

$$\chi(\omega) = \chi'(\omega) - i\chi''(\omega) \tag{5.4}$$

where $\chi(\omega)$ is the magnetic susceptibility as a function of the frequency, ω, applied by the RF generator and L_0 is the inductance of the coil. The polarization of the nucleons is related to the

magnetic susceptibility by the function

$$P = K \int_0^\infty \chi''(\omega)\, d\omega \tag{5.5}$$

where K is a constant of proportionality to be determined later. For the proton the magnetic susceptibility is zero everywhere except for a very small region around the Larmour frequency, so the integral could be carried out in a small frequency 'sweep' range set by the RF generator.

It is convenient at this point to express the polarization integral in term of the coil impedance, Z.

$$Z = r + i\omega L(\omega) \tag{5.6}$$

where 'r' is the resistance of the coil and $L(\omega)$ is the coil inductance. Using Equation 5.3 and looking at only the real part of Equation 5.6 it is now possible to write the polarization in terms of the measurable coil impedance, integrated over RF frequency.

$$\Re(Z) = r + 4\pi\eta\omega\chi''(\omega) \tag{5.7}$$

$$P = \int_0^\infty \frac{\Re(Z) - r}{4\pi\eta\omega} d\omega \tag{5.8}$$

5.3.2 NMR Setup

The series LCR circuit, called the 'Q-meter' [54] was tuned using a variable capacitor so that the circuit resonated at the proton Larmour frequency of 213MHz (106.5MHz) for 5T (2.5T). When tuned correctly, and using an RF generator to sweep around the Larmour frequency, the characteristic resonance curve, called a 'Q-curve', of the circuit could be seen in the output, as shown in Figure 5-6. The Q-curve of the circuit in the absence of any target material is called the baseline, it represents the background signal of the circuit and is subtracted from the signal curve to remove any circuit dependent background effects. After embedding the pickup coil in target

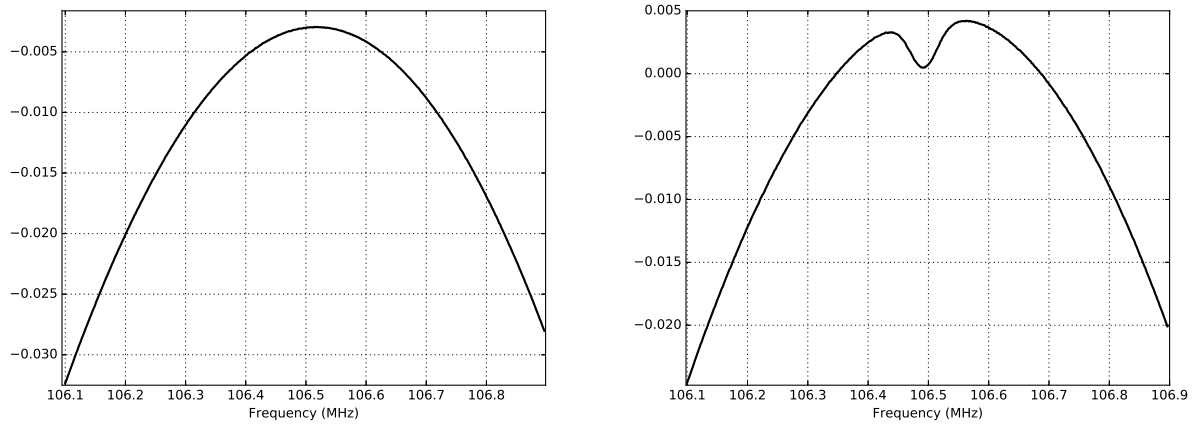

Figure 5-6: Q-curve signal without (left) and with (right) polarizable material in the inductance coil. The LCR circuit resonance is seen as the background curve. After embedding the pickup coil in the target material the effect on the coil impendence becomes apparent.

material a signal peak forms around the proton Larmour frequency due to the circuits response to the change in impedance. The material polarization was obtained by storing this 'enhanced' signal, removing the baseline, and integrating the resulting curve. Unfortunately this integrated value is only proportionally related to the polarization. One further step was required to find the constant of proportionality and the real material polarization.

5.3.3 Calibration Constants

To find the constant of proportionality, or 'calibration constant' for the material, the Q-curve needed to be measured at a known target polarization. Thankfully, this is the case when the material is at thermal equilibrium with the lattice as described in Section 5.2.1. At thermal equilibrium the proton polarization is simply a function of temperature and magnetic field,

$$\mathrm{P_{TE}} = \tanh \frac{\mu \mathrm{B}}{k\mathrm{T}}. \tag{5.9}$$

The target material will obtain thermal equilibrium with the lattice in a magnetic field naturally over time if no microwaves are being introduced. Once the material is thermalized the Q-curve

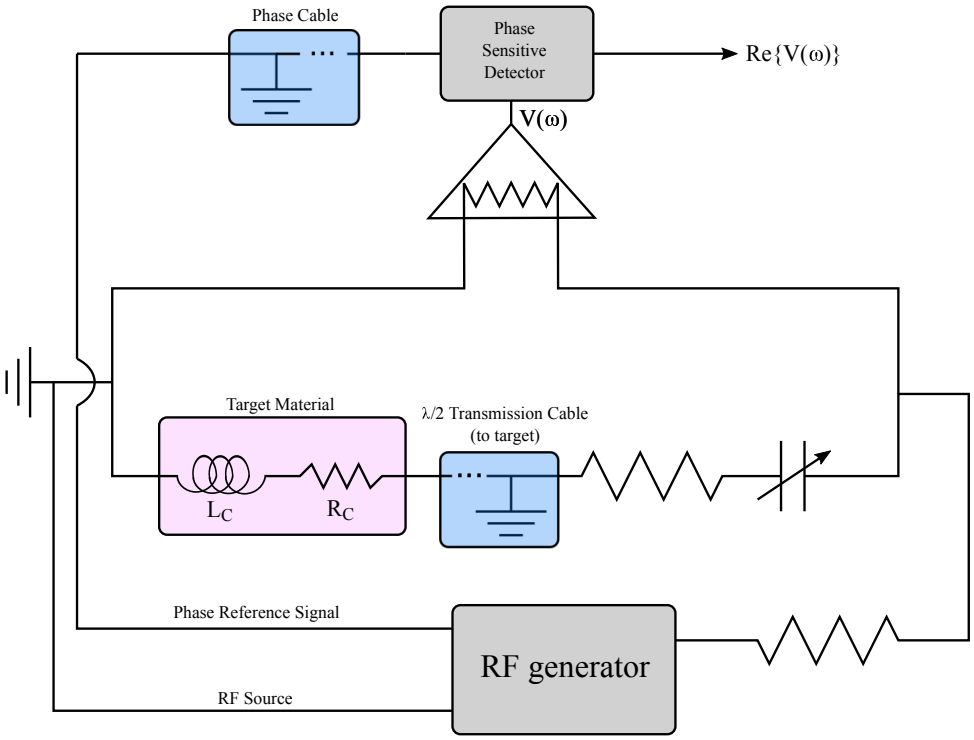

Figure 5-7: Circuit diagram for the Q-meter and surrounding systems. See text for more detail.

can again be measured and integrated to find the thermal equilibrium area, A_{TE}. The thermal equilibrium area and polarization can then be related to the 'enhanced' area and polarization linearly.

$$\frac{P_E}{P_{TE}} = \frac{A_E}{A_{TE}} \tag{5.10}$$

where 'E' stands for enhanced and 'TE' stands for thermal equilibrium polarizations and integrated areas.

Since the thermal equilibrium measurements required the polarizing microwaves be shut off this was a very intrusive calibration. Unfortunately it is also a material dependent calibration so it had to be done several times for each target material used during g_2^p. To accelerate the time it took for the material to thermalize during a TE measurement, the fridge system was warmed up slightly to ∼1.5K. This allowed the material to thermalize on the order of a few tens of minutes compared to several hours at 0.9 K. See Section 5.5 for more information on the g_2^p TE measurements and

results.

5.4 Target Material

When choosing a target material, the critical quantity to be considered for any nuclear physics experiment is the optimization of the counting rate for the reaction of interest. For the case of g_2^p this reaction was electron scattering from spin polarized protons. Several factors must be considered to optimize the counting rate; high luminosity $\mathscr{L}$, defined as the product of the target density and the electron beam current; large target polarization P, for the case of a spin polarized scattering experiment; a good 'dilution factor' f, defined as the ratio of polarizable nucleons of interest to the total number of nucleons in the target material; and running time t, a longer running time for the experiment clearly leads to more reaction counts.

It is convenient to define a target material 'figure of merit', FOM$_{exp}$ [51], to quantize the importance of each of the previously discussed quantities to help in choosing a target.

$$\mathrm{FOM}_{\mathrm{exp}} = f^2 P^2 \mathscr{L} \tag{5.11}$$

To maximize a materials figure of merit several things must be considered.

- Sufficient free electrons (radicals) present in the material to initiate the DNP process as described in Section 5.2.
- Maximized dilution factor by using a target material with a large number of polarizable nucleons compared to unpolarizable background.
- Rapid polarization of the material at temperatures and magnetic fields suitable for the experiment.
- Resistance to radiation damage in the material while being subjected to the high luminosity

electron beam.

An extensive study of various potential target materials to satisfy these requirements [55] led to the discovery of doped alcohols as a leading contender in fixed target experiment use. The most commonly used materials today are NH_3, LiH, their deuterated counterparts ND_3, LiD, and butanol. Deuterated material replaces the polarizable protons with deuterons to allow for neutron measurement experiments.

Ideally for a proton scattering experiment pure H_2 would be used to give a dilution factor of 100%. Unfortunately at cryogenic temperatures H_2 is in a spin zero state and therefor is not polarizable. For g_2^p, irradiated NH_3 was the target material of choice. After irradiation (to introduce free electron radicals, Section 5.4.2) it polarizes well in experimental conditions with a maximum theoretical polarization of $\sim$ 90% at 5T and 1K or $\sim$ 25% at 2.5T and 1K, it is highly resistant to beam irradiation and so depolarizes slowly, and provides a decent dilution factor ($\sim$ 18%) with three polarizable protons for every nitrogen atom. Ammonia is not an easy target material to deal with. At room temperature it is an extremely toxic and unpolarizable gas. Several steps had to be performed before the material was ready to be polarized at JLab.

5.4.1 Preparing Solid Material

The first step in creating a polarized ammonia target was to create small beads of solid ammonia. Ideally the finished target material will be a container full of ammonia beads each about 2mm in diameter. This configuration allows maximum thermal contact and ensures the material is of a uniform temperature in the target chamber. To first create solid ammonia, ammonia gas was flowed into an aluminum cylinder submersed in a bath of liquid nitrogen at 77K. The freezing point of ammonia is 195.5K so this process freezes the ammonia into a solid sheet which can then be crushed through a series of screens to obtain beads of approximately the size needed for the experiment. Once the beads are created they are collected and stored in small 'pill' bottles which are kept in a

bath of liquid nitrogen indefinitely.

5.4.2 Irradiation

Solid ammonia beads have no free electron radicals present so will not undergo the DNP process. The next step in preparation was then material irradiation to produce free radicals. The material was transported to the Medical Industrial Radiation Facility (MIRF) at the National Institute of Standards and Technology (NIST) in Gaithersburg, Maryland. The MIRF electron beam is capable of striking a fixed target with a beam energy of about 19 MeV and a current of 10-15 μA. The material was placed in an aluminum mesh target stick and lowered into a bath of liquid Argon at 87K, then subject to the MIRF electron beam for approximately one hour, with a 180^{o} rotation halfway through to ensure a uniform irradiation.

The process of irradiation knocks a proton out of the NH_3 to create $N\dot{H}_2$ paramagnetic radicals. This process was continued until the desired dosage of free electron radicals was roughly $10^{17}e^{-}/cm^{2}$. The irradiation process turns the color of the ammonia beads from a pale white to a deep purple,

Figure 5-8: Ammonia target material after freezing (left) and after irradiation in the MIRF electron beam (right). The ammonia changes to a deep purple hue when free electron radicals are introduced.

as shown in Figure 5-8. The irradiated material was once again stored in a liquid nitrogen bath. At liquid nitrogen temperatures the radicals are able to stay in the material for years. At that point

the target material could undergo the DNP process and was ready to be polarized at JLab.

5.4.3 Material Depolarization

Once the ammonia target material was placed in the refrigerator (Section 5.1.2) it was cooled to roughly 1K and the magnetic field was ramped up to 5.0T or 2.5T depending on the experiment configuration. The material was then showered with microwaves to initiate the DNP process for polarization. When the maximum polarization was achieved it was hit with a ∼100nA high energy electron beam. As expected with an incident electron beam introducing heat to the material, the temperature would rise slightly. This initial temperature rise causes the polarization to dip according to Curie's Law (Equation 5.2). The refridgerator system was very efficient as dissipating deposited heat from the beam with a cooling power of $\sim$ 3 W at 1.4 K, so this effect was small. The electron beam used in experiment E08-027 had a high enough energy to act as an ionizer for the target material. This meant that over long periods of time the beam broke apart NH_3 molecules into excited radicals, identical to the process of irradiation from Section 5.4.2. Initially this would cause a gradual increase in polarization as more spin-flip channels are created. An optimal does for the DNP process at 5T is $\sim 0.9 \times 10^{17}$ e/cm^2. Over time, continual ionization from the experimental beam increases the material dosage past this optimal level. The result is more channels for proton depolarization, decreasing the efficiency of the DNP process. This was seen as an exponential decay in the maximum polarization of the material over time, as shown in Figure 5-9. While experimental beam ionization continued to produce $N\dot{H}_2$ radicals, it was also creating other, more complex, radicals such as hydrazine, $N_2\dot{H}_4$, at a much lower rate. This is important to note because it was directly responsible for the materials 'end of life', in which it had to be discarded for another sample.

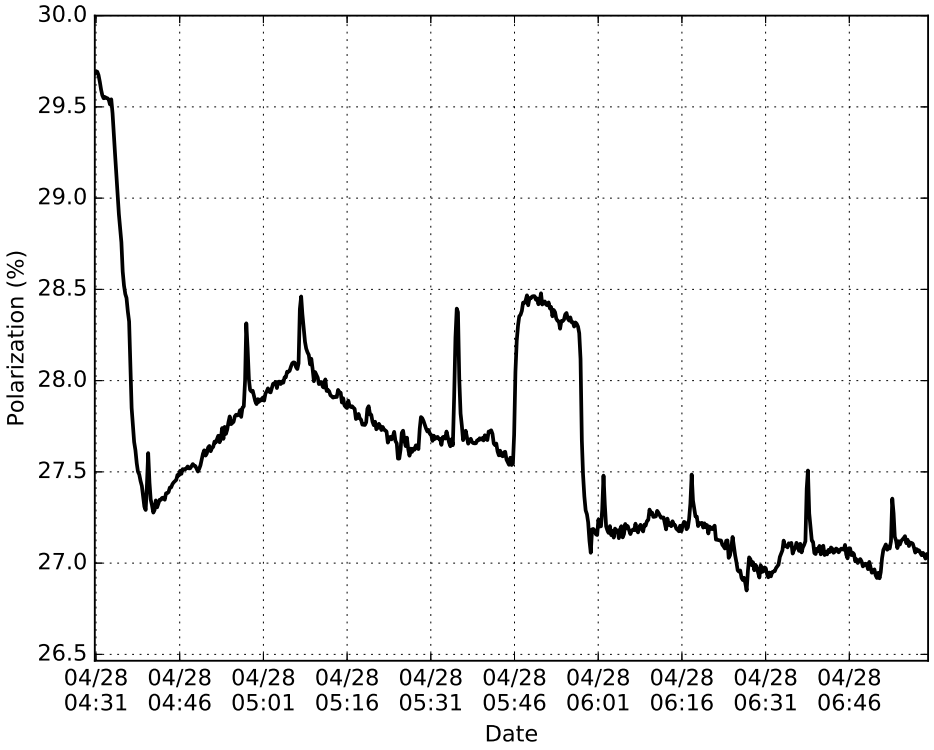

Figure 5-9: Ammonia target polarization during experimental beam running for g_2^p. An exponential decay in polarization is seen over the timescale of a few hours. Spikes in polarization correspond with a decreased heat load on the target from beam trips.

5.4.4 Annealing and End of Life

As shown in Figure 5-9 the maximum target polarization dropped significantly over a few hours. This was because the ∼50nA experimental beam quickly created an overabundance of paramagnetic radicals in the material, hindering the DNP process substantially. After roughly eight hours in beam, the target material polarization dropped to unacceptable levels for data taking. The standard process used in DNP to remedy initial polarization loss is to install a small heating coil above the target insert on the fridge. When the polarization drops too low the target stick is raised so the material cups are inside the heating coil. The heating coil is then turned on and the material is brought up to roughly 90K for 30 minutes, a process called 'annealing'. This temperature is sufficient enough to recombine radicals in the material. The temperature was closely monitored

during anneals to ensure the material did not heat up too much (> 100K), causing more radical recombinations than was desired. After roughly 30 minutes of annealing the target stick was lowered

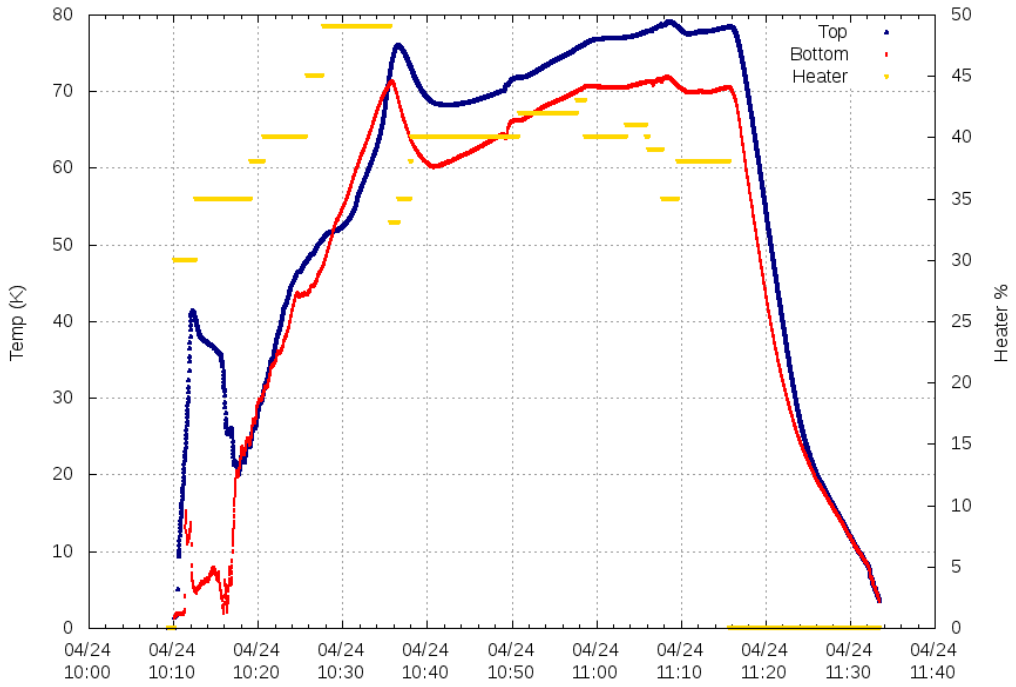

Figure 5-10: Temperature in the top and bottom target cups during an anneal. Yellow dashes indicated the amount of current being sent to the heating element. From [6].

back into the experimental beam line to continue data taking.

As mentioned in Section 5.4.3, beam ionization acted to create a small amount of more complex radicals, such as hydrazine, over time. These radicals had a much higher recombination temperature and so were not removed from the material during anneals. The creation of these radicals was slow but permanent since the temperatures required to remove them could not be achieved without potentially damaging the material. This factor led to a slow increase in the number of relaxation channels for polarized protons. This was seen as a shorter and shorter material depolarization half-life over the course of many anneal periods. After some time (on the order of days) it was no longer efficient to continue annealing and the material had to be replaced. The predictable nature of the material lifetime while in beam allowed us to estimate how many samples would be needed

for the ∼3 month running of g_2^p. In total, 10 NH_3 material cups were pre-irradiated and used during the experiment.

5.5 Polarization Analysis

The target analysis setup consisted of three stations. The Q-meter and microwave generator were located directly on top of the scattering chamber to minimize signal travel distance. The Q-meter was placed inside of a metal housing to protect the delicate electronics from radiation damage. The rest of the electronics were located on the hall floor roughly 10 feet from the target system behind a large protective concrete wall. This station included the electronics for all of the target subsystems including the magnet power supply, target stick stepper motor controller, RF generator, microwave controller, vacuum meter, and temperature sensors. These systems were networked directly to a computer in the counting house running the Polarization Display Panel (PDP), written in LabView, with the exception of the microwave frequency counter, which was controlled separately. PDP was used during the experiment to run all of the target subsystems by a dedicated target expert. The RF generator was set to sweep around the Larmour frequency of the proton every 5 seconds and the resulting Q-meter output impedance was recorded to a text file for each sweep, as well as the temperature at each location in the fridge and the magnet current.

5.5.1 Thermal Equilibrium Measurements

During the g_2^p experiment ten different NH_3 target materials were used. For each target material several TE measurements were performed to calibrate the Q-meter measurement for accurate polarization readings. During a TE measurement the target expert shut off the microwave generator and roots pumps, and waited for the polarization to thermalize. Thermalization times varied depending on the field value but took an average of 1 to 2 hours. Once the target expert determined that the material had thermalized a separate python script was run to begin collecting Q-curve integration

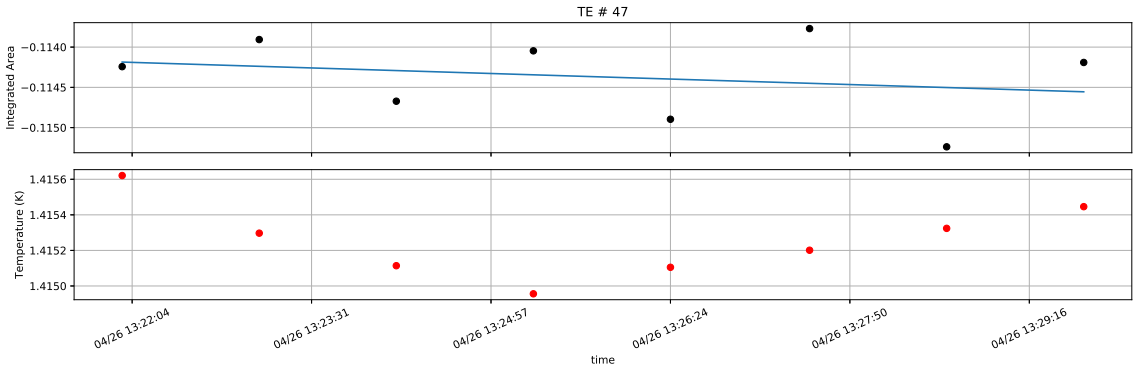

Figure 5-11: A typical Thermal Equilibrium measurement. Each NMR area point (top) is the integrated value of the Q-meter output from an RF sweep. Data taking began after the temperature and area had sufficiently thermalized.

values every 5 seconds for the duration of the TE. The amount of data taken during the TE varied depending on available time, but was always more than 10 points. Once enough data had been collected the TE was stopped and an automated script used the average integrated area, target field and temperature to calculate an 'online calibration constant'. Figure 5-11 shows the data taking period for one such TE measurement. The calibration constant was then inserted into PDP for use in determining online polarizations. The online calibration constants for TE measurements done on all materials during g_2^p are shown in Table 5.1.

Online TE measurements were done quickly to minimize the amount of time that data was not being taken and were only used to give a general idea of the polarization. A very precise measurement of the polarization was required for an accurate asymmetry measurement so additional polarization analysis was done after the running of the experiment. For this secondary analysis, the temperature and integrated area were both fit linearly starting with the final five data points of the measurement. Points were iteratively added to the beginning of the fit until the reduced χ^2 of the fit rose above one. At that point it could be said that the fluctuations in the points were no longer statistical and the integrated area and temperature were beginning to trend out of thermal equilibrium. This method also increased the number of points that could be used in each TE measurement, which further reduced the statistical uncertainty on the result. An example fit

Table 5.1: Target Materials and Associated Calibration Constants

Material	TE measurement	Online CC
7	11	-1.734839
	13	-1.753021
	19	-1.7417065
	21	-1.7435
	23	-1.72013
8	12	-1.5207665
	14	-1.4936905
	16	-1.5108
	20	-1.463427
	22	-1.400362
	24	-1.386324
11	29	-1.7541085
12	34	-1.5466705
13	47	-1.5102705
14	48	-1.8436115
17	51	-1.4249
18	52	-1.7233
19	53	-1.596351
20	54	-1.862160

to a TE measurement is shown in Figure 5-12. The thermal equilibrium polarization term was an exact calculation and did not have to be altered for the secondary analysis. Only a more rigorous uncertainty analysis needed to be done.

5.5.2 Calibration Constant Uncertainties

The calibration constant is calculated using the equation

$$\mathrm{CC} = \frac{\mathrm{P_{TE}}}{\mathrm{A_{TE}}} \tag{5.12}$$

where $\mathrm{P_{TE}}$ is the TE polarization and $\mathrm{A_{TE}}$ is the TE integrated area from the Q-meter output. As discussed in Section 5.2.1, the TE polarization is a function of only the target field and temperature so the uncertainty in the polarization is, although lengthy, a simple function of the uncertainty in

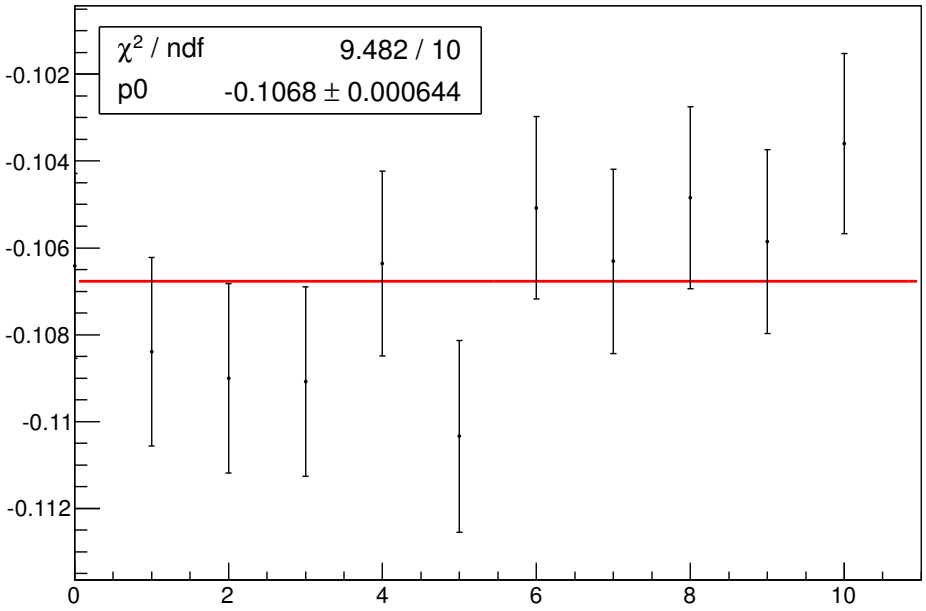

Figure 5-12: Fit to the contributing points for TE 15. The reduced χ^2 and fit result (average integrated area) are shown in the plot. The horizontal axis is arbitrary (point index number, where each point is roughly 1 minute).

the temperature and magnetic field.

$$\delta_{\mathrm{P_{TE}}} = \frac{\mu \mathrm{B}}{k\mathrm{T}} \sqrt{\left[\left(1 - \tanh\left(\frac{\mu \mathrm{B}}{k\mathrm{T}}\right)^2\right) \frac{\delta_{\mathrm{B}}}{\mathrm{B}}\right]^2 + \left[\left(1 - \tanh\left(\frac{\mu \mathrm{B}}{k\mathrm{T}}\right)^2\right) \frac{\delta_{\mathrm{T}}}{\mathrm{T}}\right]^2}. \tag{5.13}$$

The uncertainty in the temperature, δ_{T} was determined by taking the difference in temperature readings between two sensors (a ^{3}He and ^{4}He manometer) located at the target cup while the uncertainty in the magnetic field, δ_{B}, was dictated by the precision of the magnet power supply which was quoted at 0.3% [56].

The final contributing factor to the calibration constant uncertainty was the uncertainty in the Q-curve integration method, $\delta_{\mathrm{A_{TE}}}$. For the uncertainty in the integration method a Gaussian of known area was generated and integrated using the same method. The variance between the integrated area and the known area was then applied to the integration as a total systematic uncertainty. This

uncertainty varied largely based on the quality of the NMR signal but was never larger than 3%. Each calibration constant uncertainty was then propagated as

$$\delta_{\mathrm{CC}} = \frac{\mathrm{P_{TE}}}{\mathrm{A_{TE}}} \left(\frac{\delta_{\mathrm{P_{TE}}}}{\mathrm{P_{TE}}} + \frac{\delta_{\mathrm{A_{TE}}}}{\mathrm{A_{TE}}} \right) \tag{5.14}$$

for each point taken during the TE measurement. The final value of the calibration constant for a TE measurement was taken as the weighted average of all contributing points. For materials 7, 8, 19 and 20 multiple TE's were taken. In these instances the weighted average of all calibration constants were weighted again to give one resulting value for each material. The final offline calibration constants with associated uncertainties are shown in Table 5.2.

Table 5.2: Material Calibration Constants

Material	Offline CC	CC Uncertainty	% Uncertainty
7	-1.773	0.017	0.97
8	-1.443	0.014	0.94
11	-1.806	0.060	3.35
12	-1.599	0.048	2.99
13	-1.502	0.067	4.46
14	-1.840	0.068	3.67
17	-1.447	0.030	2.06
18	-1.752	0.025	1.43
19	-1.621	0.015	0.95
20	-1.879	0.048	2.58

5.5.3 Run Polarizations

During production data taking the integrated area from the Q-meter output was recorded roughly every 5 seconds. The polarization was calculated in real time as

$$\mathrm{P} = \mathrm{A} \times \mathrm{CC} \tag{5.15}$$

where A was the integrated area and CC was the calibration constant, discussed in Section 5.5.1. In this way the target polarization could easily be monitored during the experiment. For the final

polarization values the online calculated calibration constants were replaced by those from Table 5.2 and the final polarization uncertainties were propagated through as

$$\delta_{\mathrm{P}} = \mathrm{A}\delta_{\mathrm{CC}} \tag{5.16}$$

where the uncertainty in the integration method for an enhanced polarization signal was determined to be negligible due to the size of the enhanced signal. For analysis purposes it was convenient to express the polarization results in terms of a single, time-averaged, value for each run. An exponential decay was fit to the polarization for each run and the average value was taken as the final run averaged polarization, with the spread in polarization within a run being added to the final systematic. Figure 5-13 shows the final polarization values for all g_2^p production runs at 2.5T and 5T. The experiment averaged polarizations were approximately 15% for 2.5T and 70% for 5T. The experiment averaged polarizations are only rudimentary approximations and not meant to be used for anything other than a gauge of the targets performance as the polarizations varied by upwards of $\pm 5 - 10\%$ over the course of the experiment.

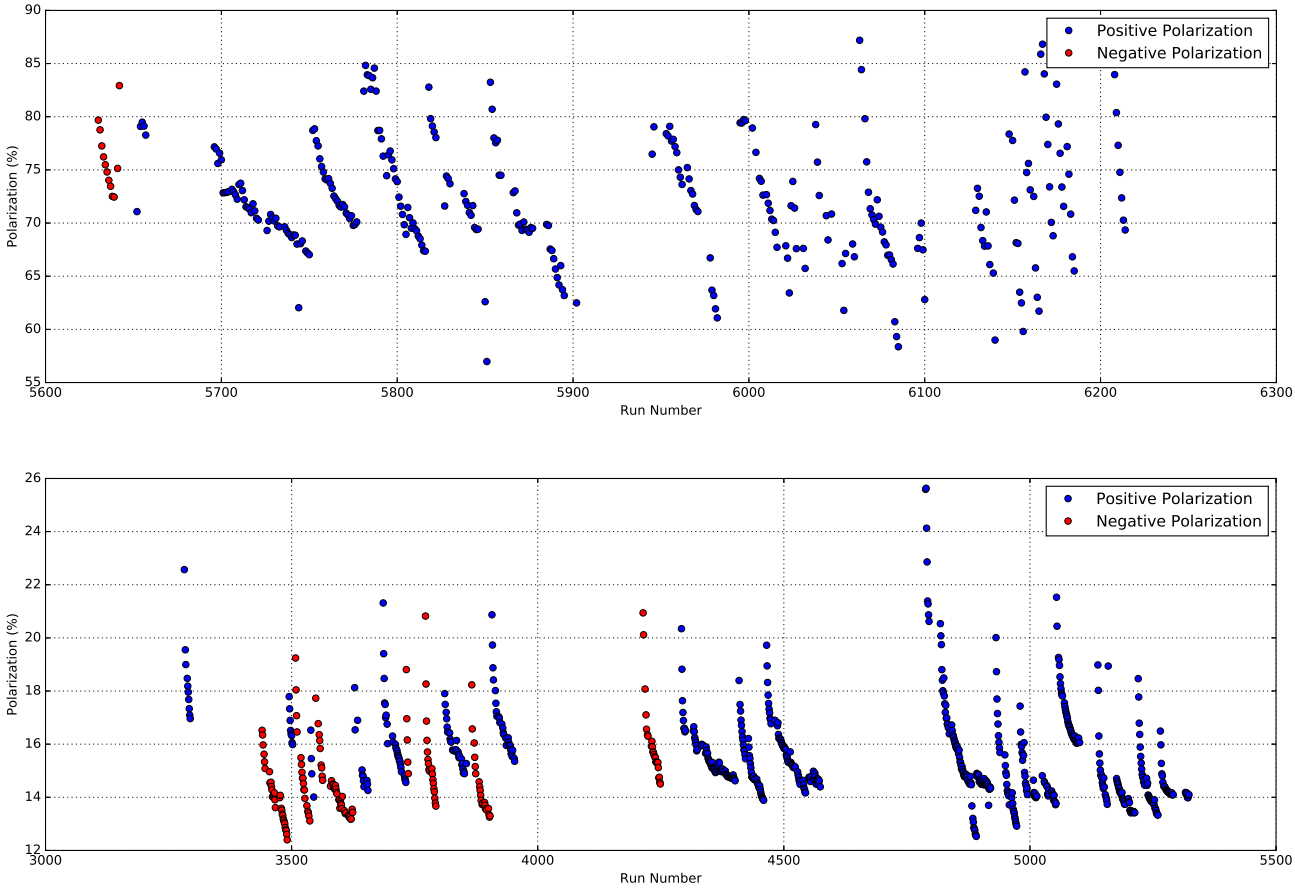

Figure 5-13: Final 5T polarizations (top) and 2.5T polarizations (bottom) for all runs.

Chapter 6

Analysis

As discussed in Section 2 the two quantities needed to extract the proton spin structure function are the physics asymmetry and the unpolarized cross section. Before these quantities could be calculated the raw data from the experiment had to go through several calibration, reconstruction and correction stages. In this chapter, the format for data storage and analysis, along with each stage in data reconstruction, will be discussed.

6.1 Data Acquisition and Storage

The g_2^p experiment collected raw data over the course of 2 months. During acquisition, data was segmented into small tabular files called 'runs', as discussed in Section 4.4.6. These runs were stored locally at the accelerator site on the Hall A data acquisition (ADAQ) machines. At the end of each day the data files were automatically copied over to tape storage at the CEBAF computer center for long term storage.

During the 2 months of running, g_2^p collected upwards of 25 billion events segmented into about 5000 runs. Each of the runs contained tabular information such as energy, position and timing, read out from the various detectors and beamline systems in Hall A for all of the 25 billion detected events. The storage requirements for this amount of information equated to several tens of terabytes. Jefferson Lab utilizes an array of magnetic tape drives, called the 'mass storage system' (MSS) to permanently store the data. A suite of user programs and server processes called 'Jasmine' is used

to interface with MSS for writing and reading purposes, while a toolkit called 'Analyzer' is used to deconstruct the data files into a useable format. Analyzer is a data analysis framework built on top of the (CERN) ROOT framework typically used in accelerator experiments. Analyzer adds several Hall A exclusive libraries to ROOT to help with data calibration and deconstruction. The procedure for bringing the g_2^p data to a local machine for analysis went as follows:

- Experimental data from the Hall A detector suite is piped through CODA and stored locally at the accelerator site on the ADAQ machines in segmented run files.
- High priority scheduled tasks in Jasmine shuttle the experimental data from ADAQ to MSS at the CEBAF center for long term storage.
- Users request data for analysis by submitting jobs through a software system called 'Auger'.
- Cached data is fed into the Analyzer toolkit where each stored attribute (energy, helicity, position, etc...) is populated with the value corresponding to each event in the data file. The populated attributes are written to 'tree structured' data files called rootfiles.
- Rootfiles are saved locally for calibration and analysis work.

Rootfiles are an extremely efficient way to analyze the large quantities of data received from the experimental hall. The tree structure of a rootfile allows for the user to call a specific attribute, or 'branch', of interest and plot the corresponding values of all events stored in that run. Furthermore, the tree structure allows a user to perform logical tasks on one branch, while observing the change in output of another branch, making data selection very simple. For example, by implementing the line of code

T.Draw("particle_energy","helicity==1")

the user can draw the event attribute 'particle energy' for all particles in the positive 'helicity' state.

More complex commands than the code snippet above were written to extensive scripts that could be executed directly in Analyzer. These scripts were custom written for any task that needed to be done on the data files, and typically written in C++ or Python scripting languages. The output drawn attributes were stored in histogram format for physics extraction.

6.2 Asymmetry and Cross Section Overview

As discussed in Chapter 2 the spin polarized proton structure function, g_2, is calculated from a combination of the transverse and longitudinal polarized cross section differences $\left(\Delta\sigma^{phys}_{\parallel,\perp}\right)$. The cross section differences are calculated as the product of the physics asymmetry and the unpolarized cross section as

$$\Delta\sigma^{phys}_{\parallel,\perp} = 2A^{phys}_{\parallel,\perp}\sigma^{phys}_0 \tag{6.1}$$

where $A^{phys}_{\parallel,\perp}$ is the parallel(perpendicular) physics asymmetry and σ^{phys}_0 is the unpolarized proton cross section.

The physics asymmetry is the difference over the sum of polarized electron scattering off of polarized protons in antiparallel polarization states. This quantity can be calculated from the detected events in each helicity state, with a correction factor to account for scattering off of unpolarized material.

$$A^{phys}_{\parallel,\perp} = \frac{1}{fP_bP_t}A^{raw}_{\parallel,\perp} \tag{6.2}$$

$$A^{raw}_{\parallel,\perp} = \frac{\frac{N_+}{LT_+Q_+} - \frac{N_-}{LT_-Q_-}}{\frac{N_+}{LT_+Q_+} + \frac{N_-}{LT_-Q_-}} \tag{6.3}$$

where $P_{b,t}$ is the measured beam(target) polarization, f is the calculated 'dilution factor' which accounts for scattering off of anything other than polarized protons, $LT_\pm$ and $Q_\pm$ are the measured live-time and accumulated charge for events in the positive(negative) helicity state, respectively, and $N_\pm$ are recorded events.

The unpolarized cross section is a scaled quantity related to the total number of detected events. A well understood region in kinematic space is required to extract the cross section so, unlike the asymmetry, a defined acceptance and energy region are required.

$$\sigma_0^{phys} = \left(f \frac{psN}{QLT\epsilon_{det}} \right) \left(\frac{1}{\Delta\Omega \Delta E' \Delta Z} \right) \tag{6.4}$$

where the first term defines the 'proton yield' with N detected events, and the second term defines the kinematic region of interest with $\Delta\Omega$ the solid angle subtended by the detectors, $\Delta E'$ the momentum region seen by the detectors and ΔZ the target length seen in the acceptance.

The cross section and asymmetry are now defined in terms of measurable quantities obtained from the detector suite. The first step in extracting these measurable quantities was to isolate 'good' events in the data using the known characteristics of the detectors, as well as their corresponding efficiencies, this is known as the detector calibration process. The efficiency of the trigger system, defined as the ratio of triggered events over the total number of 'good' events, also needed to be determined. The following several sections explain the calibration process, as well as the results of the calibrations and efficiency studies, for each detector.

6.3 Detector Calibrations and Efficiencies

The HRS detector stack contained two vertical drift chambers (VDCs), a gas Čerenkov, two scintillator planes and two lead glass calorimeters. The details of each detector is discussed in Section 4.4. The scintillators were used in conjunction with the gas Čerenkov for event triggering and particle identification selections, while the VDCs and calorimeters measured particle energy and position information.

The calibration stage of each detector had three parts. First the raw output, typically voltage, needed to be scaled into a meaningful quantity, like energy. Second, the efficiency was calculated to

determine the performance of the detector throughout the run period. Finally, an event selection was defined in terms of the scaled detector output to remove unwanted events from data. A more detailed discussion of the gas Čerenkov and lead glass calorimeter calibration and efficiency studies can be found in Ref. [7].

6.3.1 Gas Čerenkov

The gas Čerenkov consisted of 10 photomultiplier tubes (PMT's) that detected the conical wave of Čerenkov radiation due to particles passing through the chamber. Each PMT was connected to an analog-to-digital converter (ADC) that digitized the signal and stored it in the run files. Each signal contained a sharp peak, called the 'single photoelectron' peak, and a broad spectrum from multiple photoelectron scattering as seen in Figure 6-1. 'Good' electron events will only create

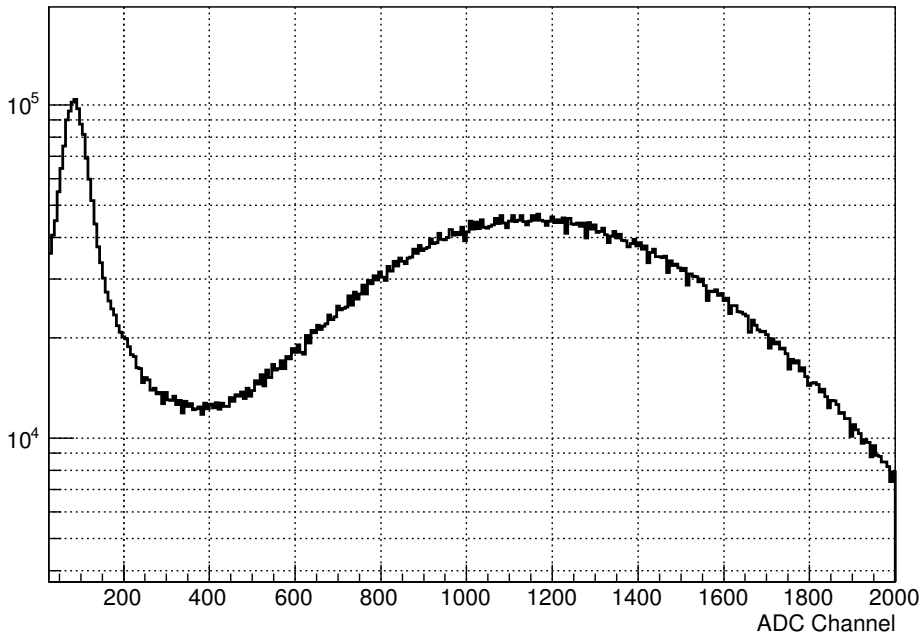

Figure 6-1: The raw ADC signal from one of ten PMTs in the gas Čerenkov. The single photoelectron peak can be seen to the left.

multiple photoelectrons so the single photoelectron peak was considered 'background' created by secondary scattering in the Čerenkov. The goal of the Čerenkov analysis was to remove this peak

from data. First the single photoelectron peak signal from each of the ten ADC's must be aligned to the same relative channel. This was done simply by fitting a gaussian-landau convolution to the peak and finding the mean value for all ten channels. An overall scale factor could be introduced to scale each peak to the same channel. Once all ten channels matched relative to each other, the signals could be added together to create a total 'Čerenkov sum' signal and an event selection region could be defined.

The event selection was done by choosing an ADC channel that maximized the multiple photoelectron spectrum while removing the single photoelectron peak. For the g_2^p analysis the ADC channel that defined this cut was run dependent, but typically around channel 200.

6.3.2 Lead Glass Calorimeters

The lead glass calorimeter calibration is significantly more involved than that of the Gas Čerenkov. Each HRS in Hall A has two calorimeters, but each pair works in different ways. The right HRS calorimeters are considered 'total energy absorbers' because as the particle passes through the dense detector medium all of its energy is converted into light and picked up by the PMTs. The left HRS is not a total energy absorber, so only some fraction of the particles energy is detected. The calibration of these two detector pairs will be discussed individually.

To calibrate the total energy absorption calorimeter the raw signal from each ADC had to be converted into an absolute value of energy deposited by the particle. As the particle traversed the lead glass detector it continuously deposited energy across all blocks that it passed through. By choosing a well defined momentum region, the sum of the ADC signal across all blocks could be subtracted from the particle momentum and a calibration constant could be found,

$$\chi^2 = \sum_i^n \left[\sum_j C_j \cdot \left(A_j^i - P_j\right) + \sum_k C_k \cdot \left(A_k^i - P_k\right) - P_{kin}^i \right]^2 \tag{6.5}$$

where $A_{j,k}$ are the ADC signal from each block, $P_{j,k}$ are a constant offset present in the ADC, called the 'pedestal values', $C_{j,k}$ are the calibration constants of interest and P_{kin} is the known momentum of the detected particle. By minimizing Equation 6.5 for each setting, a set of calibration constants could be found to convert the ADC signal into energy.

Since the right HRS calorimeters were total energy absorbers, the calibration of the detector could be checked by taking the ratio E/p where E is the detected energy of each particle and p is the HRS momentum. Since it is expected that all energy be deposited into the calorimeter, this ratio should be unity for all settings.

The left HRS calorimeters were not total energy absorbers so a different method was required for calibration. The total energy deposited in the two calorimeter planes is defined by a thickness dependent integral over a gamma distribution

$$\rho E_1 + \mu E_2 = \int \left(E_0 \beta \left(\beta t\right)^{\alpha-1} \frac{e^{-\beta t}}{\Gamma(\alpha)} \right) \tag{6.6}$$

$$\frac{\alpha - 1}{\beta} = ln\left(\frac{E_0}{E_c}\right) - 1 \tag{6.7}$$

where $E_{1,2}$ is the energy deposited in each calorimeter plane, ρ,μ, and β are calibration parameters, E_0 is the particle energy and t is the radiation thickness that the particle sees in the calorimeter. The calibration of the left HRS could also be checked by taking the ratio E/p. Unlike the right HRS, the ratio is dependent on the momentum setting, but always less than one. This is because the energy absorbed by the calorimeter was always less than the total energy of the particle.

With both the left and the right HRS calorimeters calibrated, a cut region could be defined for good event selection. Since the calorimeters were designed so that electrons would deposit all of their energy into them, event selection was chosen so that the E/p ratio was above a certain value. The exact value of the ratio was defined so that the electron detection efficiency did not fall below 99%, as defined in the next section. The ratio was momentum dependent so a separate cut was used

for each setting. The location of these cuts for the right HRS calorimeter is shown in Figure 6-2. Some low energy events would fully absorb in the first calorimeter plane and so would not create

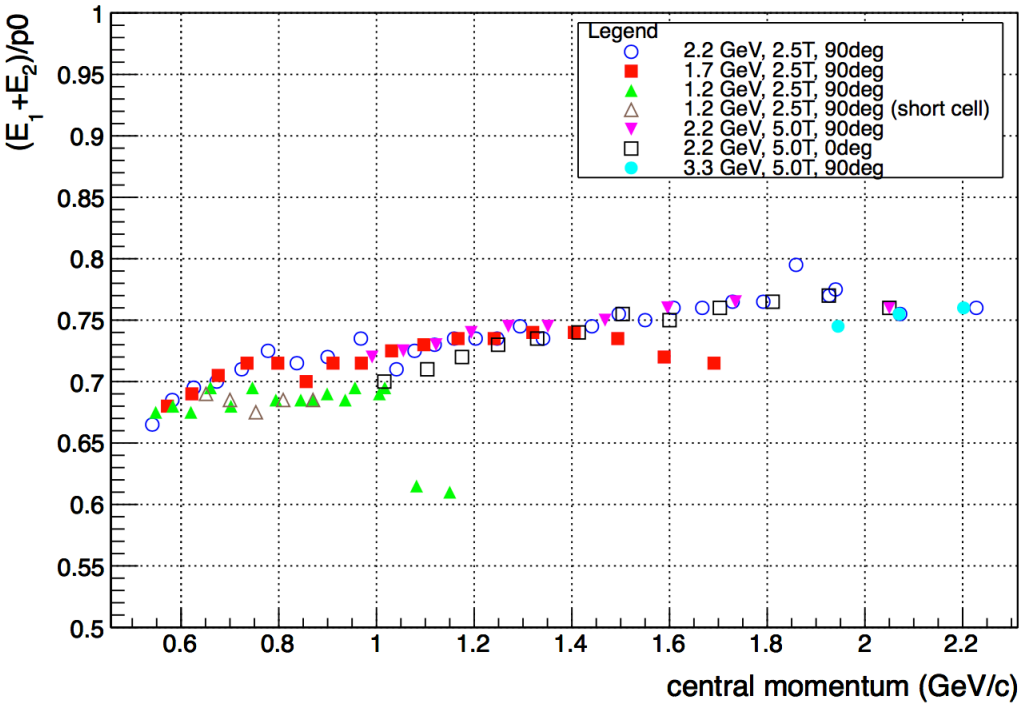

Figure 6-2: The E/p ratio selection value for all momentum settings on the right HRS. Events whose E/p value lie above the cut ratio are considered good events. Reproduced from [7].

any signal in the second. For this reason a second cut was created which simply used the E/p ratio from the first plane. If a sufficient amount of energy was deposited on the first plane it was considered a good event, regardless of the signal from the second plane.

6.3.3 Detector Efficiencies

With the gas Čerenkov and lead glass calorimeters calibrated, and good event selection cuts defined, the detector efficiencies could be studied. The detector efficiency is defined as the ratio of events detected to the total number of good events after the event selection cuts are made. Some events that should be considered 'good' events failed to fire in one of the detectors so this ratio was less

than, but ideally very close to, one.

To determine a detectors efficiency a total number of 'good' events first had to be calculated. The total number of events was defined as events that produced a signal in both the gas Čerenkov and the calorimeter detectors after satisfying the event selection cuts. Then by taking the ratio of events seen in only the gas Čerenkov *or* the calorimeter to the total number of events seen in both detectors, the number of undetected events is formed.

$$\text{efficiency} = \frac{(\#\text{ of events seen in calorimeter) OR (\# of events seen in Čerenkov)}}{(\#\text{ of events seen in calorimeter) AND (\# of events seen in Čerenkov)}} \tag{6.8}$$

where 'OR' and 'AND' designate standard logic statements between the Čerenkov and calorimeter signals seen for a single event. The efficiency of both the Čerenkov and the calorimeters for all settings is shown in Figure 6-3.

With the event selection cuts defined it became useful to quantify the background contamination

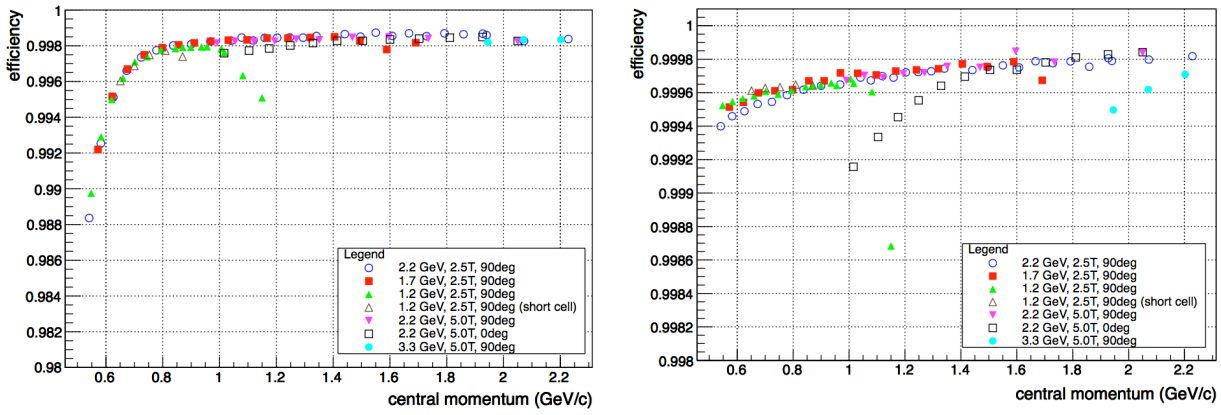

Figure 6-3: Final detector efficiencies for the lead glass calorimater (left) and gas Čerenkov (right) at all energy settings during g_2^p. Reproduced from [7].

in the data. By graphing the E/p distribution in the calorimeter both before and after the application of event selection cuts, the process of background removal became apparent. Since the total absorption calorimeter was designed to fully absorb electron energies, the peak located at unity in E/p is considered the electron signal, while any structure at a lower fraction is background from

other particles, such as pions. The background contamination to the data was then calculated as one minus the ratio of all events after event selection cuts to all events without any cuts applied. The background contamination was found to be $< 0.5\%$ for all settings.

6.3.4 Vertical Drift Chambers

The purpose of the vertical drift chambers (VDC) was to provide accurate particle position and tracking information. A more detailed description of the VDC analysis is found in Ref. [8]. A particle passing through the sensing wire plane of the VDC causes a cascade of secondary electrons as it ionizes the surrounding gas. The electron avalanche hits the sensing wire and creates a timing signal in the 'time to digital converter' (TDC). Using the TDC and avalanche drift velocity the distance the avalanche travelled to the sensing wire was calculated. Then by fitting a linear function to the drift distance for each wire, a 'particle cross-over' point was calculated, giving the exact location in the wire mesh plane where the detected particle passed through. With two wire mesh planes, two cross-over points could be calculated, giving a trajectory for each particle. The exact position of each wire in the mesh plane was known to within 100μm so an absolute calibration of the VDC was unnecessary.

Although an absolute calibration wasn't needed, an efficiency study for the VDC was still done to correct for 'multi-track' signal firing. In order to linearly fit the cross-over point of a particle the sensing wire signal needed to be recorded over a short, fixed time scale determined by the trigger supervisor. When the first sensing wire fired from an avalanche, the TDC would begin recording all subsequent sensing wire signals as a single particle trajectory, and it would stop recording after the trigger supervisor determined the event had passed. During high rate settings, multiple events would pass through the mesh at the same time, causing several sensing wires to fire. Since the trigger supervisor only separated events on a timing trigger, this caused multiple particles to be recorded as a single event. This was called the VDC multi-track signal, and these events needed

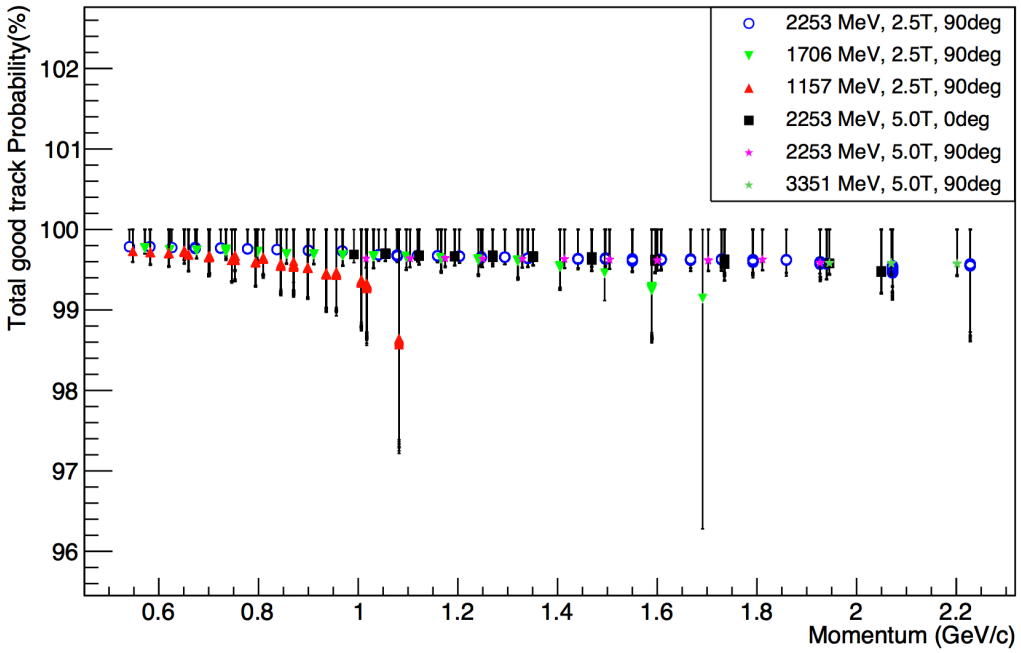

Figure 6-4: Final VDC detector efficiencies for all settings after deconstruction of multi-track events. Reproduced from [8].

to be examined more closely to determine if a single track event could be extracted. Unusable multi-track events contributed to a loss in the efficiency of the VDC.

A simple approach to looking at the VDC efficiency is simply calculating the number of single track events over the total number of detected events

$$\text{efficiency} = \frac{\mathrm{N_{single}}}{\mathrm{N_{total}}} \tag{6.9}$$

where $\mathrm{N_{total}}$ is the total number of detected events that satisfy the event selection cuts, and $\mathrm{N_{single}}$ are the total number of single track events detected in the VDC. For the high rate running of g_2^p this efficiency can drop as low as 70%. For this reason it became very important to examine the multi-track events more closely.

Multi-track events could be used in conjunction with energy deposited on the calorimeter to attempt to distinguish single events. Using a two-track event as an example, there are 3 possible scenarios.

First, the energy deposited onto the calorimeter from both tracks is much less than the momentum. This implies both events are background and both events should be removed using the event selection cuts defined in previous sections. Second, only one particle from the two-track event fully deposits its energy onto the total absorption calorimeter. In this case it was expected that one single track event was present, and could be counted as such, while the other event was removed due to not satisfying the event selection cut. The final case is when both tracks deposit all energy into the calorimeter. In this case the position of the deposited energy on the calorimeter blocks needed to be considered before it could be determined if a single-track event was salvageable.
After careful consideration of multi-track events, the VDC efficiency was increased to $> 98\%$ for all settings. The exact efficiency for each setting is shown in Figure 6-4.

6.3.5 Trigger Efficiencies

The final HRS detector to consider for calibrations and efficiencies is the scintillator plane. A more detailed discussion of the trigger efficiency analysis is found in Ref. [9]. The purpose of the scintillator, as described in Section 4.4.3, was to act as a trigger system for recording events where the trigger '$T_{1,3}$' served as the main trigger for the right(left) HRS, notifying the trigger supervisor to begin recording the event information. The efficiency trigger, defined as an event that did not satisfy the main trigger, but was seen in the gas Čerenkov, was used as a way of determining when the main trigger failed to identify an event. The trigger efficiency was then defined as the ratio of the total number of events satisfying the main trigger to the sum of the main trigger events and efficiency trigger events. The final trigger efficiencies were found to be $> 98\%$ at all settings, the exact value for each run is shown in Figure 6-5. It was important to consider the livetime of the trigger supervisor as a correction factor to be applied to the yields later on. The livetime factor was calculated as the ratio of the accepted triggers scaled by the run prescale factor over the total

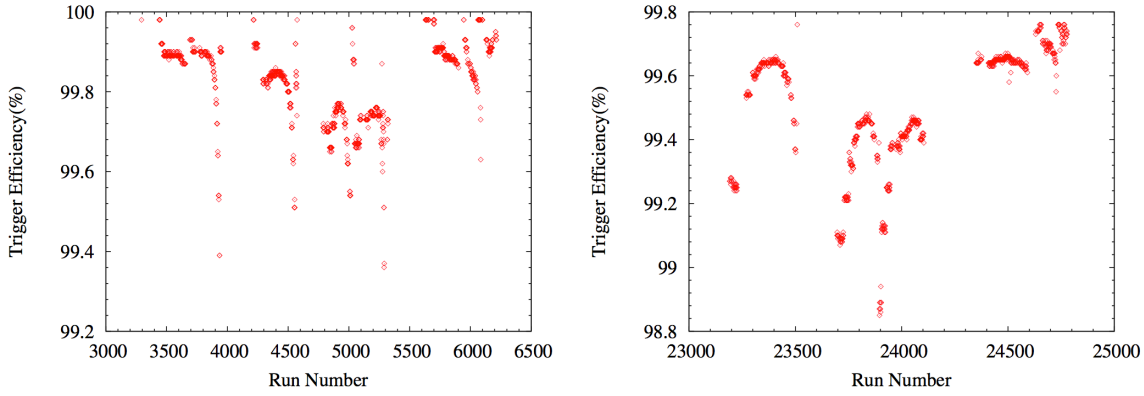

Figure 6-5: Final trigger efficiencies per run for the left arm (left) and right arm (right). Reproduced from [9].

triggers

$$\mathrm{LT} = \frac{\mathrm{psT}^{acc}}{\mathrm{T}^{tot}}. \tag{6.10}$$

The livetime depended largely on the event rate but was typically no less than 70%. The trigger supervisor livetime results are shown in Figure 6-6.

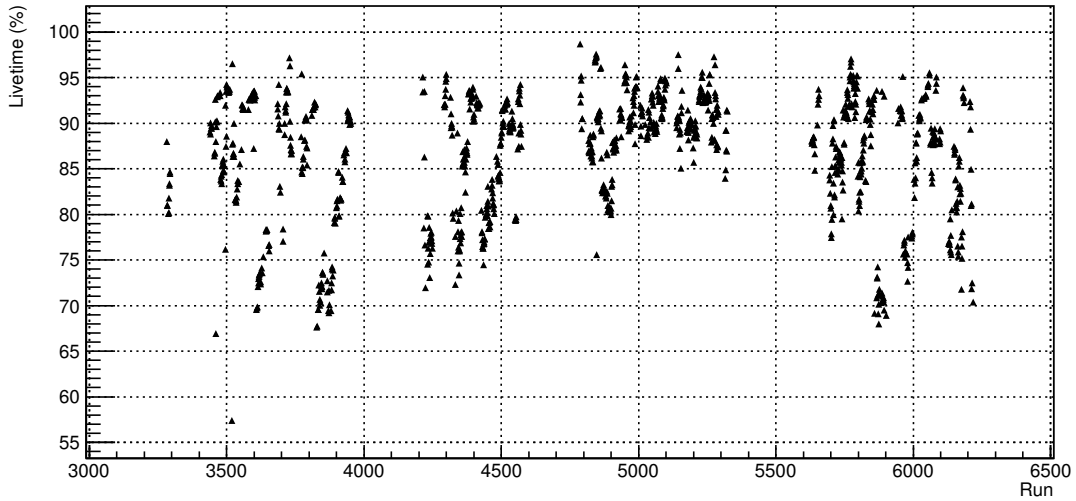

Figure 6-6: Trigger supervisor livetime for each left HRS run during the experiment.

6.4 Beamline Calibrations

The Hall A beam line contained several diagnostic tools for determining beam information before scattering. The two quantities needed for asymmetry and cross section analysis were the beam position at the target, for use in reconstructing the scattering angle, and the beam current at the target, for calculating the accumulated charge on the target.

6.4.1 Beam Current Monitor

A more detailed discussion of the beam current monitor analysis is discussed in Ref. [43]. The output of the BCM is a voltage signal which is converted to frequency in the DAQ. The signal is then connected to a scaler system which simply increments for each input, this scaler information is then stored in the data file. The result is a linear 'counting' function that is proportional to the number of charged particles that pass through the BCM. The first step to converting this to a total accumulated charge is performing a BCM calibration to determine the voltage response that the beam has on the monitor.

The BCM is calibrated by invasively moving a block of tungsten into the beam line. The tungsten is heated and the temperature, along with the BCM outputs, are recorded. The exact process is as follows:

- Beam Charging. The tungsten is in the beam pipe, all incoming electrons hit the tungsten, causing it to heat.
- Thermal Equilibration. The tungsten block is moved out of the beam pipe and given time to thermalize. During thermalization, the temperature is recorded.
- Cooling. The tungsten is placed in contact with a cooling plate and cooled down.

The total charge deposited onto the tungsten block could be calculated from the final temperature of the block.

$$Q_{beam} = K \cdot T_{tungsten} \tag{6.11}$$

where K is the heat capacity of the block, 85.55 kJ/K and $T_{tungsten}$ is the recorded temperature of the tungsten after it thermalized. The second piece of information needed for calibration is the scaler BCM counts recorded by the DAQ during the block heating process. The BCM data is a linear function so the charge recorded could be calculated as

$$Q_{BCM} = \text{slope} \times (\Delta_{\text{counts}} - \text{P} \times \Delta_{\text{clock}}) \tag{6.12}$$

where slope is obtained from a linear fit to the data, Δ_{counts} is the difference in value between the first and last scaler entry during beam heating, P is a pedestal offset value and Δ_{clock} is also a scaler value which incremented at set intervals based on a clock function. The output of the BCM charge and the charge calculated by the heating of the tungsten block could then be related to find a calibration constant. The BCM calibration uncertainty is a function of the heat capacity of tungsten, the accuracy of the temperature measurement on the block, the beam energy during beam heating, and heat loss during thermalization. The uncertainty in the BCM calibration constants was $< 1\%$ for the duration of the experiment.

The calculated calibration constants were then used in conjunction with the scaler output of the BCM monitors to find the beam charge and current in real time during experimental data taking. The integrated beam charge per run was also stored in a MySQL database and used during analysis to find the charge normalized yields.

6.4.2 Beam Position Reconstruction

A more detailed discussion of the beam position monitor (BPM) analysis is discussed in Ref. [10]. The g_2^p experiment required low beam current running to prevent rapid depolarization on the polarized target. The low current proved to be a huge challenge for the beam position analysis. The usual BPM monitor and acquisition system had to be replaced with a new system for sensitivity down to the 50nA current used during the experiment. The beam position monitors were located between the chicane magnet system and the scattering chamber on the beam line. Two monitors were used to propagate the beam location forward to the center of the target. The monitors each contained four antenna at 90° to each other around the beam line, as shown in Figure 6-7. The

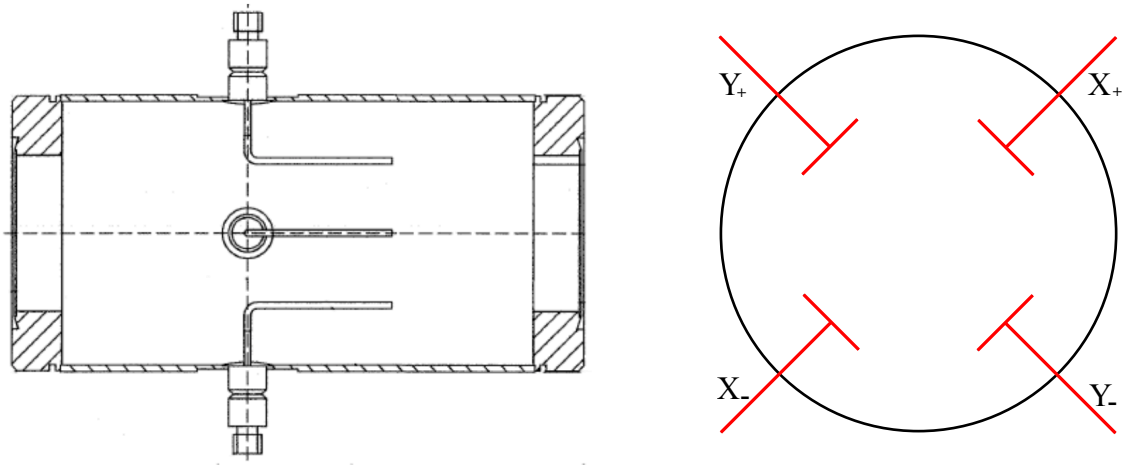

Figure 6-7: Diagram of the BPM monitor designed by the JLab engineering team. Left is a side view showing the antenna structure while right is looking along the beam line at the location of the four antenna.

output signal from each antenna was sent through an ADC in the DAQ system and stored in the data files. By taking the asymmetry between opposite antennas a relative beam location could be calculated, to within a proportionality factor.

To calibrate the BPMs, two sets of harps were used. The harp is a metal fork with three wires stretched across it. The fork was connected to a high precision stepper motor that moved it across the beam line during calibrations. When a wire crossed the beam path it produced a signal which

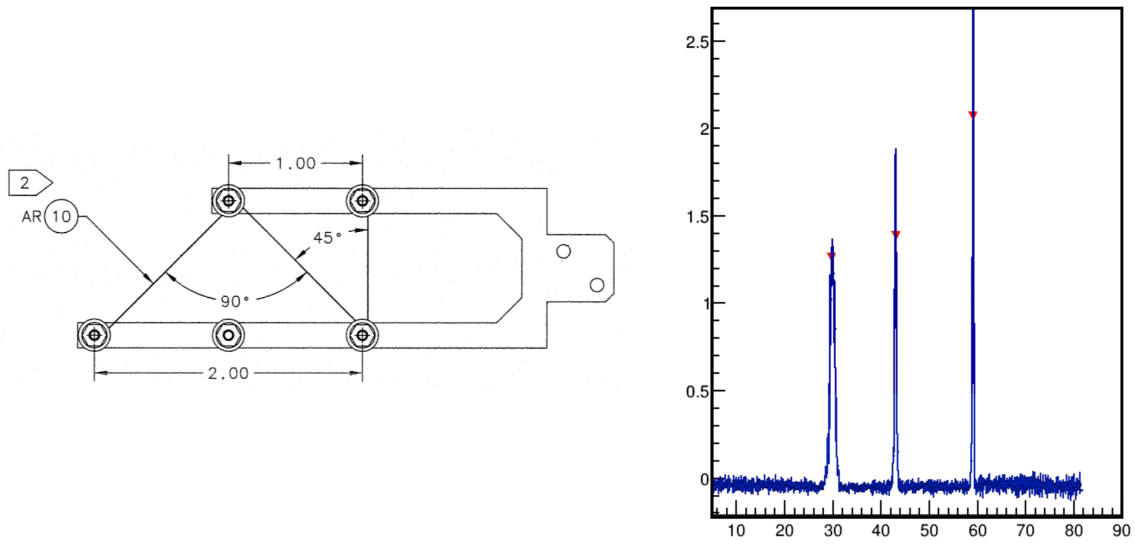

Figure 6-8: Diagram of the harp used to calibrate the BPM (left) and a sample output of a harp scan (right). Peaks in the output indicate points where the harp wires crossed the beam line. The horizontal axis of the harp scan is the stepper motor position (arbitrary units). Reproduced from [10].

was recorded for analysis. The physical position of the stepper motor could be used in conjunction with the signal peaks from the harp wires to find the real beam position and calibrate the BPM's for non-invasive, real time measurements.

Results from a typical harp scan calibration run are shown in Figure 6-8. Assigning the labels P_1, P_2 and P_3 to the first, second and third peak in the output scan data, respectively, the physical beam position can be calculated as

$$x_{beam} = x_{(\text{wire } 1)} - P_1 \tag{6.13}$$

$$y_{beam} = \frac{1}{2}\left[(x_{(\text{wire } 2)} - x_{(\text{wire } 3)}) - (P_2 - P_3)\right] \tag{6.14}$$

where $x_{(\text{wire } 1,2,3)}$ is the physical location of the wire on the harp, obtained from the JLab survey group. The wire positions are supplied with a 0.1mm uncertainty. With the physical position of the beam and antenna data from the BPM, the BPM can be calibrated to give the real position

non-invasively during the experiment. The real beam position in the BPM cavity is given by

$$x_{beam} = \frac{(A_+ - A_{+,\text{ped}} + b_+) - g_x(A_- - A_{-,\text{ped}} + b_-)}{(A_+ - A_{+,\text{ped}} + b_+) + g_x(A_- - A_{-,\text{ped}} + b_-)} \tag{6.15}$$

where $A_\pm$ is the ADC signal from the BPM antenna, $A_{\pm,\text{ped}}$ is a pedestal value offset associated with the antenna output, g_x is a signal gain factor between antenna opposite each other, and $b_\pm$ is a calibration constant offset determined by the harp scan. The same equation can be applied to both x_{beam} and y_{beam} by using the ADC signal from orthogonal pairs of antenna to determine the x and y positions of the beam in each BPM. To determine the real beam position in the lab frame, in which the z-direction is along the beam path, the y-direction is vertically up and the x-direction is orthogonally pointed left when facing the beam direction, one additional calculation had to be made

$$x_{real} = c_0 + c_1 x + c_2 y \tag{6.16}$$

$$y_{real} = c'_0 + c'_1 x + c'_2 y \tag{6.17}$$

where c_0, c_1, c_2 and c'_0, c'_1, c'_2 are constants.

With the real beam position in the hall coordinate system at the two BPM's, the next step was to propagate those positions to the target center. There were two distinct situations to consider when propagating the beam position to the target: longitudinal, or no target field, and transverse target field. For a longitudinal target field the beam transport through the scattering chamber was unbent, or 'straight-through'. In this case the propagation of the beam position to the target done using

$$x_{target} = x_{\text{bpm A}} + \frac{y_{target} - y_{\text{bpm A}}}{y_{\text{bpm B}} - y_{\text{bpm A}}}(x_{\text{bpm B}} - x_{\text{bpm A}}) \tag{6.18}$$

where x_{target} is the x position of the beam at the target, $x(y)_{\text{bpm A,B}}$ is the $x(y)$ position of the beam at the first (A) or second (B) BPM as given in Equation 6.16 and 6.17, and y_{target} is the y

position of the beam at the target.

With a transverse target field present the beam propagation to the target became more complicated. This was because of the presence of the chicane. The transverse target field acted to bend the beam out of plane as it passed through the scattering chamber. To compensate for this, two dipole magnets were added to the beam line, upstream of the BPM and scattering chamber, to first bend the beam out of plane and then back so it entered the scattering chamber at an angle. The target field would then bend the beam back into plane so it exited horizontally again. A more detailed description of the chicane system is discussed in Section 4.2.5. The propagation of the angled beam through a transverse target field was difficult to calculate, instead a simulation was used to find the exact position. In total ten thousand events were thrown at a known target field map with varying initial positions and angles. A polynomial function was fit to each track and the deviation between them was found to be $< 0.1\%$. In total, 24 polynomial fits for the six beam energy settings with a perpendicular target field were done. These 'transport functions' were then used to find the average beam position at the target for each run.

6.4.3 Raster Calibration

The raster calibration study is discussed in more detail in Ref. [10]. Two rasters were used during the experiment to spread the beam profile out over a 2cm circular area when hitting the target. This acted to reduce the heat load on the target and create uniform depolarization. The exact raster size was used in conjunction with the BPM information to determine an event by event beam position at the target. This was done by adding the calculated beam position at the target (Section 6.4.2) with the relative position of the beam within the raster pattern, as a function of time. The beam position within the raster pattern was given by a sinusoidal function which controlled the dipole raster magnet current

$$x_{raster} = \sqrt{(t + \phi_x)} \sin(\omega_x t + \phi_x) \tag{6.19}$$

$$y_{raster} = \sqrt{(t+\phi_y)}\sin(\omega_y t + \phi_y) \tag{6.20}$$

where $\phi_{x,y}$ is a phase locked between x and y by a function generator. The exact size of the raster pattern at the target was calculated using a 'carbon hole' target. The carbon hole was a small hole located on the target ladder with a known size. When the ladder was moved so that the hole was in the beam line, it would light up the hole in the raster pattern as more events scatter off of the aluminum ladder and into the detector housing, as shown in Figure 6-9. By using the known size

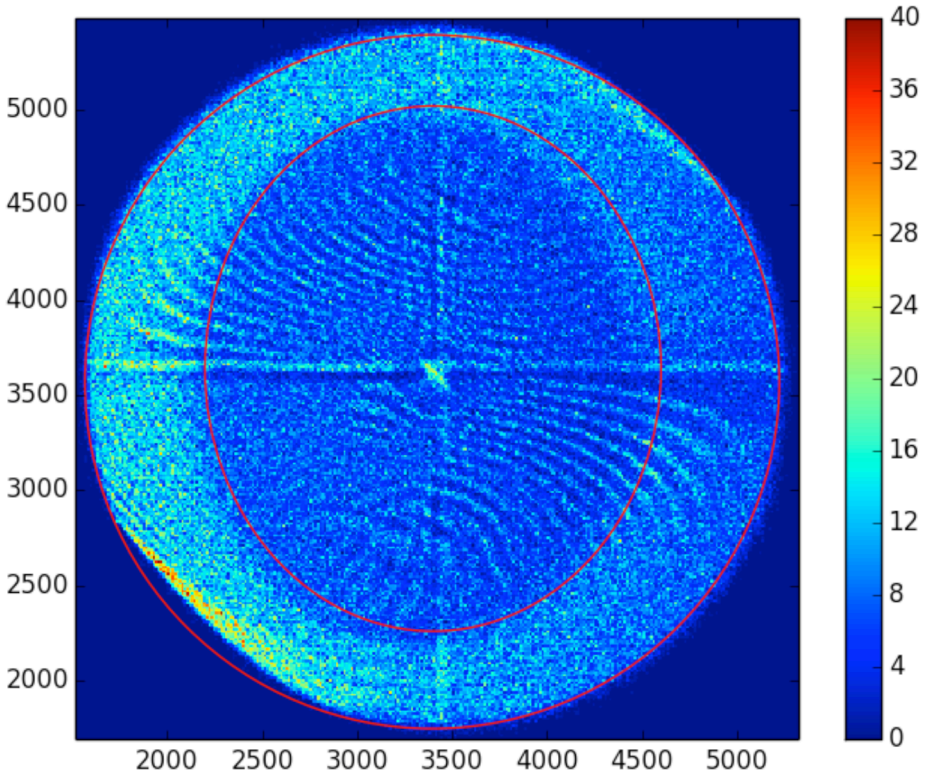

Figure 6-9: The raster pattern as seen from the detector housing when the carbon hole is in the beam line. Graphical cuts on the raster pattern were used with the known hole size to calibrate the total raster size. Units are arbitrary. Reproduced from [10].

of the hole and drawing graphical cuts on the raster shape to outline the carbon hole and the total raster size, a scale factor could be used to determine the circular raster size. The size of the carbon hole was measured to be 10mm with a 0.2mm uncertainty. The total size of the raster was then used in conjunction with Equations 6.19 and 6.20 to find the relative beam position of the rastered

beam at the target. This was then added to the central beam position from the BPM calculation to find the event by event position at the target.

6.5 Optics

A more detailed discussion of the optics and central scattering angle analysis can be found in Ref. [11, 57]. When an event is detected in the HRS detector stack, four spatial coordinates for the event are recorded by the VDC. One VDC plane is capable of measuring the events x and y position while the events θ and ϕ coordinates, which define its trajectory, are measured using a coincidence gate between two VDC planes. These four coordinates define the events spatial vector at the VDC plane, called the 'focal plane' for the analysis, $(x_{fp}, y_{fp}, \theta_{fp}, \phi_{fp})$. The purpose of the optics analysis was to reconstruct these coordinates back through the HRS quadrupole and dipole magnets and find a spatial vector for each event at the target, $(x_{tg}, y_{tg}, \theta_{tg}, \phi_{tg})$. This vector could then be used in conjunction with the incident event vector, calculated in the BPM analysis, to find the scattering angle. Along with the four spatial coordinates, the events relative momentum, δ, was needed to accurately reconstruct the target plane coordinates. The events relative momentum was defined as

$$\delta = \frac{P - P_0}{P_0} \tag{6.21}$$

where P was the measured momentum of the particle and P_0 was the central momentum setting of the HRS.

Four different coordinate systems were used to reconstruct the spatial vector from the focal plane to the target. The first to consider was the detector coordinate system (DCS). The DCS was the coordinate system in which the focal plane spatial vector was measured in. It was defined with the z direction perpendicular to the VDC plane pointed up with the x and y directions parallel to the VDC wire plane. The next two coordinate systems, named the 'transport coordinate system'

(TRCS) and the 'focal plane coordinate system' (FCS) were defined by rotations of the DCS to make reconstruction to the final coordinate system more manageable. The final coordinate system was the 'target coordinate system' (TCS). The z axis of the TCS was defined by the central ray connecting the target center to the center of the HRS. The x direction was then perpendicular to z and pointed vertically down. Details of the TCS are shown in Figure 6-10.

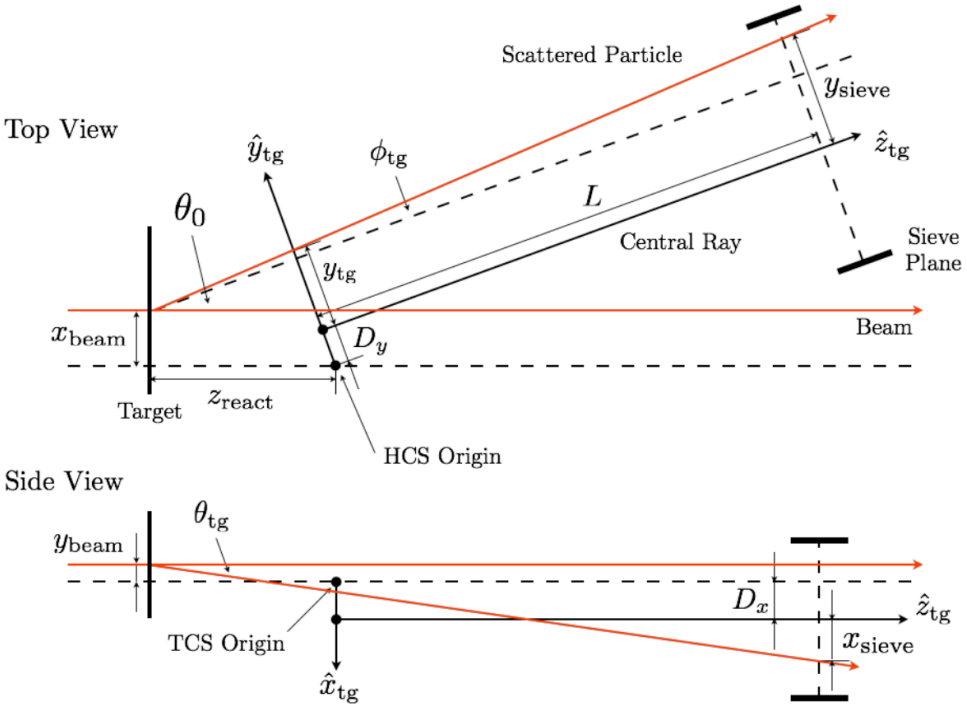

Figure 6-10: The target coordinate system (top and side view). Reproduced from [11].

6.5.1 Central Scattering Angle

Of note in Figure 6-10 is the use of θ_0, that is, the angle of a central ray passing through the HRS. The target angles, θ_{tg} and ϕ_{tg} are expressed as values relative to this central angle so its value is

needed to find the absolute scattering angle, which can be expressed as

$$\theta = \arccos \frac{\cos(\theta_0) - \phi_{tg} \sin(\theta_0)}{\sqrt{1 + \theta_{tg}^2 + \phi_{tg}^2}} \tag{6.22}$$

A sieve slit placed over the HRS entrance window was used to determine the value of the central HRS angle. A sieve slit is effectively an aluminum plate with several holes punched into it in a uniform, grid-like, pattern. In addition to being used for the angle measurement, the sieve slit was crucial in general optics calibrations, as will be discussed in the following sections. A survey measurement of the target center and sieve slit by the JLab survey group resulted in a survey angle with an uncertainty of 0.7mr. The results of the survey measurement are shown in Table 6.1.

Arm	Survey value (rad)	Uncertainty (rad)
LHRS	0.1007	0.0007
RHRS	0.1009	0.0007

Table 6.1: Survey results of the central scattering angle.

6.5.2 Transport Matrix

With a central angle and the coordinate systems defined, the spatial vector at the focal plane could be translated into the TCS. To do this an 'optics transport matrix' was found to reconstruct the focal plane vector back to the target plane. The optics matrix was used as a general function to reconstruct any event to the target plane, it could be expressed in first order approximation as:

$$\begin{pmatrix} \delta \\ \theta \\ y \\ \phi \end{pmatrix}_{\text{tg}} = \begin{pmatrix} \langle\delta|x\rangle & \langle\delta|\theta\rangle & 0 & 0 \\ \langle\theta|x\rangle & \langle\theta|\theta\rangle & 0 & 0 \\ 0 & 0 & \langle y|y\rangle & \langle y|\phi\rangle \\ 0 & 0 & \langle\phi|y\rangle & \langle\phi|\phi\rangle \end{pmatrix} \begin{pmatrix} x \\ \theta \\ y \\ \phi \end{pmatrix}_{\text{fp}} \tag{6.23}$$

For the real analysis the optics matrix was calculated out to third order. The goal of the optics analysis was to optimize the above matrix for two distinct settings, with and without a target field. The first case, no target field, is the simplest case to consider because there will be no out of plane bending due to a transverse magnetic field. To find the optics matrix a calibration run was done in which a sieve slit was placed over the acceptance window of the HRS. A diagram of the sieve slit is shown in Figure 6-11. During optics calibration runs an unrastered beam was incident on a

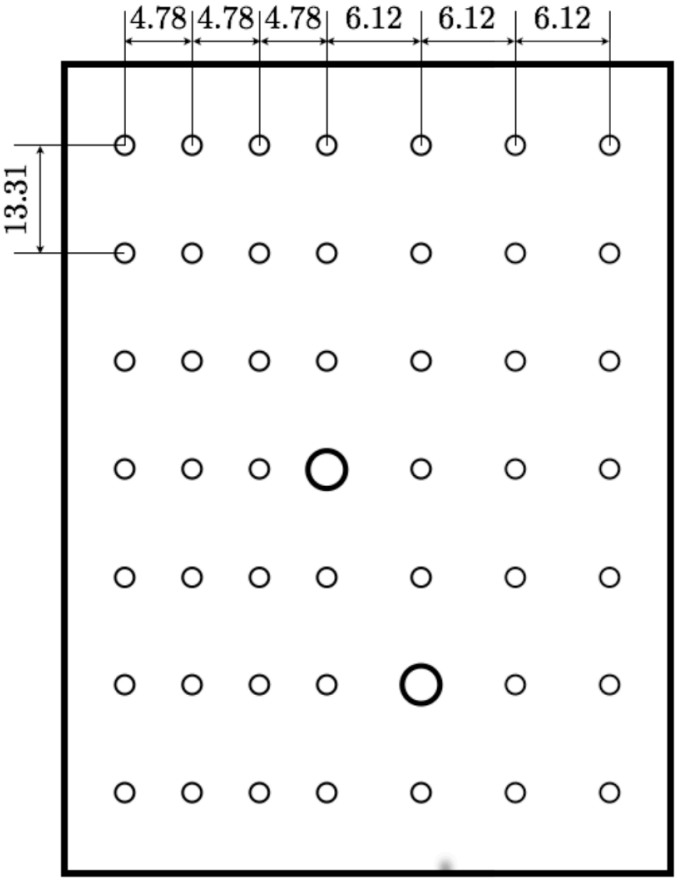

Figure 6-11: Diagram of the sieve slit used during g_2^p. Two larger holes were used to determine the orientation of the plate. Reproduced from [11].

carbon foil target. By using the sieve pattern, as seen in the HRS, the target coordinates of each event could be calculated as

$$\theta_{tg} = \frac{x_{sieve} + D_x + y_{beam}}{L - z_{react}\cos(\theta_0) - x_{beam}\sin(\theta_0)} \tag{6.24}$$

$$\phi_{tg} = \frac{y_{sieve} + D_y + x_{beam}\cos(\theta_0) + z_{react}\sin(\theta_0)}{L - z_{react}\cos(\theta_0) - x_{beam}\sin(\theta_0)} \tag{6.25}$$

$$x_{tg} = x_{sieve} - L\theta_{tg} \tag{6.26}$$

$$y_{tg} = y_{sieve} - L\phi_{tg} \tag{6.27}$$

where $x(y)_{sieve}$ was the measured $x(y)$ position of each hole in the sieve pattern, as seen from the HRS, $x(y)_{beam}$ was the incident beam position, calculated from the BPM analysis, L was the distance from the sieve slit to the center of the target and $D_{x,y}$ were horizontal and vertical offsets of the central ray, provided by survey. Finally, the relative momentum, δ, was calculated using the well known elastic scattering equation

$$P = \frac{E}{1 + \frac{E}{M}\cos(\theta)} \tag{6.28}$$

where E is the beam energy, M is the target mass and θ is the scattering angle, calculated from Equation 6.22. The relative momentum could then be calculated using Equation 6.21. With the relative particle momentum and the values of $(x_{tg}, y_{tg}, \theta_{tg}, \phi_{tg})$ the optics transport matrix with no target field could be calculated and used to reconstruct particle positions at the target during production.

When a transverse target field was present Equations 6.24-6.27 were no longer viable for calculating event positions at the target due to the fact that a linear propagation of positions was no longer valid. The scattered events at the target continued to follow a curved trajectory as they exited the scattering chamber, so more care was required when propagating back to the target center. The process involved breaking the reconstruction down into two parts. The first part was a propagation of the event coordinates from the focal plane to the sieve slit. Since the sieve slit was located outside of the target field, this propagation was identical to the case of no target field. To propagate back from the sieve slit to the target center, a simulation was used. The simulation package utilized

the electron equations of motion in a magnetic field, along with a magnetic field map that was measured prior to data taking with a precision of $< 1.2\%$. With target coordinates provided by simulation, the optics transport matrix for a transverse target field could be calculated.

6.6 Asymmetry Corrections

Circumstances could arise during data taking in which the asymmetry of the livetime and charge accumulated during runs was non-zero, that is, more events were recorded in one helicity 'spin-state' than the other. Since the physics asymmetry is normalized by these quantities, if the normalization factors are helicity dependent it will bias the result. This required an additional correction so that the asymmetry was calculated according to Equation 6.3.

6.6.1 Charge Asymmetry

The charge asymmetry was controlled by the accelerator. Any imperfections in the beam helicity production could produce more electron events in one helicity state, creating an accumulated asymmetry. An accelerator controlled correction method was to insert a half-wave plate into the beam line. The half-wave plate flipped the helicity state of the beam so each $(-)$ state became $(+)$ and vice versa, removing systematic 'artificial' polarization effects. It was still beneficial to look at, and correct for, any possible charge asymmetry defined as

$$A_Q = \frac{Q_+ - Q_-}{Q_+ + Q_-} \tag{6.29}$$

where $Q_\pm$ was the accumulated charge on the target in each $\pm$ helicity state. The BCM measured and recorded charges in each helicity state by matching the BCM signal to the output of the helicity decoder. This 'helicity gated' charge quantity was stored in a MySQL database to be used as a correction to the asymmetry for each run. The total charge asymmetry for all runs is shown in

Figure 6-12.

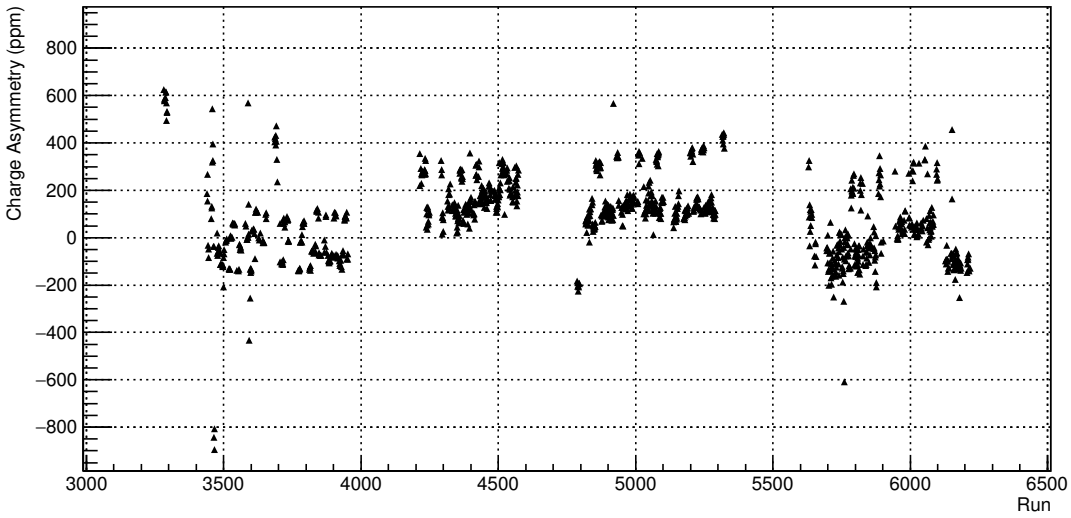

Figure 6-12: The total charge asymmetry per run for all left HRS production runs during g_2^p. The measured asymmetry was typically small (< 500ppm) but still applied to the physics asymmetry to remove the systematic entirely.

6.6.2 Livetime Asymmetry

The second asymmetry correction was due to the livetime measurement. It would be expected that the livetime asymmetry is zero because the trigger supervisor 'hang time' is independent of electron helicity state. In fact, the trigger is completely blind to the spin state of the detected electron. Situations could arise, though, in which the helicity asymmetry of incoming electrons is non-zero, and the livetime is fluctuating for unrelated reasons, such as a high event rate or an incorrect prescale factor. This coincident circumstance would lead to a non-zero livetime asymmetry, and needed to be corrected for. Similar to the charge asymmetry, the livetime asymmetry was calculated as

$$A_{LT} = \frac{LT_+ - LT_-}{LT_+ + LT_-} \tag{6.30}$$

where $LT_\pm$ is the measured livetime in the $\pm$ helicity state. The measured livetime asymmetry is shown in Figure 6-13. The helicity gated livetime was inserted into a MySQL database and applied

to the final raw asymmetry as a systematic correction.

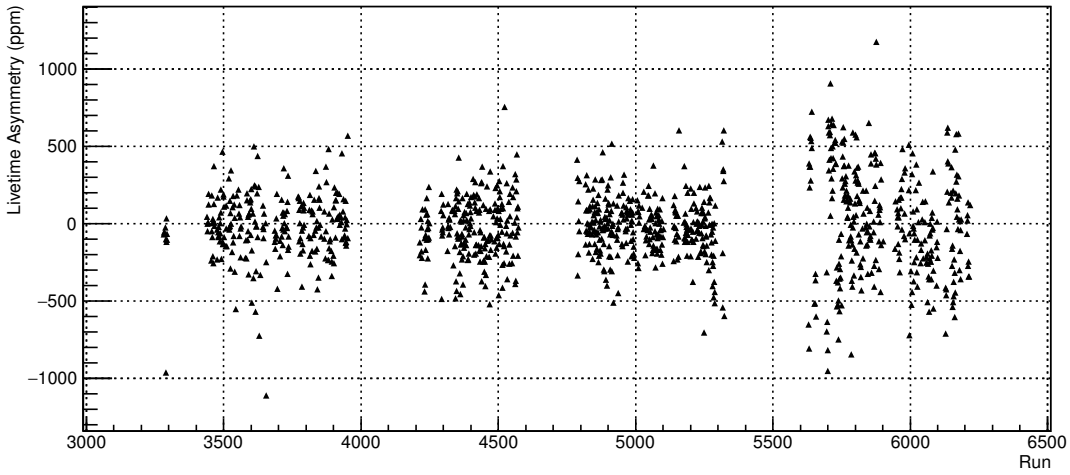

Figure 6-13: The total livetime asymmetry per run for all left HRS production runs during g_2^p. A typical asymmetry of (< 500ppm) was recorded.

6.7 Data Quality Checks

The unpolarized scattering cross section for a material is a function of kinematics, beam luminosity, detector acceptance and a number of normalization parameters as discussed in the previous sections. For the g_2^p experiment, it was very important to reduce the statistical uncertainty on the cross section to generate accurate asymmetries. To accomplish this, it was common to sit at a single kinematic setting and take a large number of runs to collect enough data for the statistical requirements. In the data analysis stage of the experiment, these runs would be normalized by their individual detector livetimes, accumulated beam charges and detector efficiencies. The resulting distribution is called the 'charge normalized yield distribution'. This normalized yield was convenient to look at because it is proportional to the cross section by a fixed scale factor (which is a function of the detector acceptance), so the asymmetry could be calculated simply by taking the asymmetry of the normalized yield, since the scale factors cancel. It is not only expected, but required that the integration of the charge normalized yield distributions for several runs at one

kinematic setting result in the same value to within statistical errors.

For the g_2^p experiment, it was found that some runs at the same kinematic settings did not have matching normalized yields. An extensive effort was given to attempt to resolve these yield discrepancies. It is important to discuss what was attempted and the current status of the data quality before continuing with analysis and physics results.

A typical yield discrepancy is shown in Figure 6-14. When attempting to resolve this issue several

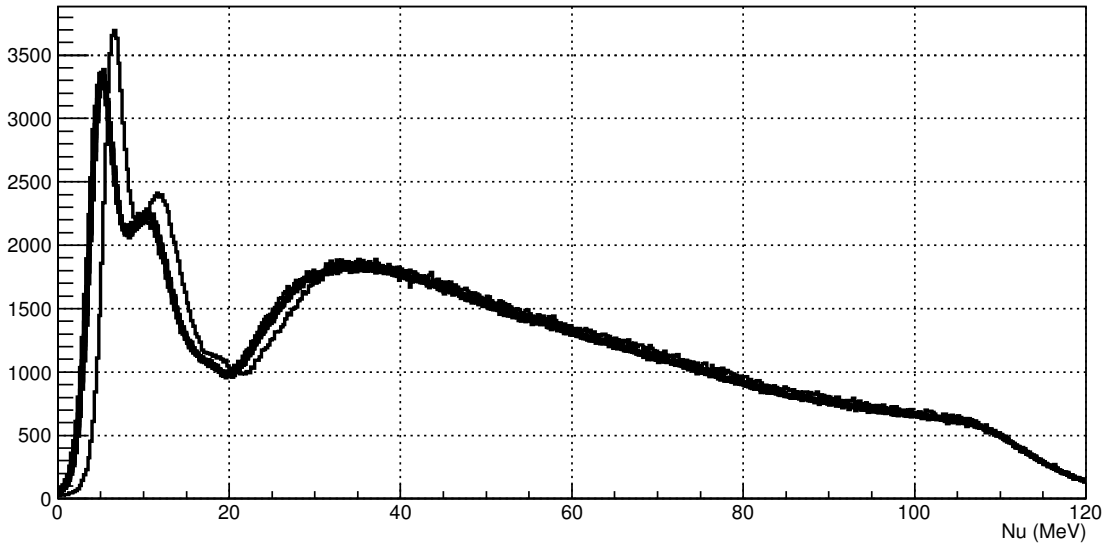

Figure 6-14: Charge normalized elastic yields for the 2.254GeV setting with a 5T transverse target field. It is expected that the yields should agree to within statistical uncertainties. A large normalization discrepancy between runs can be seen at both the nitrogen and helium elastic peaks (first peak and second peak in Nu, respectively).

things were considered. The beam raster pattern was looked at in detail to determine if there was any 'beam scraping' in which the beam hit the pipeline before entering the scattering chamber. Several cuts were placed on the raster pattern and the resulting yields were plotted in an attempt to create a correctly normalized distribution. A more strict beam current cut was also used to remove low current runs. This was done because if the current dropped too low the BCM and BPM were no longer reliable so it was possible the normalizations being applied to those runs were not correct. These corrections resolved issues for several settings but the majority of yield discrepancies remain.

At the time of this writing the main concern is in the beam position at the target. Since g_2^p ran at very small forward angles a small shift in beam position could drastically change the resulting scattering angle seen in the detectors. A different scattering angle results in different kinematics being looked at, which would give different yields. A more detailed BPM analysis is being done in an attempt to correct runs at different target beam positions.

The total number of 'usable' runs without any beam positions corrections applied is shown in Table 6.2. A run was considered usable if it fit to a continuous yield spectrum when plotted against all runs in adjacent momentum settings. The 3.350GeV setting is not included in this study because

Setting	Total Runs	Usable Runs	% Usable Statistics
1.154GeV 2.5T	340	306	90%
1.710GeV 2.5T	213	193	91%
2.254GeV 2.5T	264	232	88%
2.254GeV 5T Longitudinal	179	169	94%
2.254GeV 5T Transverse	90	86	96%

Table 6.2: Number of currently usable statistics at each energy setting for g_2^p. A run was considered usable if it fit a continuous spectrum with adjacent momentum settings.

it was found that a continuous yield drift was present in several momentum settings. Since the method for determining usable runs wasn't applicable for continuous drifts, all runs were used in the analysis and a larger systematic uncertainty was placed on the affected momentum settings. For the remaining energy settings, only runs that form a continuous yield distribution were considered while a method for correcting the remaining runs is still underway.

6.8 Packing Fraction

With a well defined set of normalized yields and cuts, physical information about the NH_3 target sample could be extracted. The first required piece of information was the 'packing fraction'. The NH_3 target material consisted of irradiated ammonia beads, roughly 2mm in diameter, packed into a cylindrical target cell volume and submersed in liquid helium. The packing fraction is the ratio

of target material to that of the liquid helium it is submersed in and is required for ammonia target length calculations later on. The packing fraction is a physical characteristic that depends on the ammonia bead shape and load size. For this reason, every time the material was switched out, a new packing fraction had to be found. During the g_2^p experiment, 10 different target materials were used, resulting in a different packing fraction value for each.

Two different methods were used to find the packing fraction for this analysis. The first to be discussed is called the 'elastic fit' method, which involves isolating the elastic peak for several different target types by fitting several predefined functions to data. The second method, which is named the 'ratio' method, involved taking yield ratios at certain kinematic ranges. The process and results of each method will be discussed in the following sections. The ratio method is the method of choice for this analysis for two reasons, the nature of fitting a functional form with a large number of parameters to the data resulted in large systematics in the resulting packing fractions, and the fit method also required elastic data for integration which was not available for the 3.350GeV setting.

6.8.1 Elastic Fit Method

The elastic fit method required elastic data on two different targets, the 'production' run and the 'dummy' run, where the production run contains the standard ammonia sample being measured, while the dummy run is a cell containing only liquid helium and foil end caps. The charge normalized counts for each material is given in terms of the material cross section by

$$N = \left(\frac{AN_0}{e}\right)\left(\frac{\rho L}{M}\right)\sigma \tag{6.31}$$

where A, N_0 and e are constants, ρ is the material density, L is the length of material in the target, M is the material molar mass and σ is the material cross section. Equation 6.31 can be used to

express the production and dummy runs in terms of individual material cross sections

$$N_{dummy} = \left(\frac{AN_0}{e}\right)\left[\frac{\rho_{He}L_{total}}{M_{He}}\sigma_{He} + \frac{\rho_{Al}L_{Al}}{M_{Al}}\sigma_{Al}\right] \tag{6.32}$$

$$N_{production} = \left(\frac{AN_0}{e}\right)\left[\frac{\rho_{NH_3}L_{tg}(pf)}{M_{NH_3}}(\sigma_N + 3\sigma_H) + \frac{\rho_{He}(L_{tg}(1-pf) + L_o ut)}{M_{He}}\sigma_{He} + \frac{\rho_{Al}L_{Al}}{M_{Al}}\sigma_{Al}\right] \tag{6.33}$$

where L_{tg} is the length of the g_2^p target cell, L_{out} is the length of helium in the nose outside of the target cell, L_{Al} is the thickness of the aluminum windows and pf is the packing fraction. By combining Equations 6.32 and 6.33 and isolating pf the packing fraction can be expressed in terms of measurable yields and simulated elastic ratios as

$$pf = \left(\frac{L_{total}}{L_{tg}}\right)\left(\frac{N_{production}}{N_{dummy}} - 1\right)\left[\left(\frac{\rho_N M_{He}}{\rho_{He} M_N}\right)\frac{\sigma_N}{\sigma_{He}} + \left(\frac{\rho_H M_{He}}{\rho_{He} M_H}\right)\frac{\sigma_H}{\sigma_{He}} - 1\right]^{-1} \tag{6.34}$$

In the above equation everything is known or measurable except the cross section ratios σ_N/σ_{He} and σ_H/σ_{He}. By using an elastic simulation code developed for g2p, these integrated cross section ratios were determined for each setting. The final step was then to isolate the elastic peaks for the production and dummy runs and integrate to obtain $N_{production}/N_{dummy}$ at each setting.

To isolate the elastic peaks in data an involved hand written fitting routine was used. The steps of the routine went as follows:

- Fit a Gaussian to the approximate location of the Nitrogen elastic and Helium elastic peaks and store the Gaussian mean values, strengths and standard deviations.
- Fit a Gaussian-Landau convolution fit to the Helium elastic peak using the stored Gaussian fit parameters as starting parameters.
- Fit a Gaussian to the approximate location of the quasi-elastic distribution and store the

relative strength.

- Fit a convolution of three Gaussian peaks to the quasi-elastic using scaled values of the Gaussian strength parameter as starting parameters for each fit. It is important to note that only the rising edge of the quasi-elastic region was fit so no radiative effects needed to be considered.

- Using parameters from all of the previous individual fits as starting parameters, fit a final custom function (Gaussian plus Gaussian-Landau convolution plus 3-Gaussians) fit to the entire spectrum.

The resulting fit has the ability to be separated into individual channels (elastic and quasi-elastic) as shown in Figure 6-15. The elastic fit could then be integrated to find $N_{production}$. A similar fit

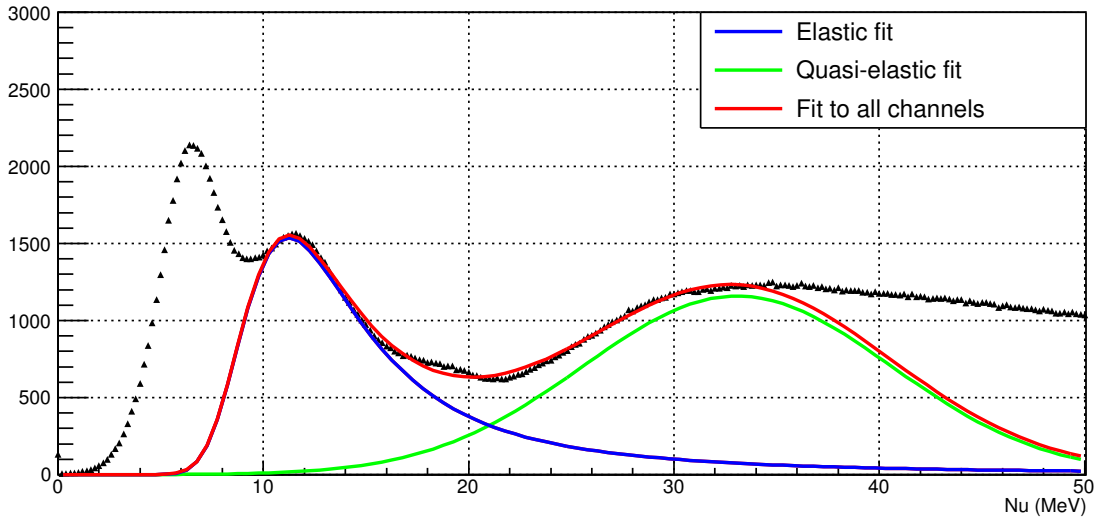

Figure 6-15: Result of complex fitting routine to elastic production data. The integration is done on data so only the falling edge of the elastic channel is fit.

procedure was done to the dummy run to find N_{dummy}. The final fit function was large, consisting of 16 free parameters for the production run and 7 free parameters for the dummy run. This, combined with the fact that the fit ranges were small due to the resolution of the HRS, meant that the final integrated values were extremely sensitive to initial parameters and chosen fit ranges

at each step. As an attempt to reduce this sensitivity, all production runs at each setting were weighted together to reduce the statistical uncertainty of the normalized yields. This forced the fitting routine, which used a basic χ^2 reduction method, to trend with the data more closely at each channel.

6.8.2 Fit Method Uncertainties

The statistical uncertainty in the fit method came from the yield ratio, $N_{production}/N_{dummy}$, as shown in Equation 6.34. Each yield was assigned a statistical uncertainty of $\sqrt{N}$ and propagated through in the standard way. The final statistical uncertainties were dominated by dummy run events but ended up being negligible compared to the systematics of this method. Final statistical uncertainties are shown in Table 6.3.

Looking back at Equation 6.34, several sources of systematic uncertainty must be considered for this method. The uncertainty in the target length, L_{tg}, was provided by survey to be 0.3%. While a detailed study of the unpolarized cross sections [12] found the uncertainty in the ratios, σ_N/σ_{He} and σ_H/σ_{He}, to be $\sim 10\%$. The systematic uncertainty in the fitting routine used to isolate the measured elastic yields was calculated by varying the fit ranges and starting parameters based on the spread of the individual yields going in to the weighted average. At lower Q^2 settings the various fit channels became less resolvable so the ability to fit each channel became more and more difficult, increasing the systematic uncertainty in the total fit. An example of the sensitivity of the fit method to these fit ranges is shown in Figure 6-16. The final packing fraction values for each material, as well as the statistical and systematic uncertainties, are quoted in Table 6.3.

This method could not be used for the 1.154GeV setting or the 3.350GeV setting. At 1.154GeV the elastic and quasi-elastic peaks were not resolvable so no estimate could be made for the amount

[1]The elastic N and He peaks are unresolvable at this setting, resulting in a poor fitting routine and final packing fraction estimate. The uncertainty reflects the problem at this setting.

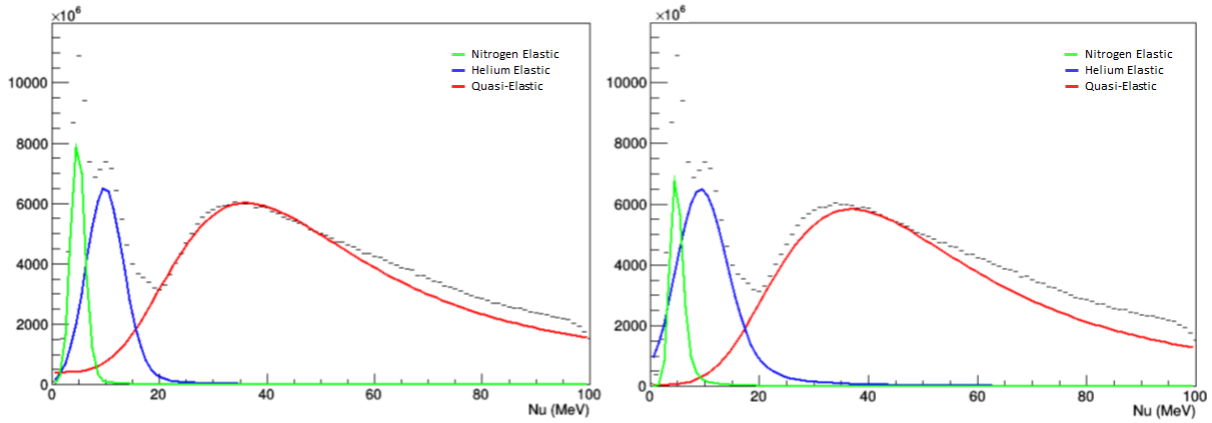

Figure 6-16: Fitting result for a quasi-elastic fit range of 25-50 MeV (left) and 30-50 MeV (right). The effect of altering the fit range by 5 MeV can be seen where the quasi-elastic fit is extrapolated to low ν. The final packing fraction in these two test instances varied by $\sim 20\%$.

Material #	Setting	Packing Fraction	PF Uncertainty (%)
7	1.7GeV 2.5T	$0.564 \pm 0.007_{\text{stat}} \pm 0.085_{\text{sys}}$	16.25%
8	1.7GeV 2.5T	$0.524 \pm 0.007_{\text{stat}} \pm 0.072_{\text{sys}}$	15.15%
7	2.2GeV 2.5T	$0.719 \pm 0.011_{\text{stat}} \pm 0.049_{\text{sys}}$	8.35%
8	2.2GeV 2.5T	$0.377 \pm 0.004_{\text{stat}} \pm 0.041_{\text{sys}}$ [1]	11.95%
17	2.2GeV 5T Longitudinal	$0.713 \pm 0.009_{\text{stat}} \pm 0.056_{\text{sys}}$	9.05%
18	2.2GeV 5T Longitudinal	$0.625 \pm 0.009_{\text{stat}} \pm 0.046_{\text{sys}}$	8.75%
19	2.2GeV 5T Transverse	$0.623 \pm 0.008_{\text{stat}} \pm 0.040_{\text{sys}}$	7.65%
20	2.2GeV 5T Transverse	$0.630 \pm 0.007_{\text{stat}} \pm 0.041_{\text{sys}}$	7.55%

Table 6.3: Packing fraction results per material for the fit method. It is important to note that these values were not used in the analysis going forward and are only shown for posterity. The ratio method (Section 6.8.3) was used in the final analysis.

of quasi-elastic contamination in the integral. For the 3.350GeV setting, as mentioned earlier, no elastic data was taken. Due to the lack of a resolvable elastic peak, and the sensitivity of the final packing fraction to the chosen fit ranges, it was found that this method was unreliable and a different method needed to be used. The packing fraction values in Table 6.3 were not used in the analysis of this work and are only shown as the result of an exersice in different attempts to extract the packing fraction for g_2^p.

6.8.3 Ratio Method

The second method for determining the packing fraction involved taking the ratio between several different run types at large ν. Two additional runs can be defined in the same way that the dummy and production runs are defined in Equations 6.32 and 6.33. They are the 'empty' run and the 'carbon' run

$$N_{empty} = \left(\frac{AN_0}{e}\right)\left[\frac{\rho_{He}L_{total}}{M_{He}}\sigma_{He}\right] \tag{6.35}$$

$$N_{carbon} = \left(\frac{AN_0}{e}\right)\left[\frac{\rho_C L_C}{M_C}\sigma_C + \frac{\rho_{He}(L_{total}-L_C)}{M_{He}}\sigma_{He}\right] \tag{6.36}$$

where L_C is the length of the carbon disk used during the carbon run. The packing fraction in the production ran can be isolated and written in terms of the three parameterized dilution runs (empy, dummy and carbon runs) as

$$pf = \frac{N_{production} - (\alpha'-1)N_{empty} - N_{dummy}}{\left(\frac{M_C\rho_{NH_3}L_{tg}}{M_{NH_3}\rho_C L_C}\right)\left(N_{carbon} - \frac{L_{total}-L_C}{L_{total}}N_{empty}\right)\left(\alpha'' + 3\frac{\sigma_H}{\sigma_C}\right) - \alpha'\frac{L_{tg}}{L_{total}}N_{empty}} \tag{6.37}$$

where α' is defined as the radiative scaling factor for helium, which accounts for the different radiative lengths of helium between the empty and production run, while α'' is a similar scaling factor for carbon but also includes a nucleon scaling factor to scale C12 to N14. The uncertainty in radiative scaling is small so the uncertainty in this method is dominated by α''.

To estimate the C12 to N14 scaling factor, an unradiated cross section model was generated for both materials. Since a fit to the packing fraction over a wide kinematic range was used, the cross section model had to match the scattering angle of the data. To accomplish this, the scattering angle at each momentum setting was fit with a Gaussian function. The mean angle was plotted against momentum and fit with an exponential to find a functional form for the angle, as shown in Figure 6-17. Using the parameters of the fit, the model is calculated using the scattering angle at each bin. A ratio between the two resulting models could then be used at all momentum settings.

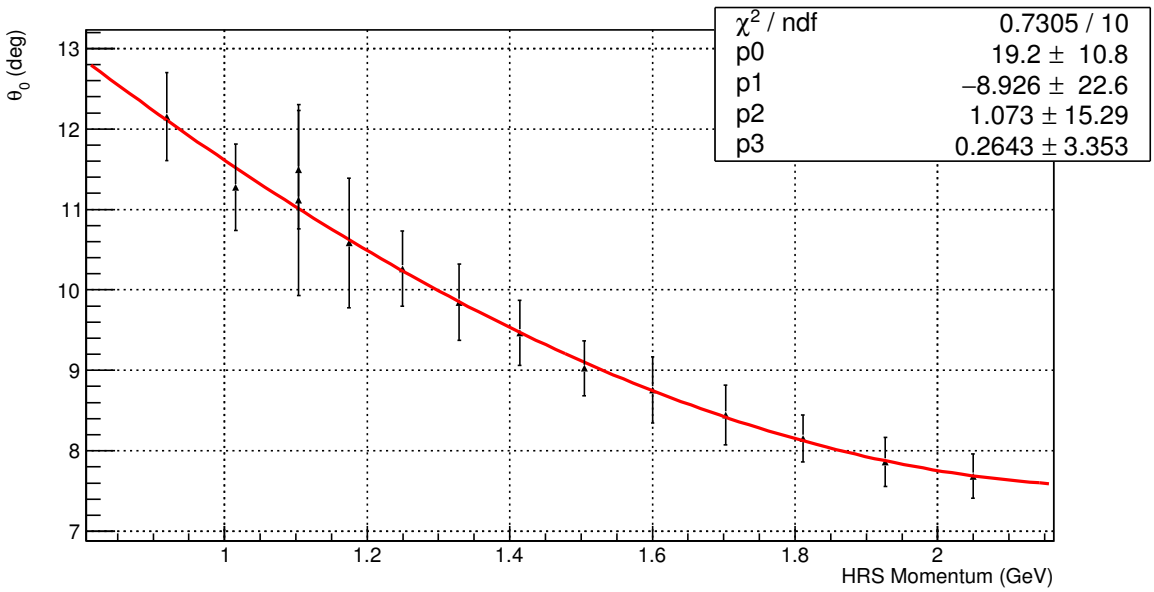

Figure 6-17: Exponential fit to the central angle at each momentum setting for the 2.2GeV 5T Transverse energy setting. Fit results are shown in the legend.

With all parameters in Equation 6.37 known, the packing fraction was generated across the entire momentum range for each energy setting and material. A 50MeV bin size was chosen so that the structure of the ratio could still be seen while reducing the statistical uncertainty of the result. A region past the delta for each target material was fit linearly and the weighted average was taken as the packing fraction. Final packing fraction values and their associated uncertainties for this method are shown in Table 6.4.

6.8.4 Ratio Method Uncertainties

Each yield of Equation 6.37 carried with it an associated statistical uncertainty of $\sqrt{N}$ which was propagated through to the packing fraction in the standard way. Due to the necessity to take the difference between yields the statistical uncertainty tended to be larger than what was seen in the fit method, but was still negligible compared to the systematics.

The systematic uncertainty was dominated by the model ratio, σ_C/σ_N. The model dependence of the ratio method becomes immediately apparent in both the absolute value and systematic

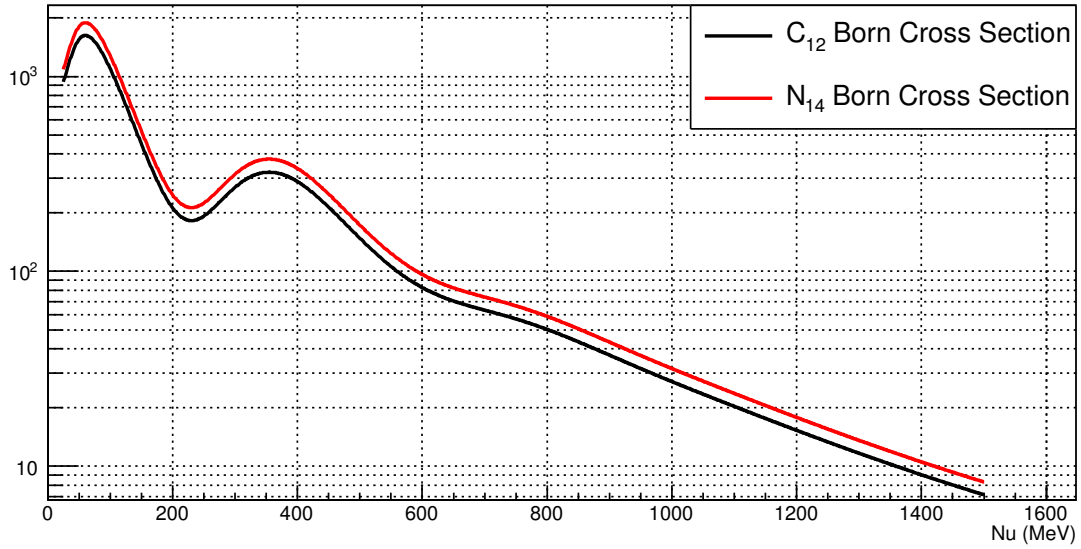

Figure 6-18: Unradiated cross section model for C_{12} and N_{14} using P.Bosted simulation script. The ratio between these models gave α''.

uncertainty of the packing fraction results. As Q^2 decreases our confidence in the model ratio also decreases due to the required extrapolation in the Bosted model. This extrapolation inherently increased our resulting uncertainty, and potentially manifested itself as a systematic shift to larger packing fraction values than are historically seen (upwards of a 10% shift from global packing fraction averages for this type of experiment). The final packing fraction values and associated uncertainties are shown in Table 6.4. The fits used to find the final packing fraction values are shown in Appendix B.

6.8.5 Packing Fraction Final Notes

Although in some instances the total uncertainty from the ratio method is comparable, or even larger than, that of the fit method, the removal of a 17 parameter fit instilled much more confidence in these results. It is very likely that the systematic uncertainty is underestimated in the fit method result as I was unable to accurately gauge the sensitivity of the final packing fraction to a chosen fit range. In the end the fit range is somewhat arbitrarily chosen 'by eye'.

Material #	Setting	Packing Fraction	PF Uncertainty (%)
11	1.1GeV 2.5T	$0.611 \pm 0.006_{\text{stat}} \pm 0.054_{\text{sys}}$	9.8%
12	1.1GeV 2.5T	$0.608 \pm 0.012_{\text{stat}} \pm 0.054_{\text{sys}}$	10.9%
7	1.7GeV 2.5T	$0.821 \pm 0.013_{\text{stat}} \pm 0.058_{\text{sys}}$	8.6%
8	1.7GeV 2.5T	$0.838 \pm 0.015_{\text{stat}} \pm 0.058_{\text{sys}}$	8.7%
7	2.2GeV 2.5T	$0.786 \pm 0.012_{\text{stat}} \pm 0.057_{\text{sys}}$	8.8%
8	2.2GeV 2.5T	$0.812 \pm 0.017_{\text{stat}} \pm 0.057_{\text{sys}}$	9.1%
17	2.2GeV 5T Longitudinal	$0.597 \pm 0.008_{\text{stat}} \pm 0.055_{\text{sys}}$	10.6%
18	2.2GeV 5T Longitudinal	$0.632 \pm 0.007_{\text{stat}} \pm 0.055_{\text{sys}}$	9.8%
19	2.2GeV 5T Transverse	$0.663 \pm 0.012_{\text{stat}} \pm 0.057_{\text{sys}}$	10.4%
20	2.2GeV 5T Transverse	$0.680 \pm 0.012_{\text{stat}} \pm 0.058_{\text{sys}}$	10.1%
19	3.3GeV 5T Transverse	$0.722 \pm 0.022_{\text{stat}} \pm 0.059_{\text{sys}}$	11.2%
20	3.3GeV 5T Transverse	$0.609 \pm 0.020_{\text{stat}} \pm 0.056_{\text{sys}}$	9.5%

Table 6.4: Packing fraction results per material for the ratio method. These are the final packing fraction values used in the remaining analysis work.

The take away from this study is that the values in Table 6.3 are shown as a document of my efforts to attempt various methods for packing fraction extraction. Moving forward in the analysis the results from the ratio method, Table 6.4, are used. The dominating uncertainty in this method is the σ_C/σ_N ratio. Lack of data to constrain the Bosted model at lower Q^2 points caused the uncertainty in this ratio to become quite large. Further work in constraining the Bosted model to existing data would greatly help in reducing the final systematic uncertainty of this result.

6.9 Dilution Analysis

Experimentally, it is impossible to scatter off of a pure polarized proton target, instead a solid $^{14}NH_3$ target submersed in a bath of liquid helium was used. The electron scattering off of the unpolarized ^{14}N, LHe and foil end caps of the target acted to dilute the measured e-p scattering asymmetry. This required an additional correction called the 'dilution factor' to determine the real physics asymmetry.

6.9.1 Dilution Formalization

A well measured target asymmetry is needed to calculate electron scattering cross section differences. The asymmetry is expressed as the difference over the sum of the number of electrons in the positive (+) and negative (−) helicity states,

$$A_{phys} = \frac{N_+ - N_-}{N_+ + N_-} \tag{6.38}$$

where $N_\pm$ is the number of detected electrons in the positive/negative helicity states, respectively. Only detected electrons that have scattered off of polarized protons in the target material are of interest. In reality, some amount of the detected electrons in each helicity state will have scattered off of unpolarized 'background' material. The measured asymmetry is then diluted as

$$A_{meas} = \frac{(N_+ + \frac{1}{2}N_{bg}) - (N_- + \frac{1}{2}N_{bg})}{(N_+ + \frac{1}{2}N_{bg}) + (N_- + \frac{1}{2}N_{bg})} = \frac{N_+ - N_-}{N_+ + N_- + N_{bg}} \tag{6.39}$$

where N_{bg} are detected electrons that have scattered off of unpolarized target material. Any scattering off of unpolarized background material only appears in the denominator of Equation 6.39, acting to dilute the final asymmetry. By introducing a correction factor of the form

$$f \equiv \frac{N_+ + N_-}{N_+ + N_- + N_{bg}} \tag{6.40}$$

the background contribution is removed, allowing for the calculation of the undiluted physics asymmetry,

$$\frac{1}{f}A_{meas} = \left(\frac{N_+ + N_- + N_{bg}}{N_+ + N_-}\right)\left(\frac{N_+ - N_-}{N_+ + N_- + N_{bg}}\right) = A_{phys} \tag{6.41}$$

which requires the calculation of the dilution factor as defined in Equation 6.40. This is done using two separate methods. The first method uses dilution run data taken throughout the experiment, while the second method uses radiated cross section models. While tuning the radiated model to

match the low Q^2 data was not ideal, complete dilution run coverage for the g_2^p kinematics was not always available. The final dilution factor results are a convolution of both methods.

6.9.2 Material Parameterization

To find the dilution factor an expression for N_{bg} in terms of experimental conditions is needed. For the g_2^p experiment a solid $^{14}NH_3$ target material submersed in a liquid helium bath between two Aluminum foil windows was used. The background charge normalized counts were then defined by $N_{bg} = N_N + N_{He} + N_{Al}$ since only electrons scattered from the spin polarized proton part of $^{14}NH_3$ contributed to the asymmetry.

As discussed in Section 6.8, charge normalized counts, N_x, can be written in detail as $N_x = AN_0\rho_x L_x \sigma_x / eM_x$ [58], where N_0 is Avagadro's numbers, A is the experimental acceptance, ρ_x is the density of material x, M_x is the atomic weight, L_x is the thickness of the material and σ_x is the fully radiated cross section for material x. The charge normalized background counts can then be expressed as

$$N_{bg} = \frac{AN_0}{e}\left(\frac{\rho_A L_{tg}(pf)}{M_A}\sigma_N + \frac{\rho_{He} L_{tg}(1-pf)}{M_{He}}\sigma_{He} + \frac{\rho_{Al} L_{Al}}{M_{Al}}\sigma_{Al}\right) \tag{6.42}$$

where pf is the length fraction of the target cell that is filled with ammonia.

Along with the $^{14}NH_3$ target, data was taken on various other targets to simulate background conditions. Ideally a pure nitrogen target would have been used to account for the ^{14}N background but such a target was not readily available. Instead a solid carbon target was used, and a nitrogen simulation was used to scale the resulting yield. In total three dilution run targets were used; a pure liquid helium target, referred to as the 'empty run', a liquid helium target with foil windows, referred to as the 'dummy run', and the carbon disk target, referred to as the 'carbon run'. Similar to the production background each of these can be parameterized in terms of the contributing

materials as follows

$$N_{empty} = \frac{AN_0}{e}\frac{\rho_{He}L_{tg}}{M_{He}}\sigma_{He} \tag{6.43}$$

$$N_{dummy} = \frac{AN_0}{e}\left(\frac{\rho_{He}L_{tg}}{M_{He}}\sigma_{He} + \frac{\rho_f L_f}{M_f}\sigma_f\right) \tag{6.44}$$

$$N_{carbon} = \frac{AN_0}{e}\left(\frac{\rho_C L_C}{M_C}\sigma_C + \frac{\rho_{He}(L_{tg}-L_C)}{M_{He}}\sigma_{He}\right) \tag{6.45}$$

As previously discussed in determining the packing fraction using the ratio method (Section 6.8.3). σ_C can be solved for in Equation 6.45 and all three parameterized dilution yields can be substituded into Equation 6.42 to find the charge normalized background counts in terms of measured dilution runs.

$$N_{bg} = a\frac{M_C\rho_A L_{tg} pf}{M_A\rho_C L_C}\left(N_{carbon} - \left(\frac{L_{tg}-L_C}{L_{tg}}\right)N_{empty}\right) + N_{dummy} - pfN_{empty} \tag{6.46}$$

where a is a scaling factor used to scale σ_C to σ_N. All of the quantities in Equation 6.46 are universally or experimentally measured and can be found in Table 6.5 except for the scaling factor a and the packing fraction, discussed in Section 6.8.

Parameter	Value
M_C	12.011 u
M_A	17.031 u
ρ_C	2.267 g/cm^3
ρ_A	0.817 g/cm^3
L_{tg}	2.8307 cm
L_C	0.1016(0.3175) cm

Table 6.5: Known background parameters, terms in parenthesis were used after run 5103.

6.9.3 Scaling ^{12}C to ^{14}N

Before the charge normalized counts can be substituted into Equation 6.42 a relation between σ_C and σ_N must be found. A very crude approximation is to consider each cross section as if it was

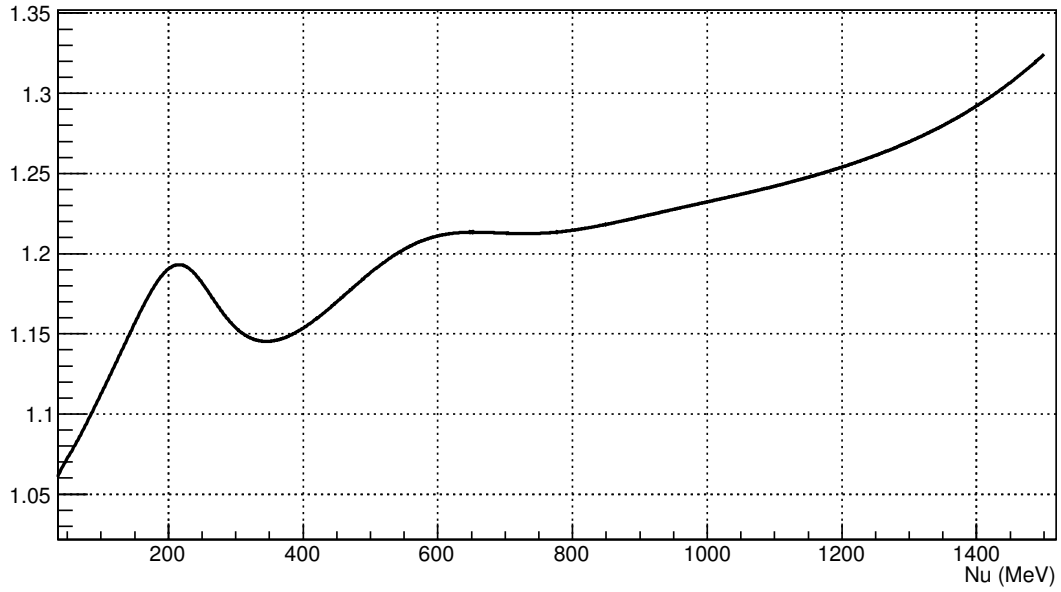

Figure 6-19: C12 to N14 scaling ratio using P.Bosted radiated cross section model.

made up solely of its constituent nucleons. In this scenario the carbon and nitrogen cross sections can be written as

$$\sigma_C = 6\sigma_H \tag{6.47}$$

$$\sigma_N = 7\sigma_H \tag{6.48}$$

$$\sigma_N = \frac{7}{6}\sigma_C \tag{6.49}$$

This is a good approximation in the deep inelastic region but breaks down in the resonances. To find the scaling factor everywhere the constant scaling factor is simply replaced with a fitting parameter

$$\sigma_N = a\sigma_C \tag{6.50}$$

and a radiated cross section ratio between carbon and nitrogen is generated to find a, which can then be applied to the carbon yield bin by bin. Such a ratio for one Q^2 setting can be seen in Figure 6-19. The models are tuned to data at larger Q^2 settings and any variance in the accuracy

is included in the final systematic uncertainty. The model uncertainty was found to be roughly 5% at all Q^2 settings [12]. It is important to note that, while theoretically the C12 to N14 ratio should approach 1.167 in the DIS region, the model ratio actually diverges quite significantly due to the differing radiation lengths and scattering angles of each material.

6.9.4 Radiation Length and Scattering Angle Corrections

An important correction factor that has been overlooked to this point is the radiative length and scattering angle dependence of each dilution run. Equation 6.46 is found by substituting the dilution run cross-sections into the parameterized definition for the production background. Each of the dilution runs uses different target materials, which results in different average scattering angles and radiative lengths. Because of this, each type of dilution run is not directly comparable. Instead a scaling factor to match the radiation length and scattering angle of each dilution cross section to their corresponding production run conditions must be introduced.

The ratio was found by generating two different cross sections for each background material. One cross section used the conditions of the dilution run material, while the second cross section used the conditions of the same material in the production run. Then, by taking the ratio of the two cross sections, a scaling factor that could be applied to the dilution yields was found.

The first and simplest condition to consider was the radiative length change. During the carbon

Run	Material	Density($\frac{g}{cm^3}$)	Thickness(cm)	Rad. Length	Rad. Thickness
Empty	He4	0.145	3.7045	94.3224	0.00569
Carbon	C12	2.267	0.1016	42.6969	0.00539
Carbon	He4	0.145	3.6029	94.3224	0.00554
Production	N14	0.817	1.5549	40.8721	0.03108
Production	He4	0.145	2.146	94.3224	0.0033
Production	Al27	2.7	0.0036	24.0112	0.0004

Table 6.6: Material Thicknesses

dilution run 0.1016cm of carbon was used which has a radiation thickness of $\frac{\rho L}{\chi_0} = 0.00539$ where the

density of carbon is $2.267\frac{\text{g}}{\text{cm}^3}$ and χ_0 is the material dependent radiation length. The nitrogen target had a thickness of $pf \times L_{tg}$ ≈1.55cm which gave a radiation length of 0.03108. So by generating a carbon cross section and radiating using each of these two radiation lengths the appropriate scaling factor was found and applied to the dilution yields. Table 6.6 contains the physical lengths, densities and radiation lengths of each material used in generating these ratios.

The second condition to be considered is the scattering angle dependance of each target material. To correct for different scattering angles a good understanding of how the scattering angle changed as a function of E' for each material was needed. First, the central scattering angle vs. HRS momentum for each run was plotted and a weighted average of overlapping bins to find θ_{sc} vs. HRS P_0 was done for each target type. The data was then fit with an exponential of the form $f(x) = e^{p_0+p_1x} + p_2x + p_3$, and the four target dependent fit parameters were saved to a text file. Figure 6-17 shows this fit being applied to a production run. A similar fit was done to the other dilution runs for scaling. Note that the difference in average scattering angles between runs is small but the cross section is highly sensitive to this ratio.

Once the fit parameters for each target type were obtained two cross section models for each material were generated, one using the fit parameters for the dilution run of interest, and the second using the parameters of the production run being scaled to. Then, by taking the ratio of these two models, the scattering angle correction was found and applied to the dilution run yields. It is worthwhile to note that the two scaling processes that have been described in this section were done simultaneously. Although it is more straightforward to explain each process separately, in reality the change in scattering angle will have an impact on the radiative effects, and vise versa. So each model must be generated with both scattering angle and radiative length dependence. As expected, the He_4 correction was typically small ($< 1\%$) due to the very small correction in radiation length, while the C12 correction was much larger because of the scattering angle difference between the Carbon and Production run types.

6.9.5 Dilution Factor Uncertainty

With all of the necessary components an expression for the dilution factor is found

$$f = 1 - \frac{N_{bg}}{N_{production}} \tag{6.51}$$

Using the definition of N_{bg} given by Equation 6.46

$$f = 1 - \frac{a(E,E')\frac{M_C \rho_A L_{tg} pf}{M_A \rho_C L_C}\left(N_{carbon} - \left(\frac{L_{tg}-L_C}{L_{tg}}\right)N_{empty}\right) + N_{dummy} - pfN_{empty}}{N_{production}} \tag{6.52}$$

where each charge normalized count now contains the proper scattering angle and radiation length scaling factor applied to it as addressed in the previous sections. The dilution factor was then calculated at each Q^2 setting bin by bin, and could then be applied to the measured asymmetry. For analysis purposes the dilution was calculated in 1 MeV bins across the entire kinematic range for each setting. To reduce the statistical uncertainties of the final result 50 MeV bins were used and a statistically weighted average of the dilution in each bin was calculated using

$$f = \frac{\sum\limits_n \left(\frac{f_n}{\delta_n^2}\right)}{\sum\limits_n \left(\frac{1}{\delta_n^2}\right)} \tag{6.53}$$

where δ_n is the uncertainty in each dilution factor. Looking at equation (6.52) it is easy to see that the propagation of the statistical uncertainty is very tedious. Each normalized count has a statistical uncertainty of $\sqrt{N}$ associated with it. Propagation was made easier by breaking the total background counts up into individual materials in the production run

$$N_{He} = \left(1 - pf\frac{L_{tg}}{L_{total}}\right)N_{empty} \tag{6.54}$$

$$N_{Al} = N_{dummy} - N_{empty} \tag{6.55}$$

$$N_N = a\frac{M_C \rho_A L_{tg} p f}{M_A \rho_C L_C}\left(N_C - \left(1 - \frac{L_C}{L_{total}}\right) N_{empty}\right) \tag{6.56}$$

where N_{He}, N_{Al} and N_N were the helium, aluminum and nitrogen background counts during the production run, respectively. The total background uncertainty was then calculated as

$$\delta_{bg}^2 = \delta_{N_{He}}^2 + \delta_{N_{Al}}^2 + \delta_{N_N}^2. \tag{6.57}$$

There were two primary sources of systematic uncertainty in the dilution factor. The first was the uncertainty in the model used for radiation length and scattering angle scaling. The second was in the determination of the scattering angle itself. The scattering angle was known to 0.1 mRad [57], so a fit to the central value of the scattering angle will have some variance associated with it. To find the uncertainty due to the scattering angle two fits were done for each target material at ± 1 standard deviation in the central angle. A cross section was generated using each of these fits and the ratio between them indicated how sensitive the cross section was to the scattering angle. It was found that the variance was always less than 5% so a total systematic uncertainty of 5% was included in the scattering angle calculation.

To find the systematic uncertainty in the generated models a detailed study of model tuning on preexisting data at different Q^2 settings was done [12]. The total scaling factor required to minimize the χ^2 for each data set was used as the systematic uncertainty in the model. The model uncertainty ranged from 5% to 10% depending on the target. The systematic uncertainty was then propagated in the standard way through Equation 6.52. The dilution results for all channels is shown in Appendix C.

Chapter 7

Results

Armed with accurately calibrated data and extracted measurable quantities we can begin constructing physical observables. Recall from Section 6.2 that the polarized cross section differences are functions of the physics asymmetry and the total unpolarized cross section,

$$\Delta\sigma_{\parallel,\perp}^{phys} = 2A_{\parallel,\perp}^{phys}\sigma_0^{phys}. \tag{7.1}$$

The following several sections will present the results for these observables, as well as calculations of the proton spin structure functions and contributions to the moments. At the time of this writing three of the six kinematic settings of experiment E08-027 have been analyzed. The following results will only address those settings with accurate calibration studies completed. Acceptance studies and beam position studies are still underway by the E08-027 collaboration for the remaining 2.5 Tesla target field data.

7.1 Physics Asymmetries

Charge and livetime asymmetries were discussed in Section 6.6 while the dilution was discussed in Section 6.9. The beam and target polarizations were discussed in Section 4.2.3 and at length in Chapter 5, respectively. With all of this information compiled, the physics asymmetries can be calculated using Equations 6.2 and 6.3.

Since data is broken up into short segments called 'runs', a method for statistically combining overlapping kinematic bins needed to be used. The final asymmetry per kinematic bin is given by

$$A = \frac{\sum_i A_i/\delta A_i^2}{\sum_i 1/\delta A_i^2} \tag{7.2}$$

$$\delta A = \sqrt{\sum_i \frac{1}{1/\delta A_i^2}} \tag{7.3}$$

where A_i is the asymmetry for each overlapping kinematic bin and δA_i is the corresponding statistical uncertainty in A. The statistical uncertainty is approximately equal to $1/\sqrt{N}$ where N is the total number of events. However, when the raw trigger rate was high enough that a prescale factor was required, as discussed in Section 4.4.3, the statistical uncertainty had to be modified to account for prescale dependent fluctuations [59].

If we define the total number of useful events in one kinematic bin as

$$C = \frac{N \cdot LT \cdot f}{ps} \tag{7.4}$$

where N is the total number of recorded events, LT is the livetime correction, f is the acceptance and ps is the prescale factor, the origin of the fluctuation can be separated into two sources:

- Fluctuation of the total number of events, N

$$\sigma_N = \sqrt{N} \tag{7.5}$$

$$\Delta\sigma_N = \frac{\sigma_N}{N} = \frac{1}{\sqrt{N}} \tag{7.6}$$

- Fluctuation due to the acceptance $LT \cdot f$

The second case can be derived via a binomial distribution which results in a fluctuation due to the acceptance as

$$\sigma_C = \sqrt{C\,(1 - LT \cdot f)}. \tag{7.7}$$

Combining Equations 7.7 and 7.6 gives the total correction to the statistical uncertainty

$$S = \sqrt{1 - LT \cdot f\left(1 - \frac{1}{ps}\right)} \tag{7.8}$$

which directly modifies the uncertainty in the counts of each helicity state, $\sigma_{N_\pm} = S_\pm\sqrt{N_\pm}$, and results in a final prescale corrected statistical uncertainty of

$$\delta A = \frac{2Y_+Y_-}{\left(Y_+^2 + Y_-^2\right)^2}\sqrt{\frac{S_+^2}{N_+} + \frac{S_-^2}{N_-}} \tag{7.9}$$

where $Y_\pm$ are the helicity gated yields in each kinematic bin.

Armed with a method for statistically weighting overlapping kinematic bins, the final physics asymmetry for each setting could be calculated. The radiated results are shown for the three kinematic settings analyzed in this work in Figures 7-2, 7-3 and 7-4. Radiative corrections are applied later at the polarized cross-section level, the details of which will be discussed in the following sections.

7.1.1 Out-Of-Plane Polarization

As discussed in Section 2.2.2 there is an additional out-of-plane polarization angle that acts to dilute the measured asymmetry. This polarization angle is formed from the difference between the electron scattering plane and the polarization plane. Ideally this angle would be close to 0° so the measured polarization is roughly equal to the real scattered polarization and any additional affects could be ignored. For the E08-027 experiment it was found that this out-of-plane angle was large enough that the effect could not be neglected.

The out-of-plane angle for several momentum settings at the 2.254 GeV, 5T Transverse beam energy setting are shown in Figure 7-1. The mean angle at each momentum setting was applied at the physics asymmetry level as an additional correction.

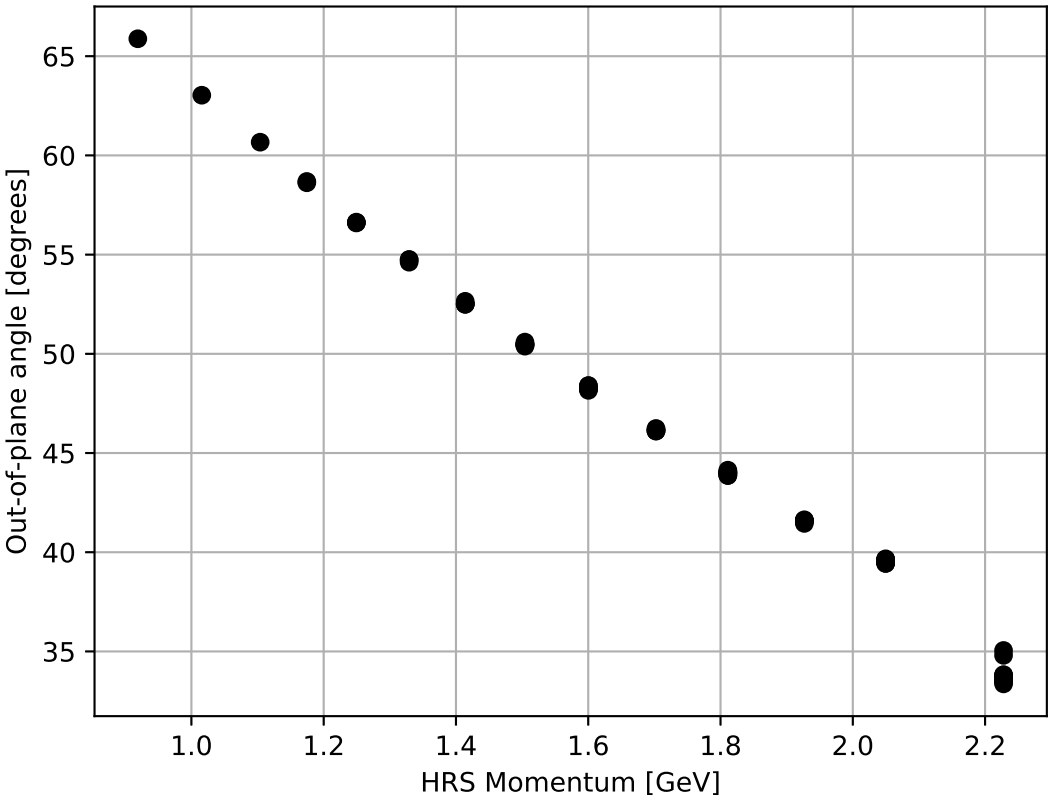

Figure 7-1: The out-of-plane polarization angle for the 2.254 GeV 5T Transverse beam energy setting at various momentums. The physics asymmetry at each momentum was scaled by the mean angle to account for out-of-plane diluting of the asymmetry.

7.1.2 Asymmetry Systematics

There are several systematic contributions to the physics asymmetry that must be considered. The largest sources come from the dilution (Section 6.9) and target polarization (Section 5.5). Other systematic sources include the beam polarization, pion contamination and the out-of-plane polarization uncertainties. Table 7.1 contains all of the relative systematics that are included in

the final physics asymmetries. A detailed study of pion contamination and asymmetry found that the systematic introduced was negligible [60].

Source	$\delta A/A$
Dilution	5-7%
P_B	1.7%
P_T	2-4%
Out-of-plane pol.	0.5-1.5%
Pion contamination	-

Table 7.1: Asymmetry Systematics.

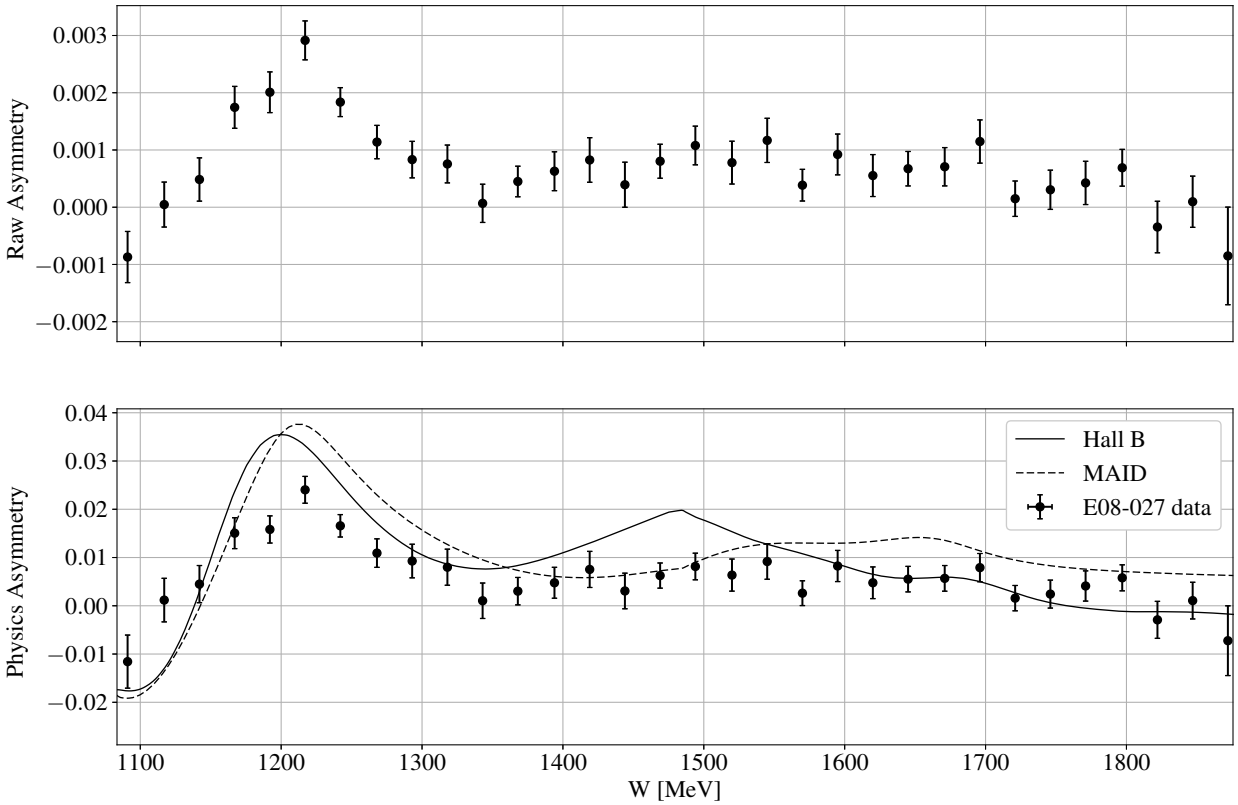

Figure 7-2: The raw (top) and scaled Physics (bottom) asymmetries for the 3.350 GeV beam energy, 5T transversely polarized target field setting. Uncertainties are statistical only. A comparison is shown between the physics asymmetry and Hall B and MAID model predictions.

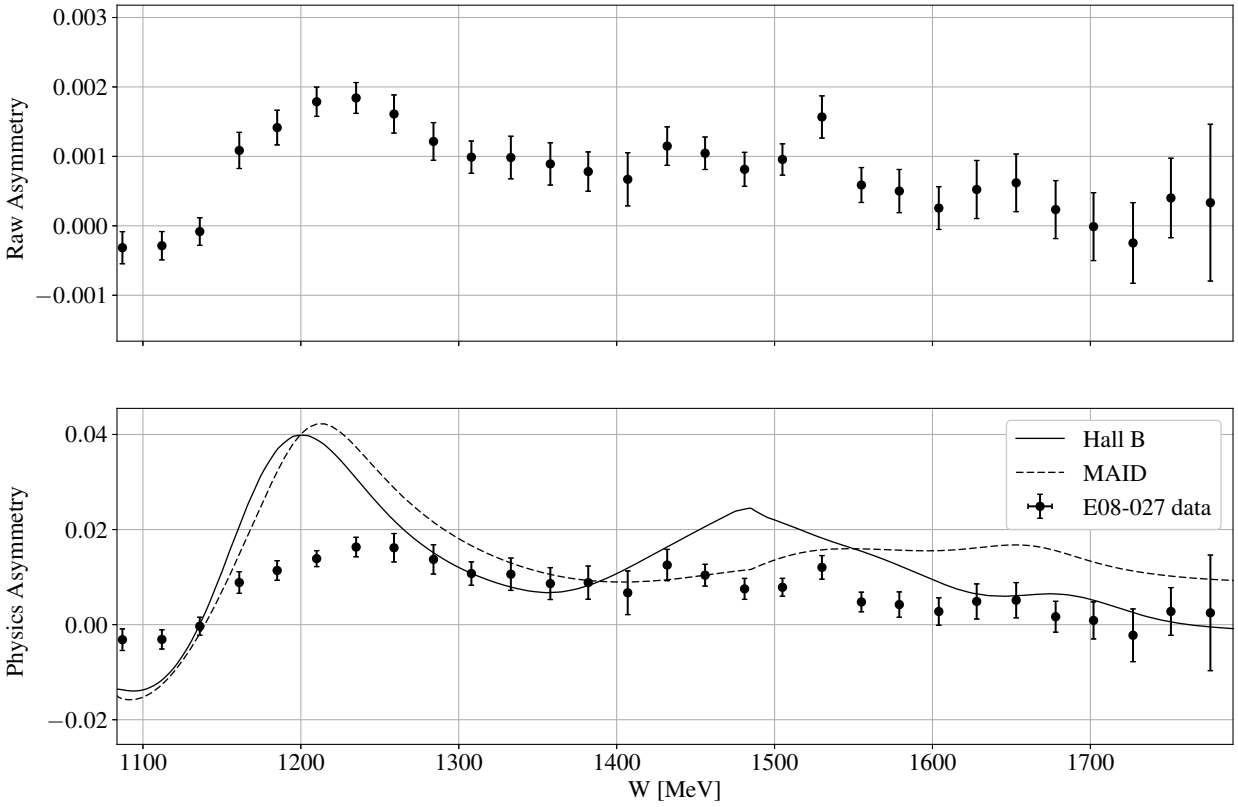

Figure 7-3: The raw (top) and scaled Physics (bottom) asymmetries for the 2.254 GeV beam energy, 5T transversely polarized target field setting. Uncertainties are statistical only. A comparison is shown between the physics asymmetry and Hall B and MAID model predictions.

7.2 Unpolarized Cross Sections

Two methods were used in finding the unpolarized cross section for this analysis. The first method used the experimentally extracted yields and necessary kinematic scaling factors,

$$\sigma_0^{phys} = \left(\frac{psNf}{QLT\epsilon_{det}}\right)\left(\frac{1}{\Delta\Omega\Delta E'\Delta Z}\right), \tag{7.10}$$

as discussed in Section 6.2. Using known yields, and a well defined dilution, the only missing component for a data extracted cross-section is the acceptance correction, $\Delta\Omega$. At the time of this

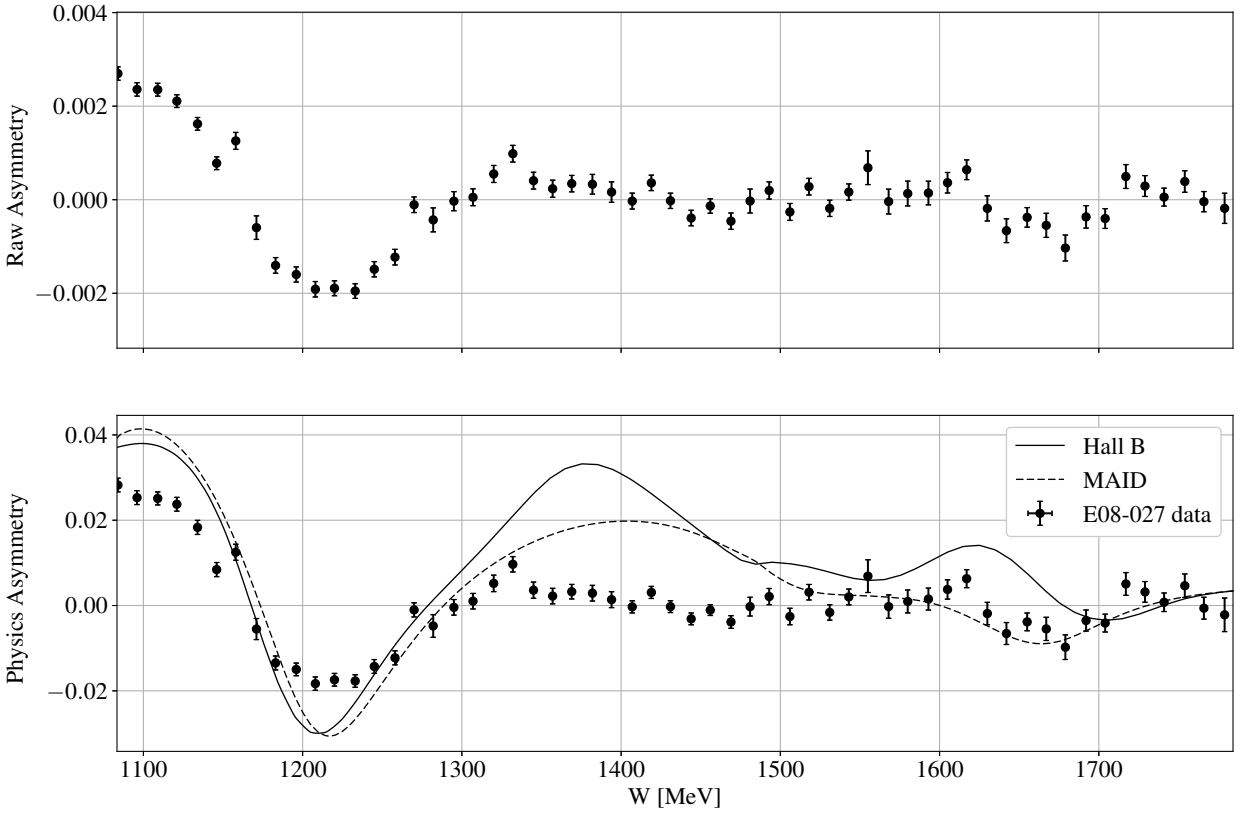

Figure 7-4: The raw (top) and scaled Physics (bottom) asymmetries for the 2.254 GeV beam energy, 5T longitudinally polarized target field setting. Uncertainties are statistical only. A comparison is shown between the physics asymmetry and Hall B and MAID model predictions.

analysis, the experimental acceptance was not well understood. A detailed acceptance study is currently underway by another collaboration member to resolve this issue. A temporary solution to this was to define a very small acceptance region which contained a relatively flat θ and ϕ distribution, and introduce an additional systematic based on the precision with which the reconstructed θ and ϕ values are known.

Figure 7-5 shows the cut region chosen for the 2.254GeV beam energy, 5T transverse target field setting. The region was chosen by minimizing the relative uncertainty in the acceptance while maintaining a flat distribution in θ and ϕ. All of the acceptance cuts used in the experimental cross section extraction are shown in Table 7.2.

Variable	Cut Region
x	< 8mm
y	< 0.8mm
θ	< 0.01rad
ϕ	< 0.005rad
dp	$< 4\%$

Table 7.2: Acceptance cuts used for Cross Section Analysis.

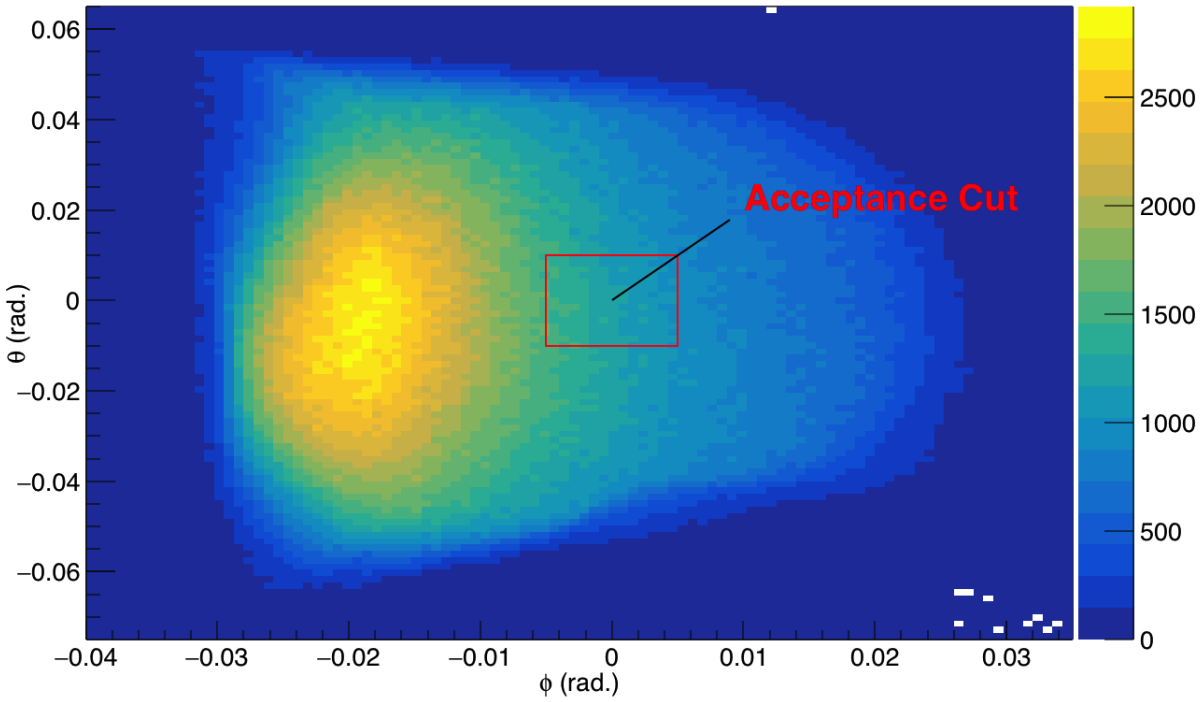

Figure 7-5: The reconstructed acceptance distribution for the 2.254GeV beam energy, 5T longitudinal target field setting. The red box indicates the acceptance cut chosen for the cross section analysis.

With a well defined acceptance region, the data extracted cross section calculation was straightforward, following Equation 7.10. The results for the three settings of interest in this analysis are shown in Figures 7-6, 7-7, and 7-8. It is important to note that radiative corrections have not yet been applied, so these are not true Born cross sections. A comparison is shown against a radiated Bosted/Christy model at the corresponding Q^2 and radiation lengths of each setting. We find agreement with the model cross section to less than 25% everywhere.

Due to the addition of a large systematic uncertainty from the acceptance correction (Sec-

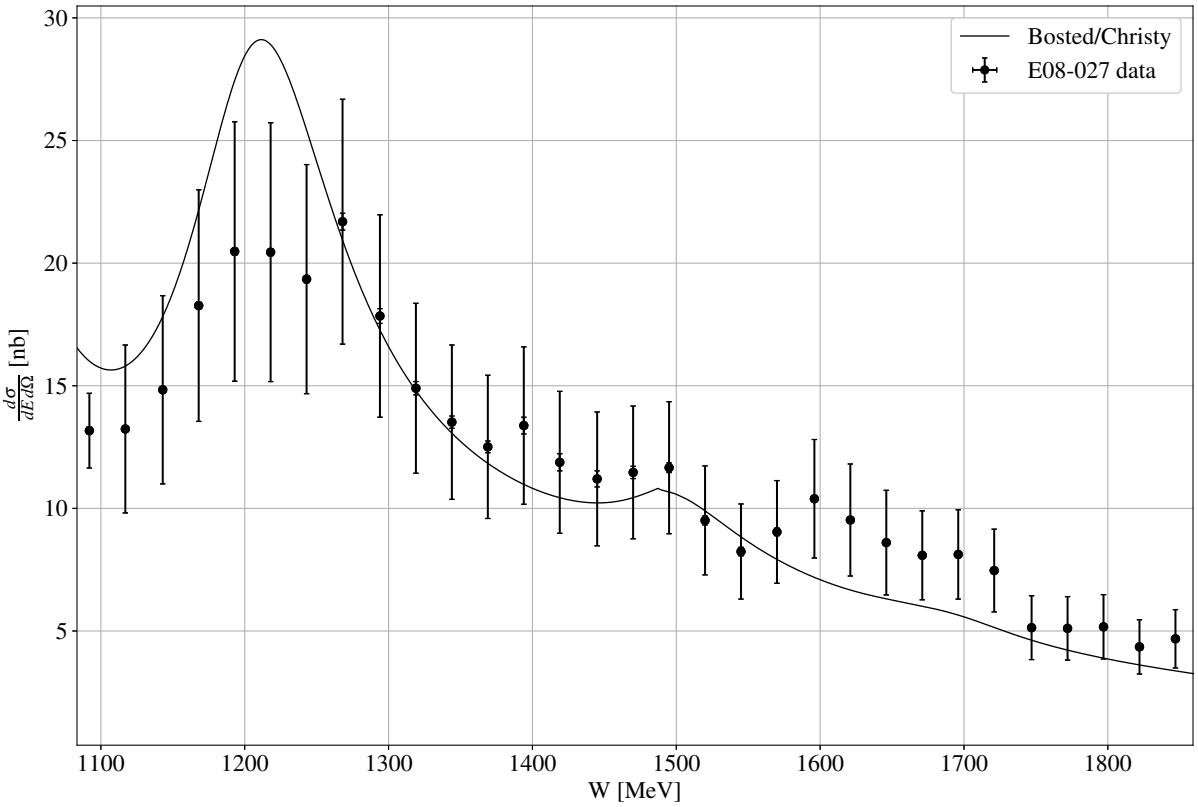

Figure 7-6: The experimentally extracted cross section for the 3.350 GeV beam energy, 5T transversely polarized target field setting. Inner and outer error bars represent the statistical and systematic uncertainties, respectively.

tion 7.2.1) a second approach to absolute cross sections was explored. The proton unpolarized born cross section is relatively well understood in the kinematic region of this experiment. Several model cross sections were looked at and compared with existing proton data to determine if there was better agreement than the level of our acceptance uncertainty. This study was done on both the Bosted/Christy and the Hall B models, and it was found that there was agreement with existing data in our kinematic region to better than 15%. An example cross section output for both models is shown in Figure 7-9. Since the uncertainty of this model is smaller than that of our data extracted cross sections, we decided to use a model cross section for the unpolarized contribution.

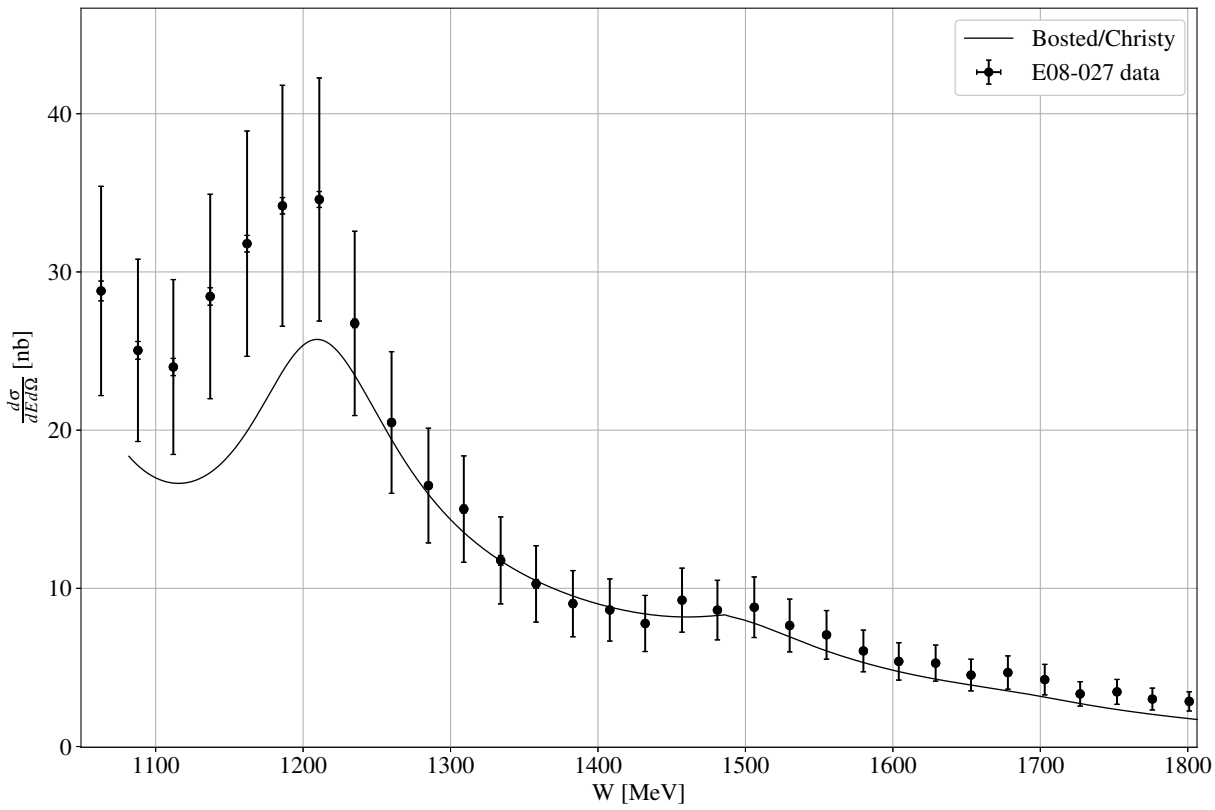

Figure 7-7: The experimentally extracted cross section for the 2.254 GeV beam energy, 5T transversely polarized target field setting. Inner and outer error bars represent the statistical and systematic uncertainties, respectively.

Work is ongoing by another collaboration member to find an acceptance function that will further reduce the 15% systematic.

7.2.1 Cross Section Systematics

The systematics for each of the two cross section methods, as discussed in the previous section, are addressed separately. Contributions to the data extracted cross section come from the dilution and acceptance corrections. The acceptance systematic can be broken down into two sources, the precision at which the central acceptance value is known, as dictated by the optics reconstruction, and the precision at which the region for which the cut is defined is known, as dictated by our

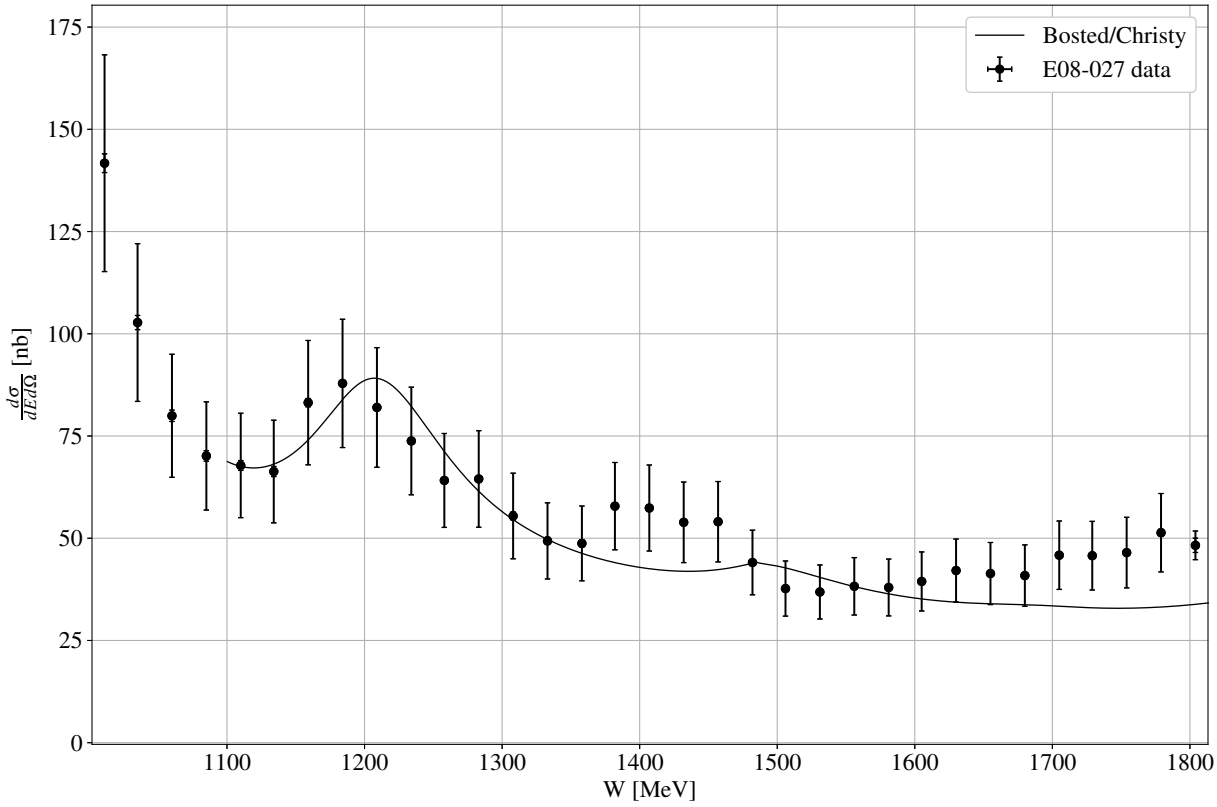

Figure 7-8: The experimentally extracted cross section for the 2.254 GeV beam energy, 5T longitudinally polarized target field setting. Inner and outer error bars represent the statistical and systematic uncertainties, respectively.

knowledge of the scattering angle. A detailed study of the acceptance systematic found an additional relative uncertainty on the order of 20% [61]. The values of these various systematic contributions for the data extracted cross section are shown in Table 7.3.

Separate systematics must be considered for the proton model cross section. The model must

Source	$\delta A/A$
Dilution	5-7%
Acceptance	22.36%
Packing Fraction	3-7%
Target Length	0.3%

Table 7.3: Data extracted cross section systematics.

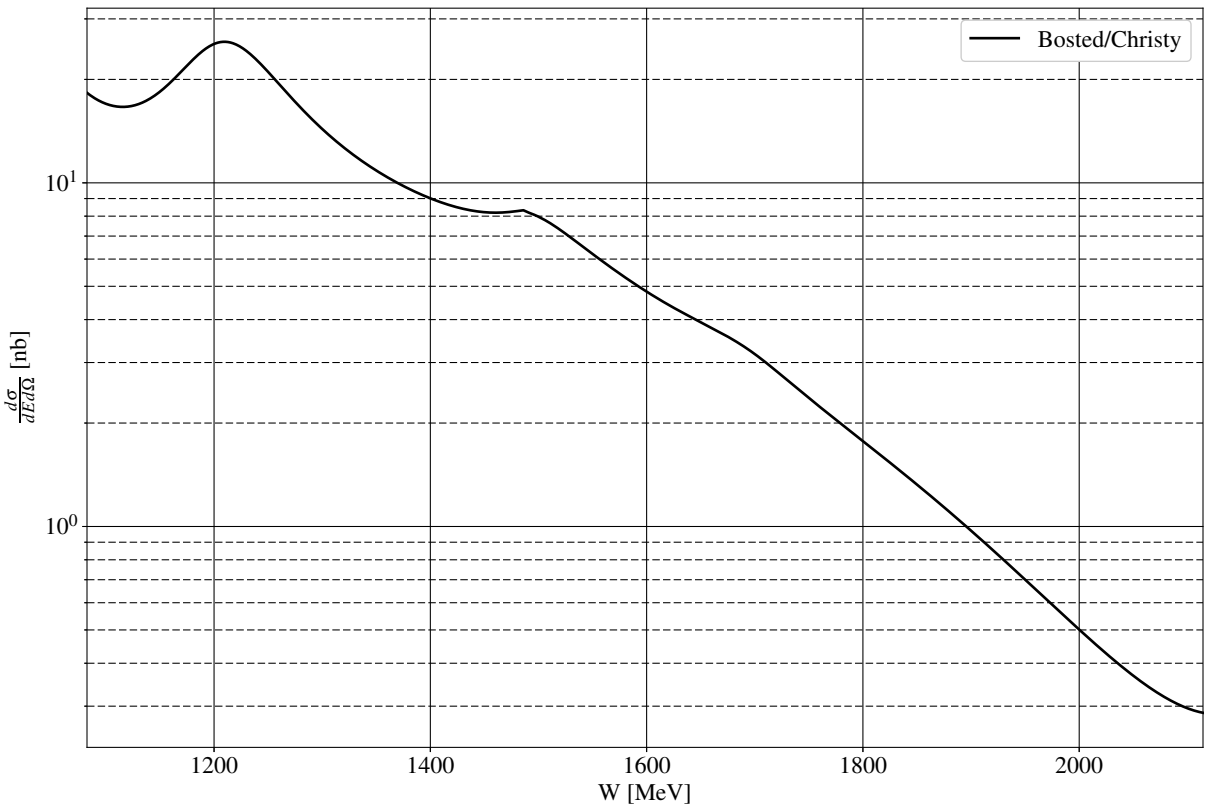

Figure 7-9: Bosted/Christy unpolarized proton cross section model at the kinematic setting of the E08-027 2.254 GeV beam energy, 5T transverse target setting.

be generated at the kinematic region as defined by the experiment. This kinematic region has an associated uncertainty from our knowledge of the scattering angle. This introduces a systematic, called the 'Mott systematic' which is not present in the data extracted cross section. The model must also be radiated to match our experimental radiative lengths, since corrections to this effect come at a later stage. A detailed radiative effects study was done [2] and it was concluded that a 3% systematic needed to be added to the model cross section. Finally, the model itself has some associated uncertainty, defined by its accuracy at reproducing existing data. This uncertainty was found by comparing it to the E08-027 data extracted cross section, and taking the average relative difference as the systematic.

A second method for determining the model uncertainty was done by comparison with existing data from other experiments. Data from SLAC E61 and SLAC ONEN1HAF was compared with the output of the Bosted/Christy models at kinematic regions comparable with E08-027. This study found a model systematic on the order of 15%, in agreement with the previous result.

7.3 Polarized Cross Section Differences

With data extracted physics asymmetries and unpolarized proton cross sections the polarized proton cross section can be calculated in a relatively straightforward manner,

$$\Delta\sigma_{\perp,\parallel} = 2A_{\perp,\parallel}\sigma_{\circ}. \tag{7.11}$$

This is done separately for each kinematic setting of experiment E08-027. Systematic and statistical uncertainties are propagated through Equation 7.11 in the standard way. The polarized proton cross sections are shown in Figures 7-10, 7-11 and 7-12 with statistical error bars only. At this point the polarized cross sections are still fully radiated and vary in Q^2 over the invariant mass range, W. Before using these results to calculate the structure functions they must be radiatively corrected and extrapolated to a constant Q^2.

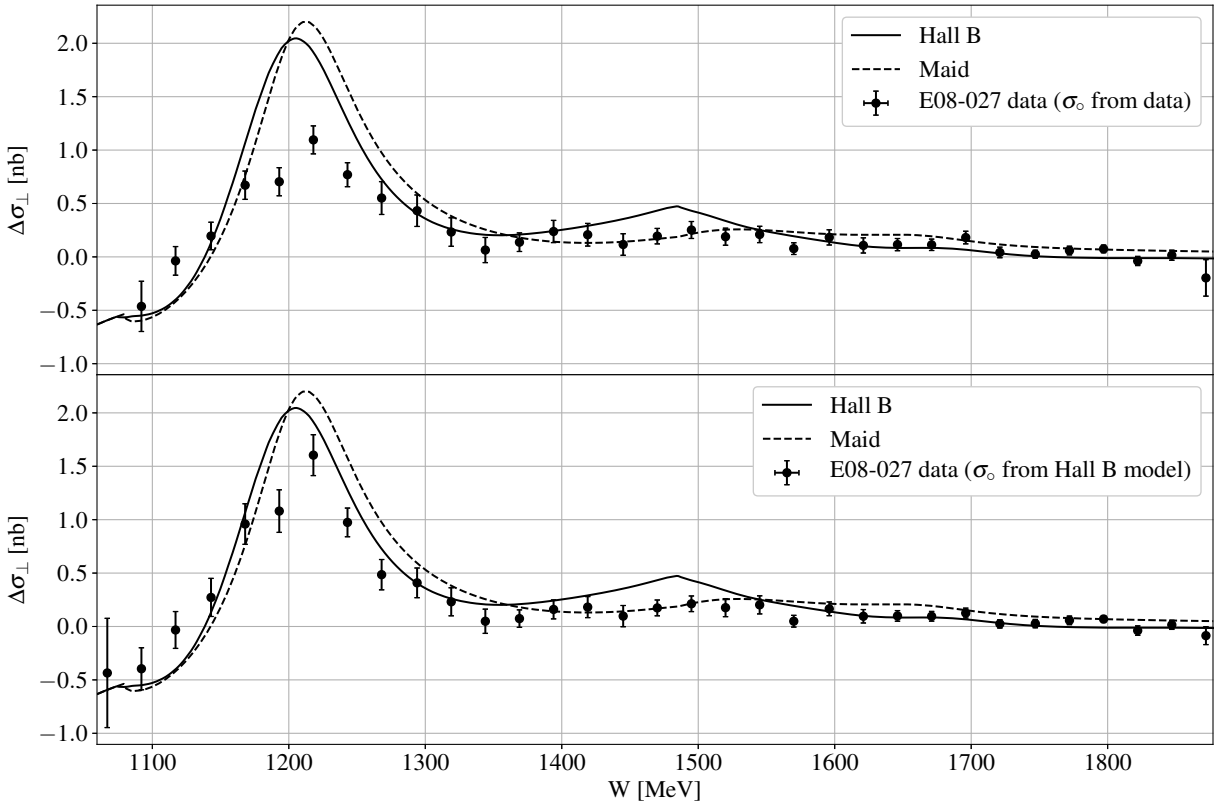

Figure 7-10: The polarized proton cross section for the 3.350 GeV beam energy, 5T Transverse target polarization setting using E08-027 cross section data (top) and the Hall B model (bottom) as the contribution for the unpolarized part.

7.4 Radiative Corrections

Up to this point we have assumed that all of the detected electrons have undergone the leading order scattering process $ep \rightarrow e'p$. In reality the electron will undergo several stages of energy loss before, during and after scattering which need to be taken into account. The energy loss processes that we consider are:

- External radiation of a bremsstrahlung photon as the electron passes through material before and after scattering.
- Internal radiation of a photon during the scattering process itself.

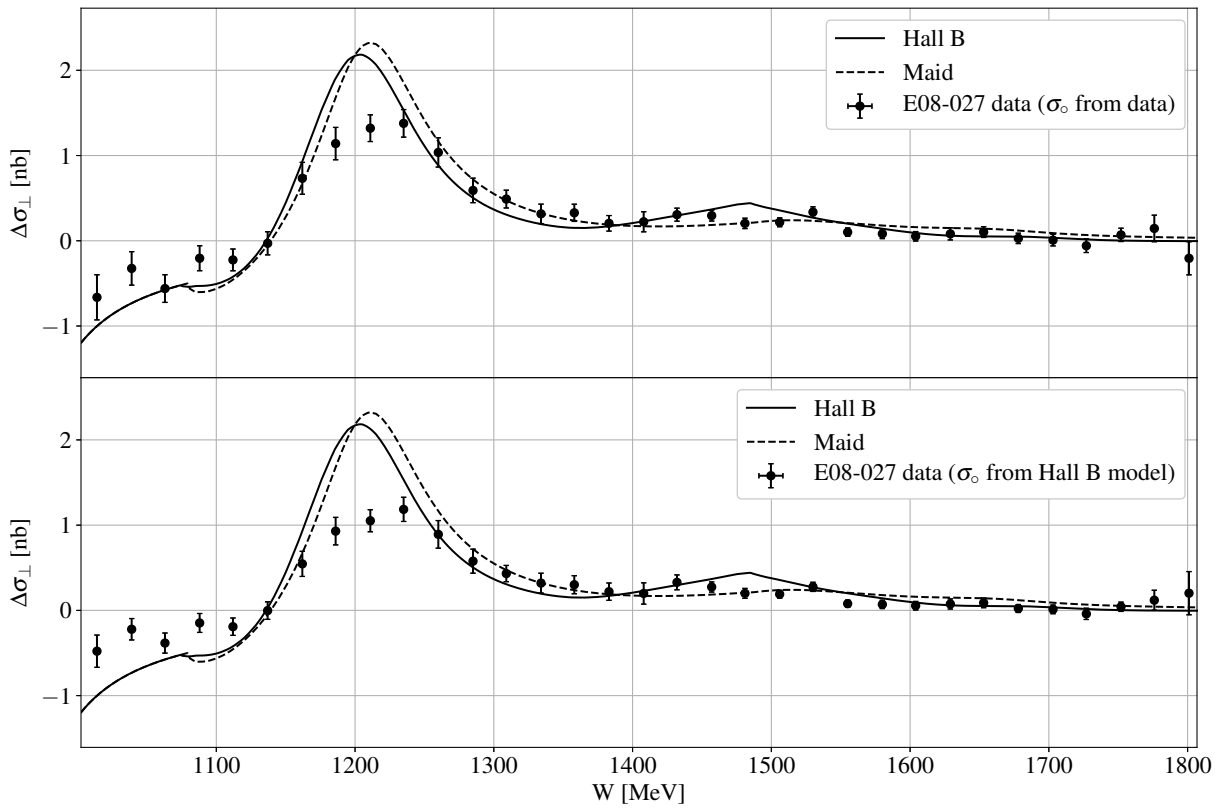

Figure 7-11: The polarized proton cross section for the 2.254 GeV beam energy, 5T Transverse target polarization setting using E08-027 cross section data (top) and the Hall B model (bottom) as the contribution for the unpolarized part.

- Higher order loop corrections to the scattering process.
- Ionizing collisions with materials in the beam path before and after scattering.

The process of taking into account all of the above mentioned energy loss processes and correcting the measured cross section to extract the born cross section is called radiative corrections. In this section a general overview of each process will be discussed, for a more detailed write-up of the radiative corrections see [12].

The external radiation of a bremsstrahlung photon occurs when the electron passes through material in the beam path before or after scattering. The amount of energy lost is parameterized by the

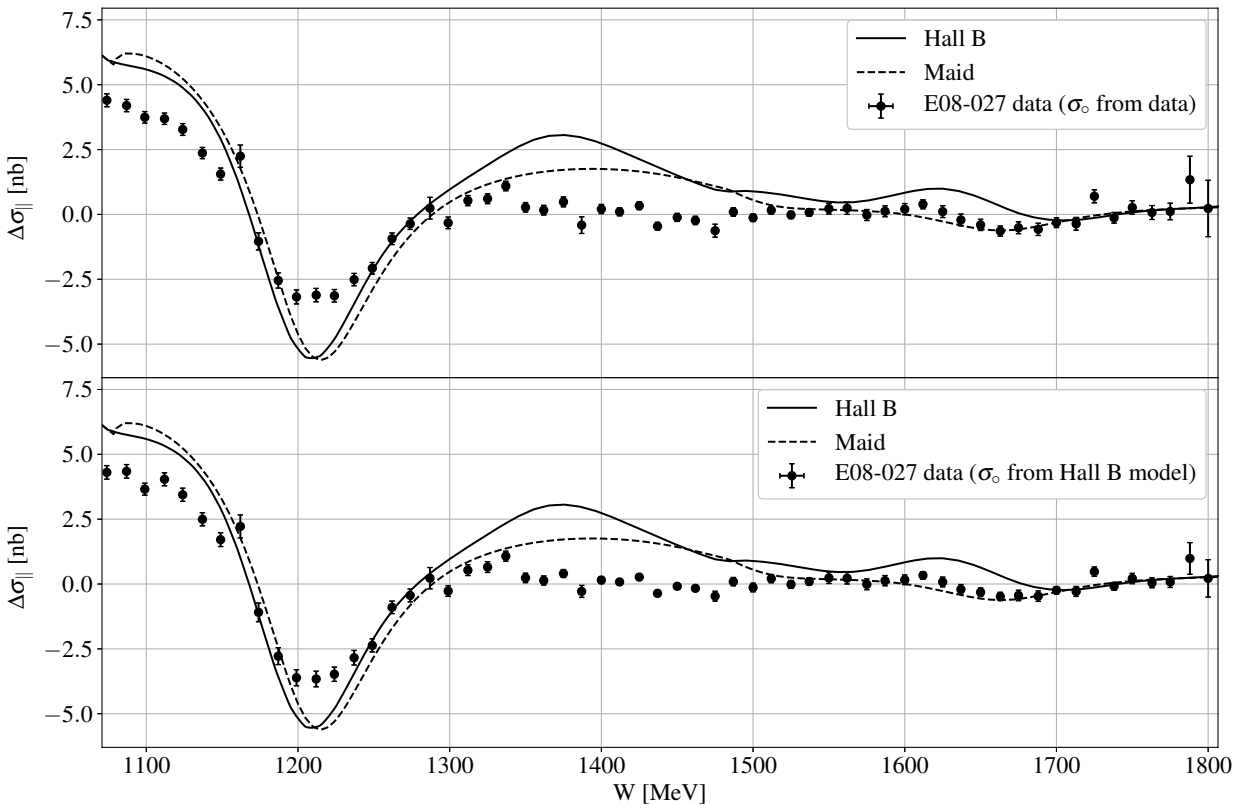

Figure 7-12: The polarized proton cross section for the 2.254 GeV beam energy, 5T Longitudinal target polarization setting using E08-027 cross section data (top) and the Hall B model (bottom) as the contribution for the unpolarized part.

materials radiation length which takes into account the physical thicknesses and densities of the materials that the electron passes through. A list of typical materials and their corresponding radiation lengths is shown in Tables 7.4 and 7.5.

In addition to the emission of a bremsstrahlung photon, other higher order loop corrections to the scattering process can occur. These loop corrections include vacuum polarizations, vertex corrections and electron self-energy. A list of all the higher order Feynman diagrams considered is shown in Figure 7-13. The final process that we consider is ionization. As the electron travels along the beam path it is possible for it to elastically scatter off of any materials in Table 7.4. This results in an energy loss on the order of a few MeV. The most probable energy loss due to

material	physical thickness (cm)	radiation thickness
Beryllium Window	0.3810	1.081E−03
Helium Bag	7.620	1.443E−05
Scat. Chamber	0.0178	2.002E−03
LN2 Shield	0.0038	4.284E−04
4K Shield	0.0013	1.462E−04
Target Nose	0.0127	1.428E−03
LHe in Nose	0.4369	6.716E−04
Target End Cap	0.0018	1.999E−04
LHe Target Cup	0.2914	4.479E−04
Solid NH3	0.3562	7.119E−03
total before	9.1229	1.354E−02

Table 7.4: Production target radiation thicknesses before scattering. Reproduced from [2].

material	physical thickness (cm)	radiation thickness
Solid NH3	0.3562	7.119E−03
LHe Target Cup	0.2914	4.479E−04
Target End Cap	0.0018	1.999E−04
LHe in Nose	1.969	3.027E−03
Target Nose	0.0127	1.428E−03
4K Shield	0.0013	1.462E−04
LN2 Shield	0.0038	4.284E−04
Scat. Chamber	0.0508	5.712E−03
Helium Bag	170.9	3.236E−04
Kapton Window	0.0254	8.889E−04
total after	173.6124	1.972E−02

Table 7.5: Production target radiation thicknesses after scattering. Reproduced from [2].

ionization is calculated as

$$E = E' - \Delta \tag{7.12}$$

$$\Delta = t \cdot x_\circ \left[\ln \frac{a t x_\circ}{E} + 1 - 0.5772 \right] \tag{7.13}$$

$$a = \frac{2\pi N \alpha^2}{m} \frac{Z}{A} \approx 0.154 \frac{Z}{A} \tag{7.14}$$

where t is the material thickness, $x_\circ$ is the radiation length of the material, E is the electron energy, α is the fine structure constant, N is Avagadro's number, m is the electron mass and Z and A are the atomic number and weight of the struck atom.

With all energy loss processes accounted for a fully radiated cross section model can be constructed

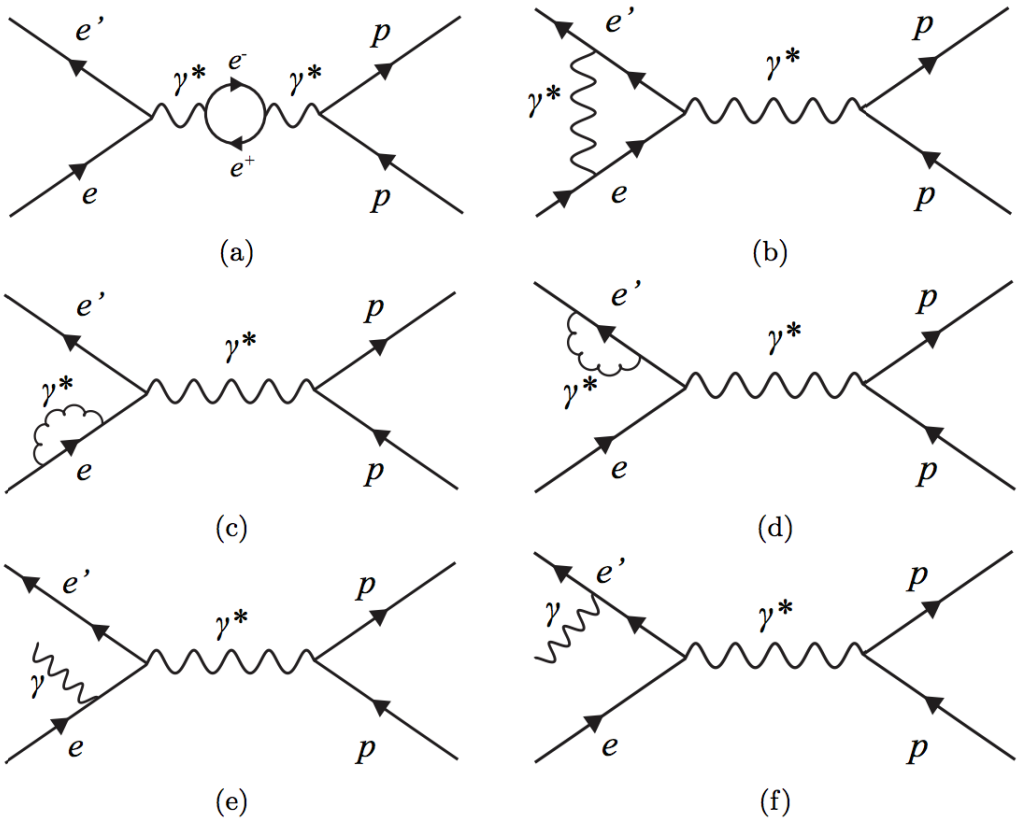

Figure 7-13: Next to leading order Feynman diagrams for internal radiative corrections. Processes include vacuum polarization (a), vertex correction (b), electron self energy (c,d) and Bremsstrahlung radiation (e,f). Reproduced from [12].

and used to correct the experimentally measured cross section. It is of note that these corrections are all 'unpolarized' as they do not consider polarized radiative effects in the *ep* scattering interaction. It was found that the difference between unpolarized and polarized radiative effects is negligible, so for simplicity only an unpolarized study was done and the results were applied to the polarized cross section.

The difference between the radiated and born polarized cross section models, as well as the radiatively corrected results to our polarized cross section, are shown in Figure 7-14. With radiatively corrected results we can move on to calculating the spin structure functions.

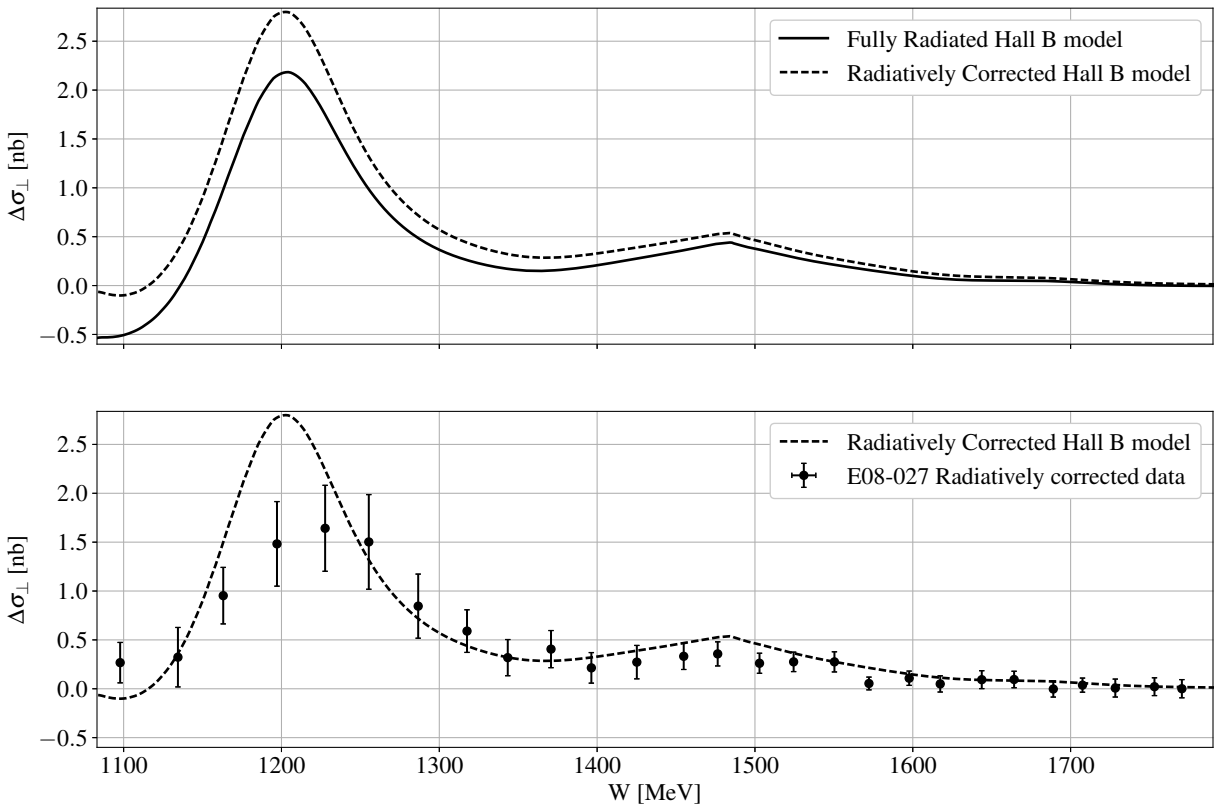

Figure 7-14: Radiated and born polarized cross section models in the kinematic region of the 2.254 GeV beam energy, 5T transverse target field setting (top) and the E08-027 radiatively corrected data for the same setting (bottom).

7.5 Spin Structure Functions

The spin structure functions, g_1 and g_2, can be calculated by taking a linear combination of Equations 2.30 and 2.31. Each of the two spin structure functions has a parallel and perpendicular contribution. For the E08-027 experiment data was only taken in either the perpendicular or parallel configuration for each Q^2 setting. To find $g_1(g_2)$ at a given setting we used the experimentally measured parallel(perpendicular) polarized cross section and $g_2(g_1)$ from the Hall B model:

$$g_1\left(x,Q^2\right) = K_1\left[\Delta\sigma_\parallel\left(1+\frac{1}{K_2}\tan\frac{\theta}{2}\right)\right] + g_2\left(x,Q^2\right)\frac{2}{yK_2}\tan\frac{\theta}{2}, \tag{7.15}$$

$$g_2\left(x,Q^2\right) = K_1\frac{y}{2}\left[\Delta\sigma_\perp\left(K_2+\tan\frac{\theta}{2}\right)\right] - g_1\left(x,Q^2\right)\frac{y}{2}, \tag{7.16}$$

$$K_1 = \frac{MQ^2}{4\alpha}\frac{y}{(1-y)(2-y)}, \tag{7.17}$$

$$K_2 = \frac{1+(1-y)\cos\theta}{(1-y)\sin\theta}. \tag{7.18}$$

The systematic contribution to the spin structure functions was adjusted accordingly from the addition of the Hall B model. The results for the three settings of this analysis are shown in Figures 7-16, 7-15 and 7-17.

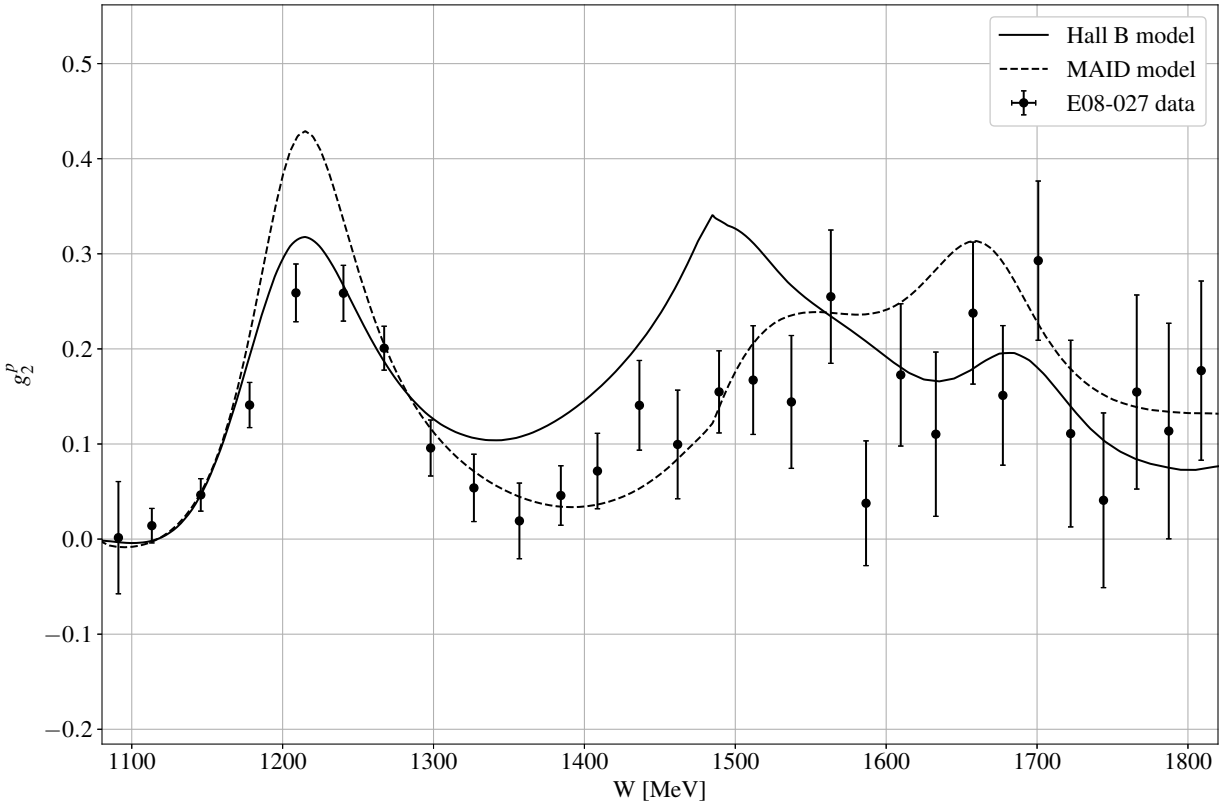

Figure 7-15: The spin structure function, g_2 for the 3.350 GeV beam energy, 5T Transverse target polarization setting. The Hall B model is used for the longitudinal contribution. Error bars are statistical only.

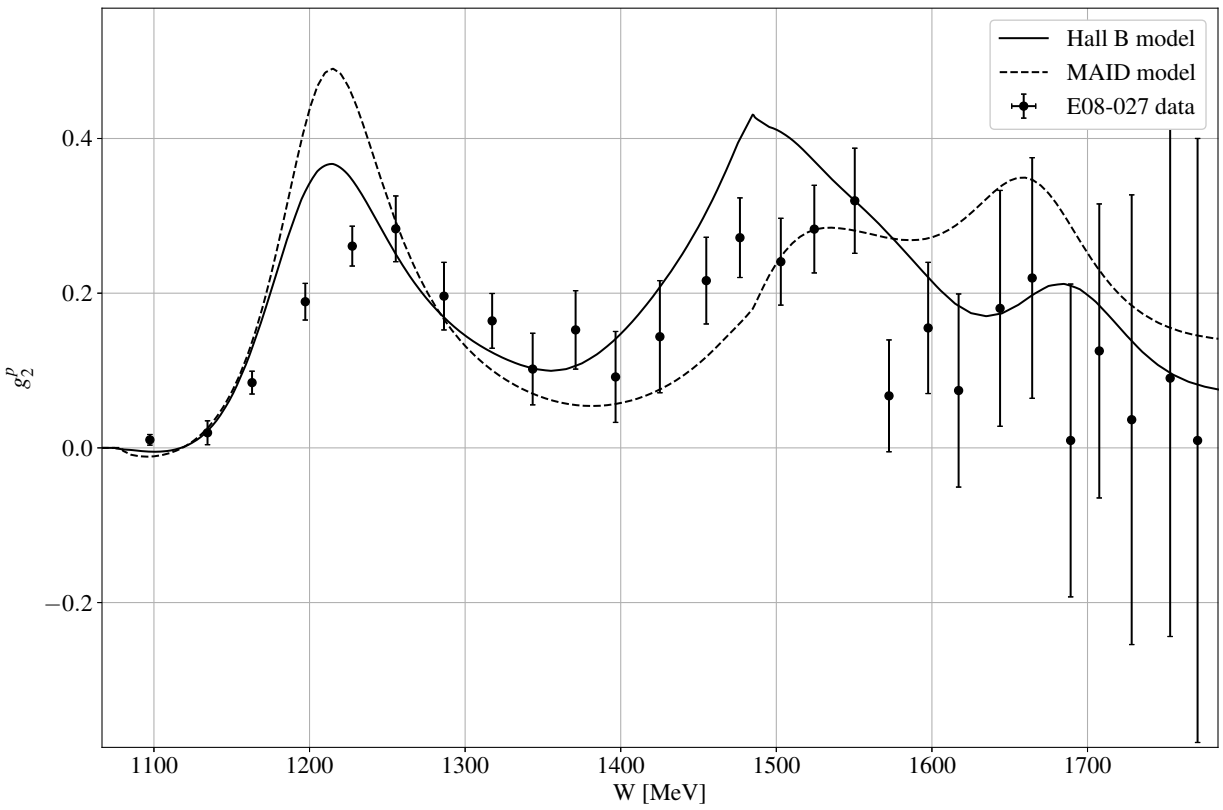

Figure 7-16: The spin structure function, g_2 for the 2.254 GeV beam energy, 5T Transverse target polarization setting. The Hall B model is used for the longitudinal contribution. Error bars are statistical only.

7.5.1 Constant Q^2 Extrapolation

The structure function data in Figures 7-16, 7-15 and 7-17 was taken over a wide kinematic range in invariant mass, W. Over this range the Q^2 value of the scattering interaction also varied. Before we can integrate the structure functions to find the corresponding moments for theory comparison we need to extrapolate the data to a constant Q^2 at each setting. This was done by selecting the Q^2 value of the data at the delta resonance, where the integration is most important, and generating

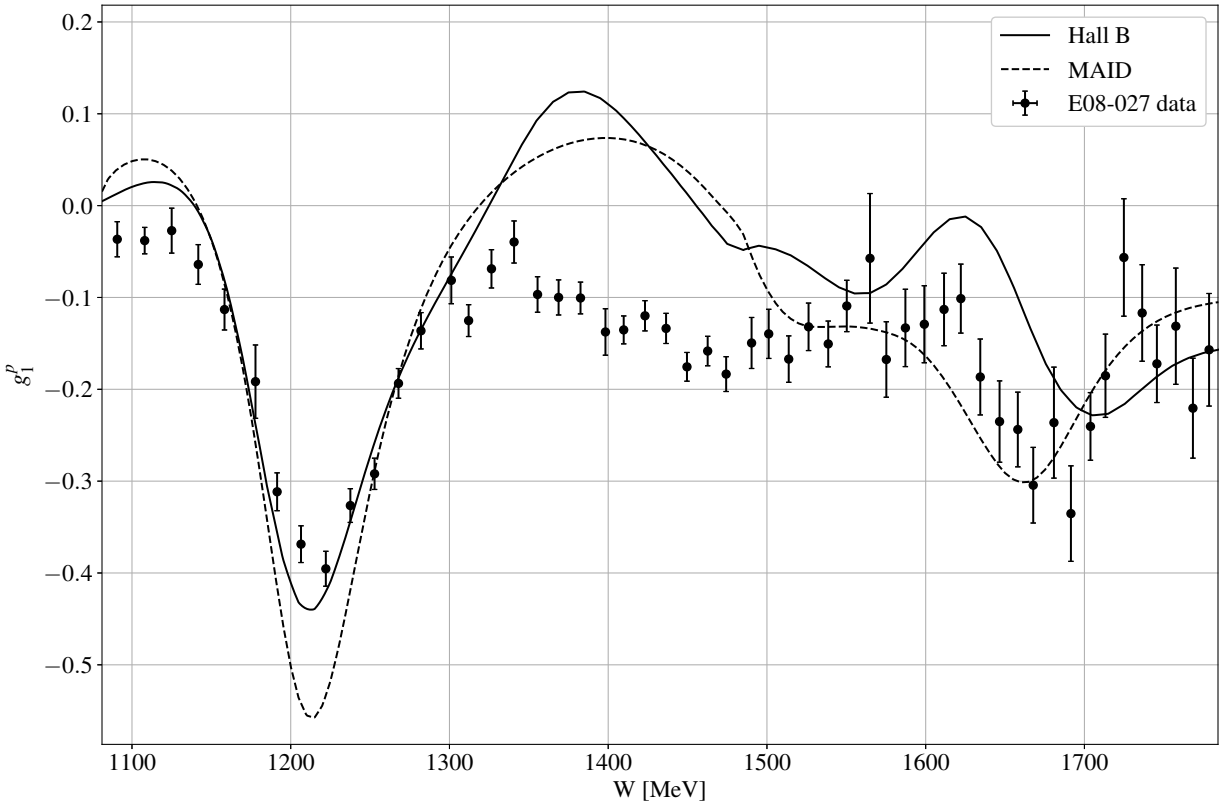

Figure 7-17: The spin structure function, g_1 for the 2.254 GeV beam energy, 5T Longitudinal target polarization setting. The Hall B model is used for the transverse contribution. Error bars are statistical only.

models to scale data around that area to the same Q^2.

$$g_{1,2}^{const} = g_{1,2}^{data} - \delta_{extrap.} \tag{7.19}$$

$$\delta_{extrap.} = g_{1,2}^{model}\left(x_{data}, Q^2_{data}\right) - g_{1,2}^{model}\left(x_{const}, Q^2_{const}\right) \tag{7.20}$$

The extrapolation had a small effect ($< 20\%$) on the transverse target field settings, due to a suppression of Q^2 variance from the target field. The longitudinal setting shows much larger Q^2 variance, with a correction on the order of 50%. The resulting Q^2 values for the three settings in

this analysis are shown in Table 7.6.

Setting	Extrapolated Q^2 [GeV^2]
3.350 GeV 5T Transverse	0.130
2.254 GeV 5T Transverse	0.086
2.254 GeV 5T Longitudinal	0.043

Table 7.6: Extrapolated Q^2 values.

7.6 Moments

With experimental results for g_1 and g_2 we can begin looking at contributions to various moments as discussed in Section 3. All of the moments of interest are x_{bj} weighted integrals of the structure functions. So before finding the moments we must translate the kinematic region from W, as shown in the previous section, to x, as defined in 2.1 and define a reliable integration method. The structure function, g_2, as a function of x_{bj} is shown in Figure 7-18. When performing the translation from W to x_{bj} the spacing between data is no longer constant. This is due to $x_{bj} \propto 1/\nu$. I used the geometric sum method written in the Simpsons integration routine to find the moments. This routine also has the convenience of carrying over the statistical uncertainty from the structure functions. To find the systematic uncertainty of the moments I deviate all values by $\pm 1\sigma$ in the systematic uncertainty of the structure functions and redo the integration. The spread in the resulting moments are treated as the final systematics.

7.6.1 Burkhardt-Cottingham Sum Rule

The full integration of the BC sum rule, as discussed in Section 3.2.2, is over the full range of x_{bj} from 0 to 1. To do this using experimental data the integral must be separated into three regions.

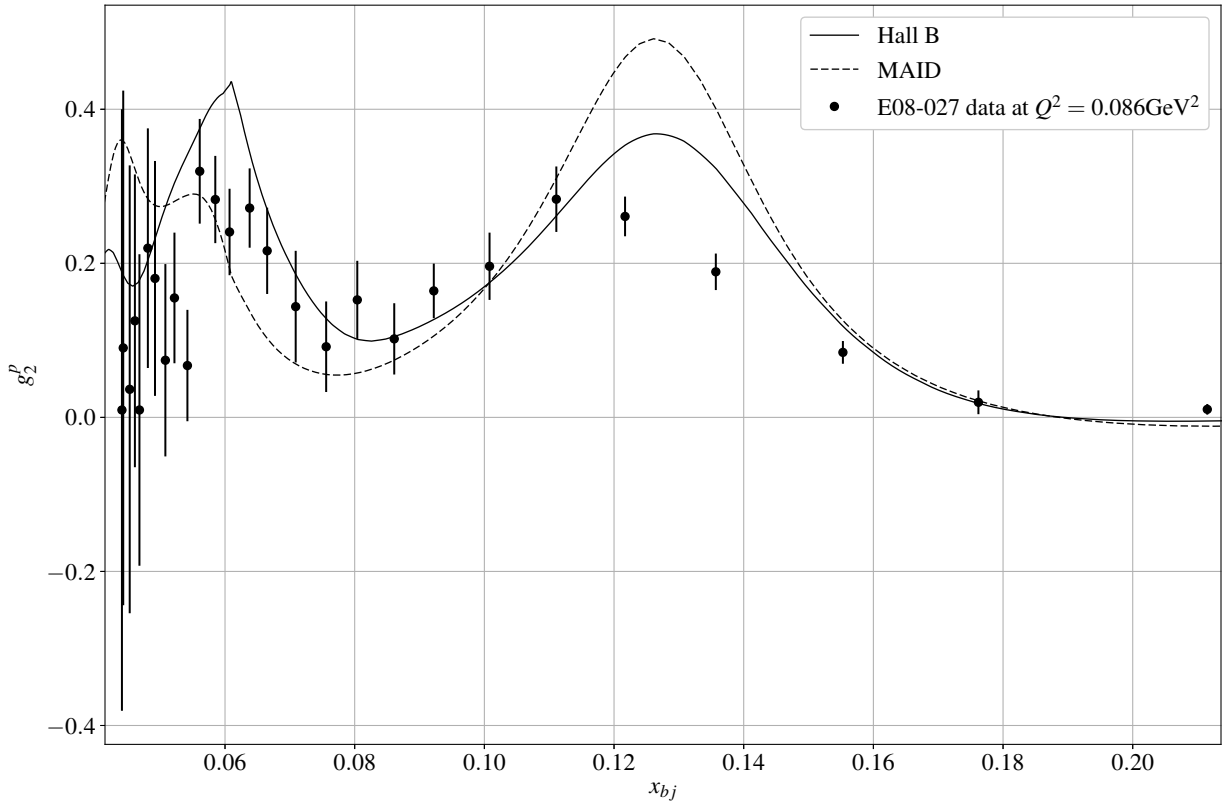

Figure 7-18: g_2^p vs. x_{bj} for $Q^2 = 0.086\text{GeV}^2$. Error bars are statistical only.

The Elastic Region

At elastic (above $x_{bj} \approx 0.25$) the integral of g_2 can be calculated using the well understood electric and magnetic form factors, G_E and G_M. The Arrington fit [62] is used to find the form factors at the Q^2 setting of our data.

$$G_E = \sum_{i=0}^{6} \left(\alpha_i Q^{2i}\right)^{-1} \tag{7.21}$$

$$G_M = \sum_{i=0}^{6} \left(\beta_i Q^{2i}\right)^{-1} \tag{7.22}$$

where α_i, β_i are the Arrington fit parameters of the electric and magnetic form factors, respectively. The integral of g_2 is then calculated using [23]

$$\Gamma_2 = \frac{\tau}{2}\mu_p G_M \left(\frac{G_E - \mu_p G_M}{1+\tau}\right) \tag{7.23}$$

where μ_p is the proton magnetic moment, $\tau = Q^2/4M_p^2$ and M_p is the proton mass.

The Resonance Region

This is the region in which experimental data was taken, sometimes called the measured region. The approximate kinematic coverage is $0.04 < x_{bj} < 0.24$ for experiment E08-027, as shown in Figure 7-18. The contribution to the BC sum rule in this region is calculated by simply taking the integral of the data using the Simpsons method discussed in the previous section.

The Deep Inelastic Region

The deep inelastic region, sometimes called the unmeasured part, is a convolution of model dependent parts and previously measured data. The kinematic coverage is from $0 < x_{bj} < x_{measured}$, where $x_{measured}$ is the lowest x_{bj} value measured experimentally. Due to the model dependence of the low x_{bj} region, and the significance of it's contribution to the integral at our Q^2 setting, great care was required in filling this region.

Several models were explored at the Q^2 setting of our experiment to determine what kind of sensitivity and uncertainty was introduced. The models included the Hall B model, MAID, and polarized parton distribution functions (PPDFs) from the AAC and GRSV collaborations [63]. The behavior of g_2 from each model in the low x_{bj} region is shown in Figure 7-19. It is interesting to note that the Hall B model in this region is simply a parameterized fit to the SLAC E155x data, which goes negative at low x_{bj}, while the PPDFs all remain positive. We note that the contribution from the unmeasured low x_{bj} part needs to be positive if the sum rule is to be satisfied. The approximate

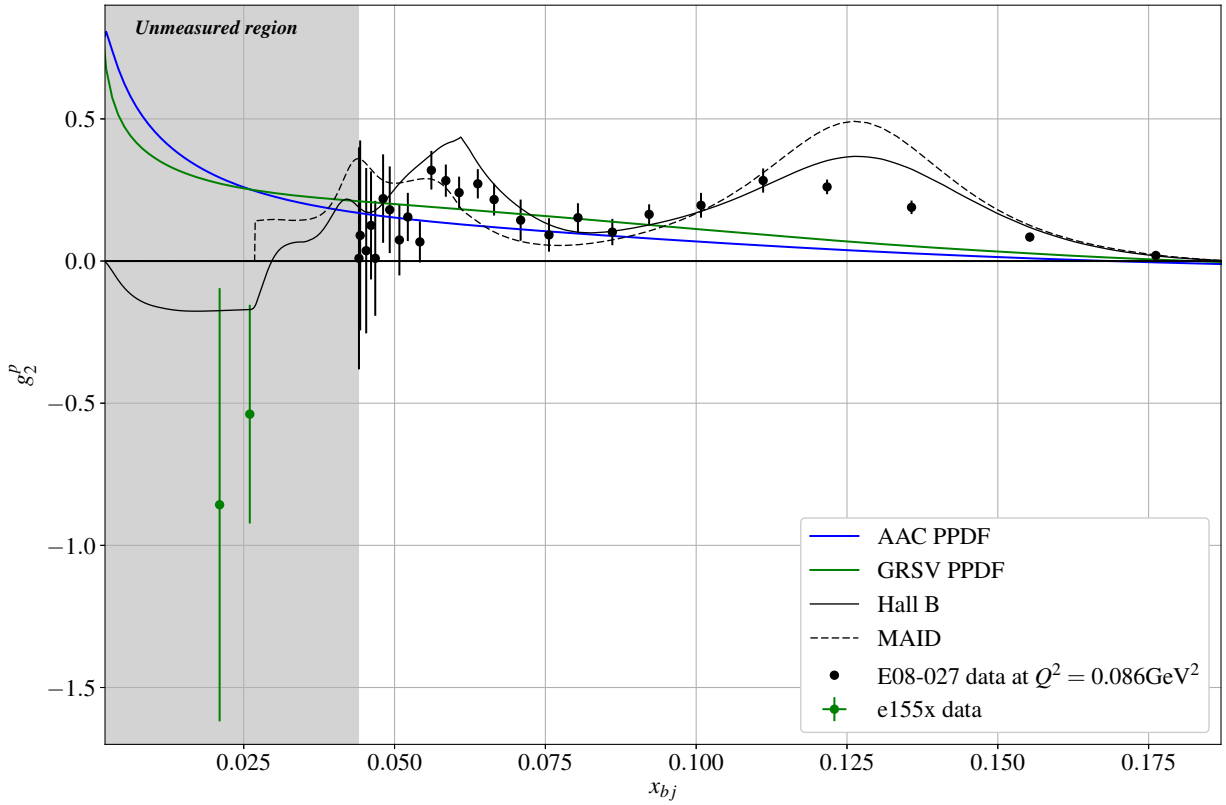

Figure 7-19: g_2 vs. x_{bj} from various models in the low x_{bj} region. Existing data at larger Q^2 from the SLAC E155x experiment as well as the E08-027 data is also shown. Note the Hall B model in this region is just a fit to the E155x data and MAID does not extend below $x_{bj} \approx 0.03$.

level of unmeasured contributions to the full integral are shown in Table 7.7.

Source	x_{bj} Integral ($0 < x_{bj} < x_{meas}$)	% contribution relative to measured region
Hall B Model	-0.003	12%
AAC PPDF	0.013	52%
GRSV PPDF	0.012	48%
Required	0.015	60%

Table 7.7: Unmeasured contribution to the BC Sum integral from various sources. Required represents the value for the unmeasured region needed if the BC Sum is satisfied at the (average) E08-027 Q^2 setting.

Summation and Result

With an accurate representation of g_2 in each region the BC sum can be calculated as

$$\Gamma_2 = \int_0^{x_{min}} g_{2_{model}}(x, Q^2) + \int_{x_{min}}^{x_{max}} g_{2_{measured}}(x, Q^2) + \Gamma_{2_{elastic}} \tag{7.24}$$

where $x_{min} \rightarrow x_{max}$ is the measured x_{bj} region of the experiment. Due to the sensitivity of $\Gamma_{2_{total}}$ to the unmeasured region, as discussed in the previous section, the result is left in terms of only the resonance and elastic contributions. By demanding the BC sum rule be satisfied in our measured kinematic regions we are able to make a definitive statement about the magnitude and sign of the unmeasured contribution, as shown in Table 7.8. Figure 7-20 shows the resonance contribution at

Q^2	$\Gamma_2^{meas.}$	$\Gamma_2^{el.}$	$\delta_{stat}^{tot.}$	$\delta_{sys}^{tot.}$
0.086 GeV^2	0.02170	-0.03624	0.0014	0.0031
0.130 GeV^2	0.02765	-0.04322	0.0022	0.0047

Table 7.8: Results for the E08-027 Γ_2 integration.

both Q^2 settings of this analysis, as well as the elastic contribution curve.

7.6.2 δ_{LT} Spin Polarizability

The δ_{LT} spin polarizability is calculated using

$$\delta_{LT}(Q^2) = \frac{16\alpha M^2}{Q^6} \int_0^{x_0} x^2 \left[g_1(x, Q^2) + g_2(x, Q^2) \right] dx, \tag{7.25}$$

as discussed in Section 3.3. The integral is done using the Simpsons integration method, similar to the method for calculating the BC sum rule, except that the integrand is weighted by x_{bj}^2, so contributions from the low x_{bj} region are suppressed.

The g_1 contribution to the integrand required a model prediction at the Q^2 values of the two transverse settings. For this purpose the Hall B model is used, where the g_1 prediction is relatively well understood, and an additional 15% systematic is introduced to account for variation between the

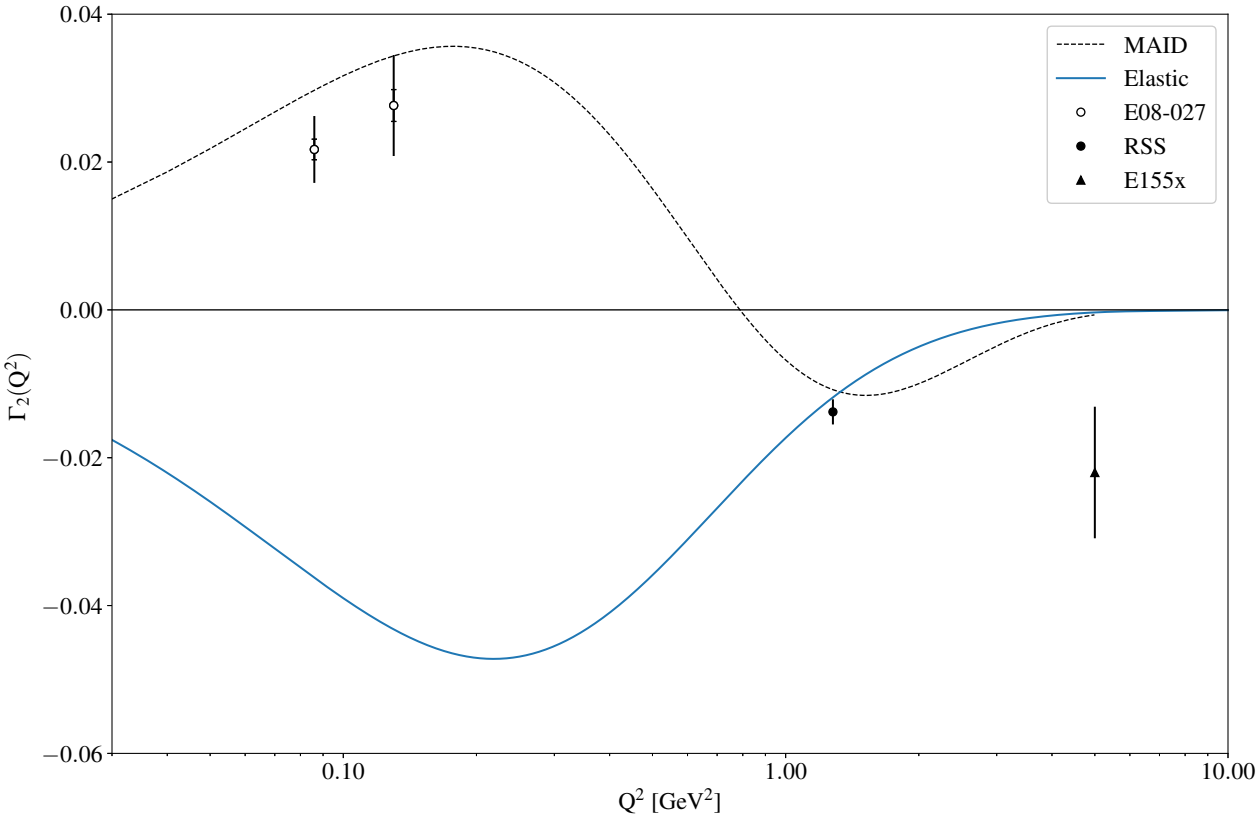

Figure 7-20: The resonance contribution to the BC sum rule for $Q^2 = 0.086$ GeV^2 and $Q^2 = 0.13$ GeV^2 with reference to the elastic contribution (blue) and the MAID model prediction for the resonance contribution (dashed). The RSS integral at $Q^2 = 1.279$ GeV^2 and the E155x integral at $Q^2 = 5$ GeV^2 are also shown.

Hall B model and existing g_1 data.

The δ_{LT} polarizability systematic is calculated by varying the g_2 input in the integrand by $\pm 1\sigma$ in the systematic of g_2 and recalculating the integral. The spread in the resulting moment is taken as the final systematic. Figure 7-21 shows the δ_{LT} polarizability for the two Q^2 settings of the experiment, along with theoretical predictions for their behavior. Numerical results are shown in Table 7.9. Reasonable agreement is seen between our measured polarizability and the Hall B and MAID models. At larger Q^2 agreement is also seen with the Pascalutsa calculation, but a 3σ divergence is seen at lower Q^2. Analysis is still underway by the collaboration to analyze the

Q^2	δ_{LT} [10^{-4} fm^4]	δ_{stat}	δ_{sys}
0.086 GeV^2	0.08143	0.0556	0.0336
0.130 GeV^2	0.08686	0.0633	0.0441

Table 7.9: Results for the E08-027 δ_{LT} spin polarizability measurement.

polarizability in the region between $0.025 < Q^2 < 0.075$ GeV^2.

It is worth noting the vast disagreement between the E08-027 measured polarizabilities and the Meissner calculation. The two theoretical predictions, called the Meissner and Pascalutsa calculations in this work, are performed in the framework of relativistic Baryon χ_{PT}, as discussed in Section 3. The main difference between the two calculations is in the treatment of the $\Delta(1232)$ resonance contribution. Data from this work favors the 'Delta expansion' result of the Pascalutsa calculation, with an upwards of 10σ disagreement with the Meissner curve. Lower Q^2 data from the E08-027 experiment will act to further drive this conclusion.

7.6.3 Higher Order Moments

Higher moments, in powers of x^n, can also be calculated for the previously discussed sum rules. The first higher order moment of interest is $d_2(Q^2)$. At large Q^2 the d_2 matrix element is related to the color polarizability which describes how the electric and magnetic fields of the proton respond to its spin. At low Q^2 the d_2 matrix element provides insight into the transition region between the perturbative and non-perturbative regions by quantifying the higher twist effects. d_2 is calculated as

$$\begin{aligned} d_2(Q^2) &= \int_0^1 x^2 \left[g_2(x,Q^2) - g_2^{WW}(x,Q^2) \right] dx \\ &= \int_0^1 x^2 \left[2g_1(x,Q^2) + 3g_2(x,Q^2) \right] dx \end{aligned}$$

where $g_2(x,Q^2)$ is the measured g_2 and g_2^{WW} is the twist-2 contribution of g_2, which is fully calculable from g_1 according to the Wandzura-Wilczek relation as discussed in Section 3.2.1. Due

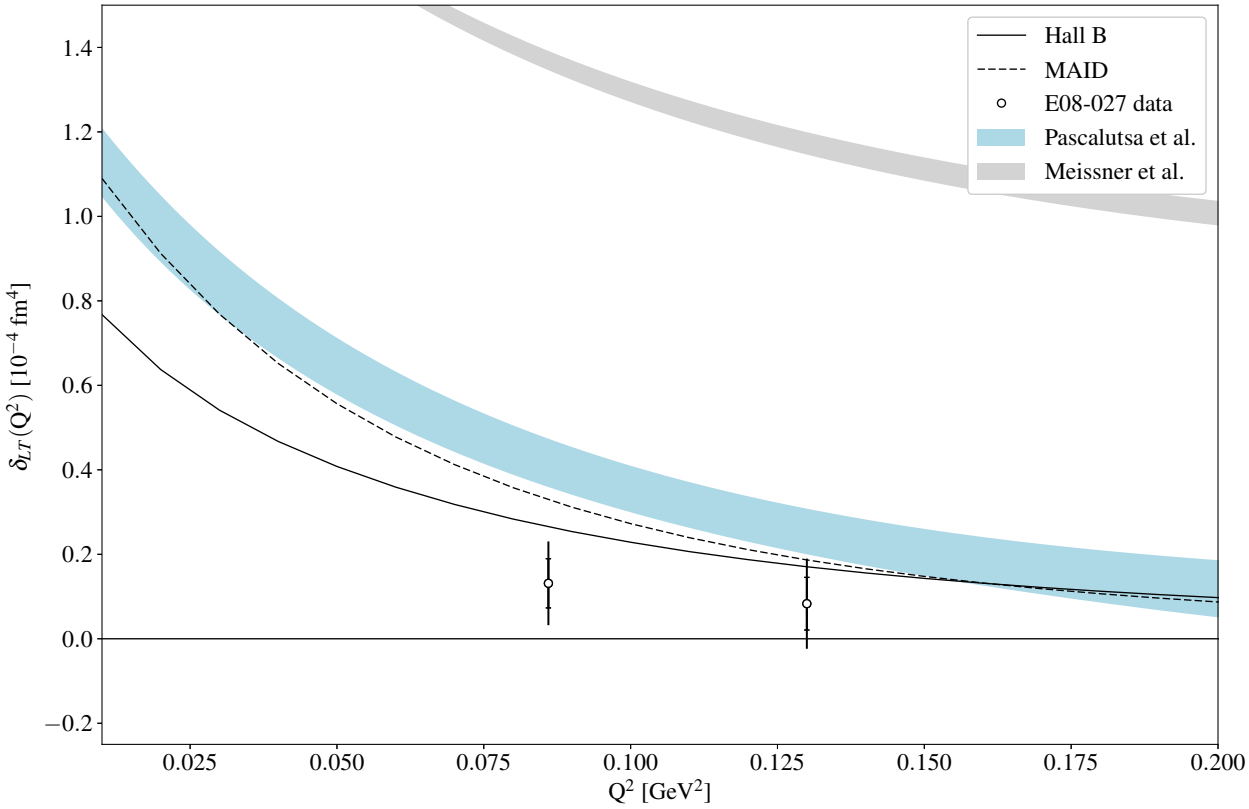

Figure 7-21: The δ_{LT} spin polarizability of the proton for $Q^2 = 0.086$ GeV^2 and $Q^2 = 0.13$ GeV^2. The blue and gray curves are the Pascalutsa and Meissner χ_{PT} calculations, respectively. Also shown are the MAID and Hall B model predictions.

to the x^2 weighting of the integrand in d_2 the low x region is suppressed. The Hall B model was used to estimate g_1 and a 15% systematic was added in quadrature with the systematic from the measured g_2 region. Numerical results for the integration are shown in Table 7.10. The results for

Q^2	d_2	δ_{stat}	δ_{sys}
0.086 GeV^2	0.00034	6.803e-5	6.641e-5
0.130 GeV^2	0.00102	2.676e-4	1.872e-4

Table 7.10: Results for the E08-027 d_2 integration.

d_2 at both Q^2 settings are shown in Figure 7-22.

The higher order moments of the proton spin polarizability are also of interest to look at. Carrying

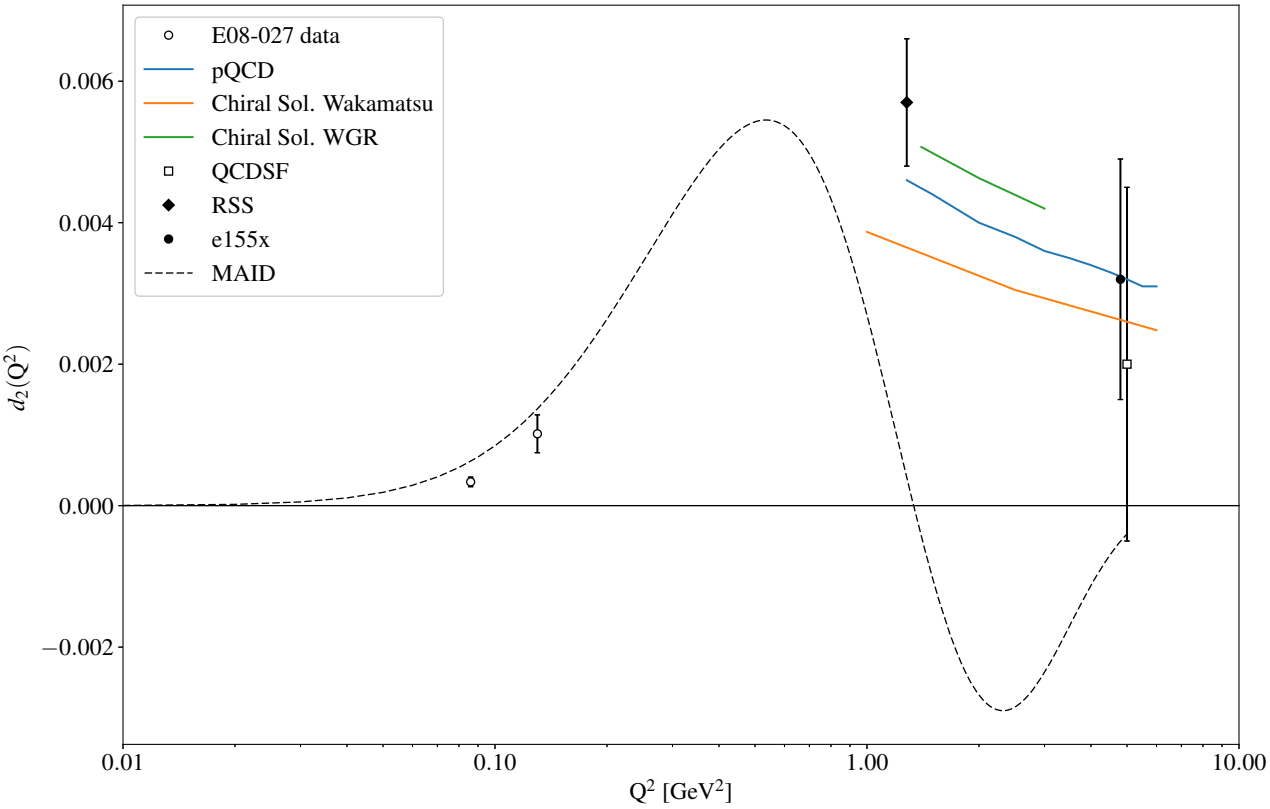

Figure 7-22: The d_2 sum rule for both Q^2 settings analyzed in this work. Contributions from g_1 and the low x_{bj} region are estimated using the Hall B model. Error bars are statistical only.

out the expansion of δ_{LT} to an additional term, as discussed in Section 3.3, gives

$$\delta^*_{LT} = \frac{64\alpha M^4}{Q^{10}} \int_0^{x_\circ} x^4 \left(g_1(x,Q^2) + g_2(x,Q^2)\right) dx. \tag{7.26}$$

This term has the convenience of an additional x^2 weighting in the integral, which further suppresses any contribution from the low-x region. Numerical results for δ^*_{LT} are shown in Table 7.11. Figure 7-23 shows the results for this higher order polarizability term. This represents the first ever measurement of the higher order moment for the δ_{LT} polarizability which may help to drive the necessity for theoretical calculations.

Q^2	δ^*_{LT} [10^{-4} fm^6]	δ_{stat}	δ_{sys}
0.086 GeV^2	0.03292	0.0285	0.0111
0.130 GeV^2	0.03266	0.0376	0.0151

Table 7.11: Results for the E08-027 δ^*_{LT} measurement.

7.7 Conclusions and Future Work

The goal of the E08-027 experiment was to extract the spin structure function, g_2, for the proton in five low Q^2 bins. This required both an accurately measured unpolarized cross section and a proton physics asymmetry at each setting. At the time of this writing the proton physics asymmetry for two settings has been fully analyzed. To incorporate the unpolarized cross section into these results we require a fully understood experimental acceptance and an accurately reproducible scattering angle. Work on both of these fronts continues by additional members of the collaboration.

The three lowest Q^2 settings require additional analysis work which is also underway by the collaboration. The results of which may help to fill in remaining questions about the behavior of the proton spin polarizability. Remaining work on these settings involves a detailed study and normalization procedure for yield drift discrepancies, as well as an acceptance and scattering angle study.

After careful study, it was determined that the Γ_2 integral at the E08-027 kinematics can not accurately be used to study the validity of the BC sum rule due to the large contribution from the DIS region. Instead, we demand the sum rule is satisfied which allowed us to make a definitive statement about the unmeasured contribution. It was found that the Hall B model is unsatisfactory at reproducing the g_2 structure function in the DIS region at low Q^2.

During this analysis we were able to place the first ever data for the proton spin polarizability. We found good agreement with the Hall B model everywhere but increasingly larger disagreement with χ_{PT} calculations as Q^2 decreased, although the data better reproduces the Pascalutsa calculation. We anticipate a more definitive statement on the polarizability with the analysis of the three low Q^2 points.

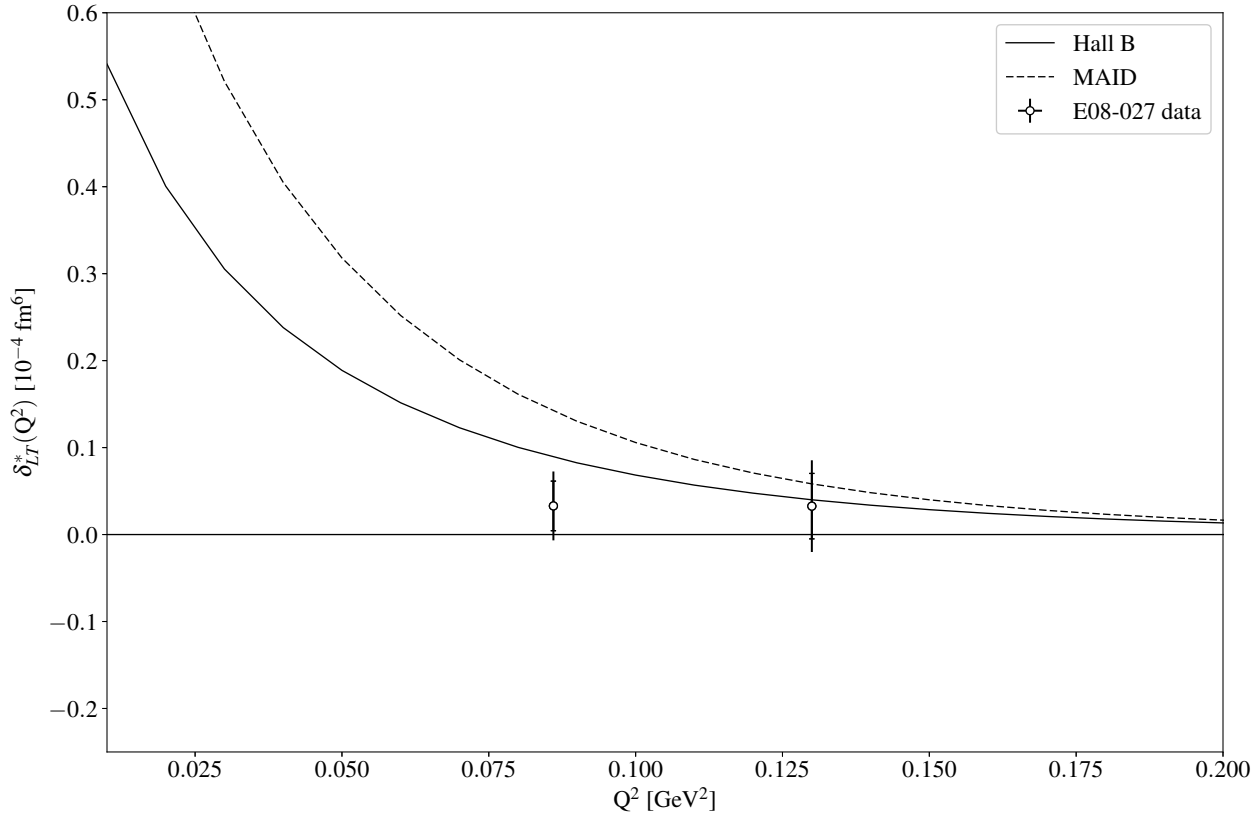

Figure 7-23: Higher order spin polarizability term, δ^*_{LT}, of the proton for $Q^2 = 0.086$ GeV^2 and $Q^2 = 0.13$ GeV^2. Also shown are the Hall B and MAID model predictions.

Appendices

Appendix A

Thermal Equilibrium Results

A total of 22 satisfactory thermal equilibrium (TE) measurements were done on 10 different target materials throughout the duration of experiment E08-027. The process of analyzing these measurements to extract target polarization information is discussed in detail in Section 5.5.
The following several pages contain the TE results used in determining the material calibration constants. Each figure contains two plots, the upper plot is the integrated area from the NMR curve over the course of the TE measurement while the lower plot is a monitor of the material temperature during the same time period. A linear fit (blue line) was done for each TE to determine if the material had sufficiently thermalized. If the slope was below a certain threshold value, determined by an upper limit on the uncertainty in the average area, then the range of measurements was deemed 'found' and the average area was calculated and used to find the corresponding calibration constant.
Several TE measurements (ex. 16, 51) were cut short due to time constraints, but the measurement was important in finding a calibration constant for the corresponding material. In these instances a larger systematic was placed on the resulting average due to the material temperature not fully thermalized.

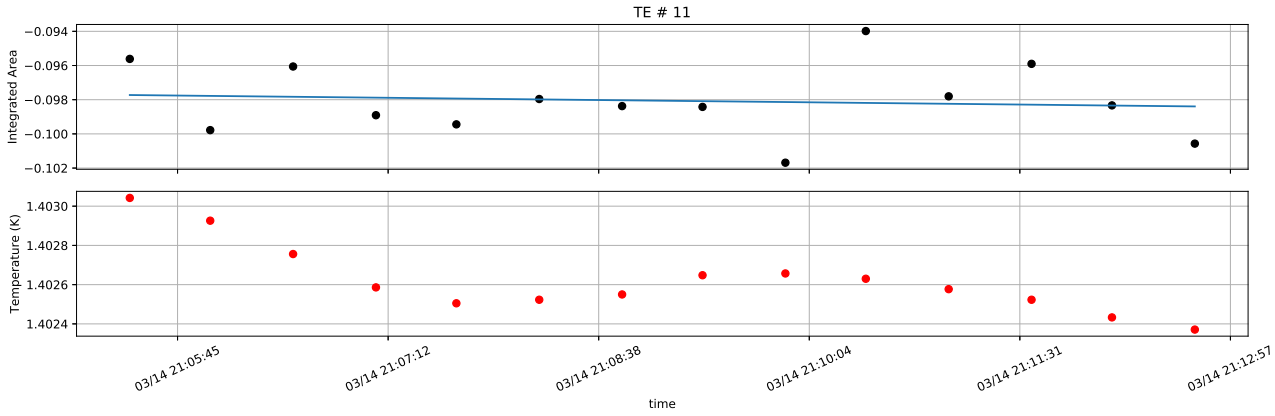

Figure A-1: Integrated area (top) and measured temperature (bottom) for thermal equilibrium measurement 11.

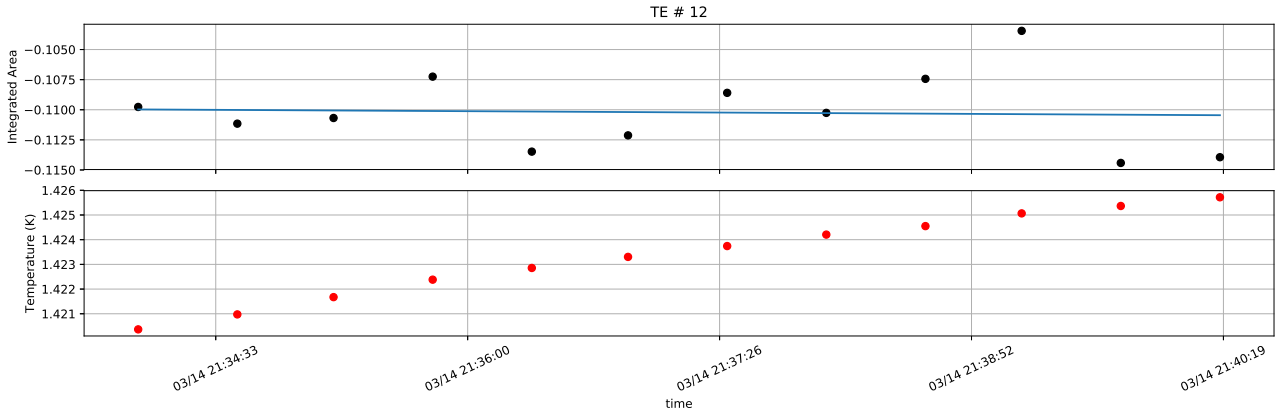

Figure A-2: Integrated area (top) and measured temperature (bottom) for thermal equilibrium measurement 12.

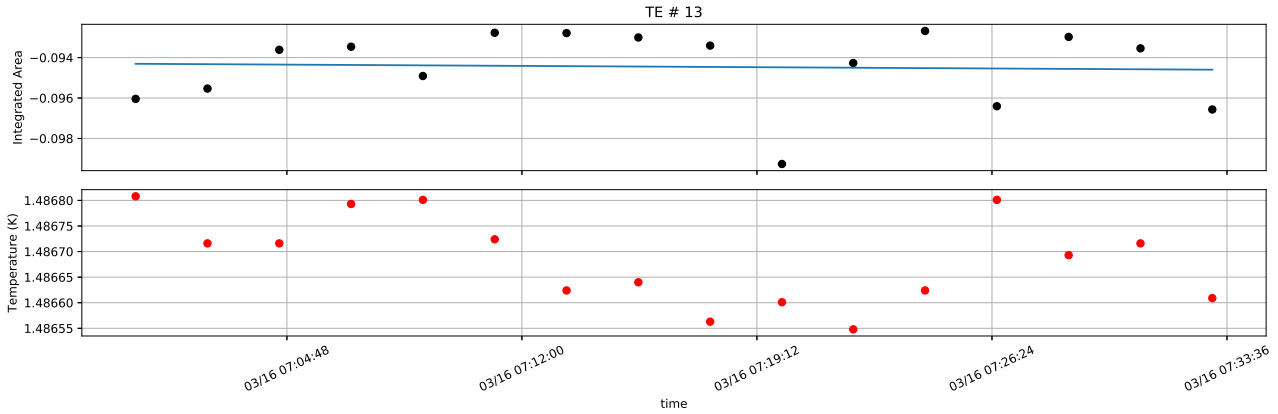

Figure A-3: Integrated area (top) and measured temperature (bottom) for thermal equilibrium measurement 13.

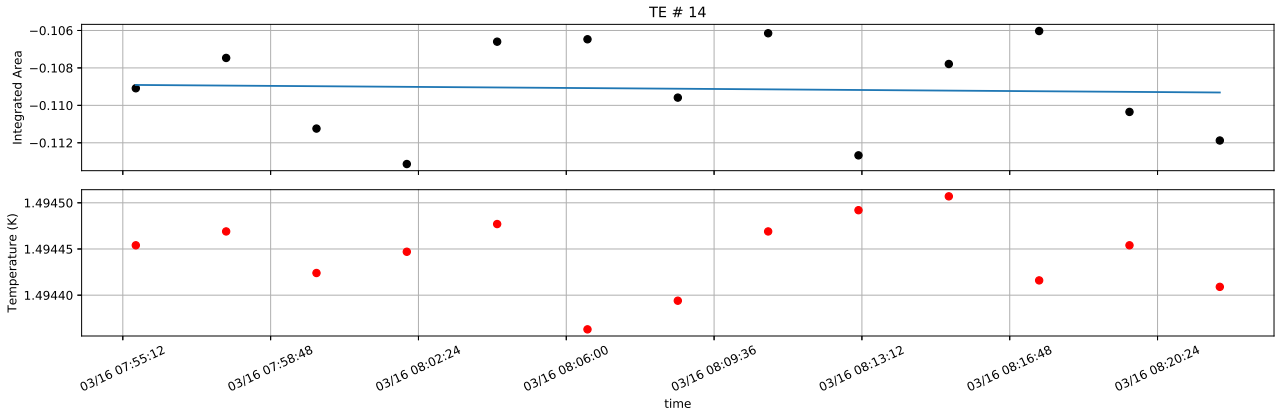

Figure A-4: Integrated area (top) and measured temperature (bottom) for thermal equilibrium measurement 14.

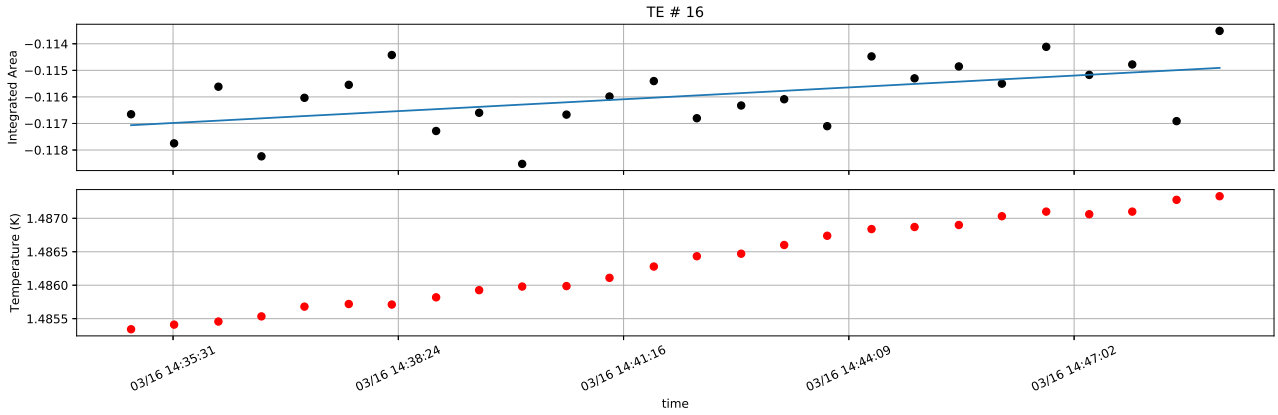

Figure A-5: Integrated area (top) and measured temperature (bottom) for thermal equilibrium measurement 16.

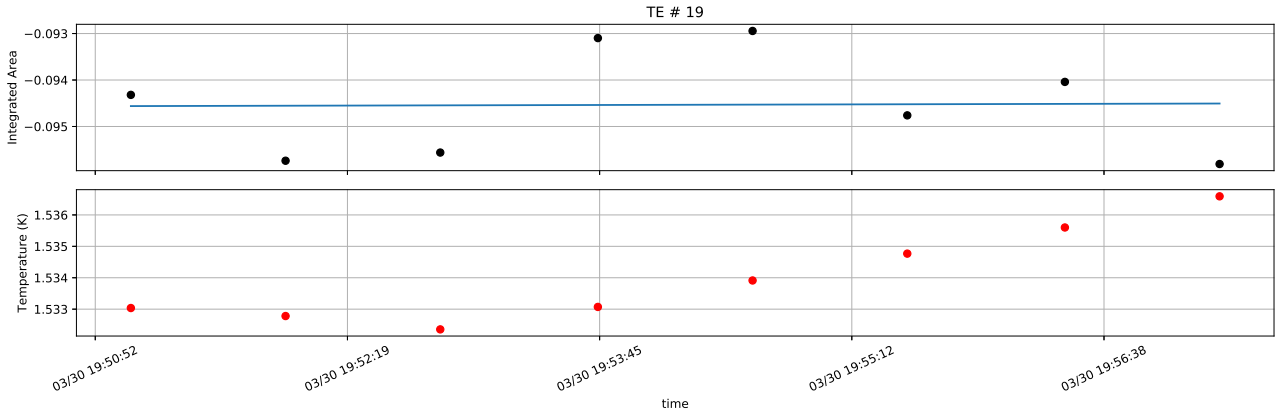

Figure A-6: Integrated area (top) and measured temperature (bottom) for thermal equilibrium measurement 19.

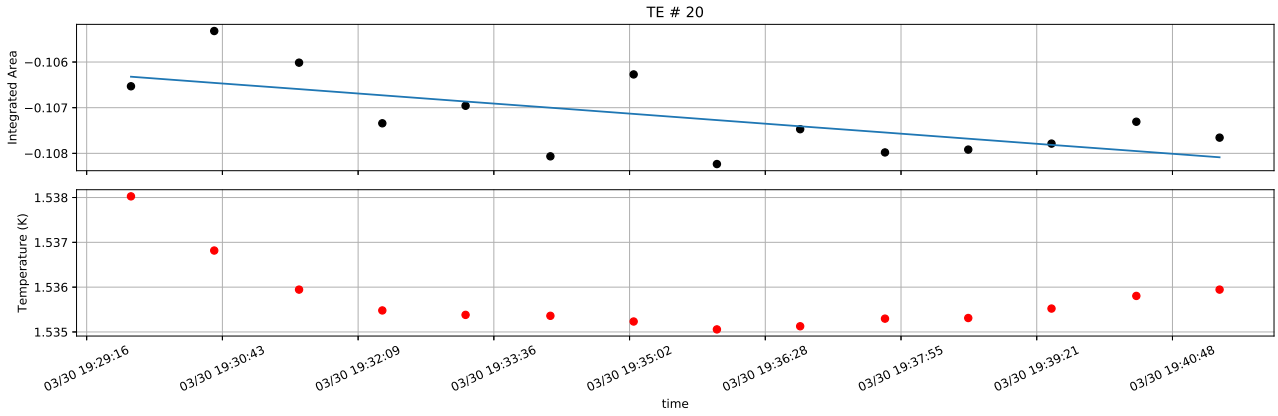

Figure A-7: Integrated area (top) and measured temperature (bottom) for thermal equilibrium measurement 20.

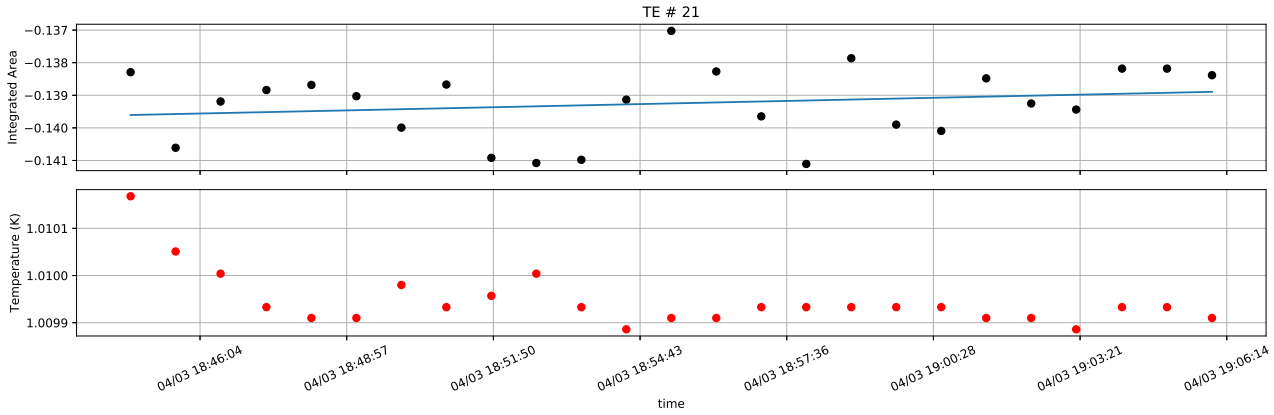

Figure A-8: Integrated area (top) and measured temperature (bottom) for thermal equilibrium measurement 21.

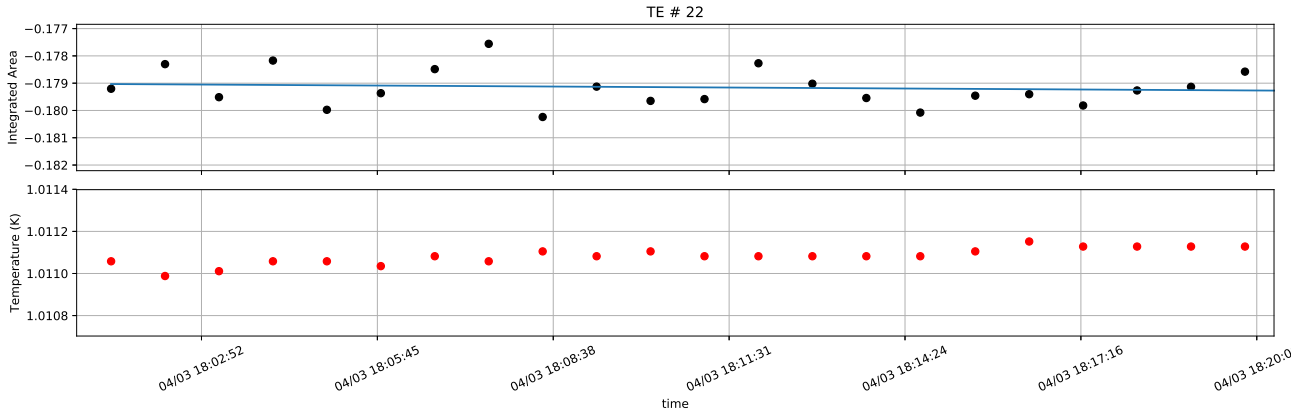

Figure A-9: Integrated area (top) and measured temperature (bottom) for thermal equilibrium measurement 22.

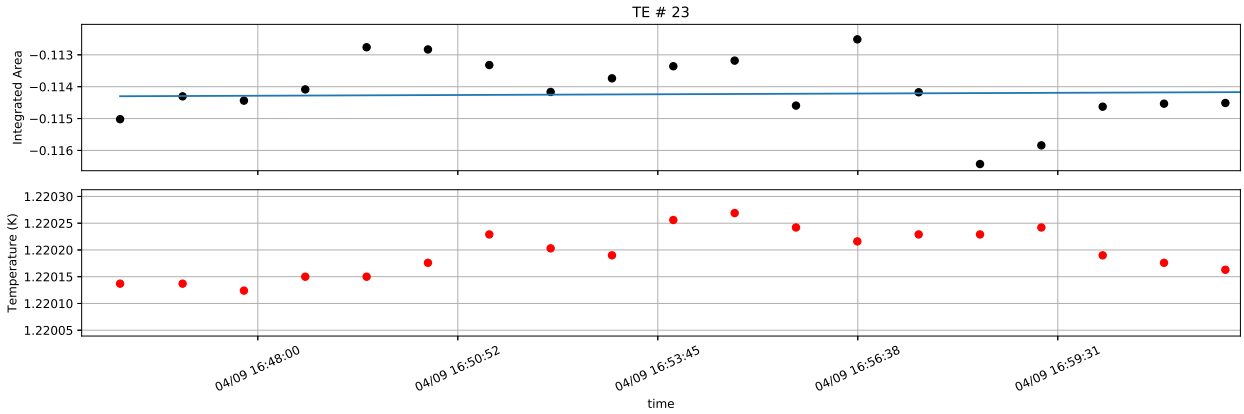

Figure A-10: Integrated area (top) and measured temperature (bottom) for thermal equilibrium measurement 23.

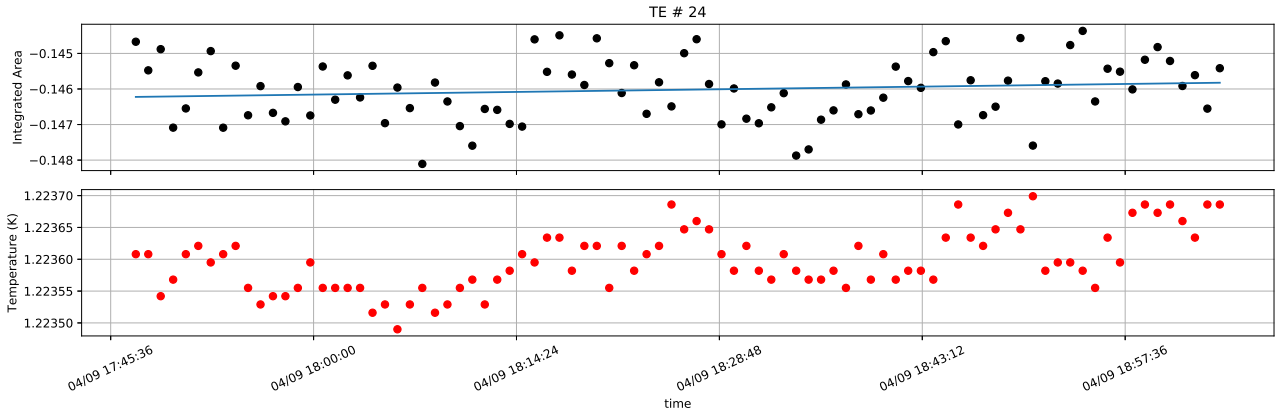

Figure A-11: Integrated area (top) and measured temperature (bottom) for thermal equilibrium measurement 24.

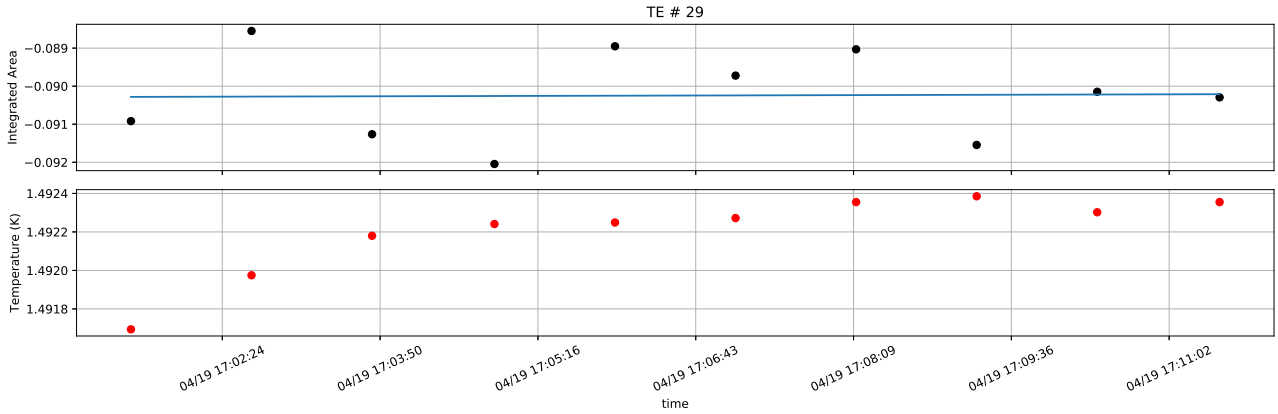

Figure A-12: Integrated area (top) and measured temperature (bottom) for thermal equilibrium measurement 29.

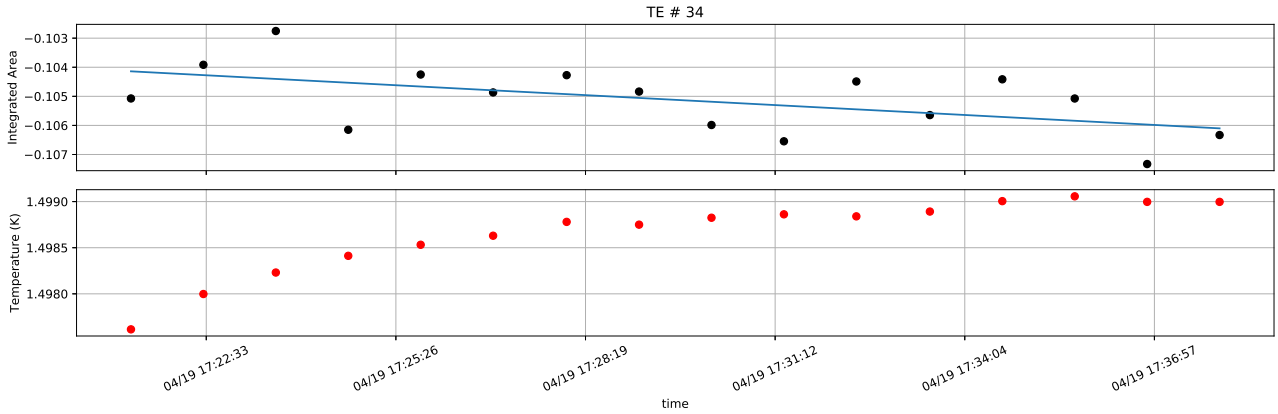

Figure A-13: Integrated area (top) and measured temperature (bottom) for thermal equilibrium measurement 34.

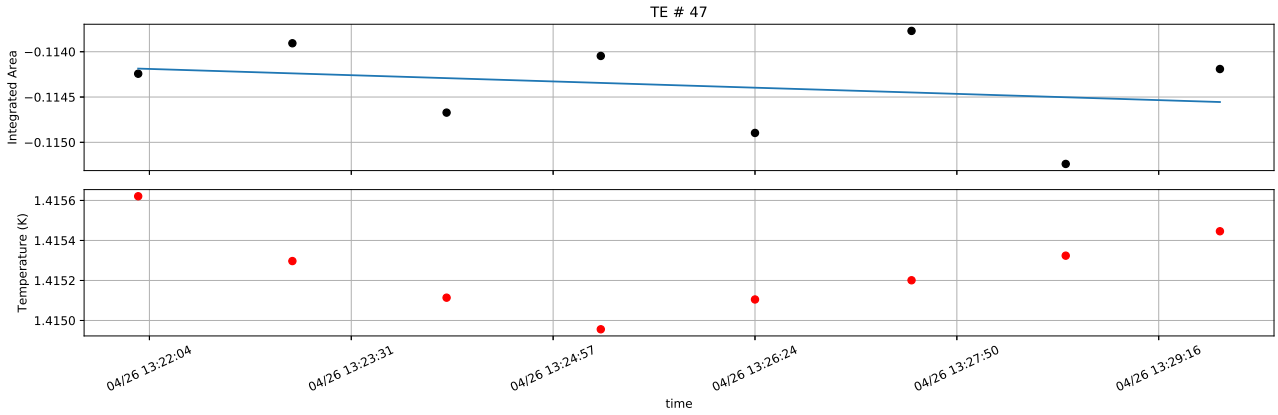

Figure A-14: Integrated area (top) and measured temperature (bottom) for thermal equilibrium measurement 47.

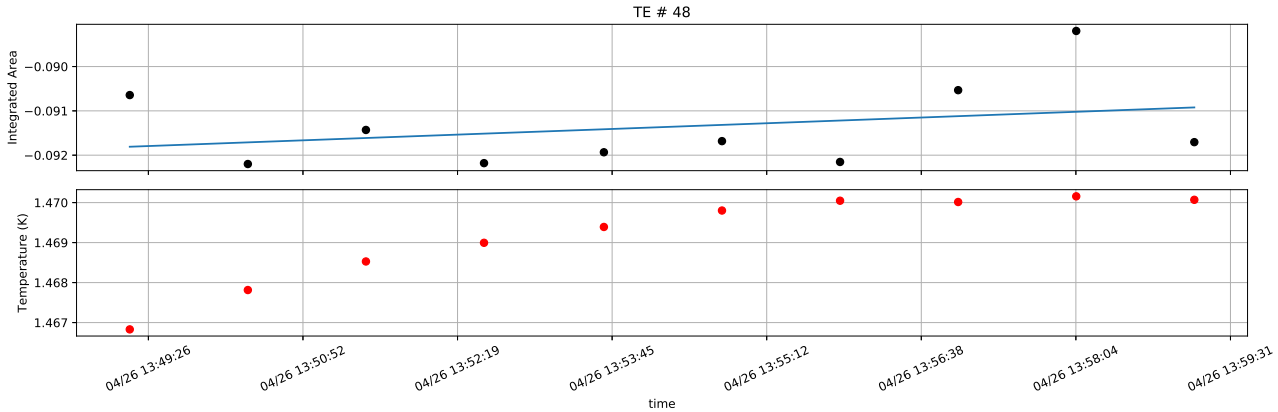

Figure A-15: Integrated area (top) and measured temperature (bottom) for thermal equilibrium measurement 48.

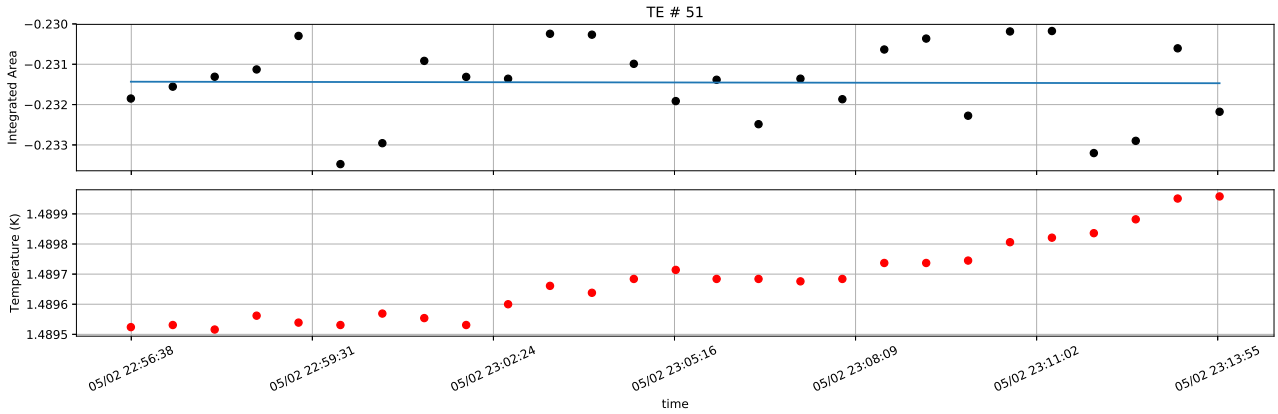

Figure A-16: Integrated area (top) and measured temperature (bottom) for thermal equilibrium measurement 51.

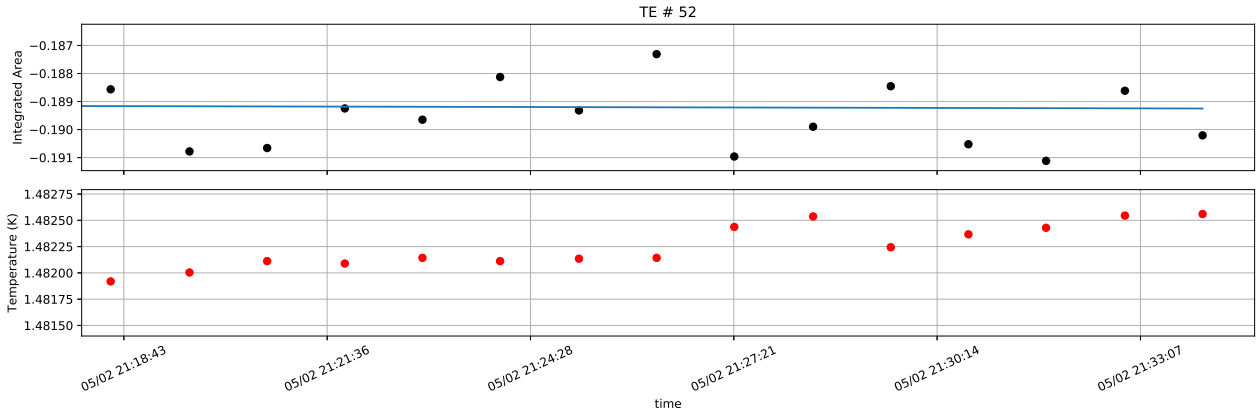

Figure A-17: Integrated area (top) and measured temperature (bottom) for thermal equilibrium measurement 52.

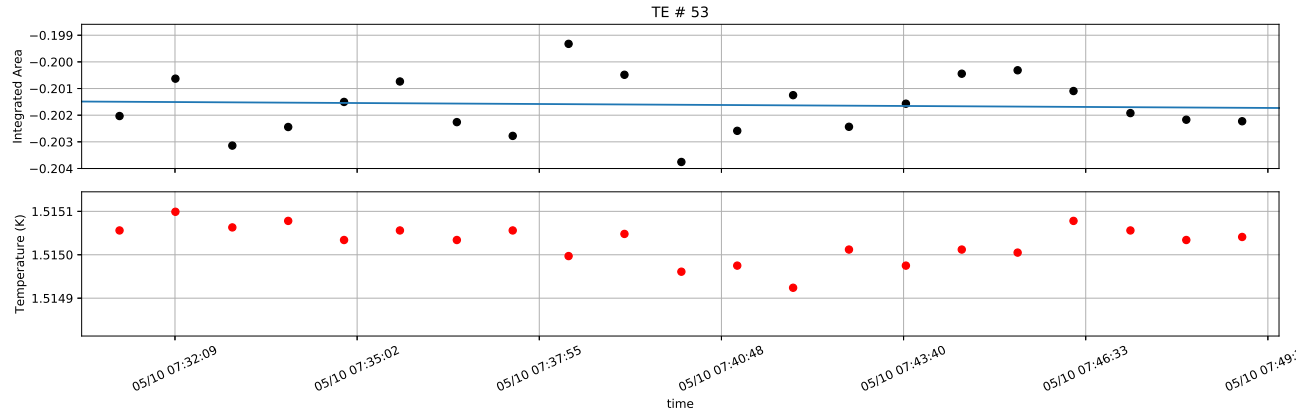

Figure A-18: Integrated area (top) and measured temperature (bottom) for thermal equilibrium measurement 53.

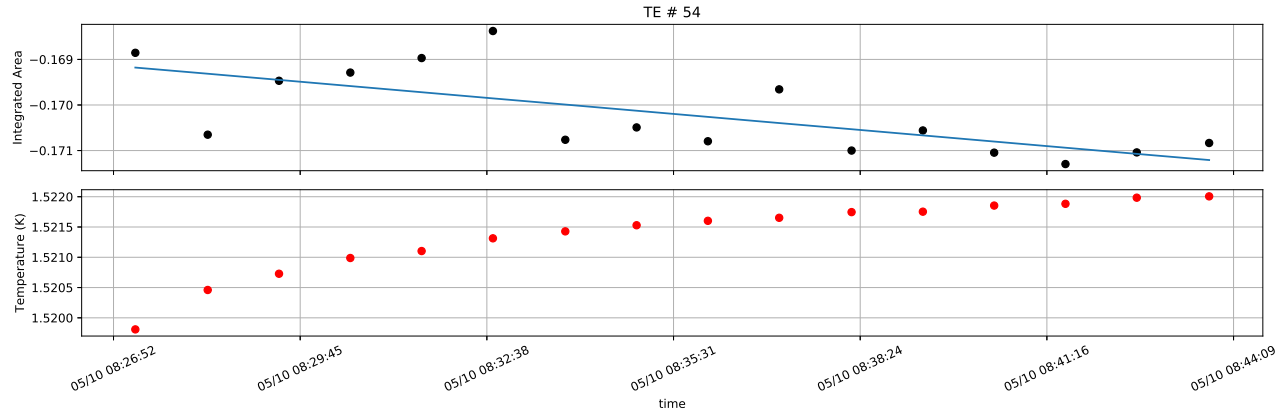

Figure A-19: Integrated area (top) and measured temperature (bottom) for thermal equilibrium measurement 54.

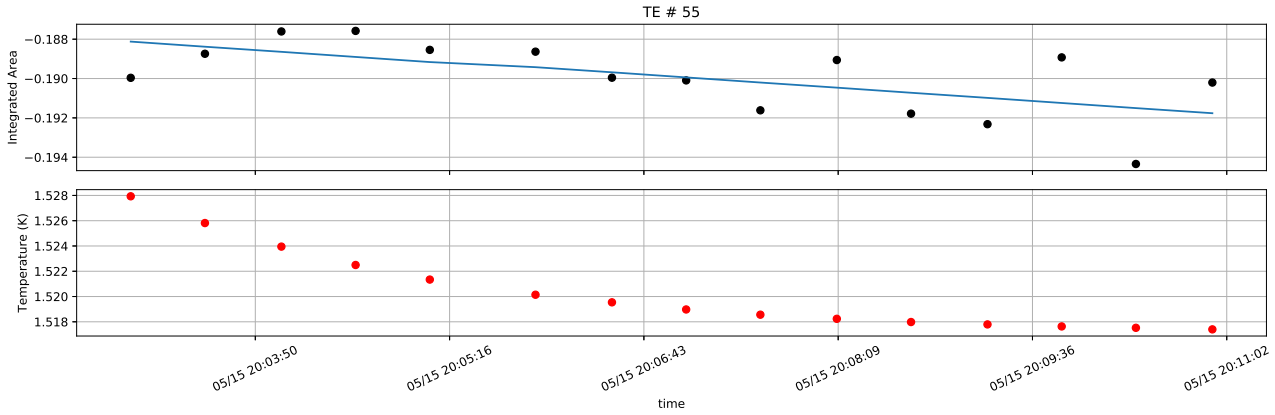

Figure A-20: Integrated area (top) and measured temperature (bottom) for thermal equilibrium measurement 55.

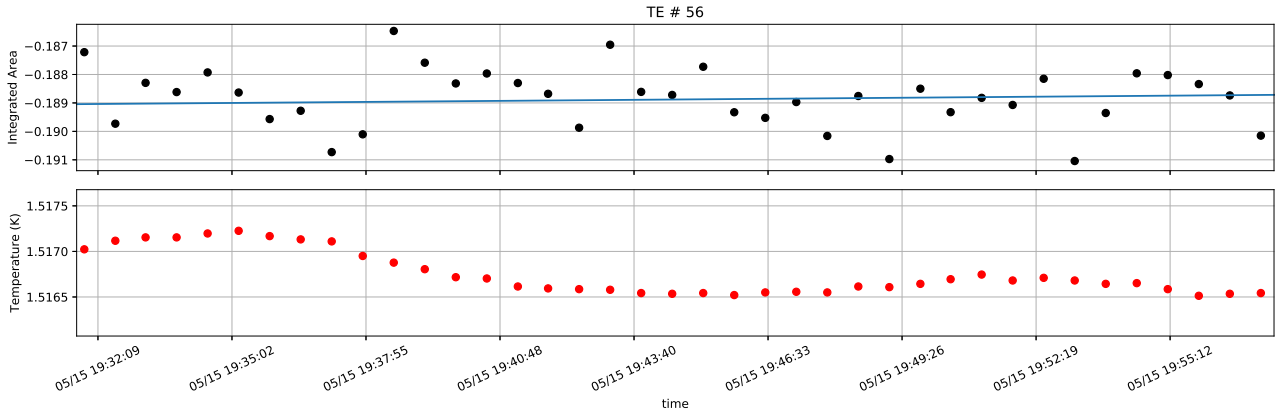

Figure A-21: Integrated area (top) and measured temperature (bottom) for thermal equilibrium measurement 56.

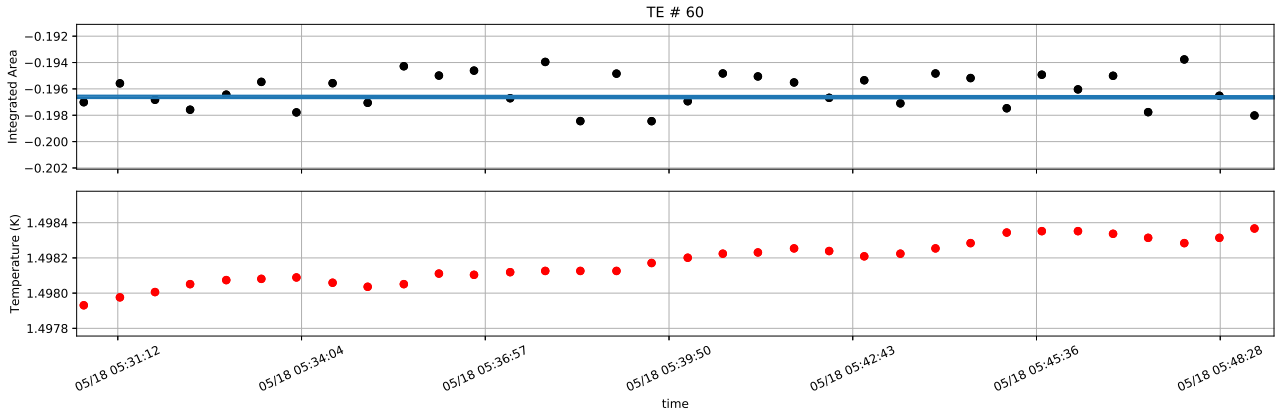

Figure A-22: Integrated area (top) and measured temperature (bottom) for thermal equilibrium measurement 60.

Appendix B

Packing Fraction Fits

After data quality selection and thermal equilibrium studies it was found that the packing fraction needed to be determined for 12 different target materials used throughout the duration of the g_2^p experiment. The ratio method (Section 6.8.3) became the method of choice in determining the final results. Below are the fits used for each material.

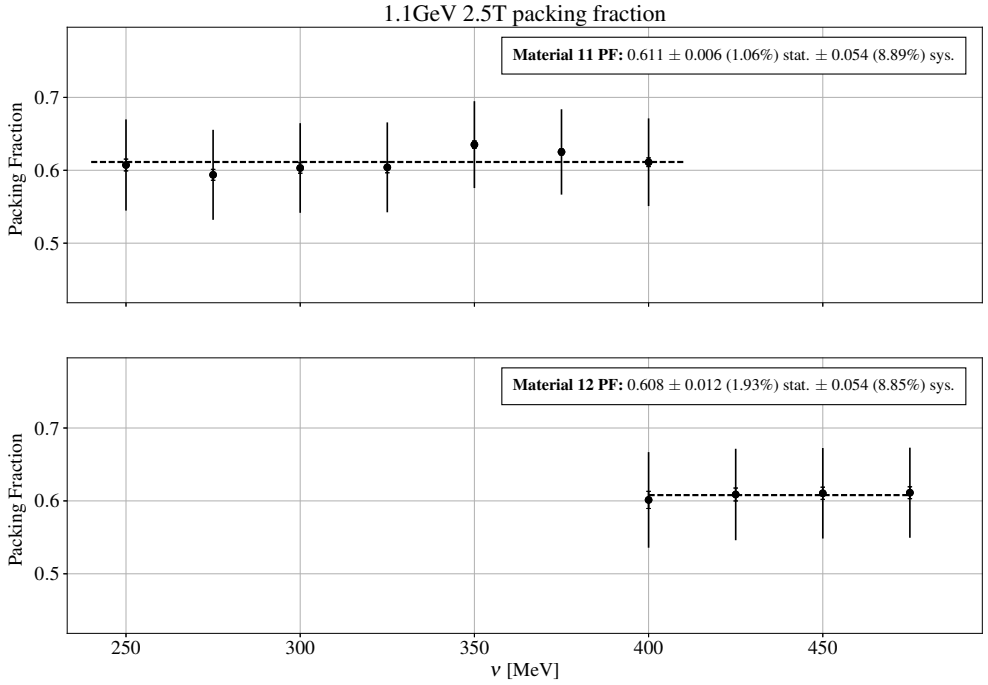

Figure B-1: PF fit result for material 11 (top) and 12 (bottom) at 1.1GeV 2.5T Transverse.

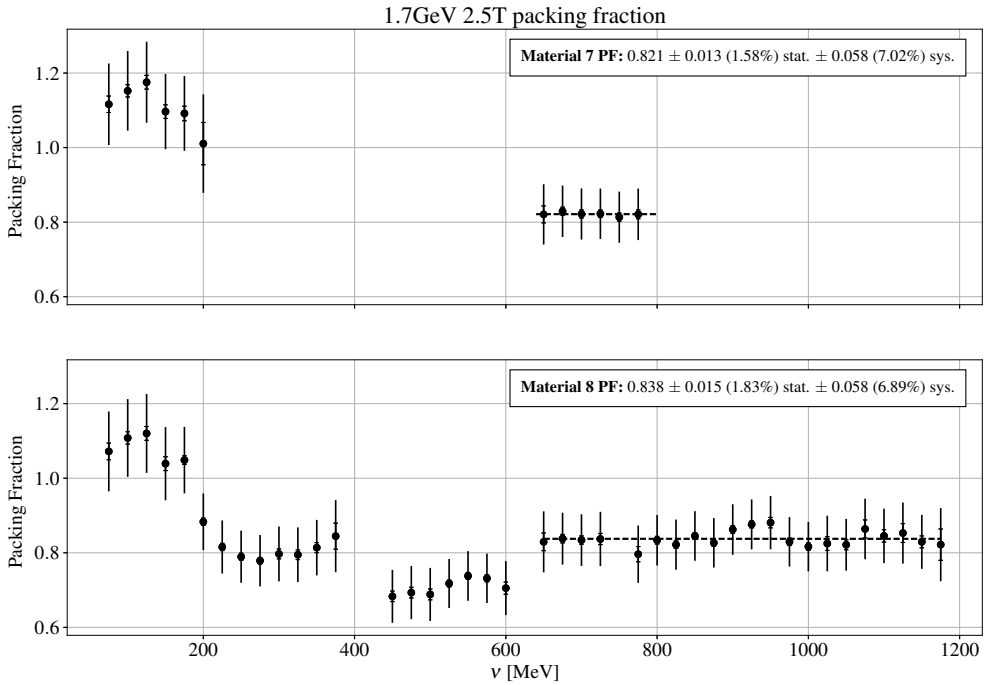

Figure B-2: PF fit result for material 7 (top) and 8 (bottom) at 1.7GeV 2.5T Transverse.

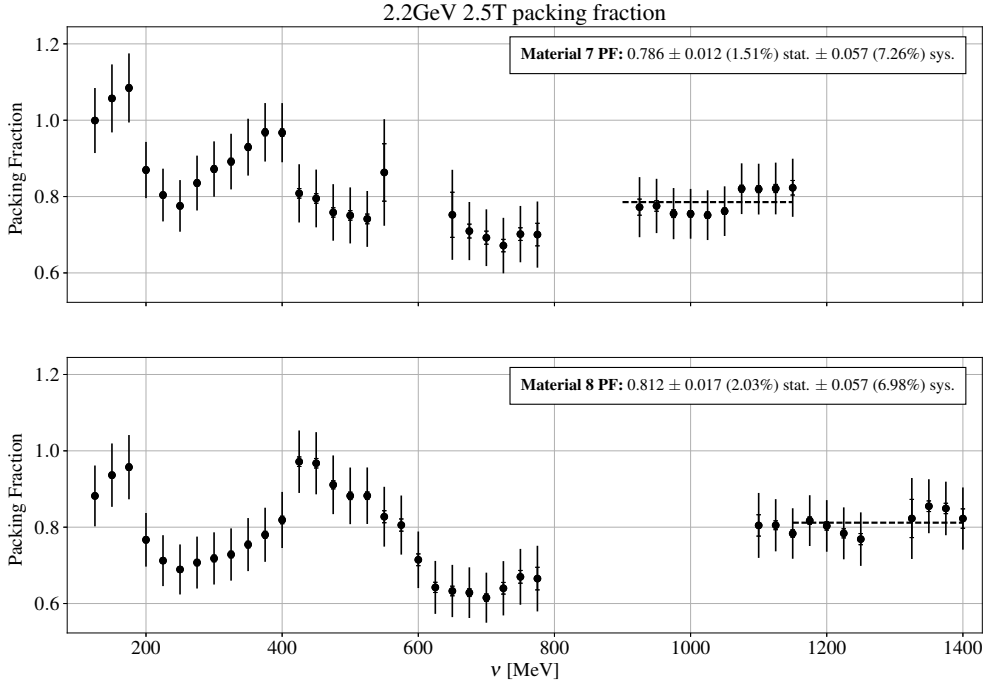

Figure B-3: PF fit result for material 7 (top) and 8 (bottom) at 2.2GeV 2.5T Transverse.

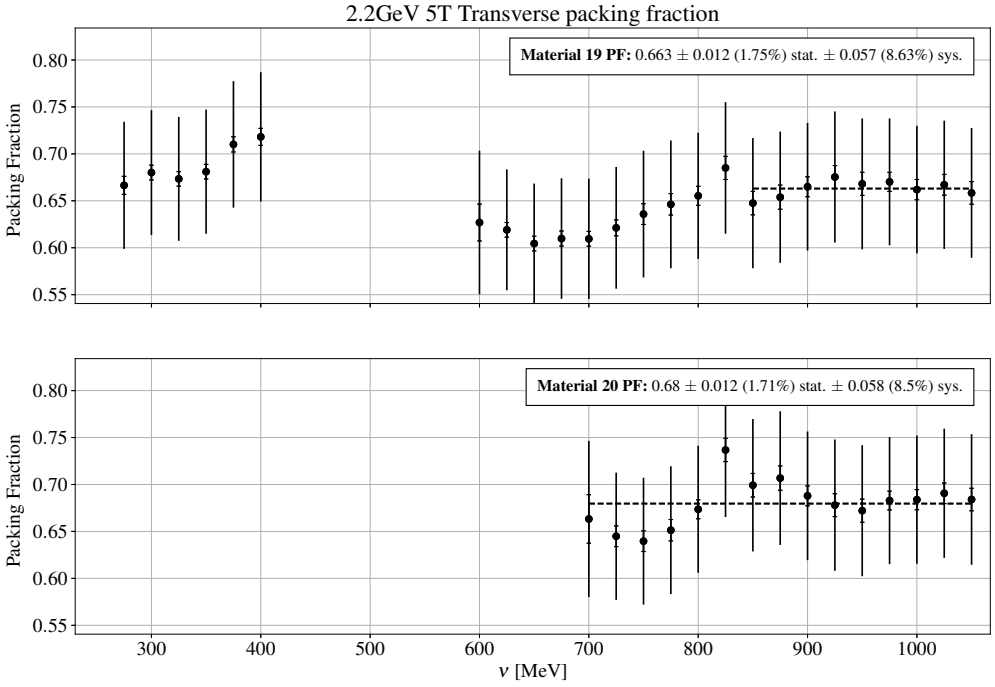

Figure B-4: PF fit result for material 19 (top) and 20 (bottom) at 2.2GeV 5T Transverse.

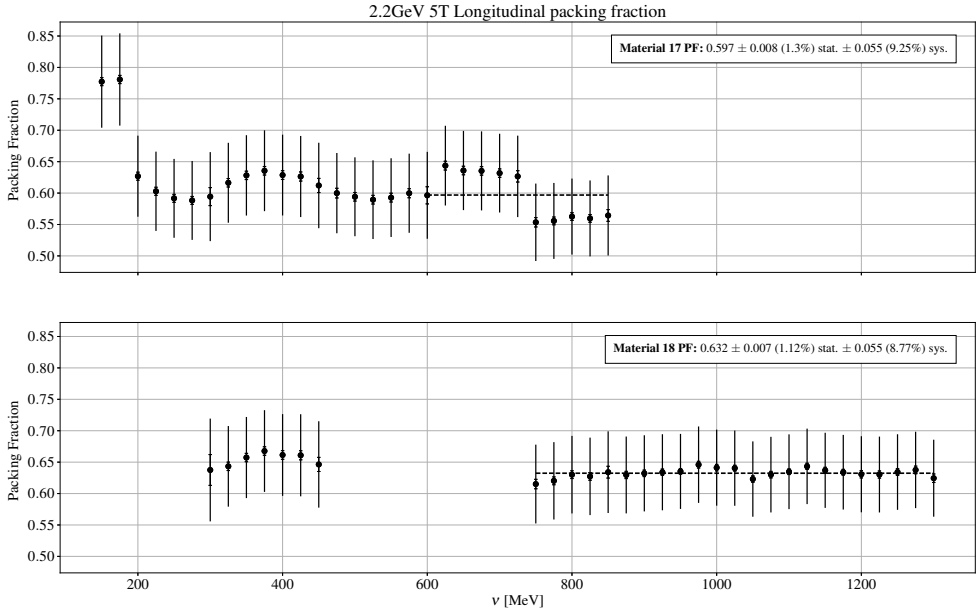

Figure B-5: PF fit result for material 17 (top) and 18 (bottom) at 2.2GeV 5T Longitudinal.

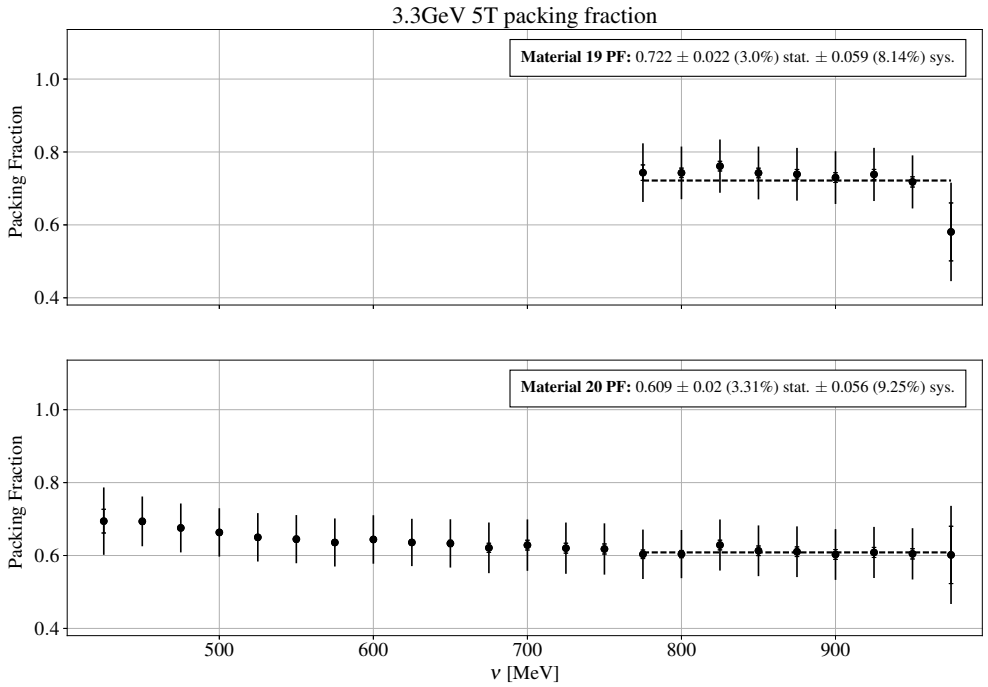

Figure B-6: PF fit result for material 19 (top) and 20 (bottom) at 3.3GeV 5T Transverse.

Appendix C

Material Dilutions

Below are the dilution results for all channels. The method for calculating the dilution is described in detail in Section 6.9.

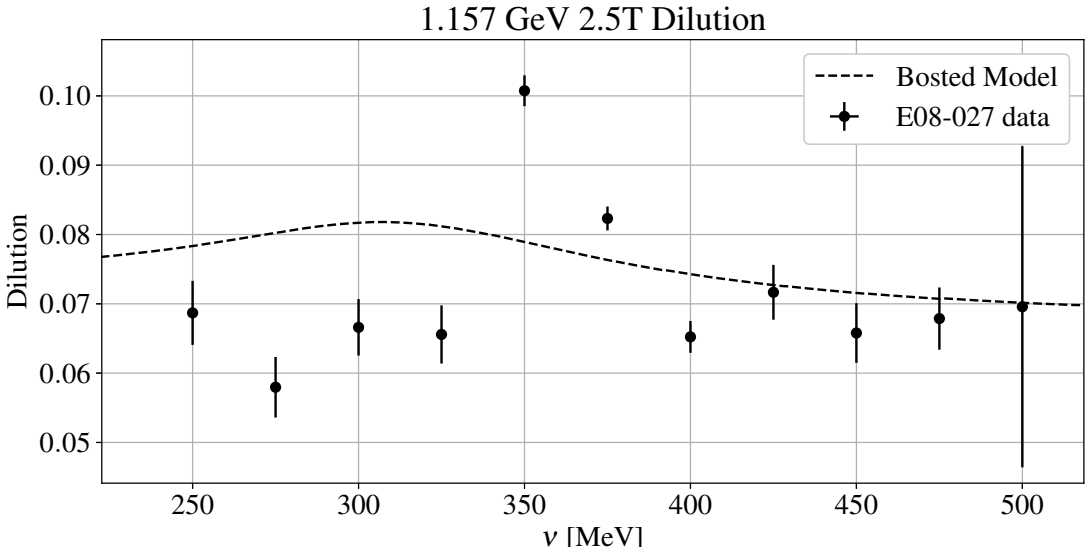

Figure C-1: Dilution analysis for E_o = 1.1GeV 2.5T Transverse.

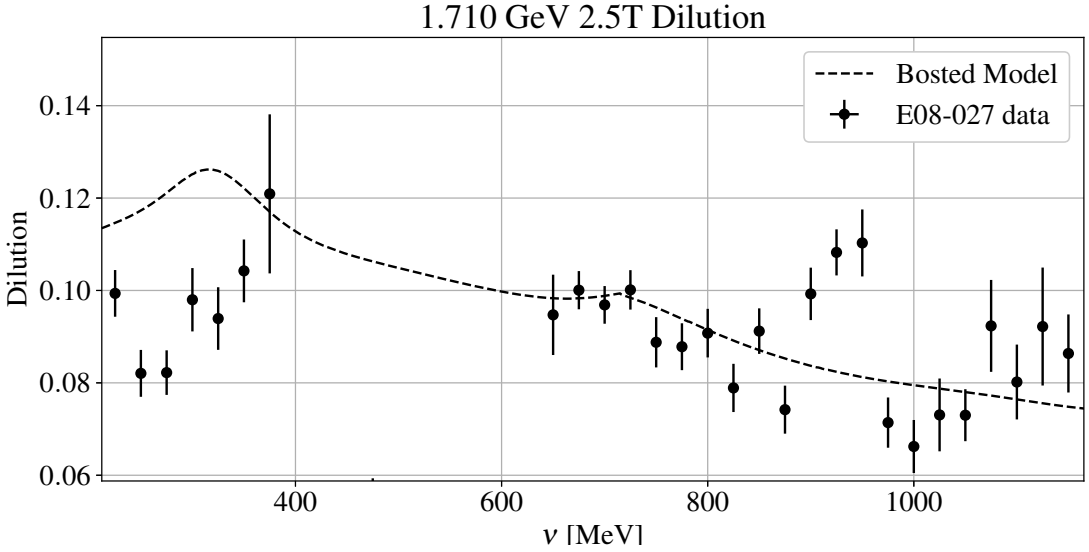

Figure C-2: Dilution analysis for E_o = 1.7GeV 2.5T Transverse.

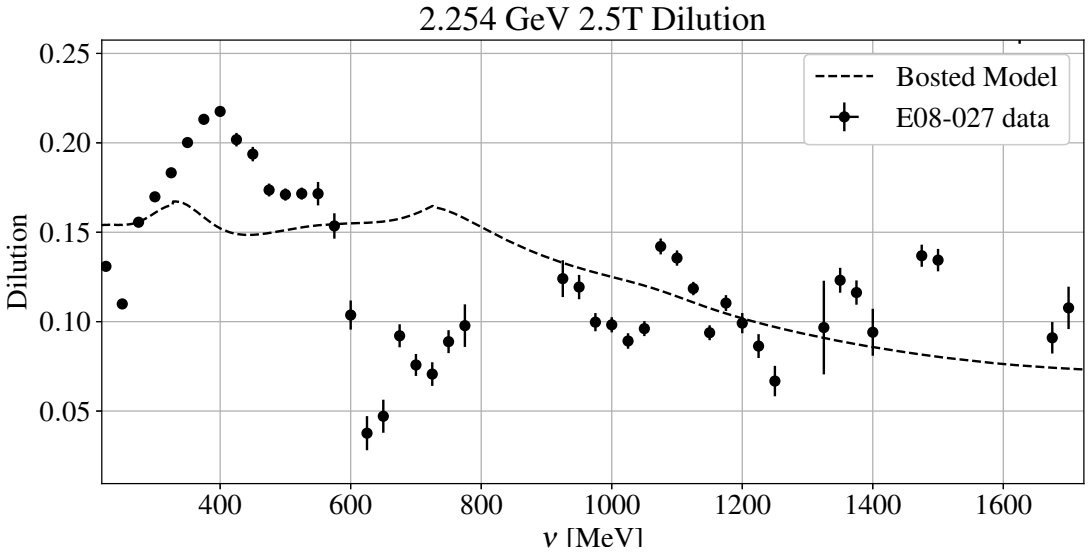

Figure C-3: Dilution analysis for E_o = 2.2GeV 2.5T Transverse.

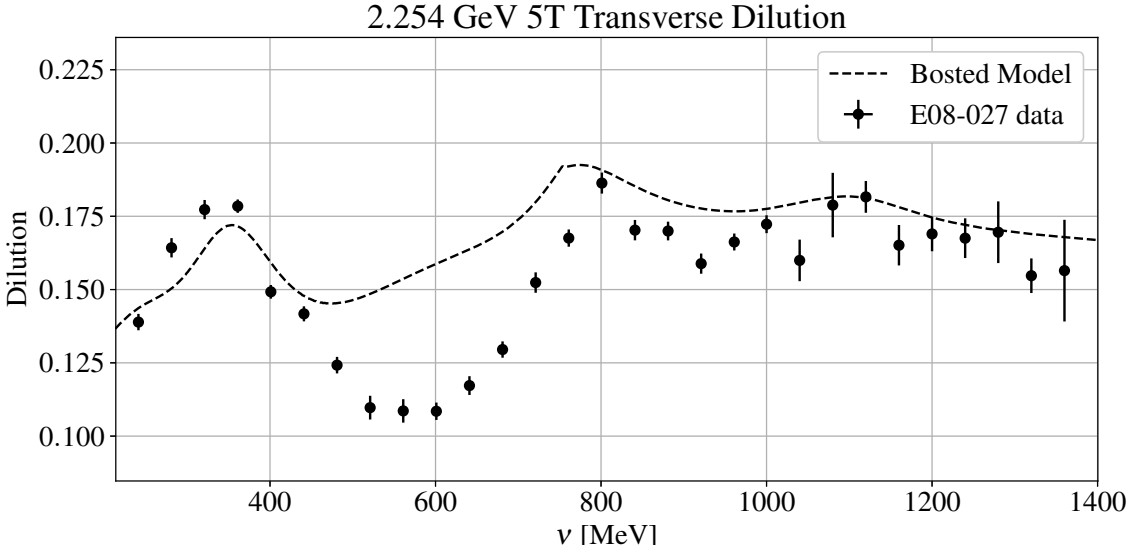

Figure C-4: Dilution analysis for E_o = 2.2GeV 5T Transverse.

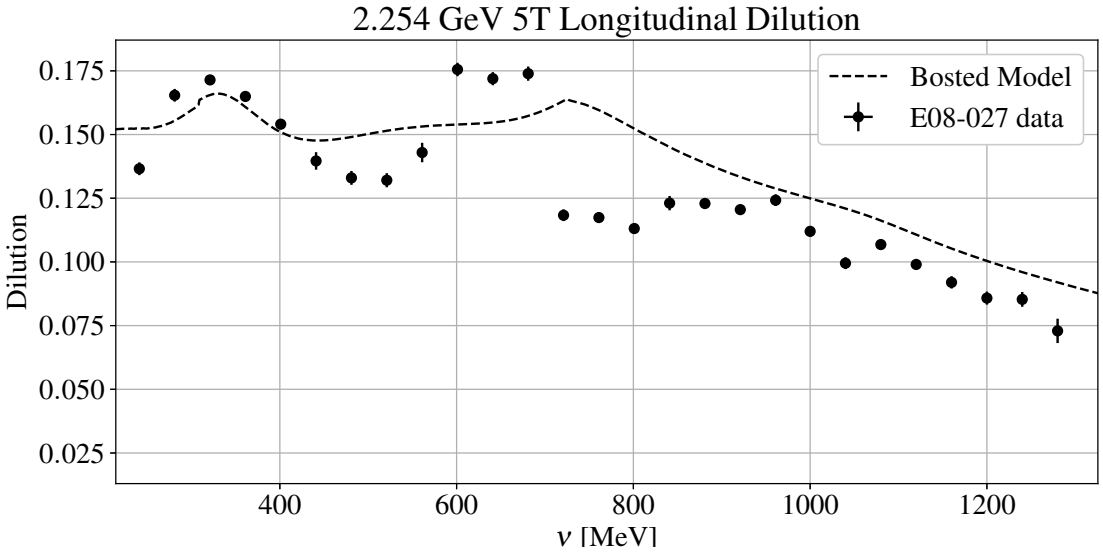

Figure C-5: Dilution analysis for E_o = 2.2GeV 5T Longitudinal.

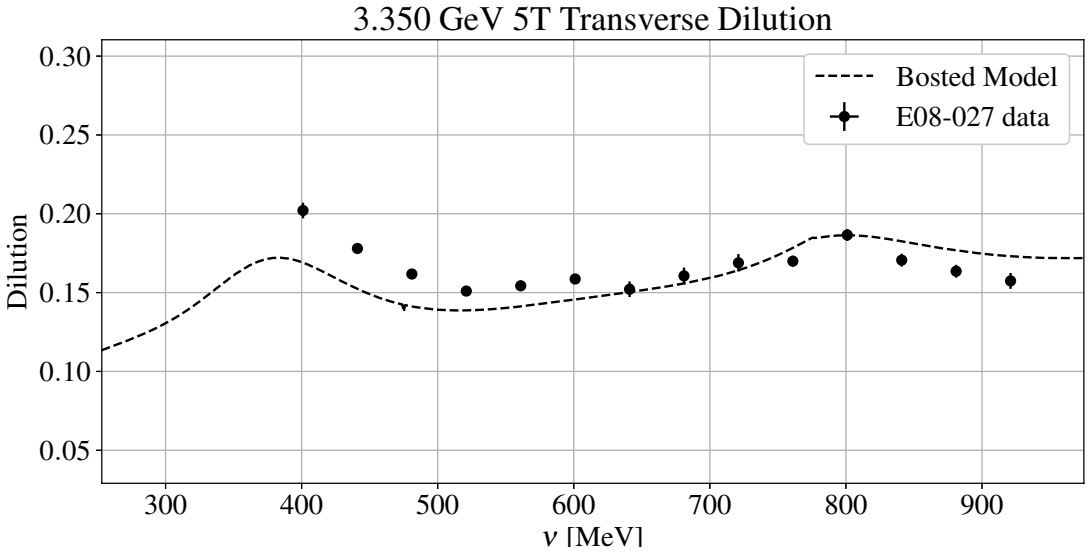

Figure C-6: Dilution analysis for E_o = 3.3GeV 5T Transverse.

Bibliography

[1] G. Lamazdi. Moller measurements for e08-027 (g2p) and e08-007. *http://hallaweb.jlab.org/equipment/moller/e08-027.html*.

[2] Ryan Zielinski. Radiation thickness, collisional thickness, and most probable collisional energy loss for e08-027. Technical report, University of New Hampshire, 2016.

[3] Christoph W. Leemann, David R. Douglas, and Geoffrey A. Krafft. The continuous electron beam accelerator facility: Cebaf at the jefferson laboratory. *Annu. Rev. Nucl. Part. Sci.*, 51:413–450, 2001.

[4] Chao Gu. Helicity decoder for e08-027. Technical report, University of Virginia, 2014.

[5] J. Alcorn et al. Basic instrumentation for hall a at jefferson lab. *Nuclear Instruments and Methods in Physics Research*, A(522):294–346, 2004.

[6] J. Maxwell. Anneal plot halog entry.

[7] Melissa Cummings. Efficiency studies and pid cut optimization for e08-027. Technical report, The College of William and Mary, 2013.

[8] Jie Liu. Vdc multi-track efficiency study for e08-027. Technical report, University of Virginia, 2013.

[9] Ryan Zielinski. Determining the trigger efficiency for e08-027. Technical report, University of New Hampshire, 2014.

[10] Pengjia Zhu. Beam position reconstruction for g2p experiment in hall a at jefferson lab. Technical report, 2014.

[11] Chao Gu. Spectrometer optics study for e08-027. Technical report, University of Virginia, 2016.

[12] Ryan Zielinski. Unpolarized radiative corrections. Technical report, University of New Hampshire, 2016.

[13] E. Rutherford. The scattering of α and β particles by matter and the structure of the atom. *Philosophical Magazine*, 21:669, 1911.

[14] W. Gerlach and O. Stern. Das magnetische moment des silberatoms. *Zeitschrift fur Physik A Hadrons and Nuclei*, 9:353-355, 1922.

[15] R. Frisch and O. Stern. Uber die magnetische ablenkung von wasserstoffmoleklen und das magnetische moment des protons. *Zeitschrift fur Physik A Hadrons and Nuclei*, 85:4-16, 1933.

[16] B. Povh, K. Rith, C. Scholz, and F. Zetsche. *Particles and Nuclei, An Introduction to the Physical Concepts*. Springer, 2008.

[17] D. Griffiths. *Introduction to Elementary Particles*. John Wiley and Sons Inc, 1987.

[18] A. Thomas and W. Weise. *The Structure of the Nucleon*. Wiley-Vch, 2001.

[19] F. Halzen and A. Martin. *Quakrs and Leptons: An introductory course in modern particle physics*. John Wiley and Sons Inc, 1984.

[20] E. Leader. *Spin in Particle Physics*. Cambridge University Press, 2005.

[21] R. Feynman. Very high-energy collisions of hadrons. *Phys. Rev. Lett.*, 23(24):1415-1417, 1969.

[22] D. Drechsel, S. S. Kamalov, and L. Tiator. Gerasimov-drell-hearn sum rule and related integrals. *Phys. Rev. D*, 63(114010), 2001.

[23] K. Slifer. *Ph. D. thesis*. PhD thesis, Temple University, 2004.

[24] F. J. Gilman. *Phys. Rev. Lett.*, 167:1365, 1968.

[25] L. N. Hand. *Phys. Rev. Lett.*, 129:1834, 1963.

[26] W. Marciano and H. Pagels. Quantum chromodynamics. *Physics Reports*, 36(3):137–276, 1978.

[27] S. Scherer. Inroduction to chiral perturbation theory. *Adv. Nucl. Phys.*, 27:277, 2003.

[28] K. Wilson. Non-lagrangian models of current algebra. *Physical Review*, 179(5), 1969.

[29] A. Manohar. An introduction to spin dependent deep inelastic scattering. *arXiv:hep-ph/9204208*, 1992.

[30] R.L. Jaffe. The nucleon's other spin-dependent structure function. *Comments Nucl.Part.Phys.*, 19(5):239–257, 1990.

[31] S. Wandzura and F. Wilczek. Sum rules for spin-dependent electroproduction. *Phys. Lett. B*, 72(2):195–198, 1977.

[32] J.P. Ralston J.L. Cortes, B. Pire. Measuring the transverse polarization of quarks in the proton. *Phys. C - Particles and Fields*, 55:409, 1992.

[33] H. Burkhardt and W. N. Cottingham. Sum rules for forward virtual compton scattering. *Annals of Physics*, 56(2):453, 1970.

[34] E.V. Shuryak and A.I. Vainshtein. Theory of power corrections to deep inelastic scattering in quantum chromodynamics. *Nuclear Physics B*, 201(1):141, 1982.

[35] J.-P. Chen. Moments of spin structure functions: Sum rules and polarizabilities. *International Journal of Modern Physics E*, 19:1893, 2010.

[36] F. E. Low. Scattering of light of very low frequency by systems of spin 1/2. *Physical Review*, 96(5):1428, 1954.

[37] D. Drechsel, S.S. Kamalov, and L. Tiator. Unitary isobar model - maid2007. *Eur. Phys. J. A*, 34:69–97, 2007.

[38] N. Guler. Measurement of longitudinal double spin asymmetries and spin structure functions of the deuteron in the clas eg1b experiment. Technical report, CLAS EG1b Collaboration, 2012.

[39] P. E. Bosted and M. E. Christy. Empirical fit to inelastic electron-deuteron and electron-neutron resonance region transverse cross sections. *Physical Review C*, 77(065206), 2008.

[40] Carlos Hernandez-Garcia, Patrick G. O'shea, and Marcy L. Stutsman. Electron sources for accelerators. *Physics Today*, 61(2)(44):44–49, 2008.

[41] Roger Flood, John Hansknecht, Scott Higgins, and Riad Suleiman. Helicity control board user's guide. Technical report, Jefferson Science Associates, 2010.

[42] R. Kazimi et al. Proceedings of particle accelerator conference. *IEEE, 0-7803-3503*, 1996.

[43] Pengjia Zhu. Beam charge measurement for g2p experiment. Technical report, Jefferson Lab, 2015.

[44] C. Yan, J. Beaufait, P. Brindza, R. Carlini, W. Vulcan, and R. Wines. Beam raster system at cebaf. Technical report, Continuous Electron Beam Accelerator Facility.

[45] Chen Yan. Slow raster system for polarized target experiments. Technical report, Jefferson Lab Hall C, 2008.

[46] A. Camsonne et al. A measurement of g2p and the longitudinal-transverse spin polarizability. Technical report, The Jefferson Lab Hall A Collaboration.

[47] K. Fissum, W. Bertozzi, and J. Chen et al. Vertical drift chambers for the hall a high-resolution spectrometers at jefferson lab. *Nuclear Instruments and Methods in Physics Research A*, 474:108, 2001.

[48] M. Iodice, E. Cisbani, and S. Colilli et al. The co2 gas cherenkov detectors for the jefferson lab hall-a spectrometers. *Nuclear Instruments and Methods in Physics Research A*, 411:223, 1998.

[49] T. Avertt et al. A solid polarized target for high-luminosity experiments. *Nuclear Instruments and Methods in Physics Research A*, 427:440, 1999.

[50] J. Pierce and J. Maxwell et al. Dynamically polarized target for the g2p and gep experiments at jefferson lab. *Nuclear Instruments and Methods in Physics Research A*, 738:54–60, 2014.

[51] W. Meyer and K. H. Althoff et. al. Irradiated ammonia as target material for polarized proton targets. *Nuclear Instruments and Methods in Physics Research*, 215:65–69, 1983.

[52] D. G. Crabb and W. Meyer. Solid polarized targets for nuclear and particle physics experiments. *Annu. Rev. Nucl. Part. Sci.*, (47):67–109, 1997.

[53] M. Borghini and K. Scheffler. Experimental evidence for dynamic nuclear polarization by cooling of electron spin-spin interactions. *Phys. Rev. Lett.*, 26(22):1362–1365, 1971.

[54] G.R. Court and D.W. Gifford et. al. A high precision q-meter for the measurement of proton polarization in polarised targets. *Nuclear Instruments and Methods in Physics Research A*, 324(3):433–440, 1993.

[55] A. Masaike. Historical review on solid polarized targets. *Polarized Sources and Targets: Proceedings of the 11th International Workshop*, pages 1–8, 2007.

[56] D. Keller. Uncertainty in dnp target data for e08-007. Technical report, University of Virginia.

[57] Min Huang. Central scattering angle measurement. Technical report, Duke University, 2014.

[58] Oscar A. Rondon. The packing fraction and dilution factor in rss. Technical report, University of Virginia, 2006.

[59] Y. Qiang. Statistical fluctuation of prescaled events, elog entry. *https://hallaweb.jlab.org/dvcslog/g2p/170*.

[60] M. Cummings. *Investigating Proton Spin Structure: A Measurement of g_2^p at Low Q^2*. PhD thesis, The College of William and Mary, 2016.

[61] David Ruth. Elastic cross section empty run acceptance study and scale factor for e08-027. Technical report, University of New Hampshire, 2017.

[62] J. Arrington et al. Global analysis of proton elastic form factor data with two-photon exchange corrections. *Physical Review C*, 2(035205), 2007.

[63] N. Saito M. Hirai, S. Kumano. Determination of polarized parton distribution functions and their uncertainties. *Phys. Rev. D*, 69(054021), 2004.